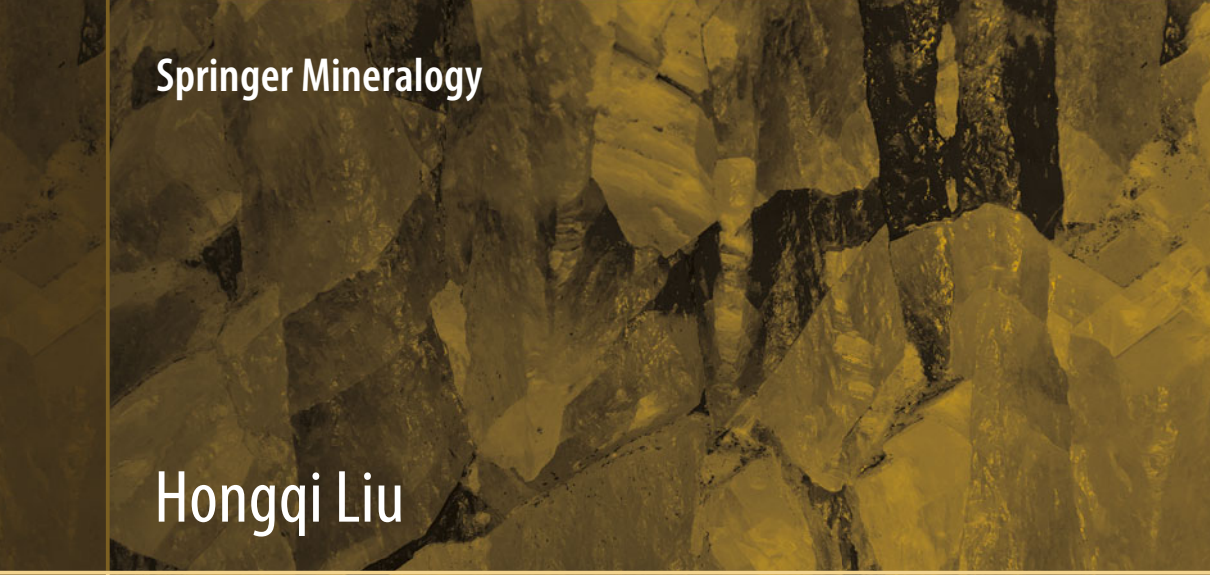

Springer Mineralogy

Hongqi Liu

Principles and Applications of Well Logging

石油工业出版社
PETROLEUM INDUSTRY PRESS

Springer

Springer Mineralogy

More information about this series at http://www.springer.com/series/13488

Hongqi Liu

Principles and Applications of Well Logging

石油工业出版社
PETROLEUM INDUSTRY PRESS

Springer

Hongqi Liu
School of Geoscience and Technology
Southwest Petroleum University
Chengdu, Sichuan
China

ISSN 2366-1585 ISSN 2366-1593 (electronic)
Springer Mineralogy
ISBN 978-3-662-53381-9 ISBN 978-3-662-53383-3 (eBook)
DOI 10.1007/978-3-662-53383-3

Jointly published with Petroleum Industry Press, Beijing, China

Library of Congress Control Number: 2016956466

Printed on acid-free paper

This Springer imprint is published by Springer Nature
The registered company is Springer-Verlag GmbH Germany
The registered company address is: Heidelberger Platz 3, 14197 Berlin, Germany

Preface 1

Well logging plays an increasingly important role in the petroleum industry, many engineers need knowledge of this technology. This book, including nine chapters, introduces conventional logging technology, imaging logging, and logging while drilling.

From Chaps. 1 to 3, we mainly present conventional logging method, i.e., normal resistivity logging, sonic velocity and amplitude logging, and natural radioactivity and induced radioactivity (neutron-gamma) logging. These three chapters are basic and are therefore very important. Chapter 4 focuses on nuclear magnetic resonance (NMR), which can provide pore's structural analysis. In Chap. 5, we emphasize about the production logging technology, which plays a prominent role ias healthy, safety and environmental (HSE) production is gradually becoming a standard for Chinese oil companies. As a milestone for the development of well logging and drilling technology, logging while drilling (LWD) and geosteering are the latest high technology, and these contents are introduced in Chap. 6. Besides LWD, imaging logging is another important phase in the history of well logging, Chap. 7 mainly explain Eclipse-5700, Excell 2000, and Sondex logging series technology. The new generation instruments can provide much higher vertical resolution and much deeper depth horizontal investigation images of well wall rather than curves. Sonic logging can provide information of compressional and shear compressional travel time, based on which rock mechanical properties can be evaluated. The basic concepts, methods, and a lot of empirical formula are included in Chap. 8. Chapter 9 presents a comprehensive interpretation, which integrates almost all the contents introduced in Chaps. 1–8. In Chap. 9, one can learn how to delineate upper depth and lower depth of permeable zone, how to identify the fluid types, and how to calculate porosity, permeability, saturation of oil, and etc.

Obviously, there are some errors and deficiencies in this version, the author do welcome suggestions and sincere advice from the readers.

Chengdu, China — Hongqi Liu

Preface 2

Although there are many excellent and famous technical books about well logging, it is still difficult to find a very suitable book for Chinese students. In twenty-first century, a lot of Chinese colleges have opened bilingual courses, and they are eager to find textbooks from the available science and technical books. Here this book meets the needs of the students who major in well logging.

A very classical Chinese novel of Qing dynasty, "A Dream of Red Mansions", has another name, i.e. "The Story of Stone". Although "Well Logging" concerns science and technology, in fact, it is also a record of a stone's story. The only difference between the famous novel and well logging lies in the former record stories of Jia Baoyu, Lin Daiyu, and other several hundreds of persons, but the latter is about the geophysical and petrophysical properties of rocks, especially the formation of water, oil, and gas.

How to find a hydrocarbon? Where to locate a hydrocarbon? And how much of the hydrocarbon can we extract from the formation? All these questions are frequently encountered during the exploration phase. As for the second phase, exploitation stage, there also many technological problems, such as evaluation of the cementation quality, safety window of drilling density, predication and calculation of the magnitude and direction of formation stress, flow quantity in the pipe, etc. All these questions can be solved completely in some degree.

Therefore, this book will tell large amount of stories about different stones, such as sandstone, shale, clay, limestone, and dolomite

This book includes conventional well logging methods, production logging, and new generation logging technology, such as imaging logging, logging while drilling (LWD).

The author would like to acknowledge the help received from a number of individuals, without which this book would not have been possible.

Hence, we owe thanks to the editors Tong He, Wei Li of Petroleum Industry Press. We also acknowledge Prof. Hongquan Xia for his advice, and graduate students Jie Tian, Bo Li, Ying Chen; they made a lot of maps and curves for this book.

Of course, the deficiencies, errors, and omissions, both in the text and in this acknowledgment, and the blames rest with us.

Chengdu, China Hongqi Liu

Contents

Chapter 1
Introduction

1.1 Origination of Well Logging

Well logging, as a terminology, is originated from France in 1927. Its primary meaning is electrical coring, which is a continuous record of characteristics of rock formations traversed by a measurement device in the well bore. Well logging, however, means different things for different people. For a geologist, it is primarily a mapping technique for exploring the surface. For a petrophysicist, it is a means to evaluate the hydrocarbon production potential of a reservoir. For a geophysicist, it is a source of complementary data for surface seismic analysis. For a reservoir engineer, it may simply supply values for use in a simulation.

The initial uses of well logging were for correlating similar patterns of electrical conductivity from one well to another, sometimes over large distance. As the measuring techniques improved and multiplied, applications began to be directed to the quantitative evaluation of hydrocarbon-bearing formations. Much of the following text is directed toward the understanding of the measurement devices and interpretation techniques developed for this type of formation evaluation.

Although well logging grew from the special need of the petroleum industry to evaluate hydrocarbon accumulations, it is relevant to a number of other areas of interest to earth scientists. A detailed analysis of measurement principles precedes the discussion of these applications. In this process, well logging is seen to require the synthesis of a number of diverse physical sciences: physics, chemistry, electrochemistry, geochemistry, acoustics, nuclear, and geology.

1.2 What Is Well Logging?

What is well logging? Well logging is the process of continuous recording various physical, chemical, electrical, or other properties of the rock or fluid mixtures penetrated by drilling a well into the earth's mantle. Logging also includes control

H. Liu, *Principles and Applications of Well Logging*, Springer Mineralogy,
DOI 10.1007/978-3-662-53383-3_1

of boreholes for technical condition, formation sampling, and sidewall coring. The process of logging involves a number of elements, which are schematically illustrated in Fig. 1.1.

The continuous recording of a geophysical parameter along a borehole produces a geophysical log. The value of the measurement is plotted continuously against depth in the well. For example, the resistivity log is a continuous plot of a formation's resistivity from the bottom to the top of the well and may represent over thousands of meters.

The most appropriate name of this continuous depth-related record is a wireline geophysical well log, conveniently shortened to well log or log. It has often been called an "electrical log" because historically the first logs were electrical measurements of electrical properties. However, the measurements are no longer simply electrical, and modern methods of data transmission do not necessarily need a wireline so the name above is recommended.

In its most usual form, an oil well log is a record displayed on a graph, with the measured physical property of the rock on one axis and depth (distance from the surface) on the other axis. More than one property may be displayed on the same graph. Some of the properties that can be measured are the following:

(1) the self(spontaneous) potential of rock/borehole fluid interface
(2) the resistivity of the rock at various distances from the borehole
(3) the acoustic travel time of the rock
(4) the neutron absorption cross-section
(5) the electron density of the rock
(6) the size of the borehole drilled in the rock

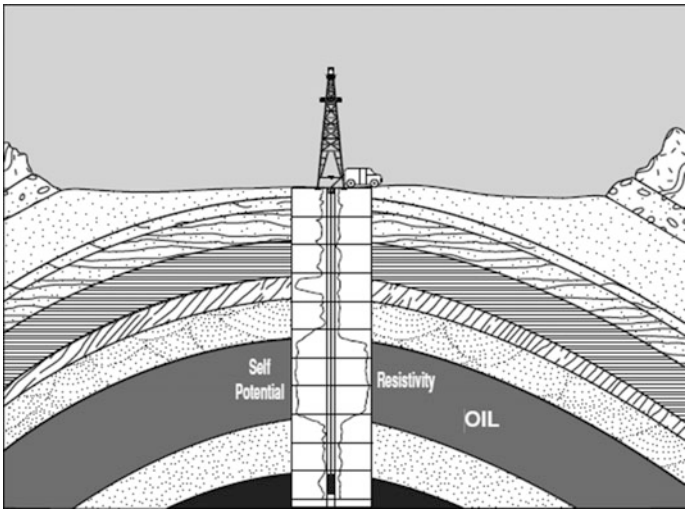

Fig. 1.1 The elements of well logging: a measurement sonde in a borehole, the wireline, and a mobile laboratory (Courtesy of Schlumberger)

(7) the flow rate and density of fluids in the well bore
(8) numerous other related or derived properties of the rock and well bore environment.

Our primary interest is the measurement device, or ***sonde***. Currently, over hundreds different categories of these logging tools, as shown in Fig. 1.2, exist in order to meet various information needs and functions. Some of them are passive measurement devices; others exert some influence on the formation being traversed. Their measurements are transmitted to the surface by means of the wireline.

1.3 Development of Well Logging

1.3.1 Resistivity Logs

The advent of well logging from the 1926 and its subsequent development into a sophisticated technology revolutionized the oil and gas exploration and exploitation industry. The ability to look and measure such things as formation type, formation dip, porosity, fluid type, and other important factors transformed the drilling and completion of oil and gas wells from an ill-defined art into a refined science. Logging development encompasses three major areas: electric logging, sonic or acoustic logging, and nuclear logging. An understanding of their development is an understanding of the industry's technical progress.

The genesis of electric well logging resides with Conrad Schlumberger, who conceived the idea of prospecting for metal ore deposits by using their electrical conductivity to distinguish them from their less conductive surroundings. Working with his brother Marcel Schlumberger, Conrad began a series of test surface surveys in Europe, Africa, and North America over a 3-year period. By lowering an electric sonde down a well in France's Pechelbronn field September 5, 1927, the brothers created the first well log.

Fig. 1.2 Different categories of well logging tools

In 1931, the accidental discovery of spontaneous potential (SP) produced naturally by the borehole mud at the boundaries of the permeable beds, led to an innovative new logging technique simultaneously recording SP and resistivity curves. This technique enabled producers to differentiate permeable oil-bearing beds from impermeable, nonproducing ones.

The 1940s were a period of rapid development in logging technology despite the intervention of World War II. In 1941, logging took another major step forward, this new tool allowed the calculation of a layer's dip. This measurement was improved further with the resistivity dip meter in 1947, and the continuous resistivity dip meter in 1952.

The Micro-log recording is also useful to delineate permeable beds, and other resistivity devices help establish the resistivity profile from the invaded zone near the borehole to the noninvaded virgin formation. The Micro-laterolog tool was developed for salt muds in 1953. The Micro-Proximity log and Micro-SFL* log have followed.

In 1951, the laterolog tool, the first focused deep investigating resistivity device, was introduced. It uses a focusing system to constrain the surveying current (emitted from a central electrode) to substantially a horizontal disc for some distance from the sonde. Focused resistivity logs are well adapted for investigation of thin beds drilled with low-resistivity muds. The laterolog device quickly supplanted conventional resistivity logs in salt muds and highly resistive formations.

Over the years, several laterolog tools were developed and used commercially. Today, the DLL* dual laterolog tool, which consists of deep laterolog and shallow laterolog measurements, is the standard. It is usually run with a Micro-SFL device as well. In freshwater muds, the original electrical log has been replaced by the induction log. The induction log was developed in 1949, as an outgrowth of wartime work with mine detectors, for use in oil-base mud. However, its superiority over the electrical log in freshwater muds was soon recognized. The DIL* dual induction log, introduced in 1963, is now the standard. It consists of deep induction, medium induction, and shallow resistivity measurements. The shallow resistivity-measuring device is now a focused resistivity device—a Laterolog 8 on the 1963 tool and an SFL device on current tools. A new dual induction log, the Phasor* induction, provides improved thin-bed response, deeper depth of investigation, and greater dynamic resistivity range.

By 1970, the sector was poised on the brink of significant advances in logging technology, particularly in the field of nuclear logging. But advances still were being made in electric logging, especially in the area of mass and speed of data collection. The year 1971 saw the introduction of combination logging systems. Combos allowed loggers to acquire different sets of data simultaneously rather than in sequential runs. Thus were born tools that provided gamma ray, SP, resistivity, sonic, and caliper measurements in a single run. In 1972, DLL Dual Laterolog tool was introduced for simultaneous measurement of shallow region invaded by borehole fluids and the deep undamaged formation. In 1977, commercialized the EPT Electromagnetic Propagation Tool was first used in oilfield.

In 1991, Schlumberger delivered their first imaging logging tool, Formation Micro-Imager tool (FMI), which marked well logging technology came into a new era.

1.3.2 Sonic Logs

Since the 1930s, logging cables have been used to lower geophones into wells to measure long-interval acoustic travel times from sound sources at the surface.

In 1946, the first sonic log was produced. This tool allowed more accurate depth measurement inside casing and more exact placement of perforations and completion equipment. Sonic logs generally work by generating signals in the 20–30 kHz range, although some tools operate at higher ranges. Most acoustic logging tools have centralizers at one end and three caliper arms at the other end to keep the tools centered in the hole. Two receivers at the lower end of the tool receive the signal.

In the late 1950s, the sonic log gained acceptance as a reliable porosity log; its measurement responds primarily to porosity and is essentially independent of saturation. The sonic log, coupled with the focused resistivity logs-laterolog and induction-made possible modern formation evaluation from well logs. The sonic log provided a measurement of porosity; the focused resistivity logs, a measurement of true resistivity of the noninvaded virgin formation.

Subsequent improvements in sonic logging included the BHC borehole compensated sonic, the LSS* long-spaced sonic, and the Array-Sonic* tools. The latter tools permit the recording of the entire sonic wave train. From an analysis of the wave train, the shear and Stoneley transit times can be extracted as well as the compressional transit time.

1978 Developed the SDT tool, the first-generation digital sonic tool for uphole processing of compressional and shear sound speeds in formations. 1984 Founded Anadrill by combining the drilling segment of Dowell and the Analysts. Developed ultrasonic CET Cement Evaluation Tool for adding azimuthal information to cement bond analysis.

1.3.3 Nuclear Logging

Logging using radiation of nuclear origin got its start in 1940. The initial nuclear logging tools recorded the natural gamma radiation emitted by the formations crossed through by boreholes. From passive radioactive monitoring in the gamma ray tool, the logging industry moved rapidly to active nuclear bombardment and measurement.

In a formation density log, first introduced in 1962, the borehole wall is irradiated with a gamma ray source. A gamma ray counter then records the reflected

rays. The logging of formation bulk density, another measurement primarily dependent on formation porosity, was commercially introduced in the early 1960s. An FDC* compensated formation density log, which compensated for the mud cake, quickly followed in 1964. In 1981, the Litho-Density* log provided an improved bulk density measurement and a lithology-sensitive photoelectric absorption cross-section measurement.

It was not until the introduction of the SNP, sidewall neutron porosity tool, in 1962 and the CNL* compensated neutron tool in 1970 that the neutron gained acceptance as a porosity measurement. The Dual Porosity neutron tool combines those two neutron measurements into a single tool.

The industry took nuclear logging one step further with the introduction of neutron logs in the late 1960s. Neutron logs also measure returned gamma rays, but in this instance, those generated by fast- or slow-moving neutrons. Neutrons are emitted by mixed radioactive sources. Most of the (neutron's) energy lost is done so during collisions with hydrogen nuclei. Since the distance a neutron can travel without hitting a hydrogen nuclei varies with the amount of hydrogen present, both porosity and formation contents can be determined. The original neutron logs were augmented later by pulsed neutron logs and neutron spectroscopy logs.

One of the biggest breakthroughs in logging history has been the advent of nuclear magnetic resonance (NMR) logging. The technology has existed since the early 1960s, but it has taken several decades to refine the process, with Numar—now a Halliburton subsidiary—the first to bring a continuous NMR logging tool to the market. The technology has proven more potentially beneficial and more confounding than its early developers could have imagined. NMR tools function by creating a magnetic field in the borehole and then sending out pulses that polarize the hydrogen in water, oil, and gas in the formation. As these hydrogen nuclei realign themselves to the original magnetic field, they induce signals in the tool's receiver, which are recorded by electronics. 1986, Prototyped CMR Combinable Magnetic Resonance tool

When time went into the 1990s and new century, well logging technology has a rapid and dramatic development, for the aim of concise content, some important things of Schlumberger company were listed in the following.

- 1980 Completed first measurement-while-drilling (MWD) job in the Gulf of Mexico.
- 1988 Introduced first logging-while-drilling (LWD) tool
- 1989 Introduced MAXIS 500 logging unit
- 1991 Geosteering was used for the first time to plan the drilling path in horizontal wells.
- 1993 Schlumberger launched IDEAL concept (Integrated Drilling Evaluation and Logging System) and ran first compressional sonic logs while drilling.
- 1995 Introduced ARC5 LWD tools, and MAXIS Express logging unit.
- 1996 Conceived real time reservoir management for improving hydrocarbons recovery and providing high-end IT solutions to industry, completed first commercial sonic imaging job.

- 1997 Introduced ClearFRAC nonpolymer, damage-free fracturing fluid
- 1998 Acquired Camco International, Inc. Introduced PS PLATFORM fifth-generation production logging tool and HRLA High Resolution Laterolog Array
- 1999 Deployed Houston remote connectivity teleport.
- 2002 Introduced proVISION real time reservoir steering tool for LWD; OrientXact perforating system; Slim-Xtreme slim-hole high-pressure, high-temperature wireline logging platform; and FlexSTONE flexible cementing system.
- 2003 Launched PowerDrive Xceed fully rotational steerable system; seismicVISION LWD system;
- 2004 Launched the PowerDrive X5 rotary steerable system with integrated measurements, sonicVISION sonic-while-drilling tool, and PowerDrive vorteX rotary steerable system.
- 2005 Launched Scope family of while-drilling technology services: StethoScope formation pressure, TeleScope high-speed telemetry, PeriScope deep directional resistivity, and EcoScope multifunction formation evaluation.
- 2006 Introduced the Quick-silver Probe wireline sampling technology, a method to deliver formation fluid samples quickly with little to no contamination
- 2007 Completed acquisitions of Geosystem (land and marine electromagnetics and seismic imaging) and Tyumen promgeofizika (geophysical and wireline logging); integrated Geosystem into Western Geco Electromagnetics.

1.4 Use of Logs

Well logging, from its origination about 100 years ago, has been proofed an utmost useful technology both in exploration and exploitation. Its measurements occupy a central position in the whole life of a well. The traditional role of well logging lies in two domains: formation comprehensive evaluation and completion evaluation.

For the first part, it can be summarized in four key questions of primary phase:

(1) Are there any hydrocarbons, and if so are they oil or gas?

For this question, resistivity logging, sonic logging and radioactivity logging can answer. For example, based on SP and GR curves, the permeable zones, which always bearing oil and gas, can be located easily. Through curves overlap, using sonic, density, and neutron curves can identify gas zone.

(2) Where are the hydrocarbons?

That means we must assure the depth of the formations which contain accumulations of hydrocarbons must be identified. Based on the GR or SP curves, the top and bottom depth of a permeable zone can be delineated, and then, we can know the thickness of a pay zone.

(3) How much hydrocarbon was contained in the formation?

An initial approach is to give a quantity evaluation of the hydrocarbon in the formation. Two utmost important parameters, porosity, and saturation of formation water or of hydrocarbon, must be acquired in order to calculate the quantity of hydrocarbon. In addition to these two parameters, thickness of formation which contain hydrocarbon was also needed.

(4) How producible are the hydrocarbons?

In fact, all questions will come down to this one practical concern, which is just the most difficult one to answer. The reason is an most important parameter, permeability of the formation, which is the most uncertainty one. Many empirical methods are used to extract permeability from logging with varying degrees of success.

The second domain of well logging is completion evaluation, which consist of a diverse group of logging tools, such as cement bond quality logging, stability of borehole wall, flow rate, density of the fluid in pipe, temperature, and pressure in pipe or formation. If a field went into late life, many pay zones will be flooded by injected water or original formation water. Production engineer concerned how much degree of the water-flooded? What about the saturation of residual oil? How long will a well sustain production?

All of these above questions can be solved completely or in some degree by well logging technology.

Assignments

1. What is well logging (WL)?
2. What are the applications of well logging?

Chapter 2
Electrical Logging

2.1 The Foundation of Electrical Resistivity

The resistivity of a substance is its ability to impede the flow of electrical currents. The ability of a formation to conduct electricity is directly related to the amount of water in the formation. This is true since the formation grains (matrix) have negligible conductivity (high resistivity). By understanding bed resistivity, it is possible to determine the "water saturation" of a formation and hence its hydrocarbon saturation. Formation resistivity can also be related to the porosity of the formation.

2.1.1 Resistivity

Electrical resistivity of any material is related to the resistance by the following equation:

$$R = r \times a/L,$$

where

a area in square meters of rock material exposed to the current flow
L length of the material in meters
r electrical resistance in ohms
R electrical resistivity expressed in ohm-meters.

Formation resistivities usually range from 0.2 to 1,000 Ω-m. Resistivities higher than 1,000 Ω-m are uncommon in permeable formations. Most formations are made up of rocks which when dry will not conduct electrical currents. Current flow in a formation is through interstitial water made conductive by salts in solution. These salts dissociate into positively charged sodium cations and negatively charged

H. Liu, *Principles and Applications of Well Logging*, Springer Mineralogy,
DOI 10.1007/978-3-662-53383-3_2

anions. Ions move under the influence of an electrical field, carrying an electrical current through the solution. Greater salt concentration lowers the formation water resistivity,

The resistivity of the water is:

$$\text{Resistivity} = (R_w \times L)/a$$

We measured R_w with a test meter. L is the length of the cube, which is 1 m. The area is 1 m by 1 m. Solving the equation:

$$\text{Resistivity} = (R_w \times 1)/(1 \times 1) = R_w$$

In this case, the resistivity of the water is the same as its measured resistance.

Now let us take one cubic meter of formation rock and insert it into the cube filled with water. What happens to some of the water? Yes, it spills over as the rock occupies the volume. Looking at Fig. 2.1, we now have a cube with formation rock that is 100 % saturated with water. The resistivity of this cube is called R_o.

When the cube had only water, it was simple to see that an ion could travel from one side of the cube to the other in a straight path. The length of this travel was 1 m. Now that we have added the formation rock to the cube, the ion must find a meandering path, greater than 1 m, around the rock grains to go from one side to the other.

The length of this ion cannot be measured. The best that can be done is simply to estimate it based on the texture of the rock, the cementation, and the amount of pore space available. We will consider this in more detail later in the text.

To complete our cubic reservoir, let us take some water out and replace it with oil. Because the oil is lighter than the water it will float on top. We still have the length L; the porosity factor; and the resistivity of the water to consider. The only difference is that we no longer have 100 % water. We took some out and replaced it with oil (Fig. 2.1). If we took out 40 % of the water, then we would have 60 % left

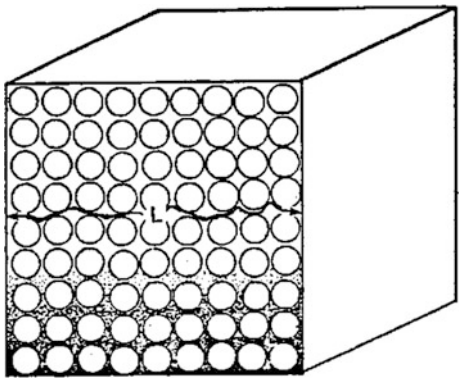

Fig. 2.1 Model of a rock bearing liquid

in the cube. This 60 % is called the water saturation, or S_w. Now the total resistivity of the cube is:

$$\text{Resistivity} = (R_w \times L)/(\emptyset \times S_w)$$

In reality, the water saturation is what we want to know. If we can measure the total resistivity, the porosity, the water resistance, and estimate the length L, then we can solve the equation for S_w. It then follows that the amount of hydrocarbons is $1 - S_w$.

It should be mentioned here that the resistivity of the water is not only a function of salinity but also of temperature. The higher the temperature is, the lower is the resistivity at a given salinity, so that water resistivity will vary according to temperature.

The following equation shows the general method for calculating formation temperature so that it can be applied toward adjusting the resistivity of the formation itself.

$$T_f = T_o + (G_g \times D_f)/100,$$

where

T_f the formation temperature
T_o the mean annual surface temperature
G_g the geothermal gradient expressed in °F per 100 ft
D_f the formation depth in feet.

Surface temperature is defined as the average annual temperature at some depth, typically from 70 to 100 ft below the surface of the earth, where seasonal temperature variations average out. This surface temperature may vary according to location.

For the purpose of log analysis, however, surface temperatures 5–10° higher than these produce more satisfactory results. Formation temperature may also be determined from the chart in Fig. 3.2.

Because mud filtrate invades the formation, it is important for us to know what the mud filtrate resistivity is. The mud filtrate resistivity is measured at the surface with a cup-type device, and that resistivity is adjusted for temperature at the formation depth.

$$R_2 = R_1 \times \frac{T_1 + 6.77}{T_2 + 6.77}$$

This is the ARPS formula for determining resistivity at formation temperature. T_1 is the mean surface temperature expressed in °T. T_2 is the formation temperature in °T. R_1 is the resistivity at T_1, and R_2 is the resistivity at T_2.

In a formation containing oil or gas, both of which are insulators, resistivity is a function of the formation factor F, the water resistivity R_w, and the water saturation

S_w. The ***saturation*** of a fluid in a formation is the ratio of the volume occupied by the fluid to the total pore volume, i.e., it is the fraction of the porosity occupied by that particular fluid. If the fluid is formation water, then its saturation S_w, is:

$$S_w = V_w/V_p$$

where, V_w is volume occupied by formation water, and V_p if volume of pores. If there no other fluids present, then $V_w = V_p$, and $S_w = 1.0$. If some hydrocarbon (V_h) is present, then $V_h = V_p - V_w$, and now:

$$S_w = (V_p - V_h)/V_p = V_w/V_p$$

N.B. Saturation is a dimensionless quantity being a ratio. It is expressed either as a decimal ($0 < S_w < 1.0$) or as a percentage ($0\ \% < S_w < 100\ \%$).

2.1.2 Archie Formula

As discussed earlier, the unknown factor is the length of the path of the ionic current. The length of this path is 1 m for R_w and greater than one for R_o, which is the true resistivity of the formation of porosity totally saturated with water of resistivity R_w. This unknown quantity is called the formation resistivity factor or simply F. This factor is defined as:

$$F = R_o/R_w$$

For a constant porosity, the ratio of R_o to R_w remains nearly constant for all values of R_w below 1 Ω-m. Experiments show that in more resistive waters, the value of F is reduced as R_w rises. This phenomenon is due to a greater influence of the surface conductance of the grains in fresh waters.

The value of R_o, should be calculated, rather than picked from the log. Finding a clean zone that is 100 % saturated with water is a difficult task. This places us in a difficult position because we must know the value of the formation factor.

Archie experimentally determined that the formation factor could be determined from three factors, i.e., porosity (φ), cementation (m) and rock texture (a). So the above equation can be expressed as:

$$\mathrm{F} = \frac{R_o}{R_W} = \frac{\alpha}{\varphi^m},$$

where a is a coefficient varies from 0.6 to 2.0 depending on the texture of rock, and m is the cementation or tortuosity factor. It varies between 1 and 3 according to the type of sediment, the pore-shape, the type of porosity, and its distribution.

If hydrocarbon is presented in pores, the resistivity of the formation is not R_o, but R_t, and the water saturation is not equals to 100 %. Through a large number of laboratory measurements, Archie determined experimentally that the water saturation of a clean formation can be expressed in terms of its true resistivity.

$$s_w^n = R_o/R_t,$$

where n is the saturation exponent. It is determined empirically, and lies between 1.2 and 2.2.

Combining the above two equations we can get the so-called Archie equation:

$$S_W = \sqrt[n]{\frac{\alpha R_W}{R_t \emptyset^m}}$$

Through extensive use of this relationship, the following values have been used with great success:

$$F = 0.81/\emptyset^2 \quad \text{in sands rocks}$$

$$F = 1/\emptyset^2 \quad \text{in carbonate rocks}$$

These two formulas are similar to the Humble formula developed from an intensive study of sandstone samples in the 1950s.

2.1.3 Electrical Properties of Rocks and Brines

There are two general types of conduction of interest to us: electrolytic and metallic. In **electrolytic** conduction, the mechanism is dependent upon the presence of dissolved salts in a liquid such as water. Examples of electrolytic conduction are provided with metal, which are not covered here.

The following Table 2.1 illustrates the resistivity of some typical materials. Notice the range of resistivity variation for salt water, which depends on concentration of NaCl. Typical rock materials are in essence insulators. The fact that reservoir rocks have any detectable conductivity is usually the result of the presence of electrolytic conductors in the pore space. In some cases, the resistivity of a rock may result from the presence of metal, graphite, metal sulfides, or clays. The table shows that the resistivity of formations of interest may range from 0.5 to 103 Ω m, nearly four orders of magnitude.

The conductivity of sedimentary rocks is primarily of electrolytic origin. It is the result of the presence of water and combination of water and hydrocarbons in the pore space in a continuous phase. The actual conductivity will depend on the

Table 2.1 Typical resistivity value of rocks, minerals, and fluids

Medium	Resistivity (Ω m)	Medium	Resistivity (Ω m)
Clay	1–200	White mica	4×10^{11}
Clay (mud rock)	5–60	Feldspar	4×10^{11}
Shale	10–100	Petroleum	10^{9}–10^{16}
Unconsolidated sand	2–50	Calcite	5×10^{3}–5×10^{12}
Tight sand	20–1000	Graphite	10^{-6}–3×10^{-4}
Oil-sand	2–1000	Madnetite	10^{-4}–6×10^{-3}
Shell-limestone	20–2000	Pyrite	10^{-4}
Limestone	50–10,000	Copper pyrite	10^{-3}
Dolomite	50–10,000	Oil and gas	
Basalt	60–10^{5}	Gas	
Granite	60–10^{5}	Brine (15 °C, 2 kppm)	3.4
Anhydrite	10^{4}–10^{6}	Fresh water	
Quartz	10^{12}–10^{14}		

resistivity of the water in the pores and the quantity of water present. To a lesser extent, it will depend on the lithology of the rock matrix, its clay content, and its texture (grain size, and the distribution of pores, clay, and conductive minerals). Finally, the conductivity of a sedimentary formation will depend strongly on temperature.

Figure 2.2 graphically presents the resistivity of saltwater (NaCl) solutions as a function of electrolyte concentration and temperature. According to the preceding analysis, the resistivity is expected to depend inversely on the charge carrier concentration.

2.1.4 Borehole Environment

Before concluding this chapter, let us examine the schematic representation of a well bore (Fig. 2.3a, b). R_{mc} is the mud cake resistivity, h_{mc} is the thickness of the mud cake, D_i is the diameter of invasion, h is the bed thickness, D_h is the hole diameter, R_{xo} is the resistivity of the flushed portion of the invaded zone, R_{mf} is the resistivity of the mud filtrate, and S_{xo} is the flushed zone water saturation.

In the uninvaded zone, R_t is the true virgin formation resistivity. R_w is the formation water resistivity, and S_w is the water saturation of the undisturbed formation. Water saturation in the undisturbed or uninvaded zone is the parameter we are most interested in. Its determination allows the log analyst to estimate the amount of hydrocarbons present in a given formation. This information, along with porosity and a permeability estimate, can be used to predict the well's ultimate production.

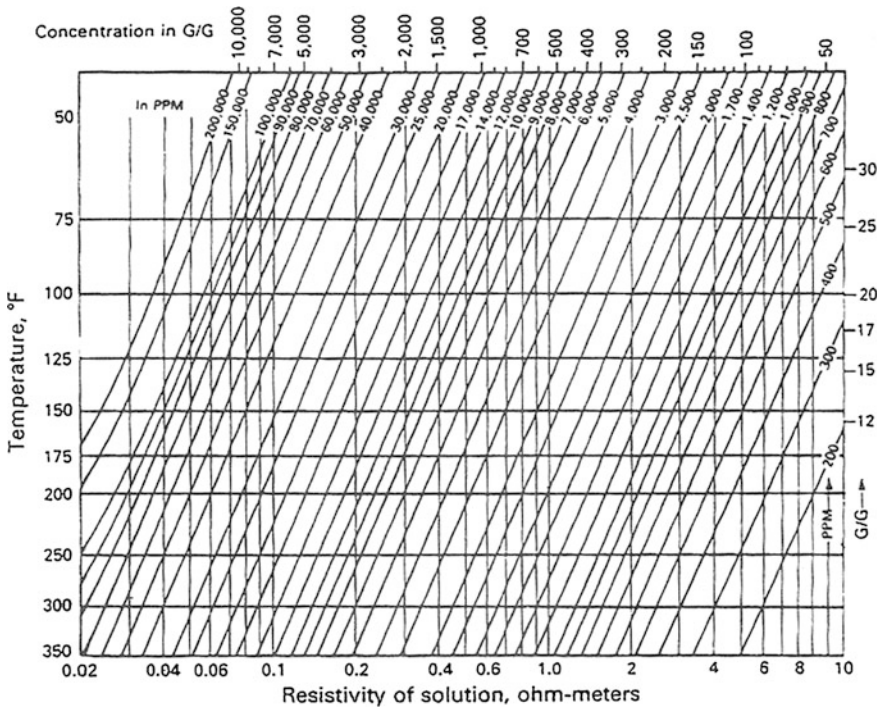

Fig. 2.2 A nomogram for determining the resistivity of an NaCl solution as a function of the NaCl concentration and temperature (from Schlumberger)

2.1.5 Conclusions

It is not important to fully understand each concept presented in this chapter. The purpose is to acquaint you with the basic terms and relationships of analysis. Everything presented here will be covered in great detail in chapters to follow.

2.2 Spontaneous Potential Logging

The spontaneous potential (or SP) curve is a recording of naturally occurring earth potentials between a moveable electrode in the borehole and a fixed surface electrode. Such potentials are in no way induced by the passive measuring equipment. For this reason, SPs are also referred to as "self potentials." The SP is generally recorded in the left-hand track of the log. The SP is used to:

- Detect permeable beds.
- Locate their boundaries and permit correlation of such beds.

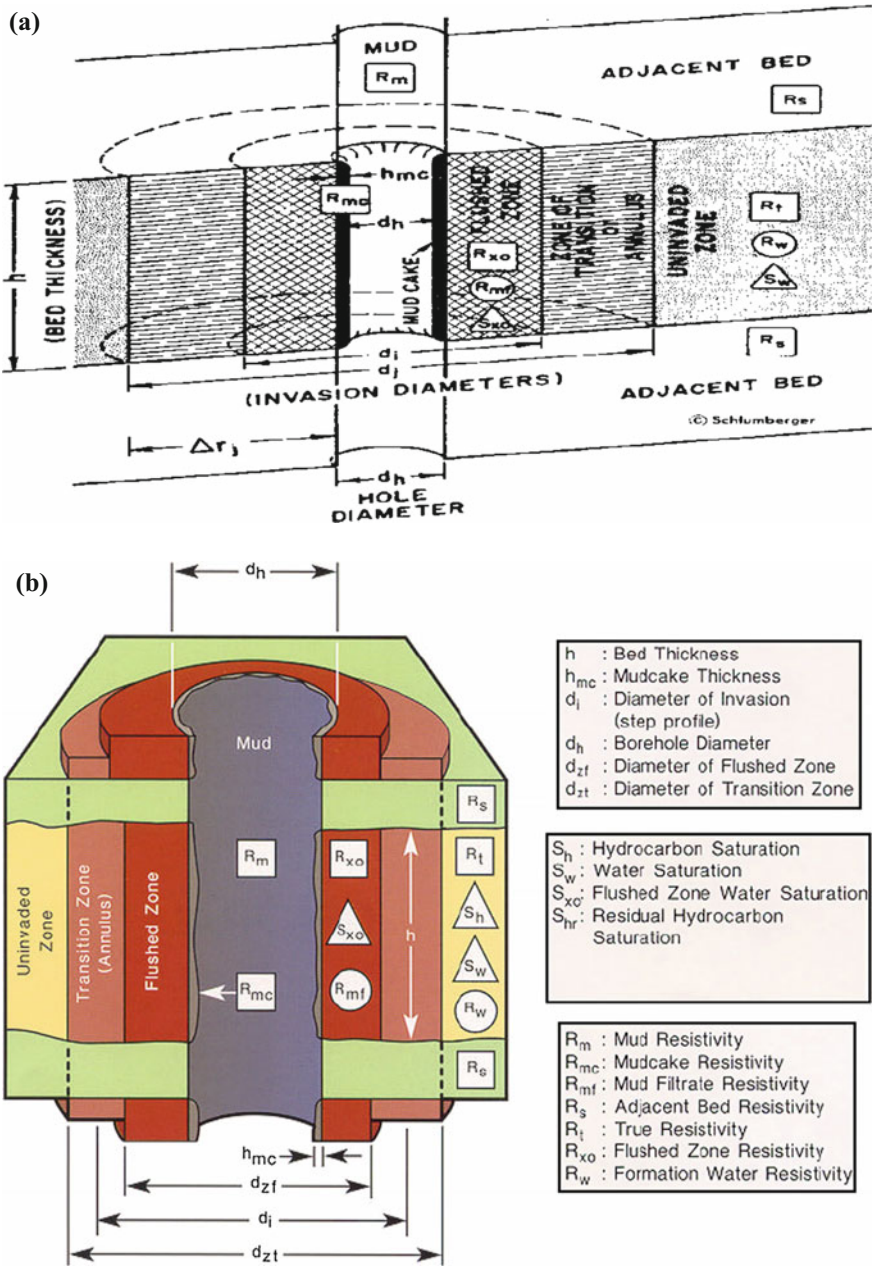

Fig. 2.3 **a** Environment around borehole, **b** Environment around borehole

- Determine values of formation water resistivity (R_w).
- Give quantitative indications of bed shaliness.

The readings of the SP in shale are usually fairly constant and tend to follow a straight line on the log, called the shale base line. In permeable formations, the SP curves show excursions from the shale base line. In thick beds it tends to reach an essentially constant deflection defining a sand line. The SP may deflect either to the left (negative) or to the right (positive) of the shale base line, depending on the relative salinities of the formation water and of the mud filtrate. Figure 2.4 illustrates the typical SP response in shale, sand, and limestone.

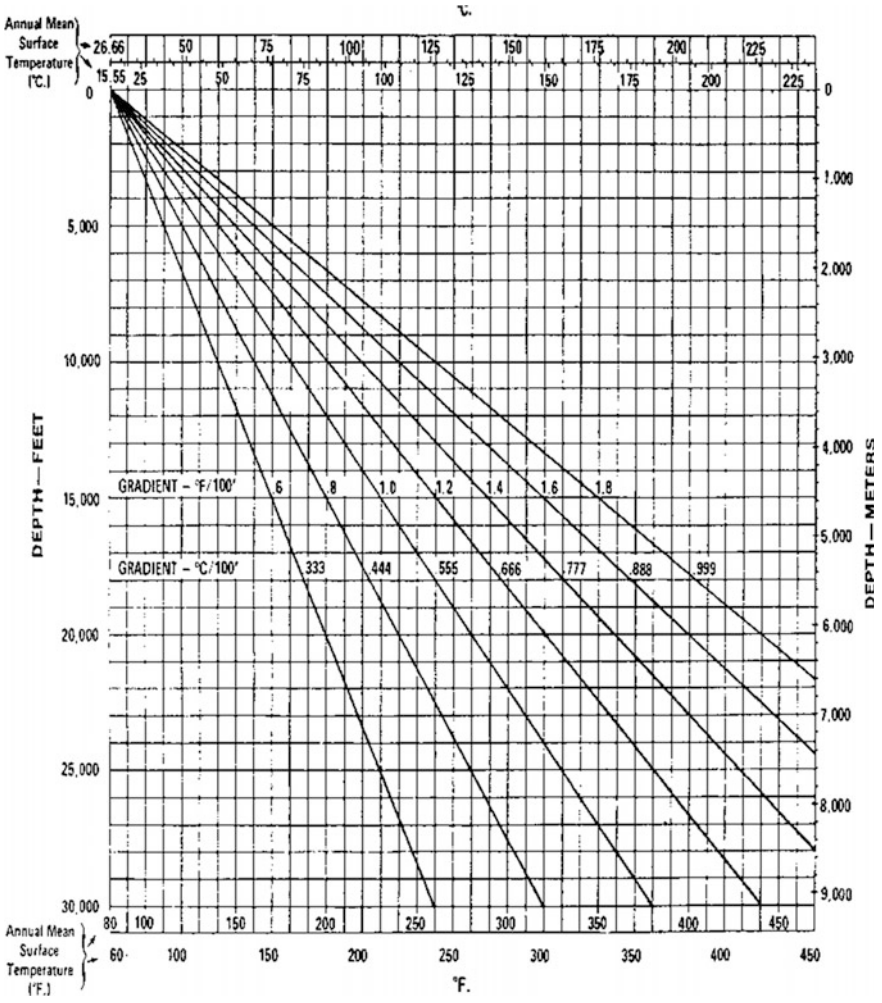

Fig. 2.4 Formation temperature-depth relationship (Courtesy of Gearhart)

2.2.1 The SP Log

Schlumberger discovered this phenomenon in 1928. An electrical potential difference exists, spontaneously, between an electrode in the borehole, and a remote reference electrode on surface. This potential varies from formation to formation, usually within the range of a few tens or hundreds of millivolts (mV). In Fig. 2.5, an electrode A, located at the end of an insulated cable C, is moved up or down the mud-filled borehole. The insulated conductor is connected to one terminal of a recording galvanometer; the other terminal of the galvanometer is connected to a potentiometer circuit P, and then to electrode B, usually placed in the mud pit or in a mud-filled hole dug for this purpose. Electrode B is called the SP ground.

The boreholes in which the SP is recorded are usually filled with water-based mud. The recording galvanometer measures all the differences of potential appearing between electrodes A and B. The deflections on the SP log correspond to phenomena occurring at the contacts between the mud and the different beds, and at the contacts between the beds themselves. These phenomena produce an electric current, which uses the mud as its return path. In doing so, it creates in the mud, by ohmic effect, potential differences which can be measured.

The position of the shale base line on the log recording has no useful meaning for interpretation purposes. SP scale sensitivity is chosen and the shale base line is

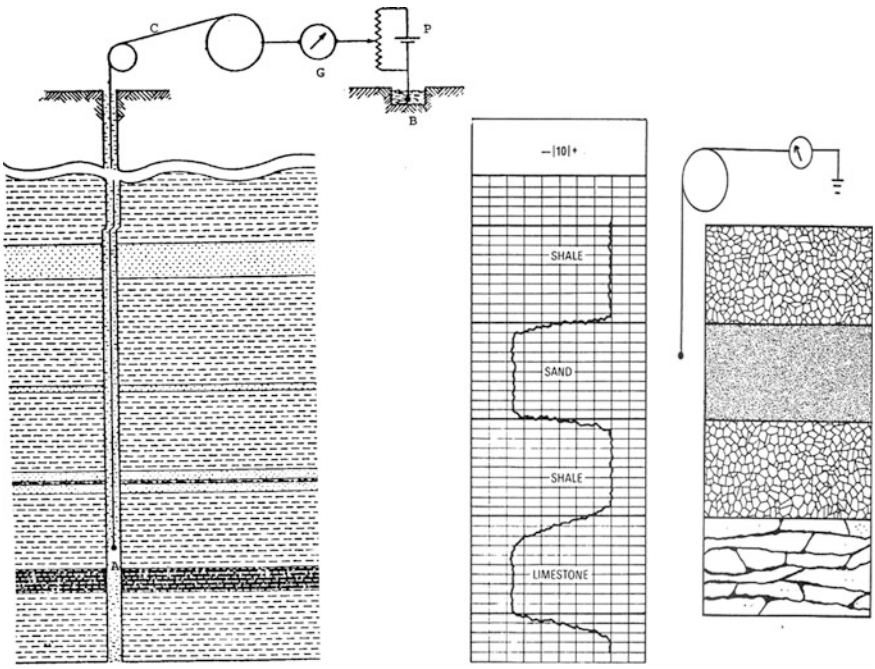

Fig. 2.5 Spontaneous potential

positioned by the logging engineer so that the SP curve deflections remain in the SP track.

The SP cannot be recorded in holes filled with nonconductive muds because such muds do not provide electrical continuity between SP electrodes and formation. Normal SP deflections occur only in porous, permeable beds. The SP log, although indicating permeability, cannot be used to quantify either permeability or porosity.

SP deflections are due to earth currents which develop an electromotive or electrical force in the mud column. These SP currents are generated by two sources called electrochemical and electrokinetic.

Greater significance is often attached to each variation in the SP curve, so the presence of spurious potentials, or potentials induced by outside sources, on the log is undesirable. If present and bothersome, proper steps by the logging engineer should be taken to remove them. Some spurious potentials have no effect on the magnitude of SP deflections. The electrodes are chosen to be stable insofar as their contact potential with the mud is concerned. In practice, lead electrodes are used. A constant difference of potential may normally appear between the surface and down hole electrodes in the absence of any SP current. This difference of potential is not recorded on the SP log; it is counterbalanced by means of the surface potentiometer circuit used to set the shale base line. Accordingly, the potential of the downhole electrode is measured on the SP log with reference to an arbitrary constant. However, variations in potential (that is, the deflections on the SP log) do not depend on the arbitrary constant.

2.2.2 Electrochemical Component of the SP

Consider a permeable formation with thick shale beds above and below. Assume that the two electrolytes present, mud filtrate, and interstitial formation water, contains sodium chloride (NaCl) only. Because of the layered clay structure and the charges on the layers, shales are permeable to the Na^+ cations but impervious to the Cl^- anions. Only the Na^+ cations (positive charges) are able to move through the shale from the more concentrated to the less concentrated NaCl solution. This movement of charged ions is an electric current, and the force causing them to move constitutes a potential across the shale.

The curved arrow in the upper half of Fig. 2.6 shows the direction of current flow corresponding to the passage of Na^+ ions through the adjacent shale from the more saline formation water in the bed to the less saline mud.

Since shales pass only the cations, shales resemble ion-selective membranes, and the potential across the shale is therefore called the membrane potential.

Another component of the electrochemical potential is produced at the edge of the invaded zone, where the mud filtrate and formation water are in direct contact. Here Na^+ and Cl^- ions can diffuse (move) from either solution to the other. Since Cl^- ions have a greater mobility than Na^+ ions, the net result of this ion diffusion is a flow of negative charges (Cl^- ions) from the more concentrated to the less

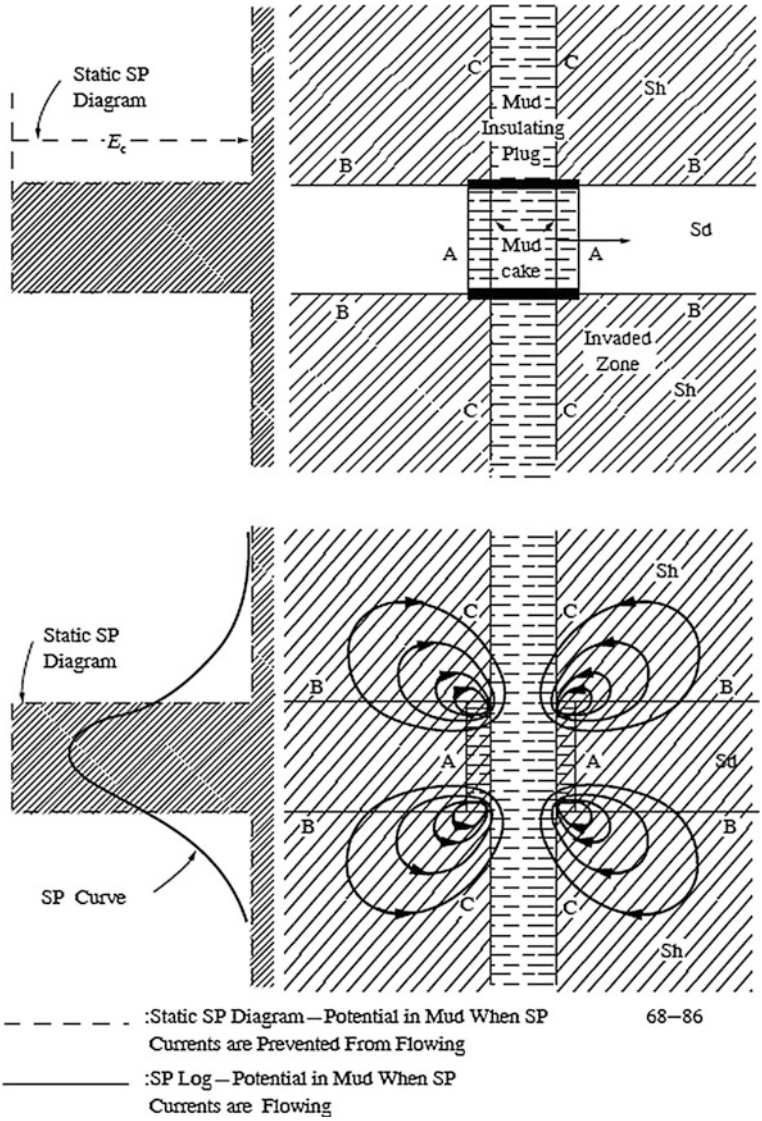

Fig. 2.6 Schematic representation of potential and current distribution in and around a permeable bed

concentrated solution. This is equivalent to a conventional current flow in the opposite direction, indicated by the straight Arrow A in the upper half of Fig. 2.6. The current flowing across the junction between solutions of different salinity is produced by an electromagnetic force (emf) called liquid-junction potential (as shown in Fig. 2.7). The magnitude of the liquid-junction potential is only about one-fifth the membrane potential.

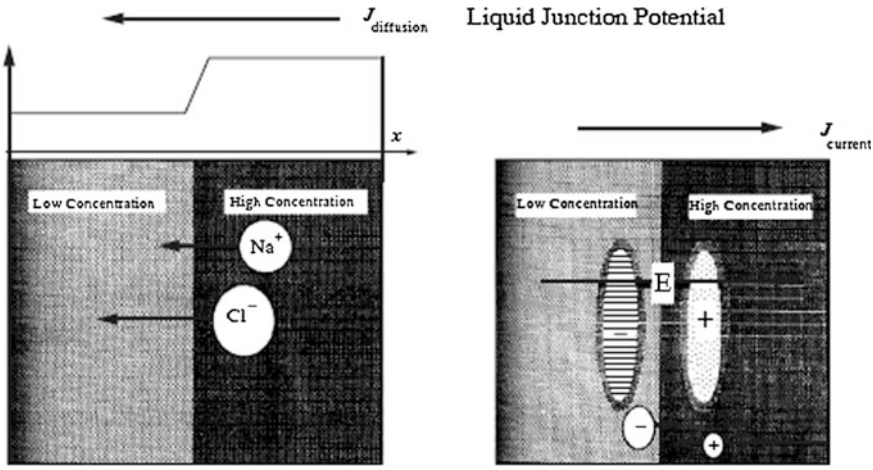

Fig. 2.7 Schematic representation of the mechanism responsible for the generation of the liquid-junction potential. A concentration gradient results in diffusion. The mobility difference between Na^+ and Cl^- causes a charge separation

If the permeable formation is not shaly, the total electrochemical emf, E_c, corresponding to these two phenomena, is equal to:

$$E_c = -K \log \frac{a_w}{a_{mf}},$$

where a_w and a_{mf} are the chemical activities of the two solutions (formation water and mud filtrate) at formation temperature; K is a coefficient proportional to the absolute temperature, and, for NaCl formation water and mud filtrate, is equal to 71 at 25 °C (77 °F). The chemical activity of a solution is roughly proportional to its salt content (i.e., to its conductivity). If the solutions contain substantial amounts of salts other than NaCl, the value of K at 77 °F may differ from 71.

If the permeable formation contains some shale or dispersed clay, the total electrochemical emf and, hence, the SP deflections will be reduced since the clay in the permeable formation produces an electrochemical membrane of opposite polarity to that of the adjacent shale bed.

2.2.3 Spontaneous Potential (SP) Tool

The spontaneous potential (SP) log is a record of the naturally occurring potentials in the wellbore as a function of depth. The SP log involves a single moving electrode in the borehole and a reference electrode, usually located at the surface in

the mud pit or some other suitable location. The recording is a relative measurement of the DC voltage in the borehole with no zero being recorded. Readings opposite shales are relatively constant and are referred to as "the shale baseline." Opposite permeable formations the SP curve typically shows excursions to the left (negative polarity) or to the right, depending upon the salinity of the drilling mud and formation waters (Fig. 2.8). The position of the shale base line has no real significance. The logging engineer sets the position and sensitivity on the log so that deflections opposite permeable beds stay within the limits of track 1 (on the log). Typically, the shale base line is set two chart divisions (where ten divisions make the total width of the track) from the right edge of the SP track. The variations of the measured SP indicate there are currents flowing within the wellbore. These currents are primarily of an electrochemical nature.

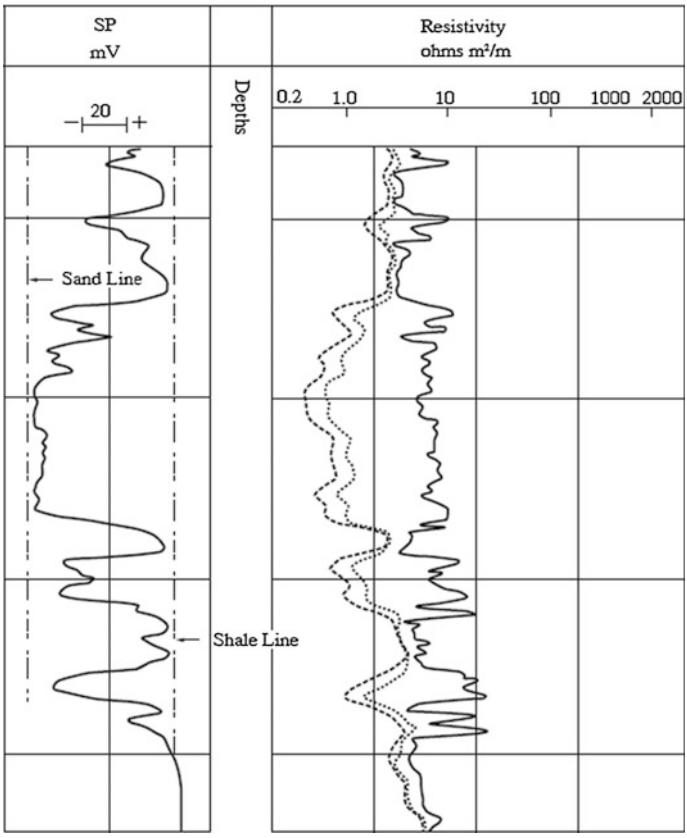

Fig. 2.8 Example of SP log in sand-shale sequence

2.2.4 R_w from the SP

If the permeable formation is not shaly, the total electrochemical force corresponding to the liquid junction and membrane potential, is equal to:

$$SP = K\text{Log}\frac{a_w}{a_{mf}} \tag{2.1}$$

Since chemical activities are of little value to the log analyst, Eq. 2.1 can be expressed in terms of water resistivity, which is also dependent on temperature.

Equation 2.2 solves for SP, given the resistivity of the formation water, the mud filtrate, and the formation temperature.

$$SP = -(60 + 0.133T)\log\frac{R_{mf}}{R_w} \tag{2.2}$$

where

$-(60 + 0.133T)$	the constant—K
T	the formation temperature in °F
R_{mf}	the resistivity of mud filtrate
R_w	the water resistivity

Equation 2.2 is the most popular form of the SP relationship. Note that an empirical relation has been substituted for the constant k, which enables its value to be calculated. Thus, if the total SP deflection can be found from the log and k can be calculated and R_{mf} can be measured from a flowline sample, the desired quantity R_w can be found.

2.2.5 Log Example of the SP

The measurement of the SP is probably the antithesis of the high-tech image of the logging techniques to be considered in subsequent sections. The sensor is simply an electrode which is referenced to ground at the surface, as shown in Fig. 2.9. The measurement is essentially a dc voltage measurement which is slowly time-varying as the passes in front of various formations.

To illustrate some of the characteristic behavior to be anticipated by the SP measurement on logs, refer to Fig. 2.10. In the left panel of this figure, a sequence of shale and clean sand beds is represented, along with the idealized respond. The shale base line is indicated, and deflections to the left correspond to increasingly negative values. In the first sand zone, there is no SP deflection since this case represents equal salinity in the formation water and in the mud filtrate. The next two zones show a development of the SP is largest for the largest contrast in mud filtrate and formation water resistivity. In the last zone, the deflection is seen to be to the

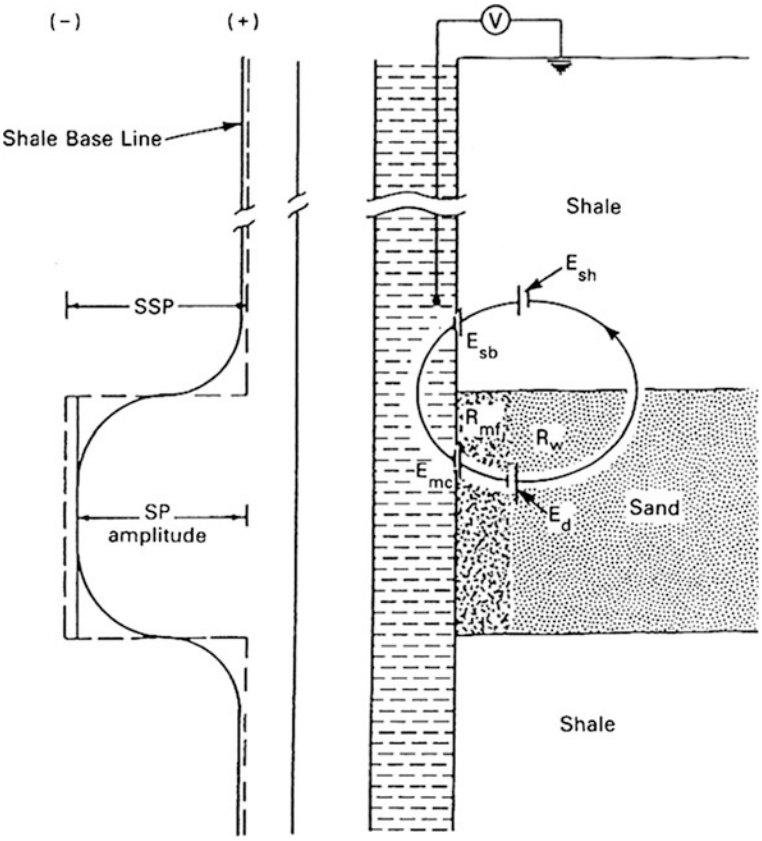

Fig. 2.9 A schematic representation of the development of the spontaneous potential in a borehole. Adapt from Dewan

right of the shale base line and corresponds to the case of a mud filtrate which is saltier than the original formation fluid.

The second panel of Fig. 2.10 illustrates several cases, for a given contrast in mud filtrate salinity and formation water salinity, where the SP deflection will not attain the full value seen in a thick, clean sand. (this latter value is referred to as the static SP, or SSP.) The first point is that the deflection will be reduced if the sand bed is not thick enough. Depending on invasion and the contrast between filtrate and water salinity, the bed thickness needs to be more than 20 times the borehole diameter to attain its full value. A second cause for reduced SP deflection is the presence of shale in rocks. In addition to these effects on the SP behavior, elaborate interpretations have been developed based on connections established between SP curve shapes and geological significant events. Some examples of using the SP curve to determine patterns of sedimentation are given in Reference 5.

Note that the SP builds up rather gradually from the base line and that the peak value is less than the SSP. This is referred to as the pseudostatic SP or PSP, and is

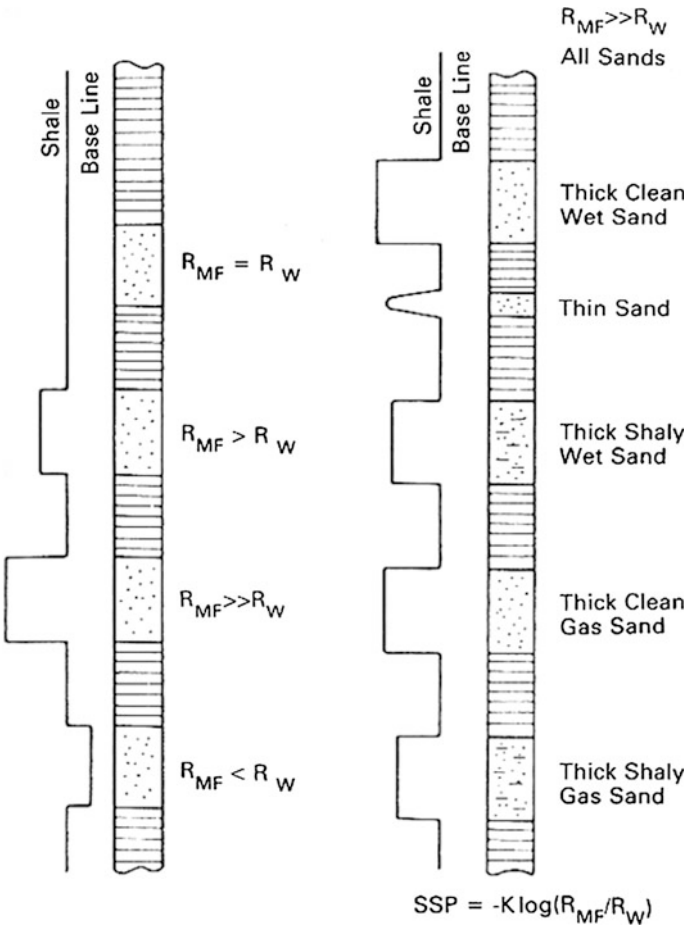

Fig. 2.10 Schematic summary SP curve behavior under a variety of different logging circumstances commonly encountered. From Asquith

strongly dependent on bed thickness, the resistivities of the invaded and virgin zones, depth of invasion, shaliness, and so on. These factors also affect the shape of the peak.

2.2.6 Applications of SP

In briefly, the applications of SP can be concluded as the followings:

(a) Identification of porous, permeable beds.
(b) Determination of R_w.

(c) A lithological indicator: shales, coal-seams, shale fraction estimation from: $V_{sh} \leq 1 - \text{PSP/SSP}$.
(d) An analysis of the facies and grading, based on the curve shape
(e) Formation correlation.
(f) An indication of possible hydrocarbon saturation in shaly sands, including the presence of a gas-oil contact.

2.3 Resistivity Logs

The measurement of formation resistivity is fundamental to the evaluation of hydrocarbon saturation. There are several measuring techniques in use, all variations of a common basic system: an emitter (electrode or coil) sends a signal (electrical current, electromagnetic field) into the formation. A receiver (electrode or coil) measures the response of the formation at a certain distance from the emitter.

Generally, an increase in the spacing of the system results in an improved depth of investigation (and a reading nearer to R_t), at the expense of vertical resolution.

Resistivity tools directly measure the effects of an electromagnetic field on the beds. Resistivity devices require a conductive fluid in the well bore to carry the current, whereas induction tools may be used in virtually any environment.

With any of these tools, different depths of investigation may be achieved by varying the spacings between signal source and sensor. Focusing coils or electrodes are often used to increase the effective depth of investigation and to improve bed boundary response.

A number of tools are of the resistivity type. Lateral log, Microlateral logs, Dual induction, 18″ normal, 16″ laterals, MicroSFL, and proximity tools are of this type. All of these are simply electrode arrangements.

Early resistivity logs, utilizing electrode-type devices, were called electric logs. Later, logs utilized a combination of induction and electrode devices and were known as induction-electric logs. An SP curve was commonly recorded in conjunction with both types of logs. Modern logs are merely developments of the induction-electric log.

No tool accurately measures resistivity of the intended zone, although some come very close. Between transmission and reception the signals transpire several distinctly different zones. Signals reaching virgin formation must cross the borehole fluid, the mud cake, the flushed zone, and the invaded zone. A portion of the total received signal will come from each of these zones. Corrections for such influences and for the influence of such factors as bed thickness must be applied to the values read from logs.

2.3.1 Normal Devices

The earliest electrical surveys used in well logging were the conventional resistivity logs with an SP. These devices consisted of electrode arrangements and some simple instrumentation. One such electrode arrangement is the short normal.

The short normal is a two-electrode measuring device which passes current from an electrode on the tool through the mud and into the formation, As depicted in Fig. 2.11. The Schlumberger short normal employs a 16″ spacing. A deeper investigating design used 64″ spacing. The deepest point at which the measurement is being made is midway between *A* and *M*. This point is considered the zero point for the device. The radius of investigation is very nearly equal to twice the electrode spacing. The mathematical relationship for this type electrode arrangement is depicted in the following:

$$R = K\frac{V}{I}, \tag{2.3}$$

where

R resistivity, Ω m;
K constant

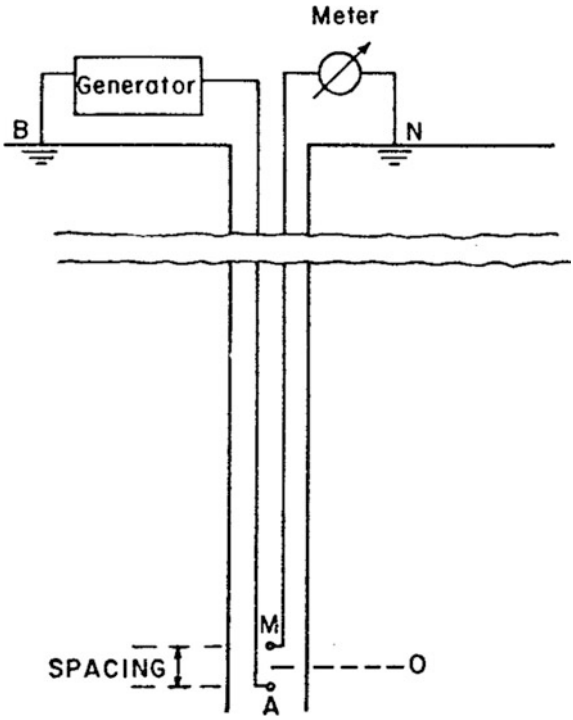

Fig. 2.11 Schematic of the normal resistivity tool

V voltage, V;
I current, A.

Resistivity is equal to K times voltage divided by current. The current, as previously stated, is constant. The proportionality constant K is related to electrode spacing and geometrical factors of the measuring device and formations. The only variable is the voltage. Log trace deflection, responding to voltage changes, can thus be scaled in resistivity units.

Looking at Fig. 2.12, we see a different electrode arrangement known as a lateral device. A constant current is passed between electrodes A and M and the potential difference is measured between electrodes M and N, which are located on two consequent spherical equipotential surfaces centered on A. The voltage measured is proportional to the potential gradient between M and N. The measuring or zero point for the device is at O, midway between M and N. Generally speaking, the spacing is approximately equal to the radius of investigation.

It is important to note that these devices record an apparent resistivity R_a. Resistivities will be affected by all the media surrounding the device, such as the borehole, the invaded and uncontaminated zones, and the adjacent beds. If quantitative R_t calculations are to be made, bed thickness must be 3–4 times the tool spacing.

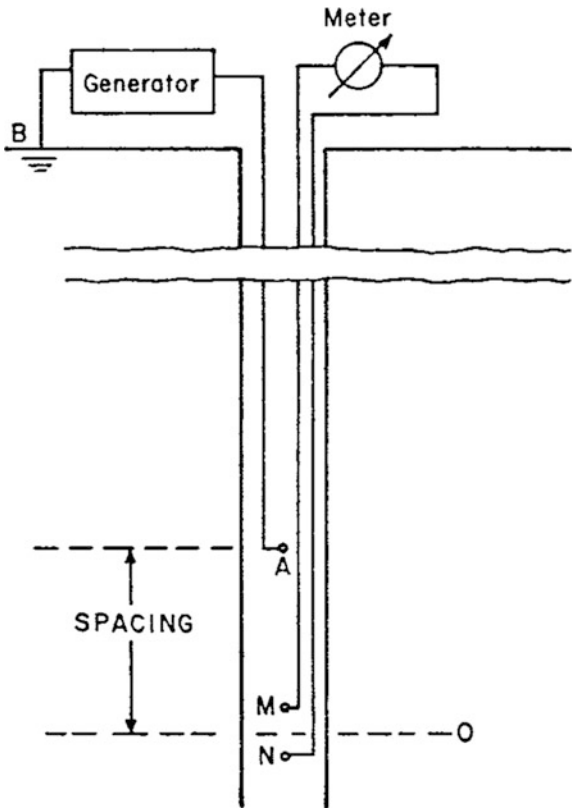

Fig. 2.12 Schematic of the lateral tool (Courtesy of Schlumberger)

In today's logging industry, there are numerous devices available for the purpose of measuring the resistivity of the formation. Each device had a different depth of investigation. Accurate resistivity determination is necessary for the interpretation of hydrocarbons from a well. Each of the modern devices is designed to produce a good resistivity measurement for very specific ranges of borehole conditions. The first of these tailored tools we shall discuss is the focused-type devices.

2.3.2 *Focused Tools*

The influences of the borehole and adjacent formations on electrode devices are minimized by a family of focused current tools. The focused family of tools is designed for accurate R_t determination where R_t/R_m ratios are large, beds are resistive or thin, drilling muds are salty and conductive (where the ratio $R_{mf}/R_w < 4$), and large adjacent-bed resistivity contrasts.

Figure 2.13 shows a typical focused tool, with bucking electrodes A_1 and A_2 generating a current field (solid lines on a constant potential V_o) which focuses the current from the alpha ring (dotted lines). Alpha ring current penetrates deeply into the formation before the focusing fields become weak enough to allow it to disperse and return to the pickup electrode.

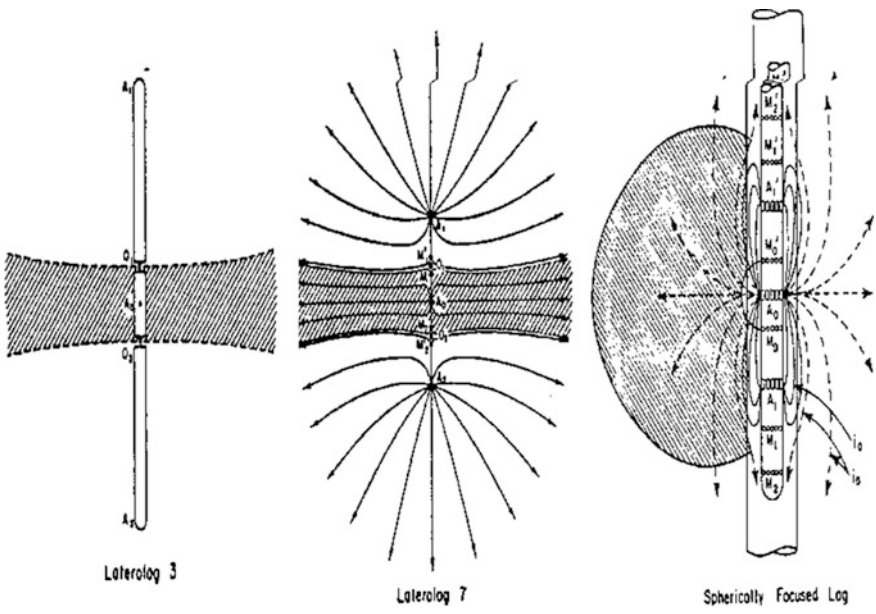

Fig. 2.13 Schematic of current flow of focused tool (Courtesy of Schlumberger)

Figure 2.14 shows an idealized focused log response. As you can see, it has reasonably good bed definition compared to normal electric logs. Also, the focused log gives us a much better definition of true resistivity. In this example, the shale resistivity is 5 Ω-m and the resistivity of the sand is 250 Ω-m. Note that the mud is highly conductive, with a resistivity of 0.05 Ω-m.

2.3.2.1 Dual Lateral Log (DLL)

The objective of any deep-reading resistivity device is to measure the true formation resistivity, R_t. Deep-reading resistivity tools were designed so that, as much as possible, their response is determined by the resistivity of the virgin formation beyond the invaded zone. Unfortunately, no single measurement has yet succeeded in entirely eliminating the effects of the invaded zone.

This need, to detect deep, medium and shallow resistivity simultaneously, resulted in the development of the dual lateral logging (DLL) and micro-spherically focused logging tool with simultaneous recordings. DLL device is developed from LL3 and LL7, and combines features of them. Figure 2.15 is a sketch of the tool showing the electrode array used for the two laterolog devices. Both use the same electrodes and have the same current-beam thickness, but have different focusing to provide their different depth of investigation characteristics. Figure 2.16 illustrates

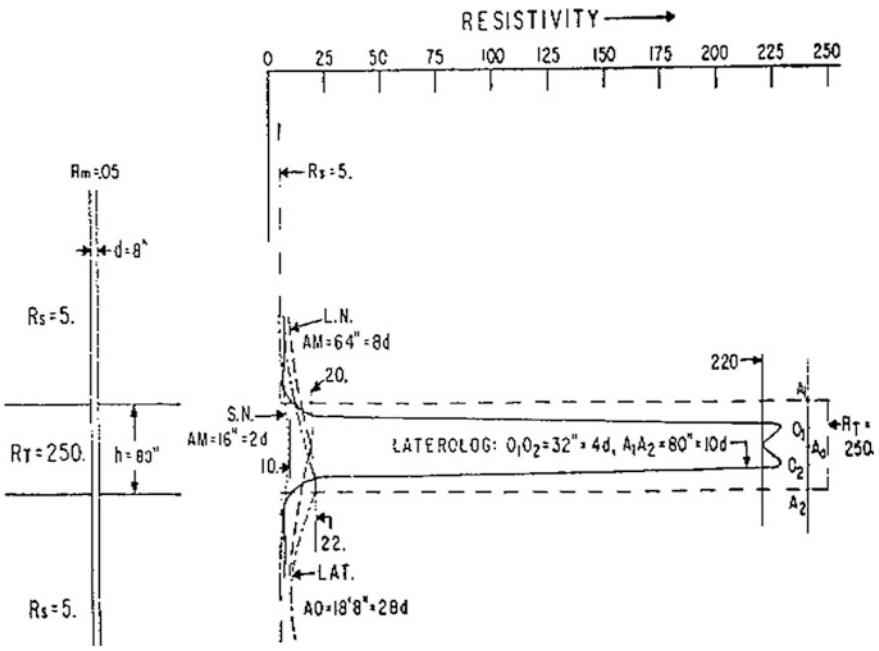

Fig. 2.14 Illustration of the focal curve response (Courtesy of Schlumberger)

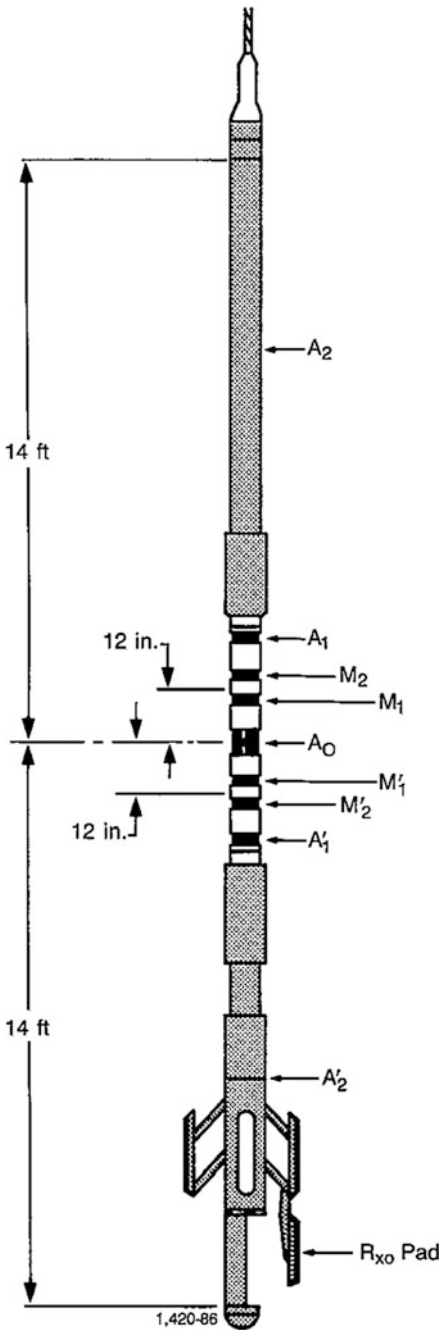

Fig. 2.15 Schematic of Laterolog and Micro-SFL tool (Courtesy of Schlumberger)

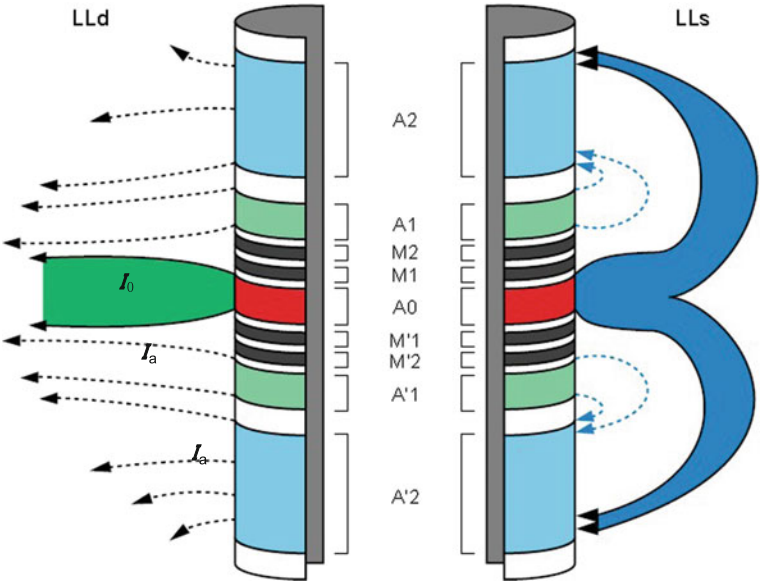

Fig. 2.16 Electrodes and current distribution of dual Laterolog tool

the focusing used by the deep laterolog device (left) and by the shallow laterolog device (right). The system is symmetrical above and below A_0, the central electrode, which emits survey current I_0. Electrodes M_1 and M_2 are shorted-circuited, as are M_1' to M_2' and A_1 to A_1'. The last pair inject an auxiliary or bucking current I_a of the same polarity as I_0. A_1A_1' and $A_2\,A_2'$ are two pairs of bucking electrodes, M_1M_1' and M_2M_2', are two pairs of guard electrodes.

A control signal representing the potential difference between M_1M_2 and $M_1'M_2'$ is sent to the surface where it governs the current delivered to A_1A_2. The system is self nulling in that the bulking current is continuously adjusted so as to maintain the condition $V(M_1M_2) - V(M_1'M_2') = 0$. Even when the mud column is taken into account, essentially no current from A_0 can flow vertically through the mud, and hence the central current I_0 was repelled into the formation. The potential measurement can be made at any of the M-electrodes. It converted to R_a through multiplicated by a sonde coefficient K, which depends only on the distances between the electrodes (i.e., electrode spacing), as in the case of the normal and lateral sounds.

The DLL tool has a response range of 0.2–40,000 Ω-m, which is a much wider range than the previous laterolog devices, LL3, and LL7. To achieve accuracy at both high and low resistivities, a "constant-power" measuring system is employed. In this system, both measure current (I_o,) and measure voltage (V_o,) are varied and measured, but the product of the two (i.e., power), I_oV_o, is held constant.

The deep laterolog measurement (LLD) of the DLL tool has a deeper depth of investigation than previous laterolog tools, about 3.28 ft. To achieve this, very long

guard electrodes are needed; the distance between the extreme ends of the guard electrodes of the DLL-R_{xo} tool is approximately 28 ft. The nominal beam thickness of 2 ft, however, insures good vertical resolution.

The shallow laterolog measurement (LLS) has the same vertical resolution as the deep laterolog device (2 ft), but it responds more strongly to that region around the borehole normally affected by invasion. It uses a type of focusing called "pseudolaterolog," where in the focusing current is returned to nearby electrodes instead of to a remote electrode, it has a relative shallow depth of investigation, about 2.46 ft.

2.3.2.2 Micro-SFL Logging (MSFL)

When the resistivity contrast between the invaded zone and the mud cake is high (i.e., high R_{xo}/R_{mc}), the current induced by the Microlog tends to escape through the mud cake (Fig. 2.17). To eliminate this problem, focused current-devices-Microlatero-log (MLL), the proximity log (PL) and the micro-spherically focused log (MSFL), were developed.

The MLL comprises one central electrode (A_0) and three ring electrodes (M_1, M_2, and A_1). These electrodes are imbedded in a pad, as shown in Fig. 2.18. The tool

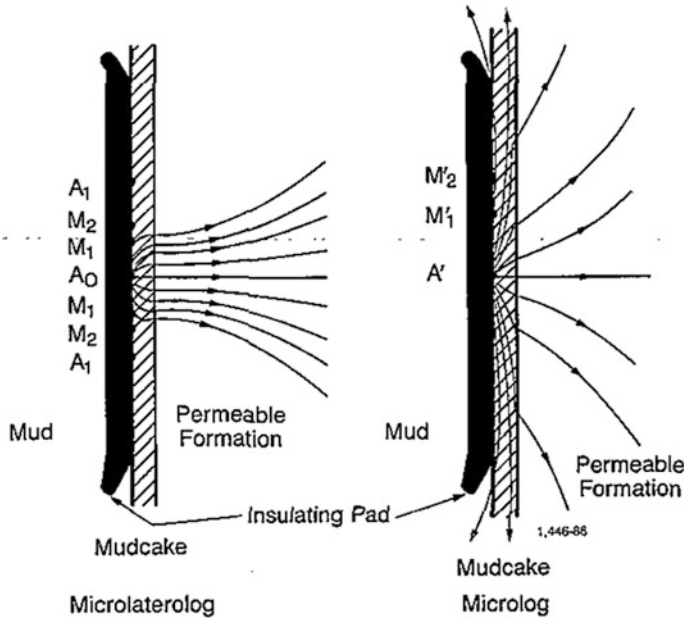

Fig. 2.17 ML current configuration of a permeable zone more resistive than the mud cake

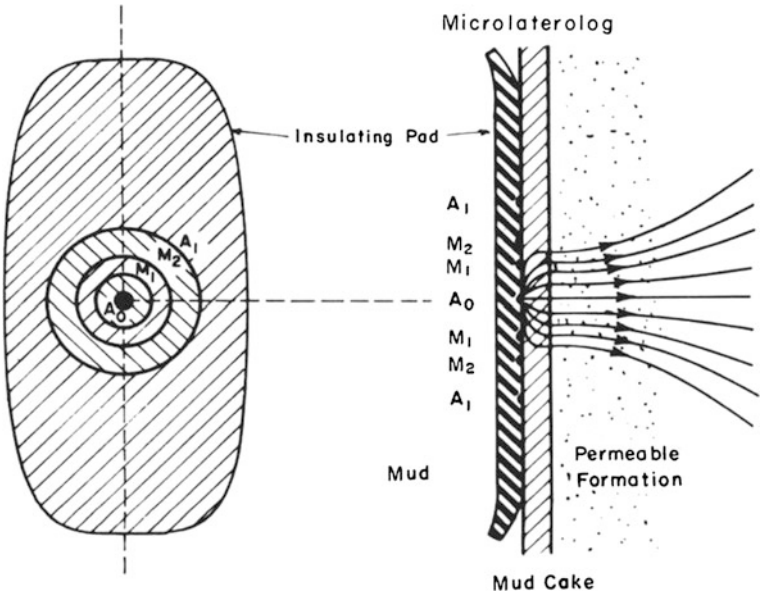

Fig. 2.18 MLL pad current distribution next to a permeable zone

functions identically to the LL7. When invasion is sufficiently deep and mud cake is <3/8 in. thick, the MLL displays an apparent resistivity value that approximates R_{xo}.

The PL is similar in principle to the MLL. When a diameter of invasion equal to or greater than 40 in. is needed for the PL to provide direct approximation of R_{xo}, if the invasion is shallow, the reading is influenced by R_t.

The MicroSFL electrodes are smaller and pad-mounted. Figure 2.19 shows the electrode arrangement and current distribution of the MicroSFL. This design minimizes mud cake effect without requiring deep invasion, as with the PL. The MicroSFL provides good values of R_{xo} in a wider range of conditions than either the PL or MLL. Another distinct advantage of the MicroSFL is its compatibility with other logging tools, such as the Dual Laterolog and the induction SFL (Fig. 2.20). This eliminates the need for a separate logging run to obtain R_{xo} data. Figure 2.21 shows a log measured a log with DLL/MSFL combination tool. The MSFL, LLs, LLD are traced on the logarithmic scale in solid, dotted, and dashed lines, respectively. The thick formation located in the depth interval of 5687–5717 ft is characterized by a separation of the three curves. This separation indicates that the zone is invaded by mud filtrate; hence, it is permeable. This interval was drilled with saltwater-based mud (R_{mf} = 0.056 at 68 °F) that has a salinity exceeding that of formation water. The resistivity displayed by the logs increases with the tool's radius of investigation because of the salinity contrast between the mud filtrate and the formation water.

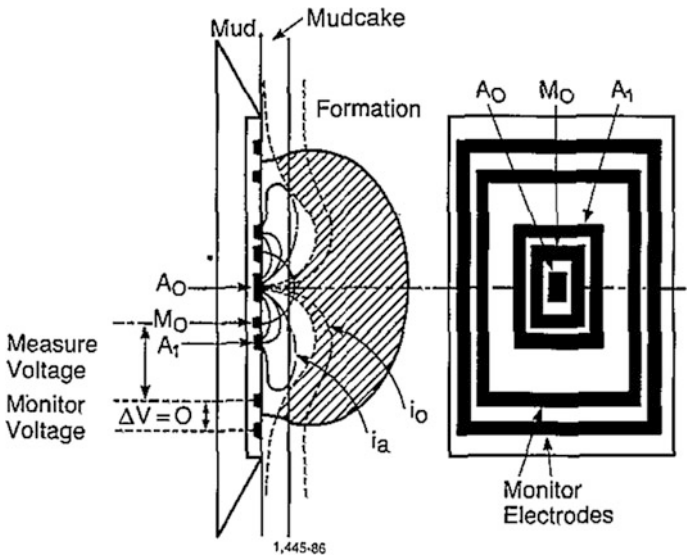

Fig. 2.19 Electrode arrangement and current distribution of Micro-SFL

2.3.3 Induction Tools

The induction log, introduced in the mid-1940s, was designed to measure formation resistivity in boreholes containing nonconductive fluids. Boreholes containing air, freshwater muds, or oil-based muds make excellent environments for induction logging. The induction log actually measures the conductivity of a formation rather than its resistivity. Conductivity is the reciprocal of resistivity, and vice versa.

Induction tools are focused to minimize the contribution of the borehole, invaded zone, and surrounding formation to the measurement. Focusing is realized by means of a system of several transmitter and receiver coils. The principle of the tool, however, can be simplified with the two-coil system in Fig. 2.22, which also shows the distribution of electromagnetic field. A transmitter coil is excited by an alternating current, $I(I_0 = \sin \omega t)$, of medium frequency (20 MHz). This current induces a primary alternating magnetic field, Φ, in the formation that surrounds the borehole can be referred a conductive ring. The magnitude and frequency of the field depends on the transmitter current. The vertical component of this induced magnetic filed, in turn generates an alternating electric filed e, which curls around the vertical axis. This electric field causes a rotational current, I', to flow in the formation in circles concentric with the borehole. The rotational current, I', is proportional to the electric field, and the formation conductivity, σ. the current that flows in a formation ring behaves as a transmitter coil and generates its own secondary magnetic field, Φ'. Φ', which is proportional to the formation conductivity, induces an electric signal, V, in the receiver coil.

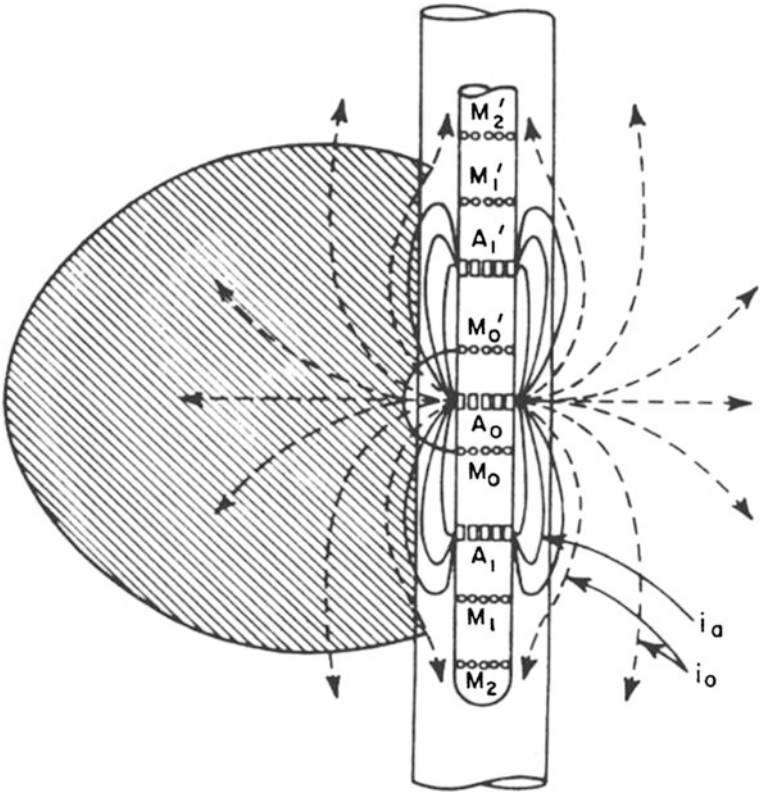

Fig. 2.20 Schematic of current pattern of the SFL

The primary and secondary alternating magnetic field will successively across the receivers, and inducing electromotive potential E_x and E_R. E_x is induced by Φ (hence by the current, I) directly coupling with receiver, and independent of conductivity of the formation, hence, it is call useless signal. E_R, however, is induced by Φ' (hence by the current, I') coupling with receiver, and dependent of conductivity of the formation, hence, it is called useful signal. By which, the electrical properties of the formation can be acquired. The process of electromagnetic field inducing is shown in Fig. 2.23.

Note that the phases of E_x and E_R are different, and the phase shift is 90°. E_R can be checked by a phase sensitive detector (PSD), and then the signal is converted to resistivity.

For an infinite homogeneous medium with conductivity σ, E_R is proportional to the σ, so:

$$E_R = K\sigma, \tag{2.4}$$

where, K is coefficient of induction tool.

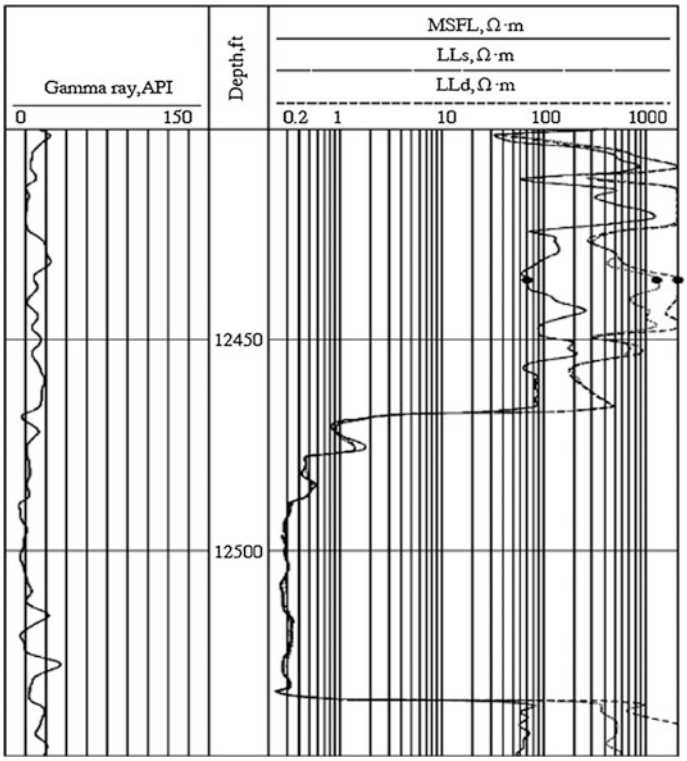

Fig. 2.21 Example of dual lateral log and MSFL log

Although dual induction tools were designed for a nonconductive borehole environment, they were found yield excellent measurement in water-based mud, provided that the mud is not too salty, the formation is not too resistive, and the borehole diameter is not too large.

A commonly used tool in oilfield is dual induction tool, which consists of a regular deep-induction device (ILD) and a medium-device (ILM). 0.8 m six-coil dual induction consists of three transmitter coils, T_0, T_1, T_2 and three receiver coils, R_0, R_1 and R_2. Among them T_0 and R_0 are central transmitter and central receiver coil respectively, and the distance between them is called main coil space. Auxiliary coil T_1 and R_1 are referred as borehole compensated coil, and T_2 and R_2 are shoulder compensated coil. Main parameters of these tools are the following, the number between two coils is the spacing of them (m), and the number in the next line is the turn number of corresponding coil, minus mean inverse direction with that of T_0 or R_0:

Arrangement (m):	R_2 0.6	T_0 0.2	T_1 0.4	R_1 0.2	R_0 0.6	T_2
Turn number	−7	100	−25	−25	100	−7

(Negative signal means direction of coil, relative to the direction of central coils)

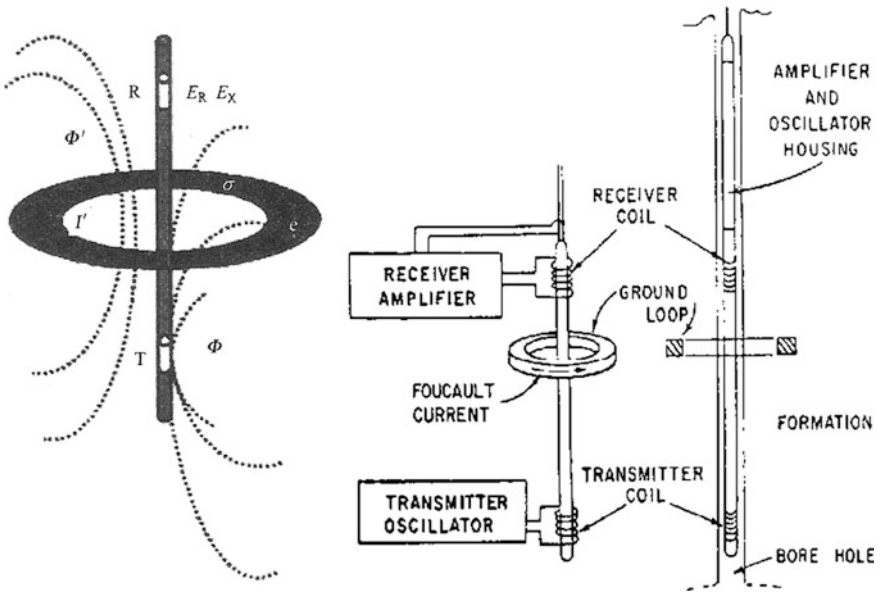

Fig. 2.22 Schematic of structure and electromagnetic field distribution of induction tool (Courtesy of Schlumberger)

Fig. 2.23 Inter-inducing process of electromagnetic field of DIL tool

$$\mathrm{I} \rightarrow \Phi \begin{cases} \xrightarrow{90^0} E_X \\ \xrightarrow{90^0} e \rightarrow I' \rightarrow \Phi' \xrightarrow{90^0} E_R \end{cases}$$

Usually, the depth of investigation of ILD is 1.2–1.6 m and 0.65–0.8 m of ILM. The vertical resolution of ILD is about 2.5 m, and 1.8 m of ILM. The DIL curves are usually recorded with a shallow Laterolog, such as the LL8, or the SFL. Figure 2.24 shows a DIL/LL8 combination log. The practices show that this combination tool can acquire reliable measurements only if the $R_t < 100\ \Omega$ m, $R_{mf} < R_w$, and if diameter of borehole, $d_h < 8$ in.(20.3 m) shallow or medium depth of invasion, and medium value of formation resistivity, this tool can still get relative reliable data.

Figure 2.25 illustrates an example of an induction log recorded in a borehole filled with an oil-based mud. The gamma ray log, discussed in Chap. 7, is recorded on the first track. The SP log usually displayed on the same track cannot be recorded in oil-based mud because it requires a conductive drilling fluid. The resistivity curve is shown on the second track. It is recorded on a linear scale, 0–10 Ω m, increasing from EPT to right. The induction conductivity is shown on third track. It is recorded on a linear scale, 0–4000 mΩ/m, increasing from right to EPT.

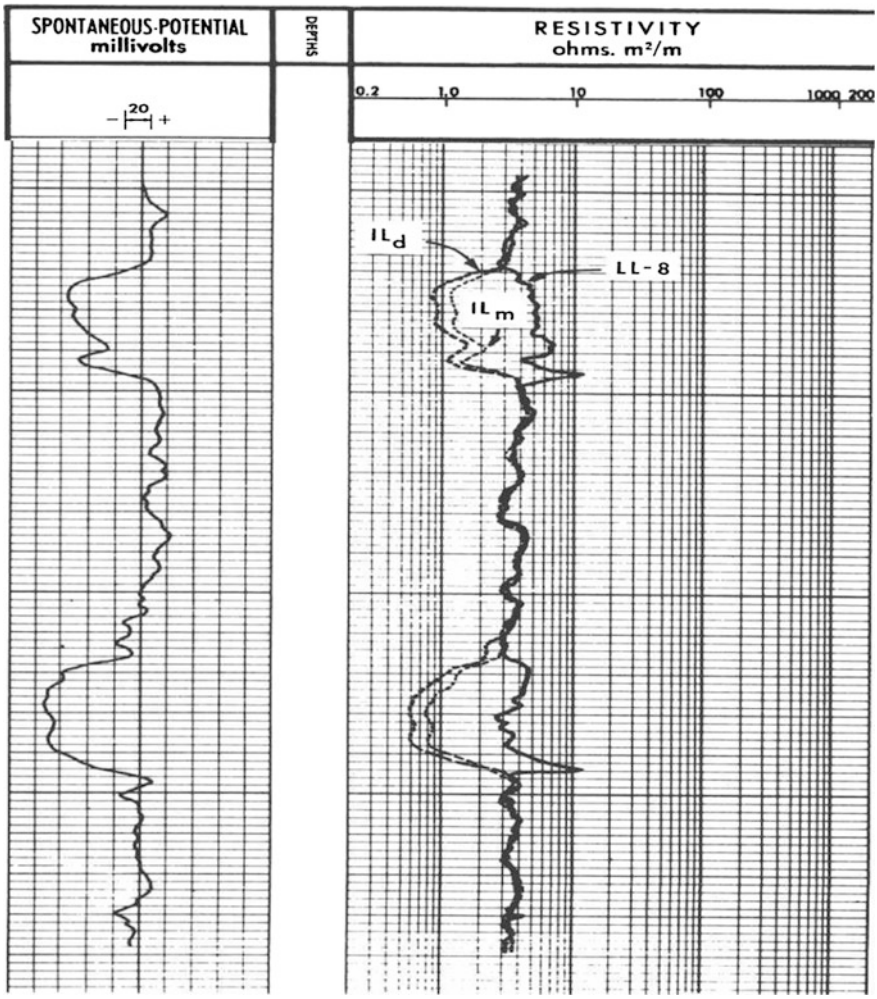

Fig. 2.24 Example of a dual induction/LL8

The scale are set up in this fashion so that the resistivity and conductivity curves move together in the same direction as the curve passes through zones of high and low resistivities.

Figure 2.26 shows a typical induction-electric log presentation. Direct output of the induction measuring circuitry is the conductivity curve in track 3. Corresponding resistivity is calculated automatically by an onboard computer, and output as the dotted induction resistivity curve in track 2. Off-scale resistivity values appear in track 2 at a different sensitivity. The solid curves in track 2 are resistivity from a shallow investigating electric device, in this case a 16″ normal. Optimal conditions for running induction logs also produce excellent SPs.

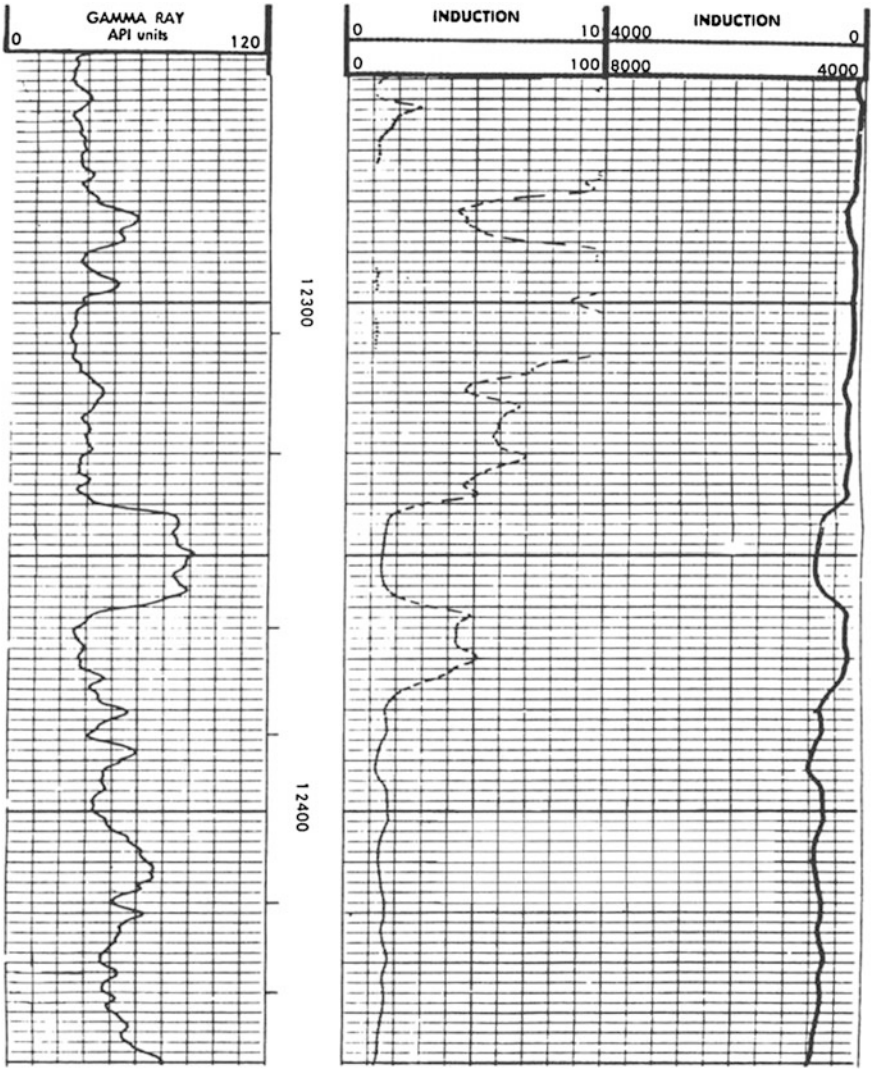

Fig. 2.25 Induction log record in a borehole filled with oil-based mud (Courtesy Amoco)

Under favorable logging conditions, the induction tool yields good values of true resistivities; however, charts may be needed where corrections can be found for bed thickness, large hole diameter, deep invasion, etc.

The dual induction tool is one of the most advanced resistivity devices available. It is particularly useful where invasion diameters are large. An SP and/or gamma ray curve is also recorded with it. The dual induction tool records three resistivity curves having three different depths of investigation. A shallow curve measures the flushed zone resistivity. A medium curve measures invaded zone resistivity. A deep

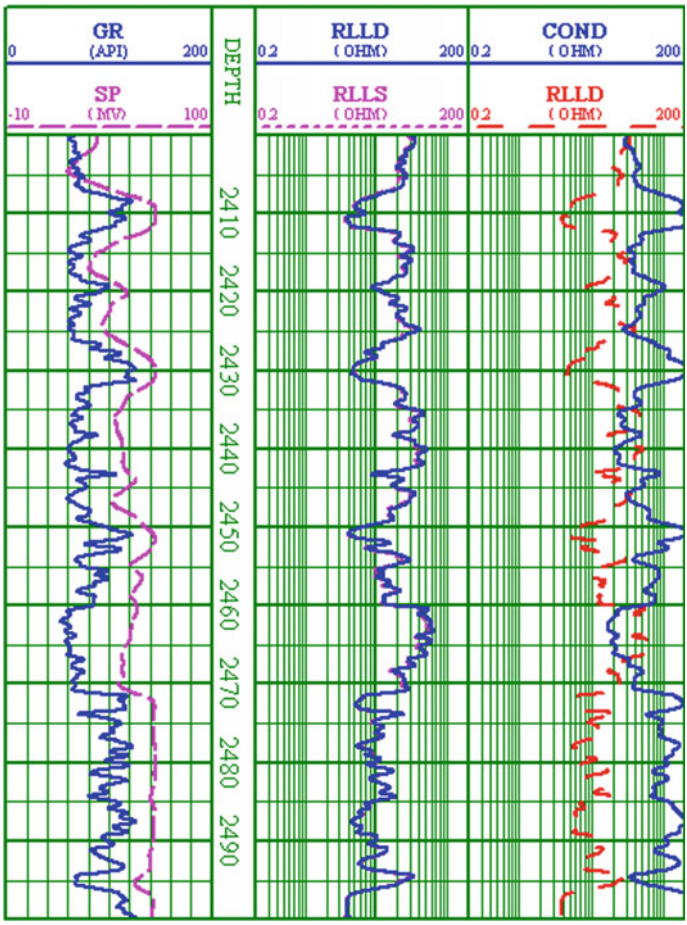

Fig. 2.26 Illustration of the conductivity and resistivity curves

curve measures primarily the uncontaminated or virgin zone and is very close to R_t The ratios of shallow to deep and medium to deep are used to determine R_w, R_t and the diameter of invasion, d*i*.

2.3.4 Array Induction Tools (AIT)

The Array Induction Imager Tools (AIT, Fig. 2.27) accurately measure open borehole formation conductivity as a function of both well depth and radius into the formation at different borehole conditions and environments. Various tools cater to special operating environments, including slim wells and hostile, high-pressure,

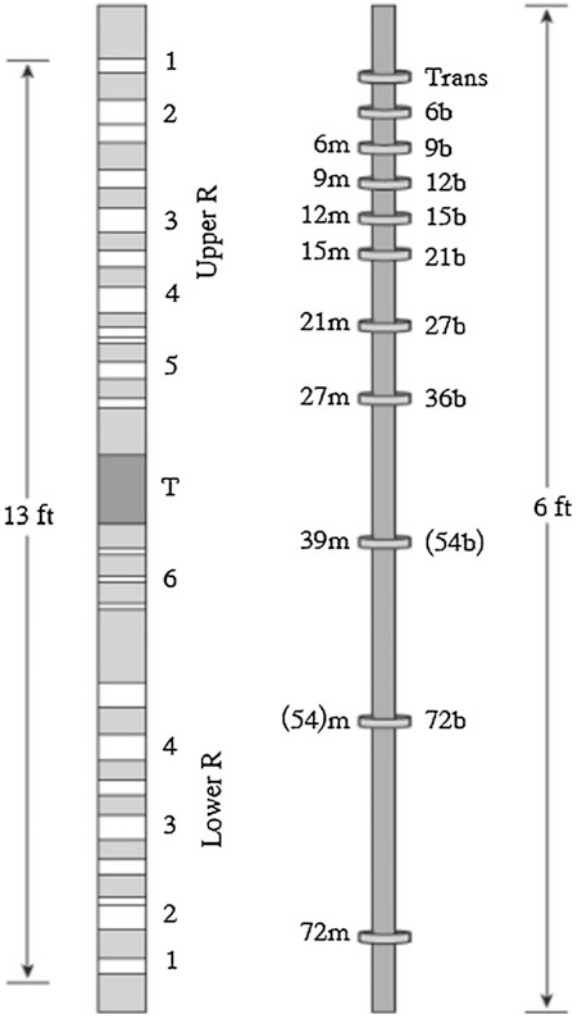

Fig. 2.27 Coil layout for the high-resolution array induction tool

high-temperature (HPHT) environments. Wireline array induction tools use an array induction coil that operates at multiple frequencies. The distance between central coils of AIT tool ranges from several inches to dozens inches, for example, 6″, 9″, 12″, 16″, 21″, 27″, 39″, and 72″. The AIT tool has three operation frequencies, 25, 50, and 100 kHz; and it can provide three different vertical resolutions, 1′, 2′ and 4′, five different radial investigations with 10″, 20″, 30″, 60″, and 90″.

The Applications of AIT can be summarized as the following:

- Reservoir delineation
- Determination of true formation resistivity R_t
- Determination of S_w

- Hydrocarbon identification and imaging
- Determination of movable hydrocarbons
- Invasion profiling
- Thin-bed analysis

2.3.5 *FMI (Full Borehole Microresistivity Image Logging)*

Since the mid-1980 there has been an explosive development imaging technology, principally in terms of tools but also in terms of producing the image. The progress has been linked with availability of downhole digitization of signals and the possibility of transmitting large data volumes in real time. Where the standard logs are sampled every 15 cm(6″), image logs may sampled every 0.25 cm(0.1″); where the standard logs have one measurement per depth point, image logs may have 250, the region of 200 kbits per second transmitted up the cable to achieve a collection rate of 60,000 samples per meter of borehole. Imaging technology is still evolving rapidly and is affecting the entire logging field. Table 2.2 lists typical image tools of some international oil field service company.

Coils 1 are two identical 3-coil arrays equidistant either side of T. Coils 2–6 are 4-coil arrays. Not all bucking coils are shown. (From Beste et al.) (Right) Coil layout for the AIT-H tool. m are the main coils and b the bucking coils. In most cases the bucking coils are co-wound with the main coils of the next smallest array. The spacings of the main receivers increase approximately exponentially from 6 in. Coil spacings are given in inches.

In the mid-1980s, Schlumberger introduced their first electrical imaging tool, the Formation MicroScanner (FMS), as an evolution of their SHDT dipmeter. The first tools only provide as image of 20 % of an 8.5″ borehole, using just two pads. Since

Table 2.2 Imaging tools of different company

Company	Symbol	Name	Description
Schlumberger	FMI	Fullbore Formation MicroImager (current tool 1996)	4pads + flaps 192(4 × 48)electrodes
Schlumberger	FMS	Formation MicroScanner (older tool 1pre-1991)	2 or 4 pads 54(2 × 27)electrodes 64(4 × 16)electrodes
Halliburton	EMI	Electrical MicroImager	6 independent pads 150(6 × 25)electrodes
Western Atlas	*STAR	Simultaneous Acoustic and Resistivity (Borehole image)	6 independent pads 150(6 × 25)electrodes

then there has been steady progress in borehole coverage. The present tool, the Fullbore MicroImager provide nearly 80 % coverage in an 8.5″ borehole of high quality images.

FMI consists of four arms, the adjacent two arms are orthogonal and each arm has two pads (Fig. 2.28), the each pad has a hinged flap. Both pad and flap have arrays of 24 electrodes.

The FMI provides an electrical borehole image generated from up to 192 microresistivity measurements. Applications of FMI are listed below:

- Structural geology
- Structural dips, even in fractured and conglomeratic formations; detection and determination of faults.
- Sedimentary features
- Determination of sedimentary dips and paleocurrent directions
- Definition and characterization of sedimentary bodies and their boundaries
- Recognition of anisotropy, permeability barriers, and permeability paths
- Recognition and evaluation of thinly bedded reservoirs

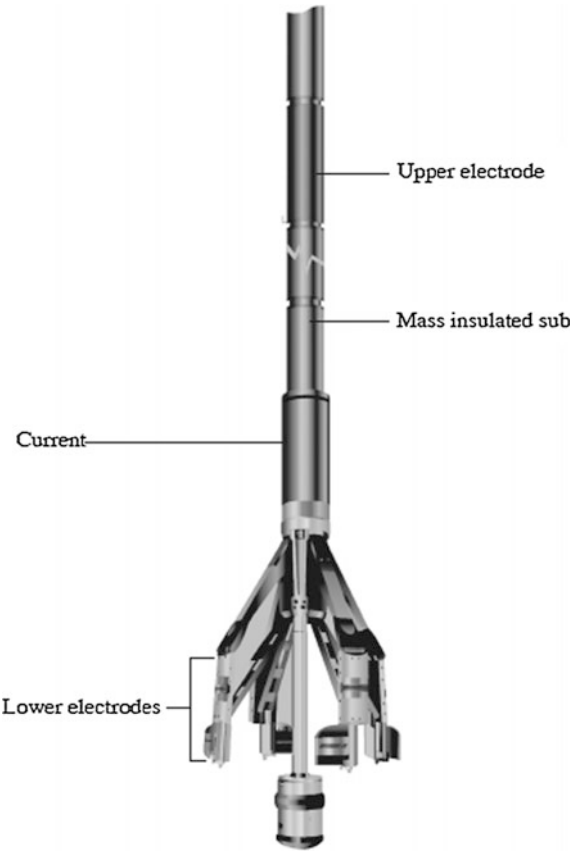

Fig. 2.28 Schematic of the configuration of FMI tool

- Rock texture
- Qualitative vertical grain-size profile; Determination of carbonate texture
- Detection and evaluation of secondary porosity
- Detection and evaluation of fracture systems
- Complement to coring and formation tester programs
- Depth matching and orientation for whole cores.

Figure 2.29 shows that FMI provided image of different formation conditions, for (a), carbonate zone with facture on the wall of well, because of the mud invasion into the fracture, the resistivity decreased, and then a relative dark block corresponding to the fracture depth. (b) also shows features of fracture formation, nearly parallel to each other of the waves implying fracture occurring in the formation. The dark color in image (c) indicates shale or clay zone with resistivity. Nonuniform distributed dark color spots in the image (d) shows that a lot of caves and vugs existed on the sidewall of well.

2.3.6 *ARI (Azimuthal Resistivity Imager)*

The ARI azimuthal resistivity imager makes directional deep measurements around the borehole with a higher vertical resolution than previously possible from conventional laterolog tools. Using 12 azimuthal electrodes incorporated in a dual laterolog array (as shown in Fig. 2.30), the ARI tool provides a dozen deep-oriented resistivity measurements while retaining the standard deep and shallow readings. A very shallow auxiliary measurement provides data to fully correct the azimuthal resistivities for borehole effects.

The ARI tool is combinable with a wide variety of other tools and is particularly effective for thin-bed evaluations in combination with the IPL integrated porosity lithology tool string.

ARI images also complement images from the UBI ultrasonic borehole imager or the FMI full borehole formation microimager because of the tool's sensitivity to features beyond the borehole wall and its lower sensitivity to shallow features.

Table 2.3 Properties of FMI tool

Tool	No. of electrodes	Hole diameter (%)			Logging speed
		6″	$8^{1/2}$′	$12^{1/4}$″	
FMI	4 pad + flaps 192	90	80	50	1800′/h
FMI	4 pad 96	50	40	25	3600′/h
FMI	4 pad 64	50	40	25	1600′/h
FMI	2 pad 54	25	20	12	1600′/h
SHDT	(8)				5400′/h

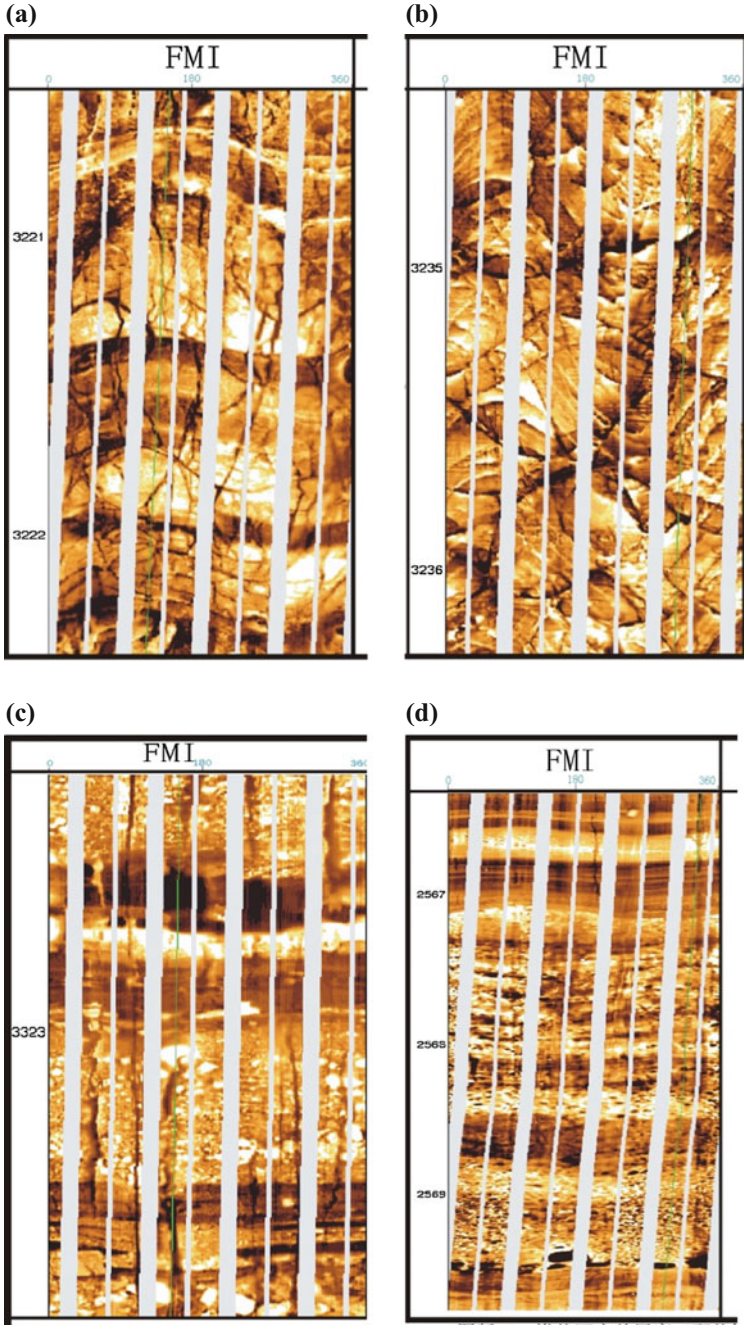

Fig. 2.29 FMI image for different formations. **a** FMI image of formation, **b** FMI image of fracture formation, **c** FMI image low resistivity shale zone, **d** FMI image of pors and caves

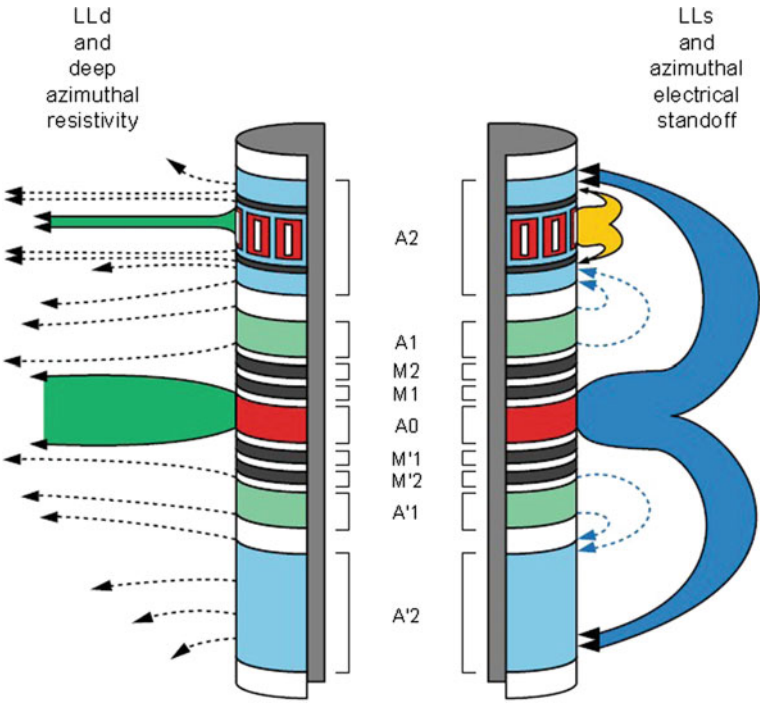

Fig. 2.30 Configuration of ARI tool

Applications of ARI

Resistivity logs and images with vertical resolution of less than 1 ft
- Thin-bed analysis
- Fracture identification and characterization
- Evaluation in deviated and horizontal wells
- Evaluation of heterogeneous reservoirs.

2.4 Dipmeter Logging

The aim of this log is to determine the angle to the horizontal and the azimuth referenced to magnetic north and geographical north of the dip of the planes cut by the well. These planes can be: bed boundaries; an open or closed fracture; an erosional surface; a stylolitic joint.

The planes can be planar, or can correspond to a convex or concave surface intersecting the well.

2.4.1 Principle

A plane is defined by a minimum of three points not lying in a straight line. It should be sufficient, therefore, to know the coordinates (X, Y, Z) of three points in space to define the plane. These three points will be the intersection of three generatrices of the borehole wall with the plane (Fig. 2.31).

2.4.2 Measurement Process

The tool consists of at least three electrodes mounted on pads in a plane perpendicular to the axis of the tool and situated at angles of 120° (3-pad tool) or 90° (4-pad tool) to each other, the configuration of this tool is shown in Fig. 2.32.

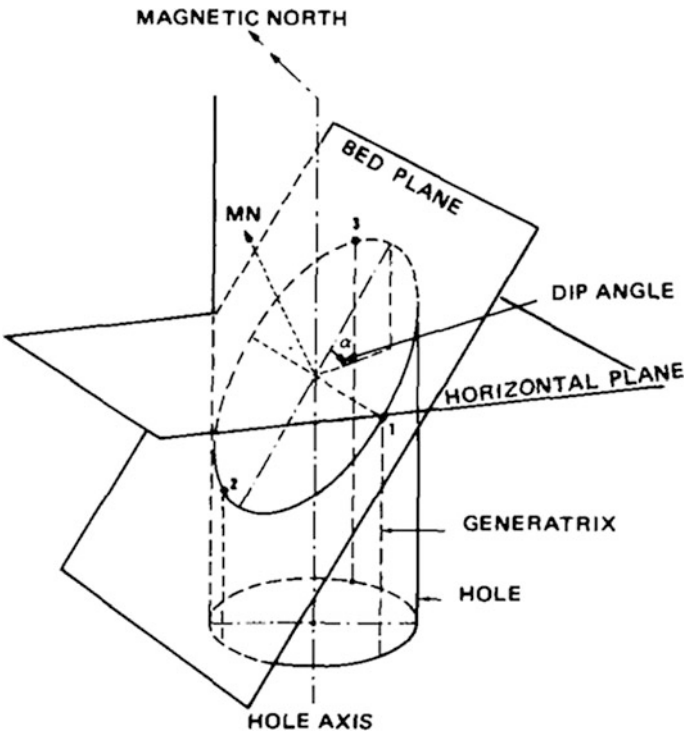

Fig. 2.31 A plane is defined by a minimum of three points not lying on a straight line. The three point are the intersection of three generatrices of the borehole wall with the plane (i.e., bed boundary)

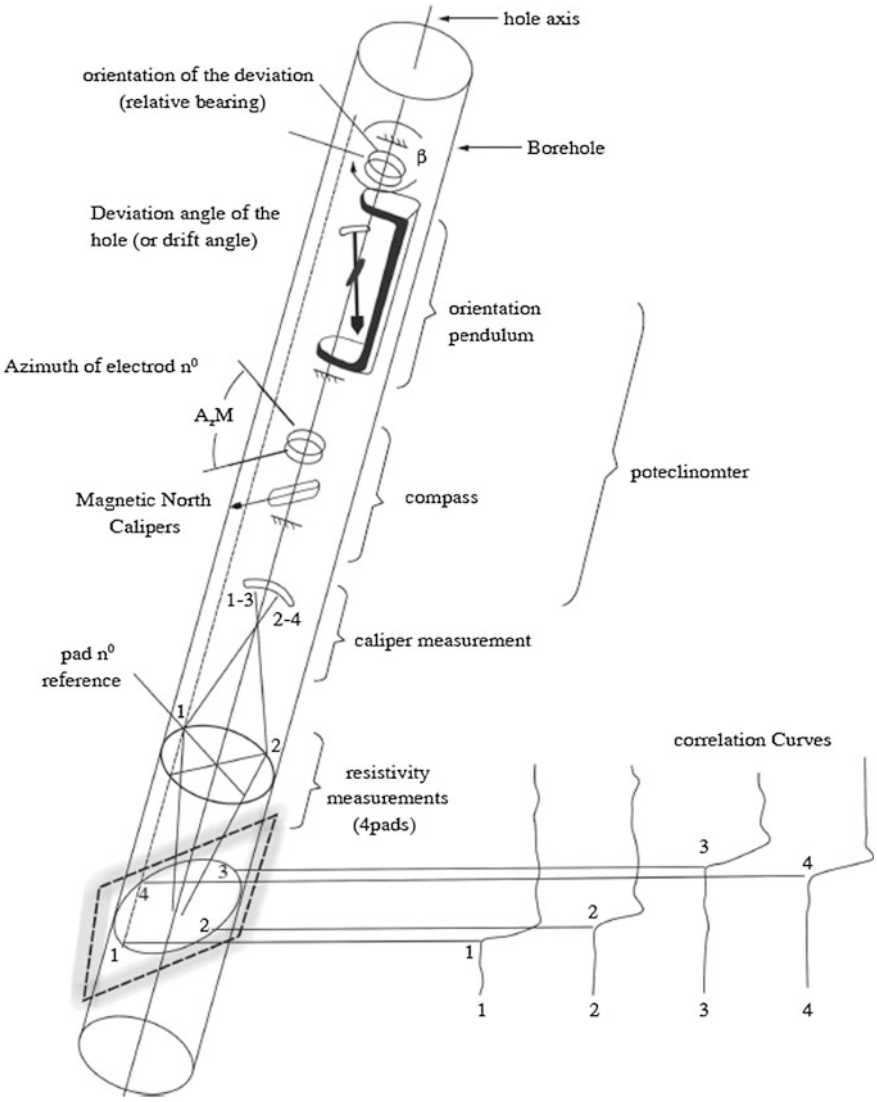

Fig. 2.32 Principle of the dipmeter showing the different measurements made by the tool (from Dresser–Atlas document)

The three electrodes each make a resistivity measurement of the borehole wall. Because of the size of the electrode and the current focusing that occurs on each pad the resistivity measurement is assumed to be a point measurement at the electrode. When the tool crosses the boundary between two formations the corresponding response change is recorded for each pad at different depths according to the

apparent dip (that is to say in relation to the borehole axis). The relative depth differences for the curves give the necessary information to evaluate the dip and the azimuth if we also know:

(a) the orientation of the sonde defined by the azimuth and one of the pads (pad number 1). This azimuth is the angle formed by the horizontal projection of the lines perpendicular to the sonde axis and passing through pad number 1 and magnetic north;
(b) the borehole deviation and its azimuth;
(c) the hole diameter (or more exactly the distance between the sonde and each pad).

The azimuth of pad 1 with respect to magnetic north is measured using a compass to which is fixed the cursor of a potentiometer. The movement of the compass pointer is reflected in changes in the potentiometer resistance. The borehole deviation is measured using a pendulum linked to a potentiometer whose resistance varies as a function of the deviation. The azimuth of the deviation is measured by means of another pendulum that is continuously aligned in a vertical plane passing through the low side of the borehole. This pendulum is linked to a circular potentiometer whose resistance is a function of the angle formed by the azimuth of the deviation and of the azimuth of pad number 1 as reference (called the relative bearing). Finally the hole diameter is measured using potentiometers linked to the sideways movement of the pads.

2.4.3 SHDT

The Schlumberger SHDT (Sedimentary Dipmeter Tool) dipmeter, for example, with four independent arms, each carrying a pad with two small circular electrodes side by side and 3 cm apart. The sampling is made every 1/10 in. (2.5 mm). This system acquires more information on sedimentary structures: lithological or textural changes over very short distances can be detected. In addition the tool deviation is more precisely measured by a new magnetometer. The tool also has an accelerometer which allows better speed corrections, resulting in a more accurate dip measurement. The Emex current is automatically adjusted to always have the highest contrast in resistivity.

A typical dipmeter field log will show not only the raw microresistivity curves, but also most of the orientation and caliper data. The example chosen is from a western Atlas, 4-arm(pad) Diplog (Fig. 2.33). In track 1 are the deviation of the borehole from the vertical (DEV) and azimuth (DAZ), the azimuth (AZ) of the reference pad (pad1) and a gamma ray. In track 2 and 3 are the raw acquisition curve, the tension and the two calipers. The tension curve is useful in identifying zones of tool sticking although these are usually evident on the caliper and the raw

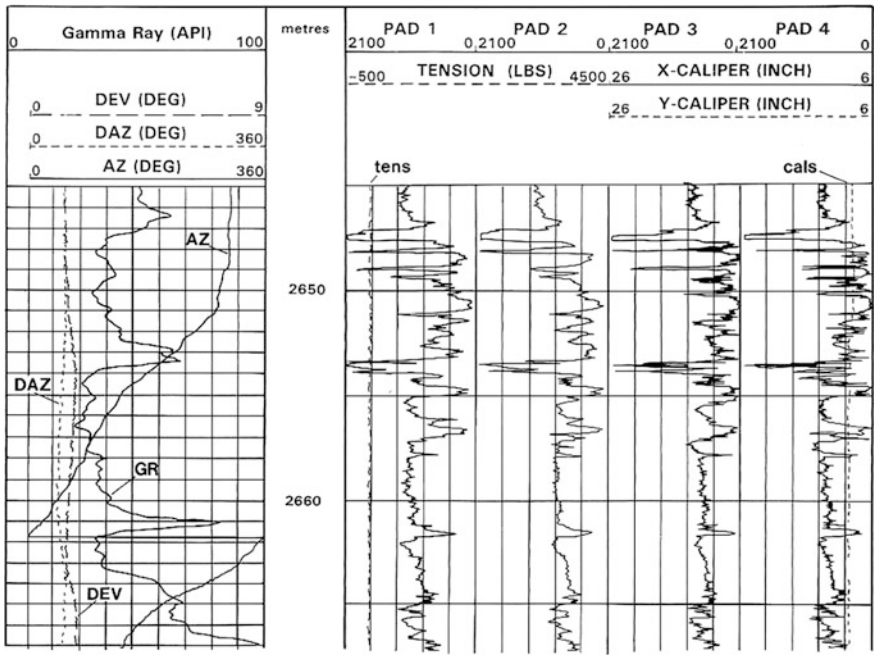

Fig. 2.33 Standard log presentation of raw dipmeter data. The dipmeter curves are sampled every 0.5 cm (0.2″) while the standard logs are sampled every 15 cm(6″) (western Atlas Dip log). *DEV* Hole deviation from the vertical. *DAZ* Azimuth of hole deviation. *AZ* Azimuth of pad 1. *pad 1-4* Pad conductivity curves

curves themselves. The format of the raw dipmeter data varies between companies although the basic information included is similar. The log is plotted at a 1:200 scale.

2.4.4 Colored Dip Patterns

More than 20 years ago, the pioneers of log-derived dip interpretation devised a color-coding scheme for different computed dip patterns. Structural dip is usually colored green on computed dip arrow plots, a method to identify graphically those intervals having consistent magnitude and direction of dip. The color is, of course, arbitrary, but the color-coding scheme has evolved into an acceptable industry standard. For studies of sedimentary dip, it was found useful to sort out the apparent confusion of dip arrows with different colored lines joining groups of dip arrows that fit different dip patterns and/or directions. The color scheme, as shown in Fig. 2.34, is that which is generally accepted in the industry today.

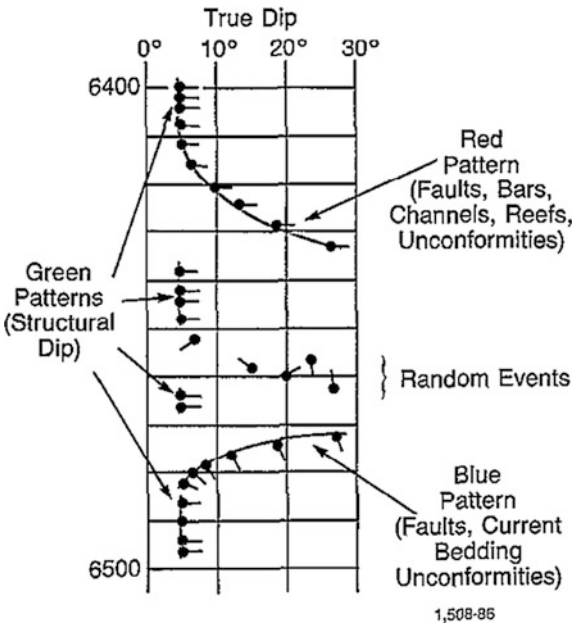

Fig. 2.34 Four colored dip patterns for common formation structure

2.4.4.1 Red Pattern

Red dip patterns connect those dips that increase in magnitude with increasing depth, the azimuth remaining roughly constant. Red dip patterns are usually associated with such geological features as:

(a) faults and folds,
(b) unconformities,
(c) differential compaction (e.g., above reefs, bars, domes, etc.),
(d) within channels, troughs, and valley fills.

2.4.4.2 Blue Pattern

Blue dip patterns connect dips that decrease in magnitude with increasing depth, with the azimuth remaining roughly constant. Blue dip patterns are usually associated with features such as:

(a) faults or folds,
(b) unconformities,
(c) paleocurrent features.

Blue dip patterns associated with paleocurrent features are usually found over short depth intervals, while blue dip patterns associated with faults, folds and unconformities might persist over much longer depth intervals.

2.4.4.3 Green Pattern

Green dip patterns are usually found in shales. However, shale do not always exhibit such coherent dip because of slumping, fracturing, diapirism, etc. conversely, a green dip pattern does not always represent post-depositional structure. Parallel crossed-bedding will also reflect consistent dip azimuth. Low structural dip (<5°) is the most difficult to identify because dip azimuth is often widely scattered. If the scatter is restricted to low dip magnitudes, structural dip is essentially flat, with no preferred direction indicated. For more than a 2° dip magnitude, the average direction can usually be determined by auxiliary plots.

2.4.4.4 Random Pattern

Random events correspond to a chaos of dip and azimuthal, which are changed irregular with increasing depth. Random dip pattern are usually associated with fault and fracture zone caused by tectonic movements.

2.4.5 Results Presentation

The results of computer processing of data recorded in a well are presented in various forms.

(1) **Listing presentations**

The Service Company gives dip computation results in the form of listings.

In the case of MARK IV the listings given by Schlumberger give the following data in 13 columns: Depth; Dip angle; Dip azimuth; Deviation angle; Caliper 1-3 diameter; Caliper 2-4 diameter; LOG1 corresponding to the program logic (Table 2.4).

(2) **Graphical presentation**

Dip results may be presented graphically in many ways.

1. Arrow plots (Fig. 2.35)

This is the most widely known presentation, and can be produced at depth scales of 1/1000, 1/500, or 1/200. Each calculated point is plotted:

(a) In abscissa according to the dip angle.
(b) In ordinate with depth.

The point is extended by a short straight line in the dip direction, with geographical north towards the top of the plot (or log). Also shown are: (a) the angle

Table 2.4 Normal listing of MARK IV (Courtesy of Schlumberger)

Depth (m)	DIP (°)	DIP AZM(°)	DEV (°)	DIAM1-3 (in.)	DIAM2-4 (in.)	PLA (°)	CLO (°)
952.4	15	94	1.2	12.5	12.3	11	100
953.3	14.3	108	1.4	12.5	12.4	85	53
954.3	10.2	158	1.3	12.4	12.4	0	100
955.3	36.7	221	1.4	12.6	12.5	0	0
956.3	10.6	352	1.4	12.6	13.4	0	100
957.3	24.3	288	1.4	13.6	13.4	0	51
958.3	23.7	102	1.5	14.2	13.4	0	100
959.3	37.2	181	1.6	13.3	12.9	0	100
960.3	26	170	1.6	13.2	13	0	95
961.3	19.9	149	1.6	13.3	13	0	16
962.3	13.9	144	1.5	12.5	12.4	0	100
963.3	41.2	268	1.4	12.3	12.4	0	100

and azimuth of the borehole deviation (intervals of 50 m or 100 ft, usually); and (b) a scaleless resistivity curve allowing depth correlation with other logs. This curve is drawn with low resistivities to the EPT.

Different symbols are used to represent points:

(a) A black circle indicates a good quality result.
(b) An open or white circle indicates a point for which the quality is undefined
(c) A cross shows that the four-pad logic has been used, however, this symbol is not used in the standard presentation.

2.4.6 Stick Plot

A stick plot represents dip as a line. Because no azimuth can be indicated, stick plots are usually presented in two (sometimes more) sections, one at 90° to the other: typically a north-south and an east-west set. The sticks represent the apparent dip in the orientation indicated (Fig. 2.36). The plots are most effective using broad interval averages and small vertical scales to illustrate an entire well. Figure 2.36 shows a standard dipmeter tadpole plot with corresponding dip azimuth against depth plot (center) and two, orthogonal orientations of stick plot (right). The azimuth plot is especially useful in structural analysis. The stick plot is used on correlation cross-sections and for seismic comparisons. Stick plot can be useful added to correlation diagrams.

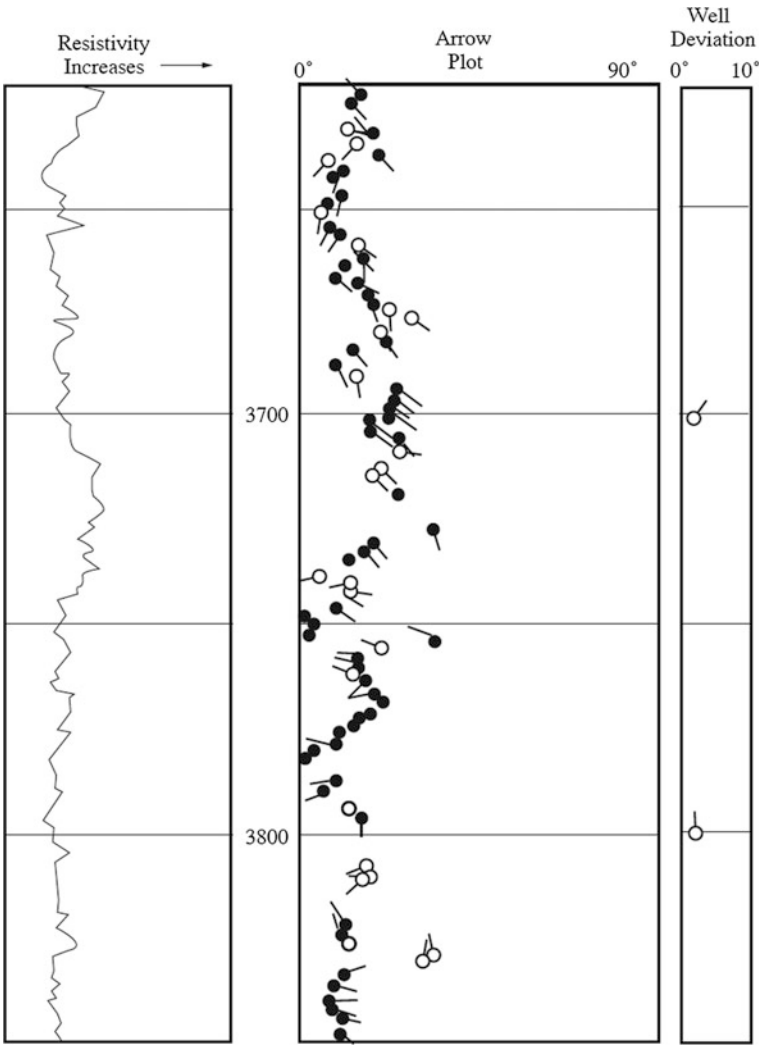

Fig. 2.35 Example of *arrow* plots

2.4.7 Azimuth Frequency Plots

Calculated azimuth values in a depth interval are plotted in the form of circular histogram (Fig. 2.37). The value of the azimuth is read clockwise from 0° to 360° and the frequency of occurrence is shown as a radial line whose length is proportional to the number of points whose azimuth falls in the range. Zero values are at the center.

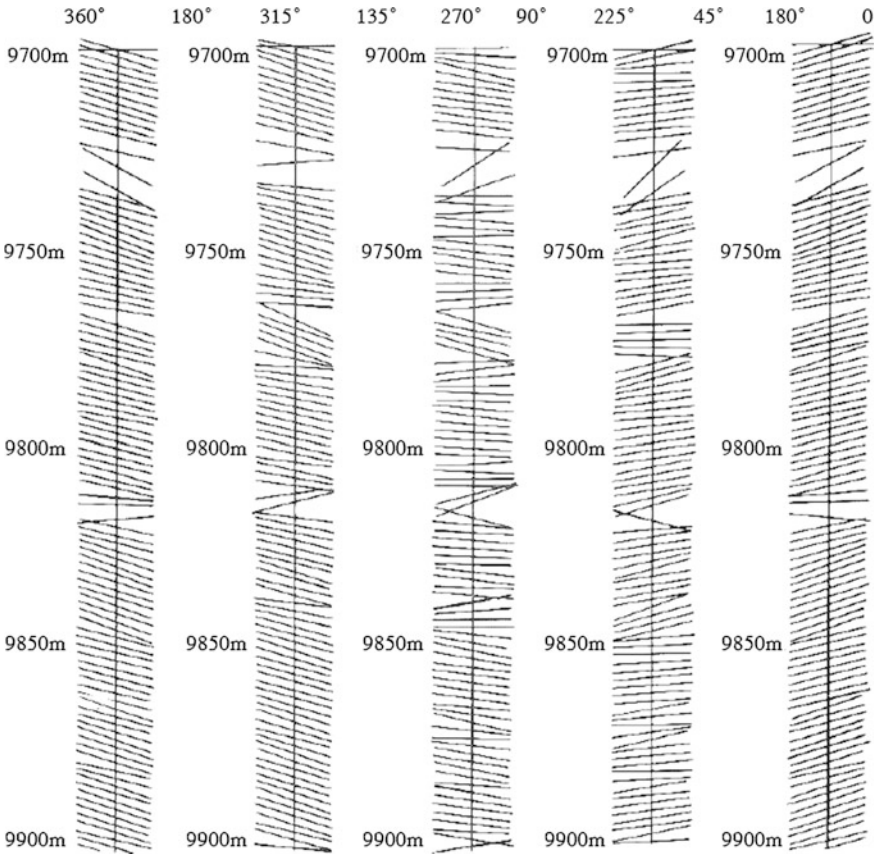

Fig. 2.36 Standard tadpole and stick plot

The plots allow the determination of azimuth trends, the azimuth or regional dip, sedimentary dip. The plots are also widely used to identify geological structure, sedimentary environments, fracture zone, fault, unconformity. Meanwhile, the caliper, azimuth and dip curves can be applied to determine the stress, stability of wall.

2.5 Summary

Resistivity devices display apparent resistivity values, R_a. The apparent resistivity, R_a, measure at a depth of interest is affected by the resistivity geometry of four zones that surround the tool: the borehole, adjacent beds, and the invaded and uninvaded zones of the bed of interest. The apparent resistivity value should be corrected for the borehole and the adjacent-bed (also called bed thickness)effects. The corrected value R_a'', bears the influence of the invaded and uninvaded zones.

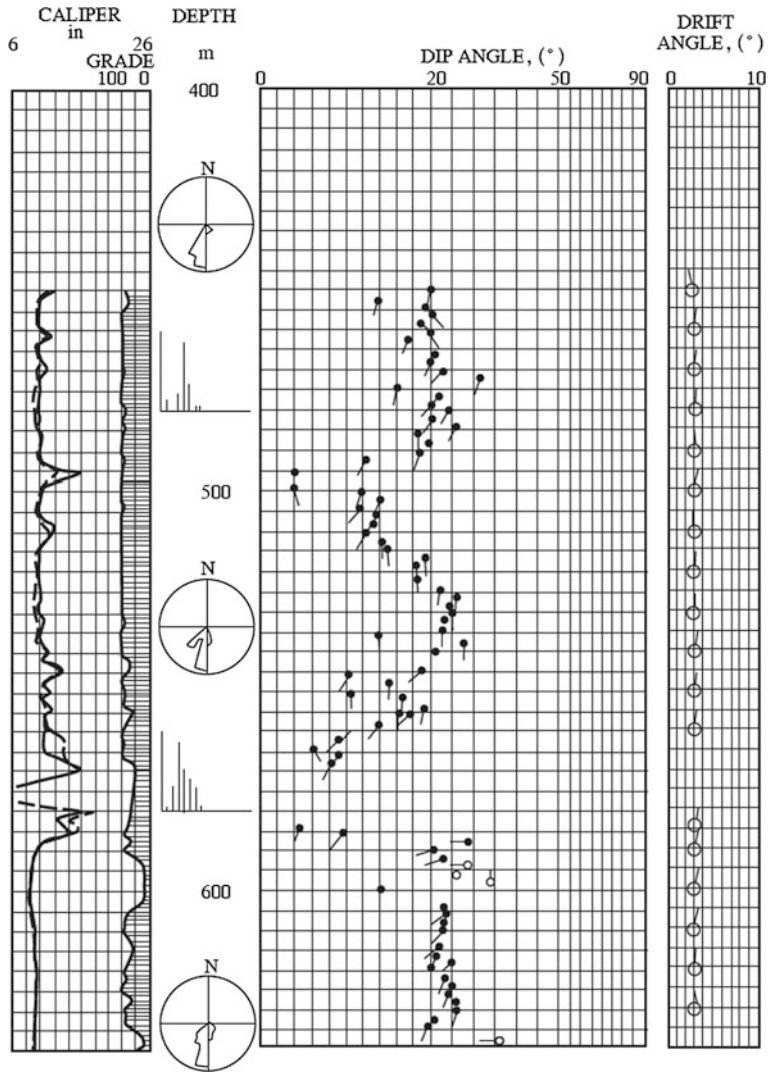

Fig. 2.37 Azimuth frequency plot

Depending on the type and number of resistivity logs available, R_a'' is used to calculate R_t, R_{xo}, or both. Departure curves (charts) are usually used to perform these corrections and calculations.

Determining R_t and R_{xo} requires three steps.

The apparent resistivity R_a, is first corrected for borehole effects by use of Rm and dh. Correction of readings of microresistivity devices requires R_{mc} and h_{mc} instead. For each resistivity tool, optimum measurement conditions exists in which the borehole effect is nil or negligible.

The value obtained from Step 1, R_a', is then corrected for bed thickness effect with the resistivity of the adjacent bed R_s, and the thickness of the bed in question. No adjacent-bed corrections are necessary when the bed thickness exceeds a certain value. This value depends on the tool's vertical resolution and the resistivity contrast R_t/R_s. Reading of microresistivity tools are free from this effect.

The last step is to use the value R_a'' obtained in Step 2 to calculate R_t and R_{xo}. The calculation calls on the geometric factors. Departure curves or a system of equations is used. If the diameter of invasion is small, the effecting invasion is negligible and $R_t = R_a''$. On the other hand, for microresistivity devices, when invasion is deep, the effect of the uninvaded zone becomes negligible and $R_{xo} = R_a''$.

In certain measurement environments, the three effects (borehole, bed thickness and invasion) are negligible. In these cases, R_t or R_{xo} can be read directly from the log.

In some instances, the data available lead to unrealistic results, such as negative values, or the data fall off the tornado chart. In the most instances, such an occurrence is the result of values improperly read or improperly corrected for borehole or bed thickness effects. However, in cases of very deep invasion with an invasion profile that cannot be approximated by a step profile, such a case may result. Treatment of other invasion profiles, such as the transition and annulus profiles, requires extensive data; four resistivity readings are usually needed.

Problems

2.1 What are the characteristics of resistivity of rocks?
2.2 Draw a sketch of the environments of borehole in view of resistivity
2.3 Describe the Archie's experiment and the formulas to calculate S_w.
2.4 Explain the mechanism of the occurence of SP
2.5 What are the properties of SP and its applications?
2.6 What is the principle of focused resistivity logging?
2.7 Describe the configuration of DLL tool.
2.8 Explain the measurement principle of DLL method.
2.9 What are the characteristics of DLL curve?
2.10 How to determine the fluid type of the formation by using DLL curves?
2.11 Explain the principle of DIL method
2.12 What is the characteristics of DIL curve?
2.13 How to determine the fluid type of the formation by using DIL curves?
2.14 What is the advantages of image resistivity logging?
2.15 What 'is the configuration and applications of AIT?
2.16 What is the configuration and applications of FMI?
2.17 What is the principle of dipmeter logging?
2.18 What is dip pattern of dipmeter logging presentation?
2.19 Explain the characteristics of the four dip patterns respectively?

Chapter 3
Sonic Logs

Last chapter focused on formation resistivity, one is R_t, the resistivity of true zone; another one is RXO, the resistivity of flushed zone. According to Archie formula, if we calculate S_w, saturation of formation, besides resistivity, porosity is a necessary parameter. In practice, Sonic logging is usual method that is used to provide this parameter.

Through detecting the propagation properties of sound waves while traveling across the drilling fluids in the borehole and formation, acoustic logging can present the knowledge of formation characteristics and the situation of borehole. Three major types of acoustic logging depend on its investigating parameters such as sonic velocity logging, sonic amplitude logging, and sonic frequency logging. We can group together as acoustic logs those that involve recording a parameter linked with the transmission of sound waves in the formation.

These parameters are mainly:

(1) The propagation speed of a wave in the formation calculated from the time taken to travel through a certain thickness of formation. This is the sonic log (AC).
(2) The amplitude at the receiver of the first or second wave in the signal train, either on arrival of the compressional wave or the shear wave. This is the sonic amplitude log, which has an important application in cementation evaluation, such as the Cement Bond Log (CBL), Variable density logging (VDL), and Segment bond logging test (SBT).
(3) The frequency of sound also reflects the properties of the medium that sonic wave travels, through this method, we can learn the type of fluid that flows outside the pipe or tube. The noise logging is a classic frequency test (NL).

H. Liu, *Principles and Applications of Well Logging*, Springer Mineralogy,
DOI 10.1007/978-3-662-53383-3_3

3.1 The Foundational Principle of Acoustic Logs

3.1.1 Elastic Properties of Rocks

Elastic properties are the characteristics that define the ability of a body or rock to resist permanent deformation when deformed slightly. A hypothesis for the rock elastic properties is that all solids, including rocks, follow Hooke's law which gives the proportional relation between the tension and the constraint (force).

The ratio of constraint to tension in a simple linear compression or dilation is known as Young's modulus.

$$\mathrm{E} = \frac{F/S}{\mathrm{d}L/L}, \tag{3.1}$$

where (F/S) is the constraint or force applied per surface area and dL/L is the stretch or compression per unit length under the effect of the force.

The ratio of force to tension under hydrostatic compression or dilatation corresponds to the elastic bulk modulus.

$$\mathrm{k} = \frac{F/S}{\mathrm{d}V/V}, \tag{3.2}$$

where (dV/V) is the change per unit volume under the effect of the force. Usually, the inverse of the elastic bulk modulus k, called compressibility, c, which is an important parameter to evaluate the degree of consolidation of rocks.

The ratio of force to tension under a shear force or one that is applied tangential to the displaced surface is known as the shear modulus, μ

$$\mu = \frac{F/S}{\mathrm{d}V/V}, \tag{3.3}$$

where (F/S) is the shear force and dV/V is the shear tension or the deformation without a change in total volume.

Poisson's ratio, σ, is a measure of the change in shape, or ratio of the lateral contraction to the longitudinal dilation.

$$\sigma = \frac{\mathrm{d}l/l}{\mathrm{d}L/L}, \tag{3.4}$$

where dl/l is the transverse or lateral change.

Space modulus, M, is given by

$$M = K + \frac{4}{3}\mu \tag{3.5}$$

It is a measurement of the resistance to deformation from compressional and shear force in an elastic medium.

3.1.2 Acoustic Waves

There are several types of sound waves, each one characterized by the special kind of particle movement.

1. *Compressional waves (or P-wave) (Fig. 3.1)*

In this wave the particles move in a direction parallel to the direction of propagation. The speed of propagation is largest for this kind of wave compared to others and so it arrives first. It is the only wave propagated in liquids.

2. *Transverse or shear waves (or S-wave) (Fig. 3.1)*

Particle movement is in a direction perpendicular to the wave direction. As mentioned, the speed of propagation is less than the *P*-wave with a ratio of about 1.6–3. No shear waves are transmitted in liquids.

In the formation, sound energy is transmitted by both compressional and shear waves. In the mud, energy is transmitted solely by compressional waves.

The energy transmitted by the slower shear wave is much higher than that of the compressional wave which is first to arrive. In the wave pattern received, we can identify the shear wave by this feature.

3. *Stoneley waves (Fig. 3.1)*

Stoneley waves that are boundary acoustic waves at a liquid–solid interface resulting from the interaction of the compressional wave in the liquid and the shear wave in the solid. By definition, the Stoneley wave must have a wavelength smaller than the borehole diameter. Particle motion in the solid will be elliptical and retrograde similar to a Rayleigh wave. The velocity of the Stoneley wave will be less than that of the compressional wave in the fluid or the shear wave in the solid. N.B. Sound waves transfer energy step by step by the movement of particles under elastic forces.

The speed of sound in the formation depends on the kind of minerals making up the rock. The effect of the minerals is determined by their densities and their parameters of elasticity.

These parameters are not always well known. However, the transit time has been measured for a few of the common minerals (Table 3.1).

4. *Rayleigh waves (Fig. 3.1)*

Rayleigh waves are the waves in which the particle motion is elliptical, and retrograde with respect to the direction of propagation. These waves are not transmitted in liquids and their velocity is around 90 % of that of transverse waves (*S*-wave).

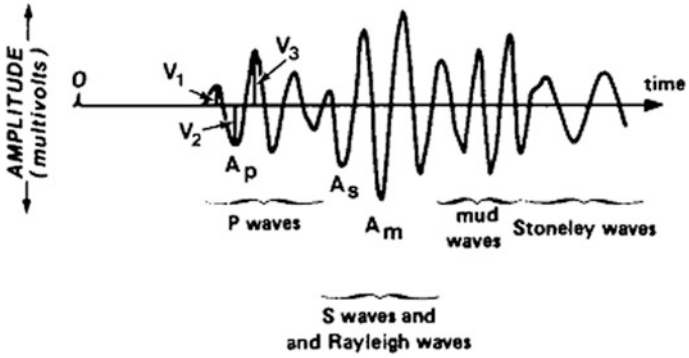

Fig. 3.1 A typical full acoustic waveform recorded in a borehole P-wave, S-wave, Stoneley waves and Rayleigh waves

Table 3.1 Interval transit time and speed of *P*-wave of the most common minerals and rock

Material	v_p (m/s)	Δt (us/m)
Anhydrite	6100–6250	164–163
Tight limestone	6400–7000	156–143
Dolomite	7900	125
Halite	4600–5200	217–193
Light sandstone	5500	182
Oil	1070–1320	985–757
Methane (1 atm)	442	2260
Air, 0 °C	330	3000
Shale	1830–3962	548–252
Steel	5340	187
Drilling fluid	1530–1620	655–622

3.1.3 Sound Wave Propagation, Reflection, and Refraction

Huyghens' principle states that each point reached by a wave oscillation acts as a new source of oscillation radiating spherical waves (Fig. 3.2).

The surface described by the in-phase oscillation at any given time is known as the wave front. The surface of separation between the set of points not in motion and those that (or were) make up a particular wave front is called the wave surface.

Sound waves follow Snell's law. Suppose we have two homogeneous media, isotropic and infinite with velocities v_{L1}, v_{T1}, and v_{L2}, v_{T2}, separated by a plane surface.

Every wave L, even those purely longitudinal or transverse, incident at a point I on the separating surface at an angle z, gives rise to four new waves. Two of these are reflected waves, one compressional L_r, at an angle r_1, one transverse T_r, at an angle r_2, and the other two are refracted waves, one longitudinal L_R, at an angle R_1, and the other transverse T_R at angle R_2 (Fig. 3.3).

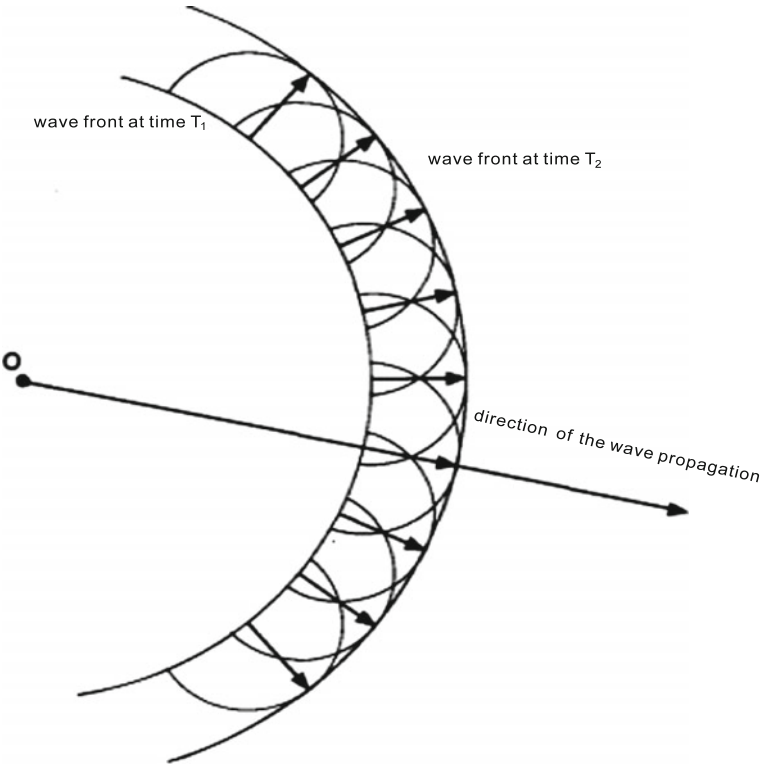

Fig. 3.2 Illustration of wave propagation

Other sound waves may appear due to diffraction or dispersion. If we only consider longitudinal waves the reflection law is $i_1 = r_1$

And the refraction law is $\sin i_1/v_{L1} = \sin R_1/v_{L2}$

If $v_{L2} > v_{L1}$ the angle of total refraction or the critical angle of incidence, l, (R_1 = 90°) is given by the equation

$$\sin l = v_{L1}/v_{L2}$$

We can define two critical angles of incidence, one for longitudinal and the other for transverse waves. If we consider the reflected and refracted waves given by a transverse wave, we have

$$\frac{\sin i_1}{v_{L1}} = \frac{\sin r_2}{v_{T1}} \quad \text{and} \quad \frac{\sin i_1}{v_{L1}} = \frac{\sin T_2}{v_{T2}}$$

N.B. In the case of a wellbore where medium 1 is a fluid the reflected transverse wave does not exist.

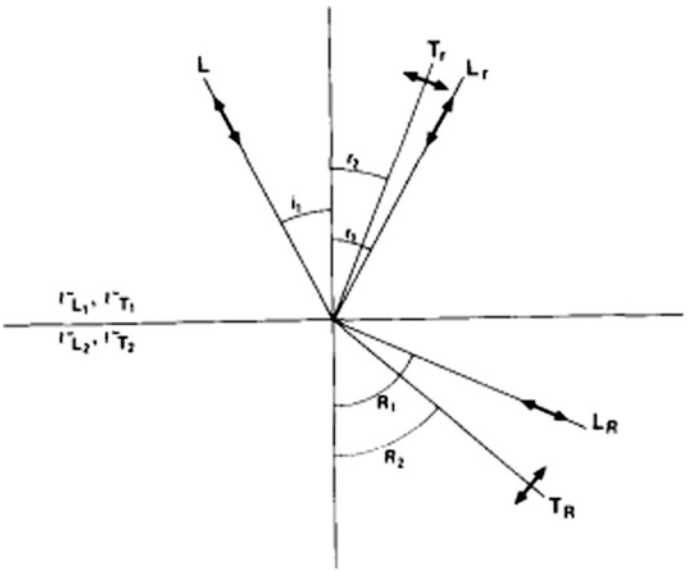

Fig. 3.3 Reflection and refraction of an acoustic wave

Acoustic impedance

This is given by the product of the density of a medium by the velocity of sound in the medium:

$$\mathrm{r} = v_1 p_1$$

Reflection coefficient

In the case of an incident wave normal to a surface, this is the ratio of reflected energy to incident energy:

$$R_{1-2} = \frac{v_2 p_2 - v_1 p_1}{v_2 p_2 + v_1 p_1}$$

When the angle of incidence varies, the ratio changes from $R_{1\text{-}2}$, and depends on i_1, v_{T1}, and v_{T2}.

3.2 Sonic Log

3.2.1 Principle

A magnetostrictive transducer, excited from the surface by a signal, emits a sound wave (Fig. 3.4) whose average frequency is of the order of 20–40 kHz.

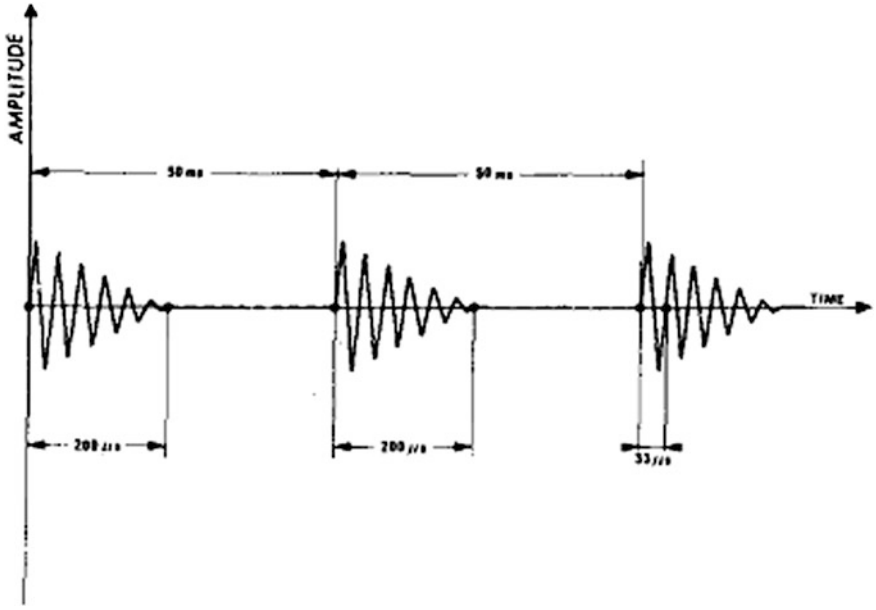

Fig. 3.4 Schematic representation of the signal emitted by the transducer

The duration of the emission is short but it is repeated several times per second (10–60 times depending on the tool). The wave spreads in all directions from the transmitter producing spherical wavefronts. The wavefront passing through the mud is incident upon the borehole wall with increasing time and increasing angle of incidence as the distance from the transmitter increases (Fig. 3.5).

We can consider several cases:

(a) If the angle of incidence is less than the critical angle each incident longitudinal wave gives rise to: (1) two longitudinal waves, one reflected, one refracted; and (2) one refracted transverse wave (the reflected transverse wave cannot propagate in the mud).
(b) If the angle of incidence is larger than the critical angle the incident longitudinal wave produces a single reflected longitudinal wave.

The incident or reflected longitudinal waves traveling in the mud are slower than the refracted compressional waves propagated in the formation, since the speed of sound in the ground is greater than that in mud.

Among the refracted longitudinal waves we are particularly interested in those waves refracted at the critical angle (Fig. 3.6), since they propagate along the borehole wall at a speed V_{L2}. Each point reached by this wave acts as a new source transmitting waves, so creating effectively cones of waves in the mud traveling at a speed V_{L1}.

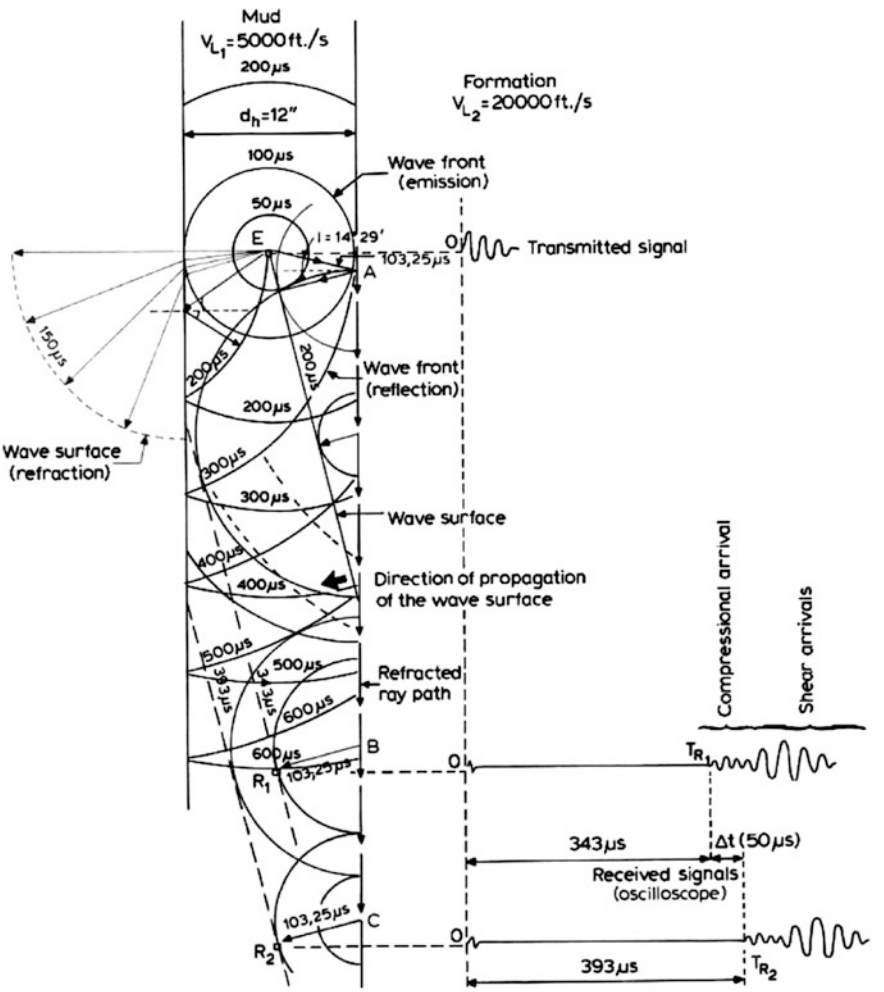

Fig. 3.5 Propagation of acoustic waves in a well. Principle for measuring the interval transit (tool with two receivers)

If we place two receivers, R_1 and R_2, at certain distances from the transmitter and along the axes of the tool and of the hole (supposed the same), they are reached by the sound at times T_{Rl} and T_{R2}, respectively, given by

$$T_{R1} = \frac{\overline{EA}}{v_{L1}} + \frac{\overline{AB}}{v_{L2}} + \frac{\overline{BR_1}}{v_{L1}} \tag{3.6}$$

$$T_{R2} = \frac{\overline{EA}}{v_{L1}} + \frac{\overline{AB}}{v_{L2}} + \frac{\overline{BC}}{v_{L2}} + \frac{\overline{CR_2}}{v_{L1}} \tag{3.7}$$

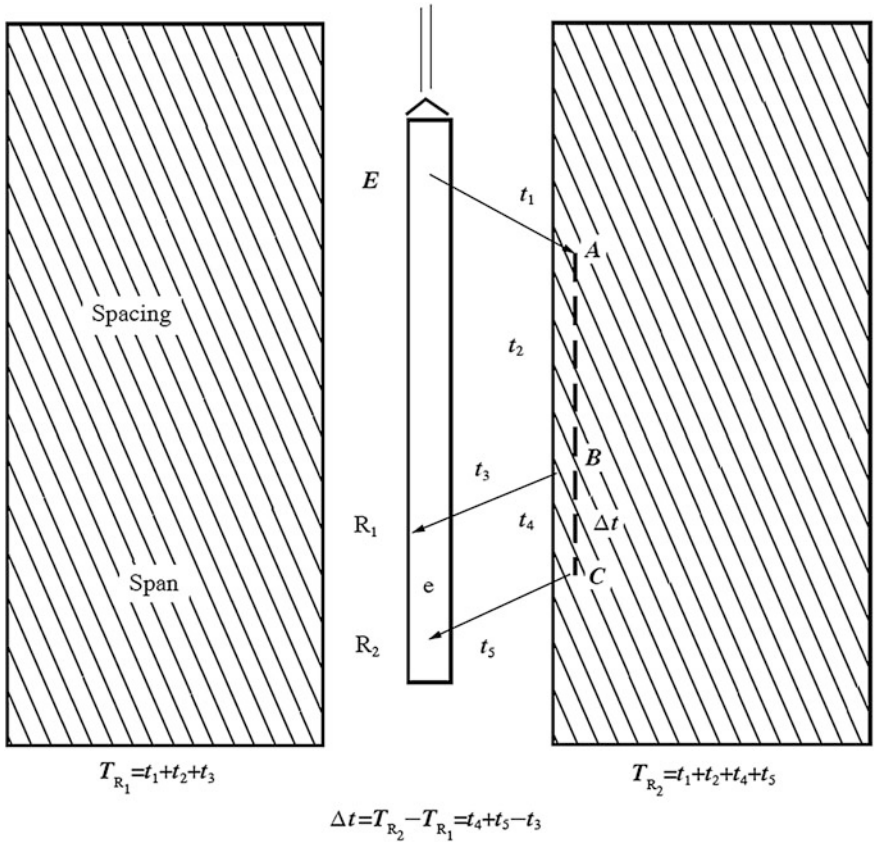

Fig. 3.6 Schematic of the principle for measuring the interval transit time (tool with two receivers)

If the tool is at the center of the hole and the hole is of uniform diameter we have, in effect:

$$\Delta t = T_{R2} - T_{R1} = \frac{\overline{BC}}{v_{L2}} \qquad ((3.8))$$

As

$$\overline{BR_1}/v_{L1} = \overline{CR_2}/v_{L1}$$

and

$$\overline{BC} = \overline{R_1R_2}$$

3.2.2 Borehole-Compensated Sonic (BHC)

If there are caves in the borehole wall or, where the tool axis is inclined to the hole axis, for some reason, the transit time is in error since the mud travel time is not the same for both receivers.

A way to counteract this is to use a tool that has two transmitters and four receivers arranged in pairs, two to each transmitter. Figures 3.7 and 3.8 show how the cave or tool inclination effect is inverted for the second transmitter–receiver pair. The average of two measurements, one for each receiver, should eliminate the effect. The tool first transmits from E_1, using receivers R_1, and R_1', and then from E_2, using R_2, and R_2'. The average is taken from the two measurements. It is this average that is recorded (Fig. 3.9).

As Fig. 3.8 indicates, in a region of changing borehole size, a single source–detector sonic device will measure abnormally long transit times when the hole becomes enlarged. This is a result of the increased transit time from the transmitter across the mud to the formation and back to the receiver. A partial solution to this problem is obtained by the use of one transmitter and two receivers. By determining the travel time to the two detectors and using the difference to determine the travel time, as indicated in the figure, the effect of the borehole diameter is eliminated except at the boundaries, where "horns" can appear on the log response.

The more general logging situation is shown in Fig. 3.9. Not only can there be changes in borehole diameter, but the tool is not necessarily centered in the

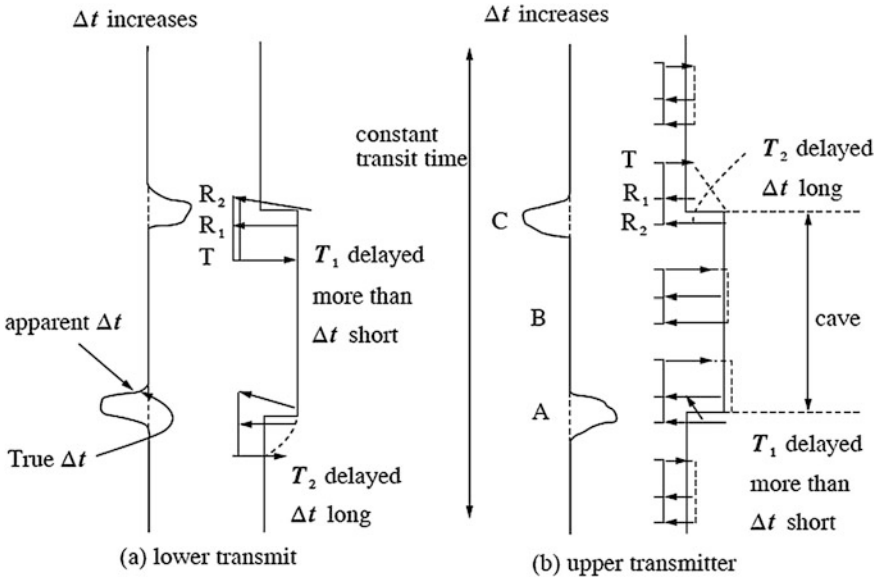

Fig. 3.7 Influence of a cave on the Δt measurement. **a** Transmitter above receivers. **b** Transmitter below receivers

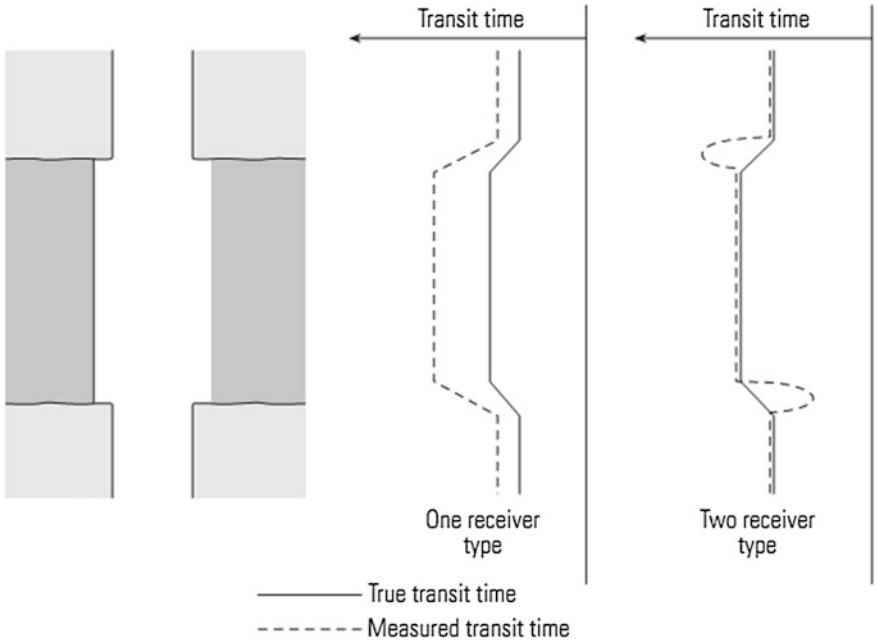

Fig. 3.8 The effects on the integrated travel time at the boundaries of hole diameter changers

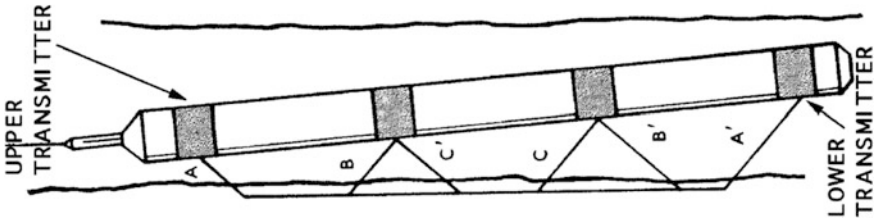

Fig. 3.9 The use of four detectors to compensate for borehole size and tool tilt

borehole, because of deviation of the borehole and differential sticking of the tool string. As indicated, this more general case can be solved by the use of two transmitters and two pairs of closely spaced receivers. Two sets of differential travel time measurements are made: an up-going one and a down-going one. In the case sketched in Fig. 3.10, the up-going transit time will exceed the down-going case. By averaging the two results, the effect of existing unequal mud travel paths is eliminated, and the measurement reflects the travel time of the formation. Tools of this type are said to be borehole-compensated (BHC).

The average is taken from the two measurements. It is this average that is recorded (Fig. 3.10).

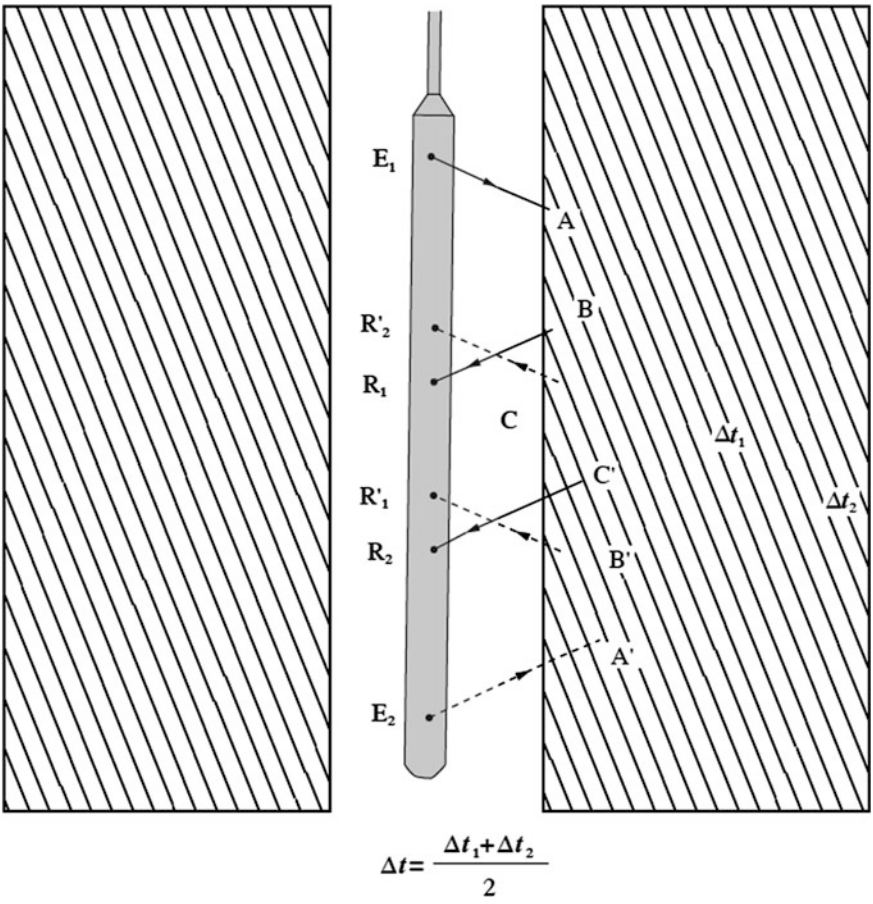

Fig. 3.10 Principle of the borehole-compensated sonic

A striking example of the former type of shale alteration is shown in Fig. 3.11, which shows the transit time measured in the same well 2 months apart.

3.2.3 Long Spacing Sonic (LSS)

The measurement of compressional velocity was natural. Since this wave has a larger velocity, it always arrives at the detector first. The shear arrival can be masked if it arrives in the midst of the ringing portion of the transmitter signal, or it can be lost in some of the other modes produced by acoustic waves in boreholes. In the best cases, the problem of detecting the shear arrival is one of just looking for it after the compressional arrival. Such a case is illustrated in Fig. 3.12. In the waveform shown, the shear arrival is clearly distinguishable.

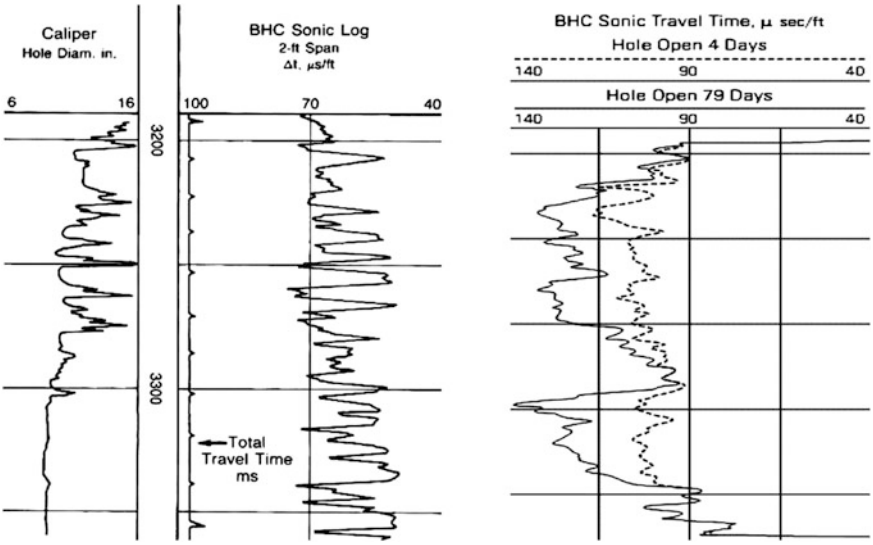

Fig. 3.11 Log example of the effect of formation alteration observed between two logging runs with 75 days of elapsed time

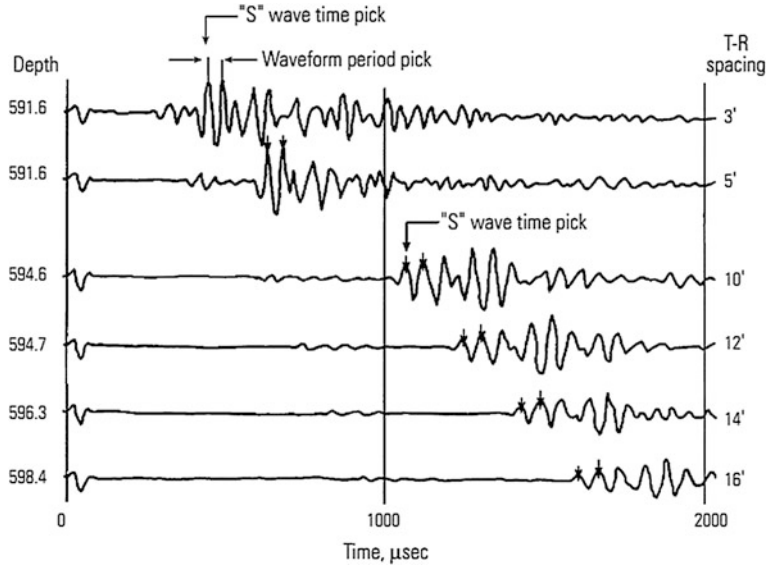

Fig. 3.12 The effect of spacing on the separation of shear and compressional arrivals

The stacked waveforms from six receivers placed from 3 to 16 ft from the transmitter, as shown in Fig. 3.12, indicate that the separation of shear from compressional arrivals is greatly aided by spacing. This was one of the motivations

for the development of long spacing sonic sondes. A second reason for their development was to combat the problem of the altered zone. The longer the spacing, the more reliably one can measure the transit time of the faster, undamaged formation. A common detector configuration is at 8 and 10 ft from the transmitter.

The quantification of this improvement for early acoustic tools operating in the 20 kHz range can be found in Fig. 3.13. It indicates the reliable zone of measurement (to the left of the indicated curves) for the conventional and long spacing sonde. The change in velocity of the damaged zone which can be tolerated as a function of its thickness is indicated as a function of the formation travel time. In a formation characterized by a Δt of 100 μs/ft, a 20 μs/ft alteration can be tolerated up to 5 in. thick for the conventional sonde, but it can be up to 14 in. thick with the long spacing device. This tolerance to alteration also eliminates problems with direct mud arrival in very large borehole sizes.

Another variation of the borehole compensation technique, used for long spacing devices, is shown in Fig. 3.13. In this case, two transmitters and two receivers are used to produce the same result as the six-transducer tool of Fig. 3.9. For the long spacing device, there are two receivers at the top of the tool and two transmitters at the bottom (a saving of two transducers).

The measurement is made in two phases. At one position in the well, the bottom transmitter fires and the transit time between the two top receivers is measured. Shortly after, when the tool has moved so that the two transmitters are nearly in the position previously occupied by the two receivers, the two transmitters are fired in succession, and the two transit times (from the different transmitters) are measured to the lower detector. As the figure indicates, this is equivalent to the use of two transmitters and four receivers, and the technique is referred to as depth-derived borehole compensation (Fig. 3.14).

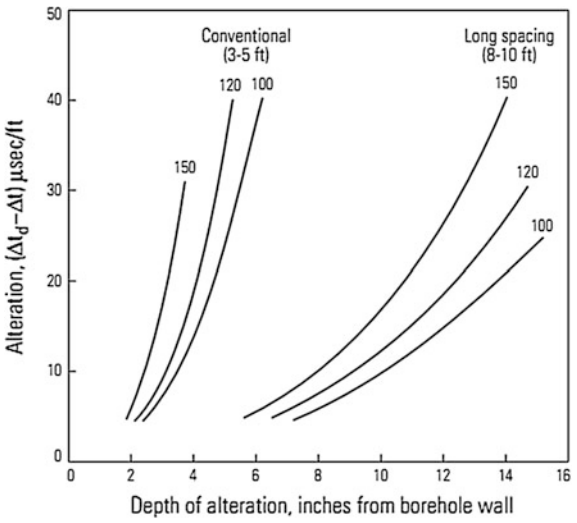

Fig. 3.13 The effect of alteration as measured by the difference between the observed interval transit time and the formation transit time as a function of alteration depth into the formation. As expected, the long spaced tool is able to tolerate deeper alteration before noticeable effects appear

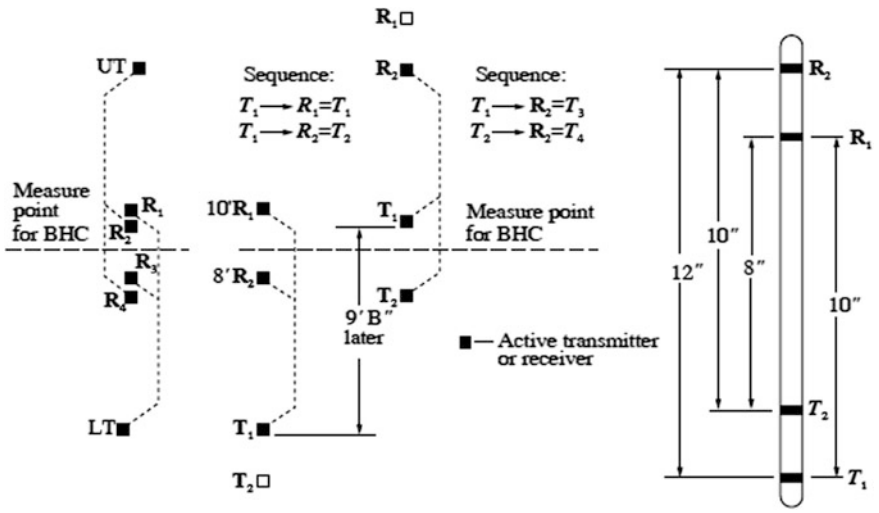

Fig. 3.14 The principle of the depth-derived borehole compensation (Courtesy of Schlumberger)

3.2.4 Dipole Shear Sonic Imaging (DSI)

1. *Principle*

The reliable borehole measurement of shear velocity awaited the development of the dipole source. An early identification of this problem and solution was made by Kitsunezaki who sketched out a few ideas for transducers, including an electromagnetically actuated double-ended piston, similar to a speaker, that is currently used today. Such a device, seen in Fig. 3.15, when activated, produces a positive pressure pulse on one side of the tool and a negative pressure on the other; and then the cycle reverses.

Although a dipole source can also be constructed of two oppositely phased ceramic monopole transducers (see Fig. 3.16) they generally are not capable of coupling enough energy into the formation wall at low frequencies to be of practical use. For LWD sonic applications, quadrupole sources are of interest for coupling energy into the formation rather than into the drill collar. In principle, these can be made of an assemblage of four properly phased monopole sources. Figure 3.16 shows schematically the arrangement of four monopole sources that constitute a quadrapole.

Acoustic array tools containing a battery of receivers, variable detector spans, waveform digitization were used to make progress in extracting reliable shear measurements. An example of one of these devices with eight receivers is shown in Fig. 3.17. In an array tool such as this, waveform processing and signal extraction is aided by the possibility of stacking signals recorded at the same depth from different receivers, for noise elimination as well as discrimination against other

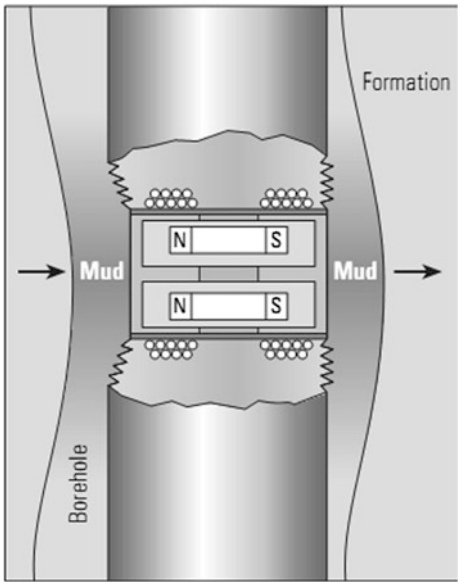

Fig. 3.15 A schematic of an electromagnetic piston dipole source, which induces a flexural wave in the surface of the borehole wall

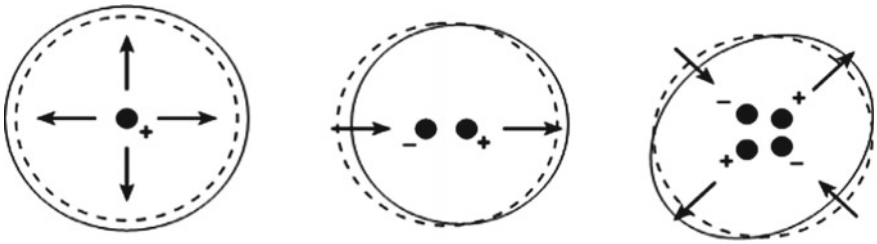

Fig. 3.16 A schematic shows how dipole and quadrupole transmitters can be formed by appropriately phased monopole acoustic transmitters. The convention is that a positive pressure pulse is produced radically by the monopole indicated by a "+" sign

acoustic signals produced within the borehole. Typical waveforms from a more modern device with 13 receivers are shown in Fig. 3.18; clearly seen are the compressional, shear, and Stoneley arrivals.

The investigation of DSI varies with formation, travel time of P-wave and S-wave, spacing, etc. DSI has five different working modes based on the combination of receivers and transmitters.

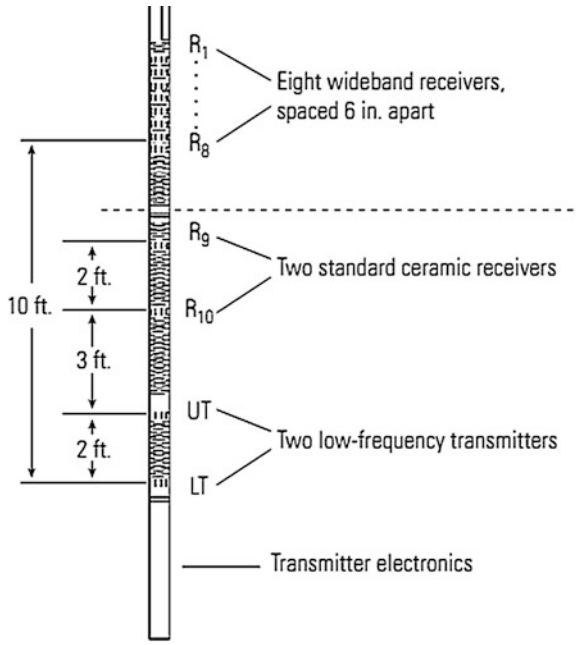

Fig. 3.17 An eight-receiver sonic array tool

- *upper and lower dipole mode*
  To acquire waveform of eight tracks from any dipole transmitters, sampling when pulse transmitted from the transducer, the sampling interval is 40 us, 512 pulses for each wave train.
- *Cross-dipole mode*
  To sample 32 standard wave trains totally from two cross-dipole transducers
- *Stoneley wave mode*
  To acquire eight wavefroms, each one from low-f pulse from monopole transducer. Sample interval 40 us, 512 pulses for each wave train.
- *P or S mode*
  To get eight waveforms. Begin with high-f pulse from monopole transducer. Sample interval 10 us, 512 pulses for each wave train.
- *Head wave checking mode*
  To record eight group of data over the threshold of monopole transducer derived by high-f pulse. Mainly used to derive monopole compressional travel time.

2. *Presentation of DSI*

DSI can provide velocity of *P*-wave, *S*-wave, and Stoneley-wave, and based on which, the Poisson ratio and full wave-train time sequance can be acquired. DSI

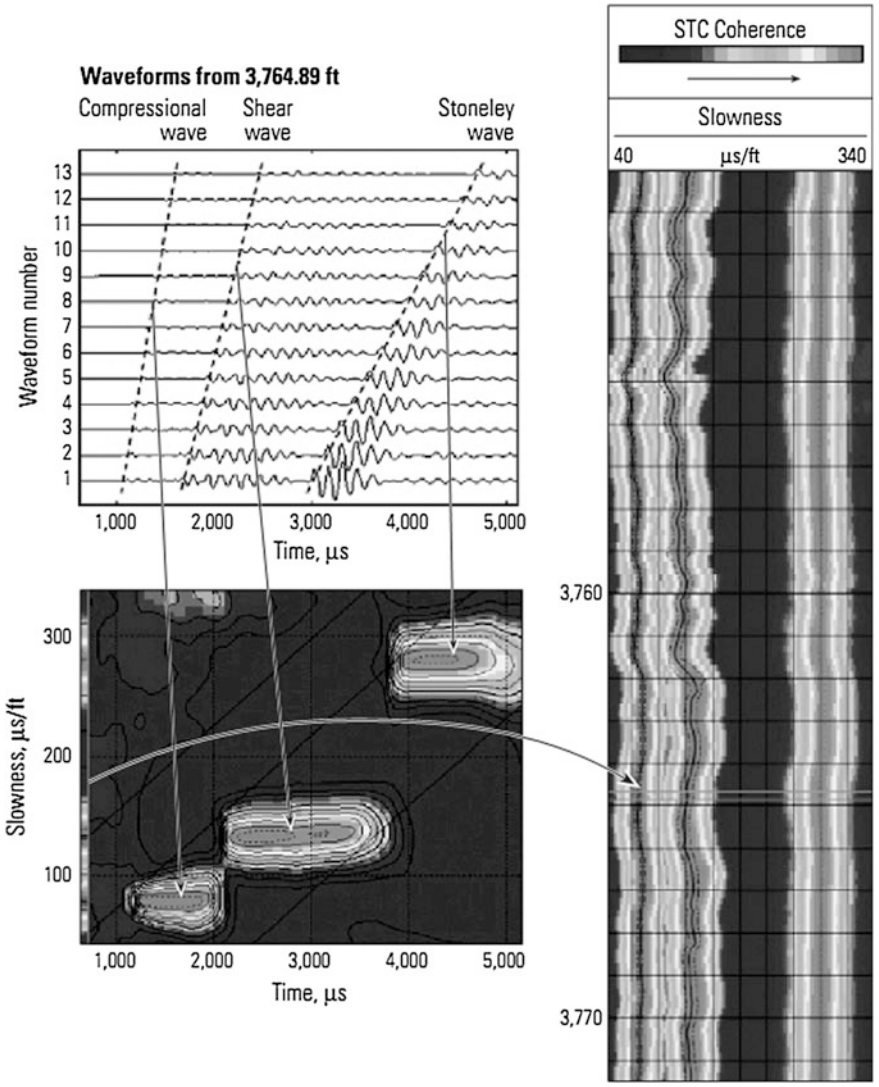

Fig. 3.18 Waveforms from a 13-receiver array tool clearly show the compressional, shear, and Stoneley arrivals (*top left*). The STC plot (*lower left*), for a particular depth, contains a thin strip, on the left-hand side of the plot, of the projected coherence values that appear on the generated slowness log (*right*) as regions of confidence

extends the application of sonic logging comparing with common acoustic logging method, for example, composite of *P*-wave and *S*-wave data, we can discern lithology, fluid type, to calculate poisson ratio, and using Stoneley wave, we can identify fracture, estimate permeability, and to achieve formation mechanical stress profile

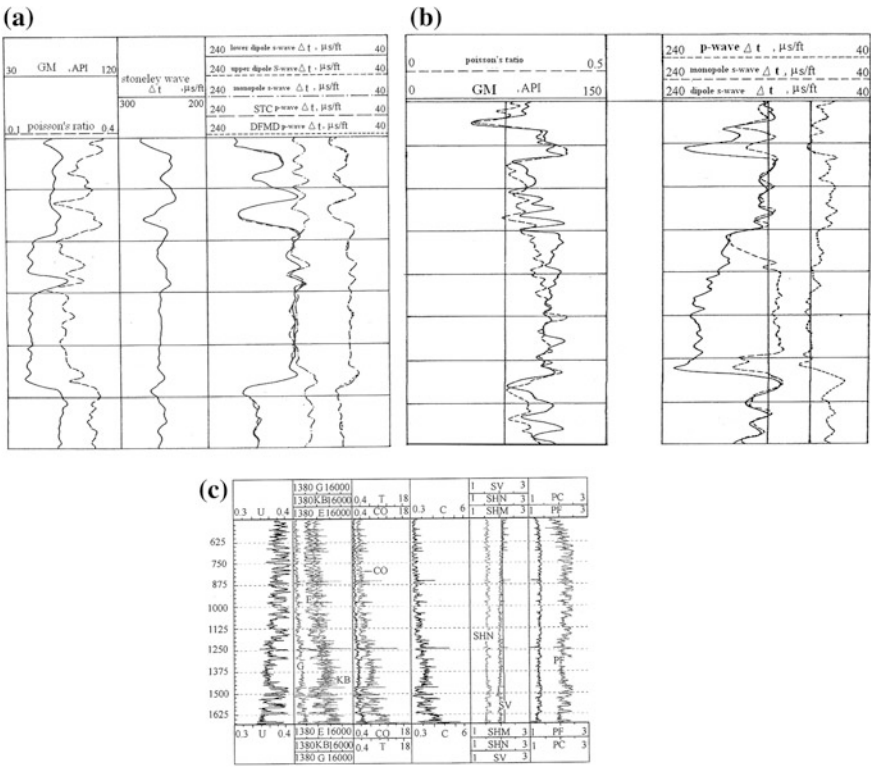

Fig. 3.19 The presentation of the DSI logging information

versus depth through *P*-wave, *S*-wave, and density of rocks. Figure 3.19a, b illustrates the presentation of DSI, and Fig. 3.19c is mechanical property curves, such as δ, *E*, *G* modulus, derived from DSI data; where *U* represents poisson ratio, *E*. dynamic young modulus, *G* dynamic shear modulus, K_b dynamic bulk modulus, CO compressional strength, *C* cohesive force strength, *T* tensile strength, excluding *U*, the dimension of other parameters is MPa. In the last two tracks, SV means vertical stress, SHN, maximum horizontal stress. P_C collapse pressure, P_F fracture pressure.

In summary, DSI tool employs combined dipole transmitter and receiver, which overcomes the disadvantages of BHC and LSS tools. This model tool presents abundant information that the former two tools cannot do,which provide more detailed and advanced technology to evaluate the formation.

3. *Shear Wave Anisotropy and Crossed Dipole Tools*

The development of sonic devices with arrays of detectors, the development of sophisticated processing of the array of receivers for extracting slowness without having to rely on the crucial measurement of "first motion," and the development of dipole transducers lead to a natural evolution into a type of tool referred to as

crossed dipole array devices. A number of service companies have had such devices since the early 1990s. These arrays of detectors are generally arrays of dipole receivers, both aligned and perpendicular to a pair of dipole transmitters which are also crossed. This allows for four sets of detector/transmitter orientations at each array spacing. The use of crossed dipoles allows collection of the data necessary for characterizing anisotropic formations, at least in vertical wells.

The crossed dipole sonic tools served as stimulation for a great deal of theoretical and laboratory work as well as realistic computational modeling of acoustic wave propagation in the borehole/tool environment. Numerous studies elucidated the role of borehole size and tool characteristics in determining the nature of the *P*- and *S*-wave dispersion curves. Advances in signal processing allowed the determination of the dispersion curves from arrays of detectors. One of the results from the routine display of dispersion curves was the discovery of a method to identify the presence of stress-induced anisotropy.

3.2.5 Interpretation

We can see that the sonic log can be used as an indicator of lithology and of porosity, both intergranular and intercrystalline.

For any given lithology, with the zone of investigation of the tool mainly in the invaded zone containing mud filtrate, the speed of sound (or the interval transit time Δt) is a function of porosity.

In fact, for rocks that are sufficiently compacted we can, to a first approximation, accept that the variation of the speed of sound with the depth (temperature and pressure) of the fluid and matrix is negligible and that a terminal velocity is reached.

Wyllie et al. (1956) have proposed an empirical equation based on numerous laboratory experiments on clean formations. This links interval transit time directly with porosity by taking the total interval transit time as equal to the sum of the interval transit times in the grains of the matrix and in the pores:

$$\Delta \mathrm{t} = \emptyset \Delta t_{\mathrm{f}} + (1 - \emptyset)\Delta t_{\mathrm{ma}}, \tag{3.9}$$

where Δt_{f} is travel time of the fluid and Δt_{ma} is the travel time, us/ft.

From the above equation, it follows that

$$\emptyset_s = \frac{\Delta t - \Delta t_{\mathrm{ma}}}{\Delta t_{\mathrm{f}} - \Delta t_{\mathrm{ma}}}, \tag{3.10}$$

where $\emptyset_s$ denoted porosity from sonic logging.

In uncompacted formations, the Wyllie equation gives porosities that are too high. It is therefore not directly applicable. A correction factor is needed, to take

into account the effects of temperature and pressure, or in other words that the terminal speed of sound is not reached. The above equation is then written as

$$(\emptyset_s)_c = \frac{\Delta t - \Delta t_{ma}}{\Delta t_f - \Delta t_{ma}} \cdot \frac{100}{c \cdot \Delta t_{sh}}, \tag{3.11}$$

where c is the compressibility, Δt_{sh} is the travel time that sound transmits shale.

The Δt_{ma} can be given by the chart in Fig. 3.20. The best way to compute $c\Delta t_{sh}$ is to compare computed sonic porosities with the true porosity from another source.

3.2.6 Environmental and Other Effects

1. *Cycle skipping*

In some cases the signal arriving at the second receiver is too low to trigger the detection on the first arrival. The detection then occurs at the second or third

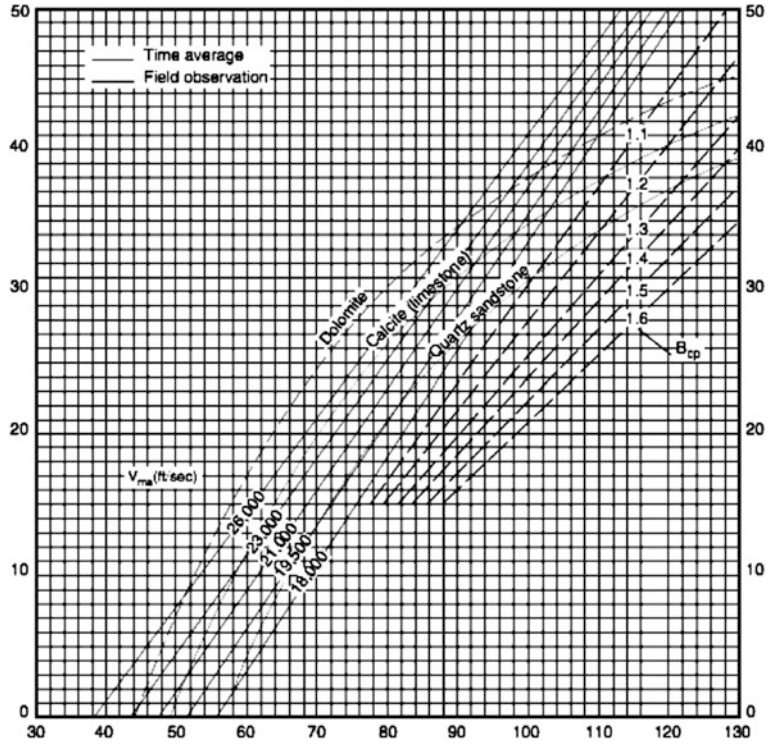

Fig. 3.20 Chart for estimating porosity from compressional interval transit time. In addition to the Wyllie time-average solution and compaction corrections, another empirical solution by Raymer et al. Courtesy of Schlumberger

arriving cycle (Fig. 3.21). We therefore have missed or skipped cycles. This shows up as sudden and abrupt increases in the interval transit time.

If cycle skipping appears on only one of the far detectors, the increases in Δt is between 10 and 12.4 μs/ft for the second cycle and 20–25 μs/ft for the third. If cycle skipping occurs on both far receivers the error on Δt is between 20 and 25 μs/ft for one cycle missed and 30–37.5 μs/ft for two.

This sudden jump in Δt is often linked to the presence of gas and sometimes oil. It can also happen in fractured zones. This is due to a strong attenuation of the signal.

2. *The borehole*

Hole size. This comes into effect only when the sum of the transit times from emitter to borehole wall, and the wall to the receiver is greater than the distance from the transmitter to the receiver directly. In this case the first arrival is straight through the mud. This only happens in holes larger than about 24 in. for common rocks.

For the borehole, compensated sonic (BHC) caving has little effect except where the caving is very large.

The drilling mud. If the borehole is air-filled or if the mud is gas-cut, the attenuation of the sonic signal is too high to allow detection on the first arrival. This problem may arise in front of zones that are producing gas into the mud (Fig. 3.22).

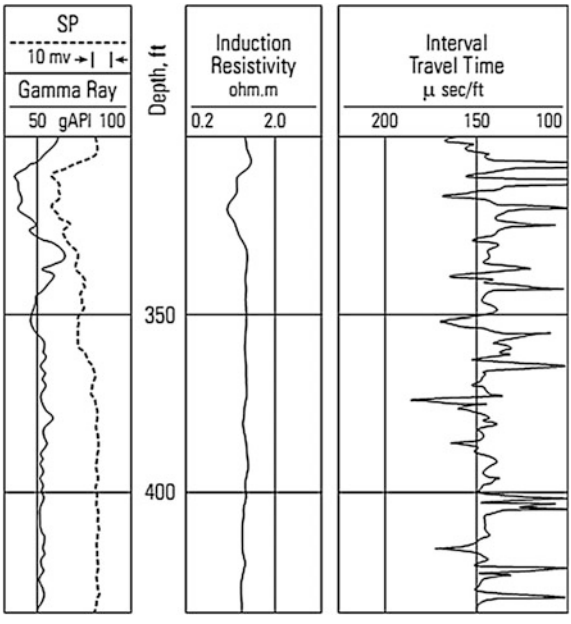

Fig. 3.21 An example of cycle skipping on the interval transit time log

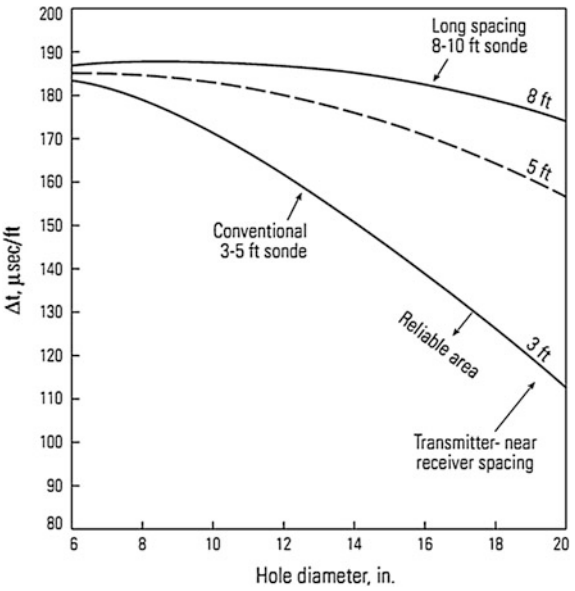

Fig. 3.22 Areas of confidence for conventional two-receiver tools as a function of borehole diameter

3.3 Acoustic Wave Amplitude Logging

3.3.1 Introduction

Many production logs are aimed at evaluating the competence of a well completion. Among them acoustic logging techniques, primarily the Cement Bond Log (CBL) and Variable Density Log (VDL), have been used for many years to try to measure directly the quality of the cement between the casing and the formation. BoreHole TeleVision (BHTV), UltraSonic Image (USI), and UltraSonic Borehole Imager (UBI) techniques have been developed to eliminate some of the deficiencies of the cement bond log for cement evaluation. These logs are intended to identify poorly cemented regions during the completion stage of the well so that these regions can be repaired with cement squeezes before the well is perforated for production, although their application for this purpose varies significantly from company to company.

3.3.2 Cement Bond Logging (CBL)

Tools and Operation Theory

A cement bond log is an acoustic amplitude log with a transmitted acoustic signal detected by one or two detectors. The basic principle of cement bond logging is that if the casing is free to move, an acoustic signal is not greatly attenuated, whereas if

the pipe is held firmly in place by cement, vibrations are rapidly dampened and the received acoustic signal is low in amplitude.

Figure 3.23 shows a typical cement bond log tool configuration. Acoustic signals are emitted by a crystal transmitter that is switched on and off, generating sound impulses with frequencies of about 20 kHz. The sound waves are elastic compressional waves that propagate spherically from the acoustic source. Two receivers generally are used to detect the transmitted sound waves, one spaced about 3 ft below the transmitter and one spaced about 5 ft below the transmitter. Some cement bond tools have a single receiver spaced 3–4 ft from the transmitter; however, experiments in a test well showed that single-receiver tools are generally inadequate.

Cement bond tools measure the bond between the casing and the cement placed in the annulus between the casing and the wellbore. The measurement is made using acoustic sonic and ultrasonic tools. In the case of sonic tools, the measurement is usually displayed on a cement bond log (CBL) in millivolt units, decibel attenuation, or both.

CBL uses relative amplitude to evaluate the bonding, and uses the following formula to calculate this parameter:

$$\text{relative amplitude}\,(I_a) = \frac{\text{amplitude of interest zone}}{\text{amplitude of free zone}} \times 100\,\% \tag{3.11}$$

Usually the quality of cementation can be divided into three types based on the relative amplitude I_a:

(1) good cementation I_a: less than 20 %
(2) mediate cementation I_a: larger than 20 % and less than 40 %
(3) poor cementation I_a: larger than 20 %

The evaluation method of CBL, however, is not always effective, because the measurement detection result of CBL is the average of the formation.

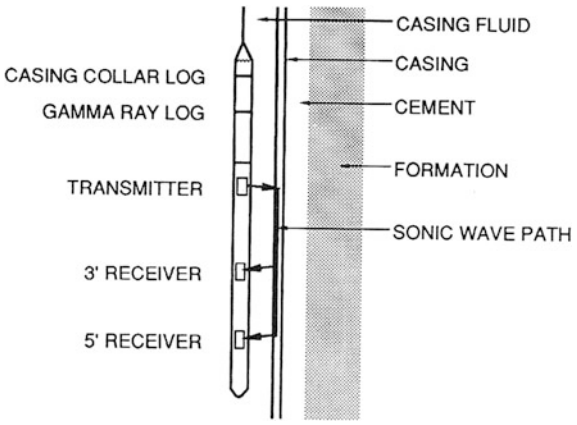

Fig. 3.23 Configuration of CBL Tool

3.3.3 *Variable Density Log (VDL)*

Another acoustic amplitude logging is Variable Density log (also called a micro-seismogram), which detects the tool sonic interfaces, i.e., the one boundary between the pipe and the cement, another is between the cement and the formation. The presentation of VDL logging is constructed by assigning strong positive signals a dark mark on the log, while zero-amplitude signals are bright white. All intermediate signals are shades of gray, depending on their relative amplitude. These interpreted wave signals are then recorded continuously with depth. Figure 3.24 illustrates the construction of the Variable Density log. It displays the full wave train of acoustic signals, with the amplitude indicated by the contrast between the dark and light bands—the higher the contrast, the higher the amplitude. This is particularly useful in identifying good acoustic coupling with the formation. Because the acoustic transit time in the formation varies with changes in lithology, the Variable Density log is wavy when responding to formation signals, much like an openhole sonic log.

Variable Density Log Interpretation

The following examples illustrate the cement bond log responses expected for a variety of cement conditions.

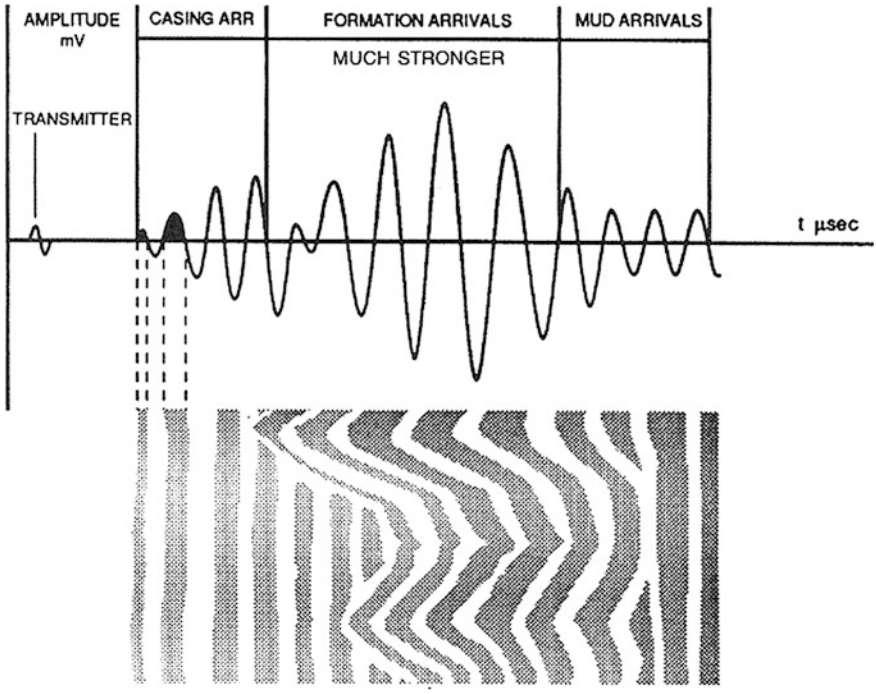

Fig. 3.24 Variable density log construction (Courtesy Schlumberger)

1. *Free pipe* In uncemented casing, the amplitude log shows high amplitude and the transit time corresponds to the casing arrival time. The Variable Density log shows strongly contrasting parallel vertical lines with no indication of formation signals. Casing collars show up distinctively on a cement bond log in free pipe. Collar reflections, shown as chevrons on the Variable Density log, result in a decrease in amplitude and an increase in transit time. Figure 3.25 shows a cement bond log in free pipe. It is important to log in an area of free pipe if possible when a cement bond log is run. Any deviation from the expected response in free pipe indicates either a malfunctioning or an improperly centralized tool. Logging in free pipe calibrates the tool in a known environment under logging conditions.

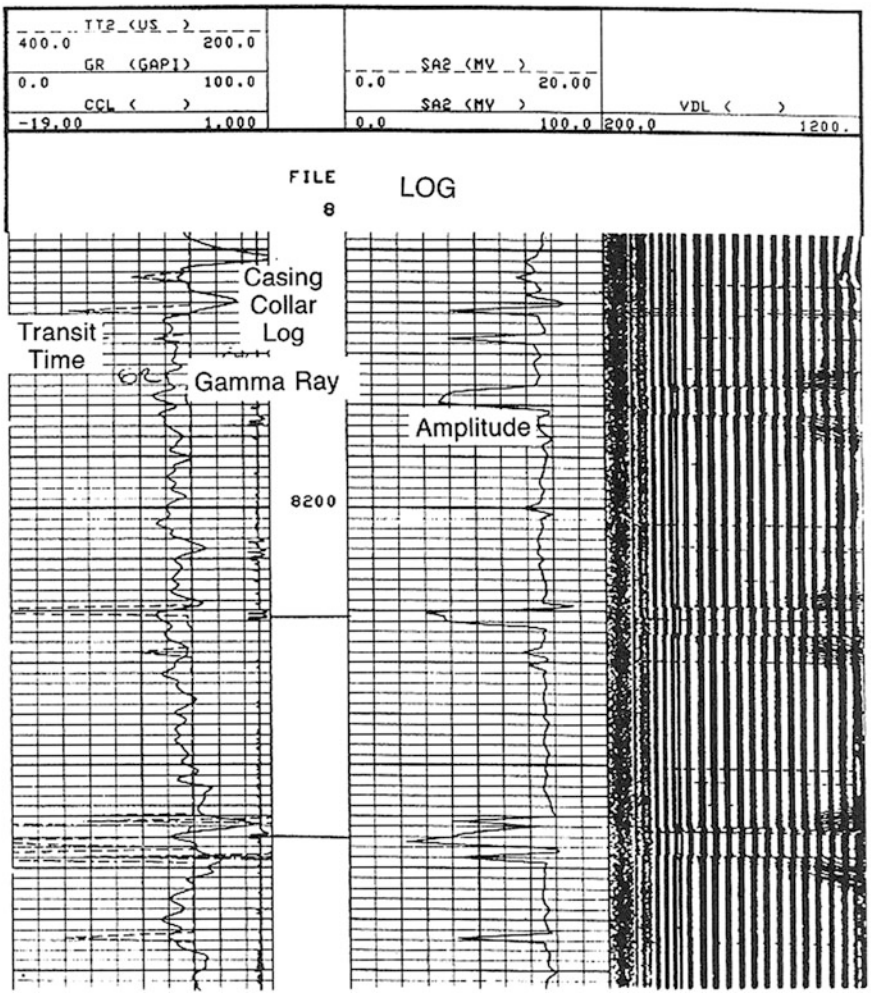

Fig. 3.25 Cement bond log response in free pipe

2. *Good bond to formation and casing* With good bonding, the amplitude is low. The full wave-train display shows weak or no casing signals and strong formation arrivals unless the formation attenuation is high, as would be observed for an unconsolidated gas sand, weak shales, or other low-velocity formations. Comparison of the cement bond log with an openhole sonic log can help identify regions of high attenuation in the formation. Figure 3.26 presents an example of good bonding to the pipe and the formation.
3. *Good casing bond, but poor formation bond* This situation is characterized by weak casing arrivals, indicated by low amplitude and low contrast on the Variable Density log at casing arrival times, and weak formation signals on a full wave-train display. At some occasions, the formation signal will disappear. Unfortunately, these same characteristics can be caused by other factors, including high formation acoustic attenuation and tool eccentricity. Good bonding to the pipe but not to the formation can easily occur opposite to permeable zones where a mud cake is built up that is not displaced by cement. Figure 3.27 presents a case where both casing and formation amplitudes are low.
4. *Micro-annulus* In some instances, a small gap is present between the casing and the cement. This gap is called a micro-annulus if it is not large enough to allow any significant fluid migration. A micro-annulus can be caused by a casing pressure that is lower during production than during cementing, by heating the

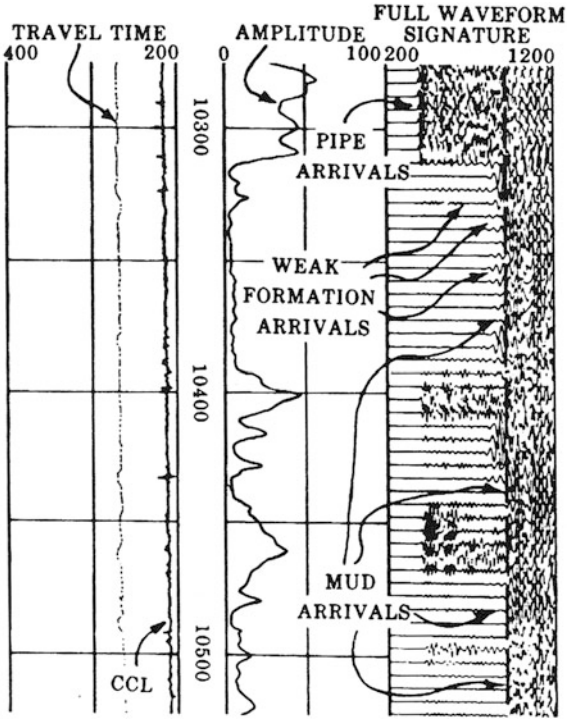

Fig. 3.26 Cement bond log response to good pipe, poor formation bonding

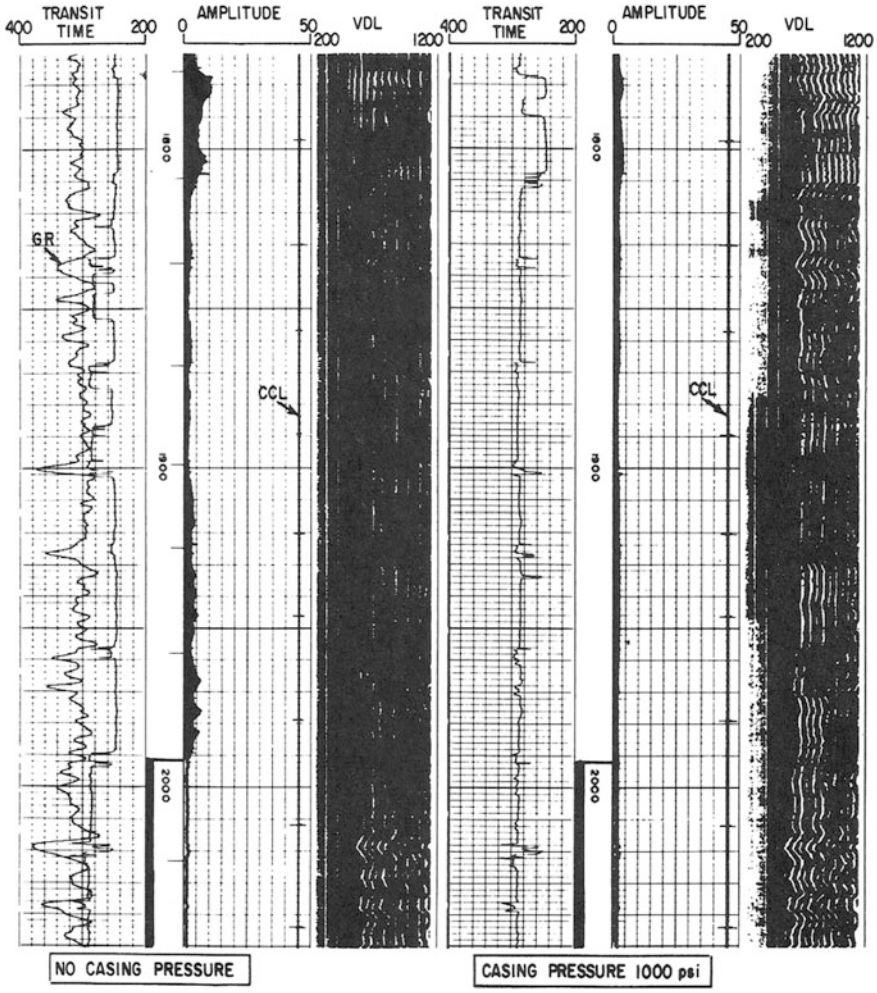

Fig. 3.27 Effect of micro-annulus on cement bond log response

casing during cement setting and subsequent cooling, or by cement dewatering. A micro-annulus exhibits moderate to poor bonding on a cement bond log. The amplitude is moderate to high, and a full wave-train display exhibits weak to somewhat high casing signals and moderate formation arrivals. This case is shown in Fig. 3.27.

5. *Channeling* Unfortunately, channeling in cement cannot be positively identified with a cement bond log. A channel in the cement affects the cement bond log much as a micro-annulus does, resulting in moderate to high amplitude, moderate to strong casing signals on a full wave-train display, and moderate formation signals. Figure 3.28 illustrates cement bond log responses before and after squeeze cementing in a region of channeling. Before the cement squeeze,

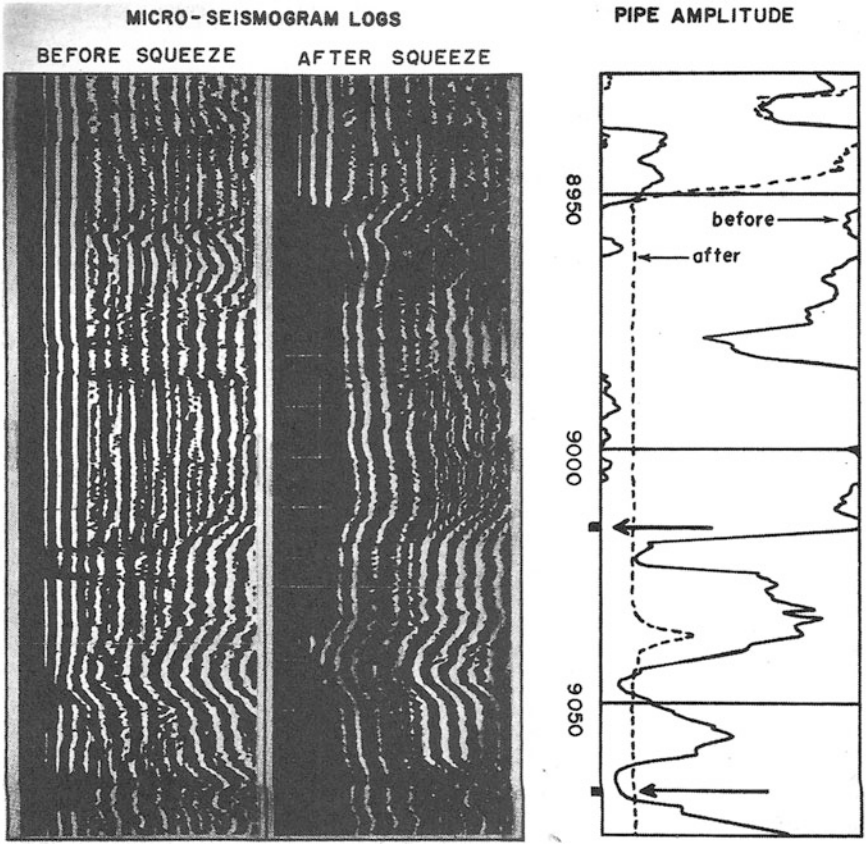

Fig. 3.28 Cement bond logs before and after cement squeezing of a channel

the Variable Density log shows fairly strong pipe arrivals (note that collars can be distinguished), but strong formation signals are also evident, indicating some bonding to the formation.

6. *Eccentric tool* It is extremely important that a cement bond tool be well centralized—at least three strong centralizers should be used. When the tool is eccentric, the acoustic waves travel paths of different lengths and thus arrive out of phase, resulting in reduced amplitudes. Tool eccentricity makes the Variable Density log look wavy in the pipe-arrival region, yield artificially low amplitude, and exhibit a transit time less than the expected casing arrival time. Figure 3.29 shows tool eccentric effects.

As these examples show, cement bond log interpretation is most uncertain in the cases where "intermediate" bonding is inferred. This condition, characterized by moderate to high signals from both the casing and the formation, can be caused by a number of factors, including a micro-annulus, channeling, poor bonding to the

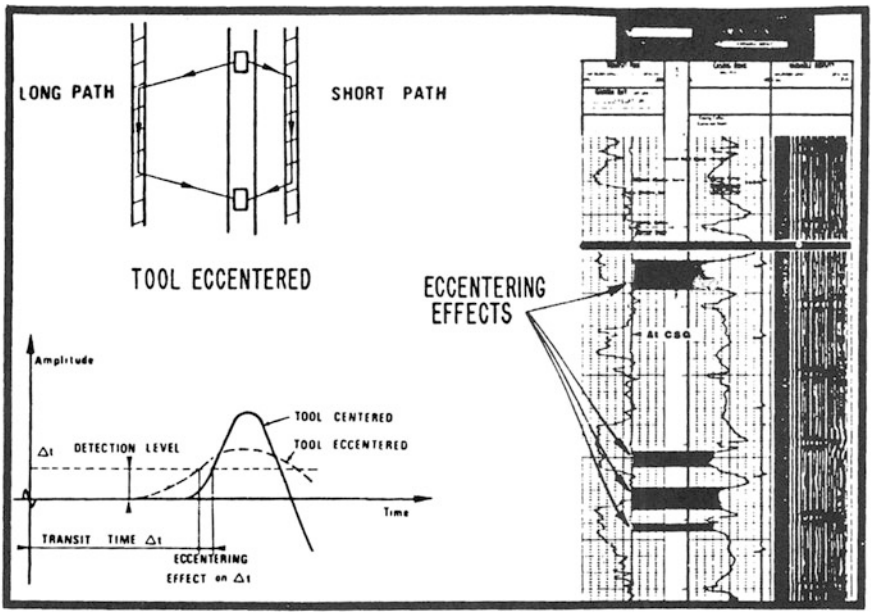

Fig. 3.29 Tool eccentric effect (Courtesy Schlumberger)

formation, or a thin cement sheath. To narrow the possibilities, the cement bond log should be run with additional wellbore pressure applied to eliminate the effects of micro-annuli and other information about the wellbore conditions, e.g., openhole sonic logs, caliper logs, and records of the casing design should be used (Fig. 3.30).

Let us give a summary of the response of acoustic wave form cementation annulus and the formation.

In **free pipe** (Fig. 3.31a) a high amplitude signal beginning at the pipe-arrival time is measured. This is caused by the pipe "ringing" with little dampening of the acoustic signal. Figure 3.31b illustrates the sonic wave train observed with good bonding to a low-sonic-velocity formation. The amplitude of the signal is very low at pipe-arrival time, including the good shear contact between the pipe and the cement. The high amplitude of formation arrivals that arrived later than the pipe arrivals is indicative of the low-velocity formation and good bonding between the cement and the formation. Good bonding is also assumed in Fig. 3.31c, but the signal represents a fast formation. In this case, formation arrivals can be as early as or even earlier than pipe arrivals, yielding artificially high acoustic amplitudes at pipe-arrival time. In Fig. 3.31d good bonding exists between the casing and the cement. But poor bonding occurs between the cement and the formation. Thus, low amplitudes are measured at pipe-arrival times because of the good bonding and also formation-arrival times because of the limited acoustic coupling between the cement and formation.

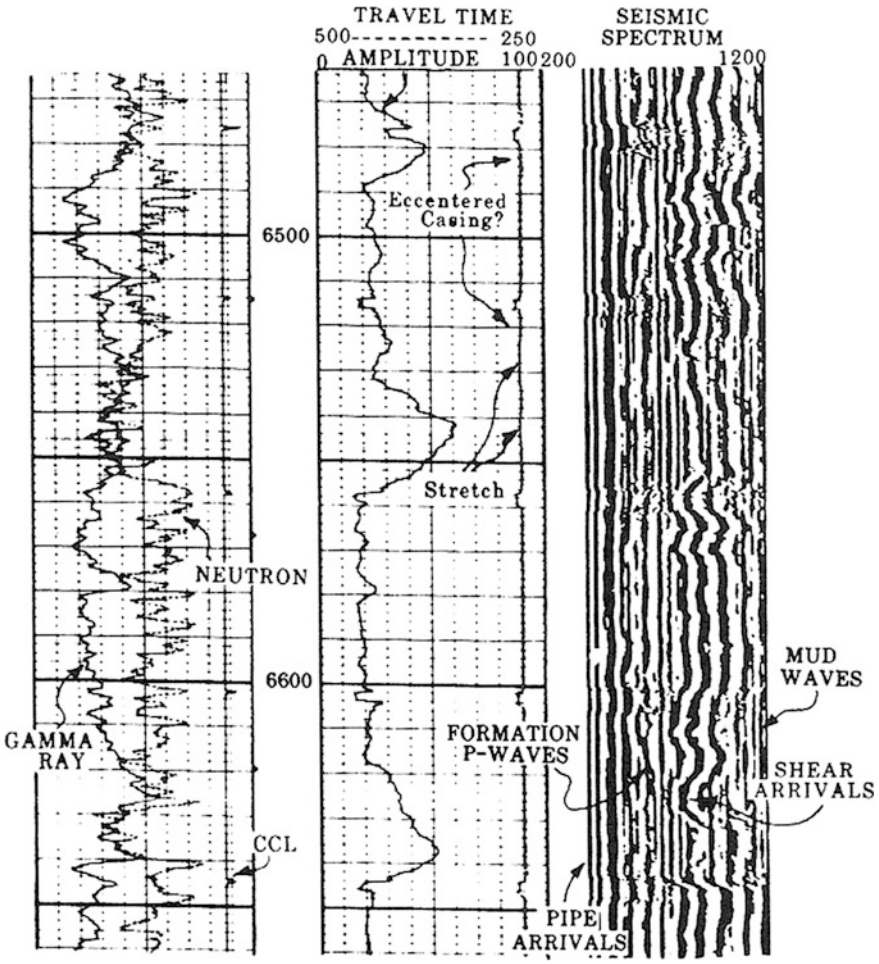

Fig. 3.30 Misleading amplitude log caused by thin cement sheath

3.3.4 Cement Evaluation Tool (CET)

Cement placement is a critical component of well architecture for ensuring casing mechanical support, protection from fluid corrosion, and most importantly isolating permeable zones at different pressure regimes to prevent hydraulic communication.

Cement evaluation tools measure the bond between the casing and the cement placed in the wellbore annulus between casing and wellbore. This real-time measurement is made with acoustic sonic or ultrasonic tools. Hydraulic isolation between reservoir layers is essential to avoid potential reservoir problems such as crossflow between reservoir zones behind the casing. The detection of poor cement,

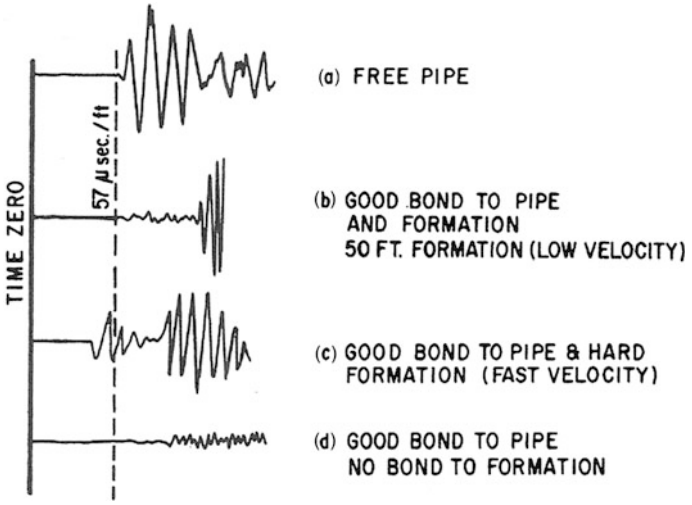

Fig. 3.31 Different cementation acoustic wave form

or the absence of cement, can lead to remedial action before the well is completed, avoiding potential well problems and the associated costs.

3.3.5 Segmented Bond Tool (SBT)

The Baker Atlas Segmented Bond Tool (SBT) service quantitatively measures the cement bond integrity in six angular segments around the casing. The SBT service can find and define channels, micro-annulus, quality of bonding, etc.

The SBT service offers significant operating advantages over conventional and pulse-echo tools because of its insensitivity to heavy or gas-cut borehole fluids, fast formations, temperature and pressure variations, and moderate tool eccentric.

For ease of interpretation, the SBT measurements are displayed in two log presentations. Both presentations are available in the logging mode as the SBT data are acquired, processed, and plotted in real time. The secondary presentation consists of six, 60°. segmented arrays, variable-attenuation cement map, and a tool-orientation trace overlay (Fig. 3.32).

3.4 Ultrasonic Imager Logs (USI)

Ultrasonic imager techniques were developed in recent years to overcome some of the deficiencies of traditional cement bond logs. The primary advantage of the ultrasonic devices is that they provide a circumferential picture of cement quality

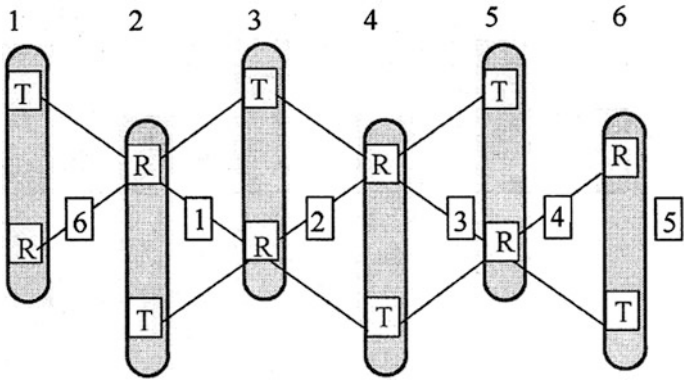

Fig. 3.32 Structure of SBT tool

using eight transducers arrayed around the tool. In addition, they are less affected by micro-annuli than cement bond tools. The ultrasonic measurements are less sensitive to acoustic coupling to the formation. Pioneered by the Schlumberger Cement Evaluation Tool (CET), the measurements from Ultrasonic imager logs are fundamentally different from those obtained from cement bond logs.

An Ultrasonic imager tool consists of an array of eight ultrasonic transducers spaced around the body of the tool, as Fig. 3.33 shows. On this tool, the transducers are arranged in a helix with a spacing of 45° between transducers, while other ultrasonic tools use a double helical array. A ninth transducer is aligned axially and aimed at an acoustic mirror so that an in situ measurement of travel time in the wellbore fluid can be made.

By adding the responses of transducers spaced 180° apart, four measurements of casing diameter are obtained. Sometimes all four measured diameters are displayed; alternatively, a maximum and a minimum diameter or one average diameter can be presented on the log. In addition, tool eccentricity—i.e., the difference between the maximum and minimum distances from transducers to the casing wall—is often displayed.

The degree of cement bonding, as inferred from the integrated response, is typically displayed in two ways. Because there are eight transducers arrayed around the logging tool, eight measures of cement integrity are obtained. A maximum and a minimum cement compressive strength are usually recorded on the basis of highest and lowest values measured by the transducers, as well as on the basis of an average for all eight transducers. The relative bonding from all eight transducers is presented by assigning a shading from white (no bonding) through shades of gray to black (excellent bonding); the relative response from each transducer is displayed on a separate track. Because the range is small, this shading is difficult to accomplish and many logs appear to have just black and white in the display.

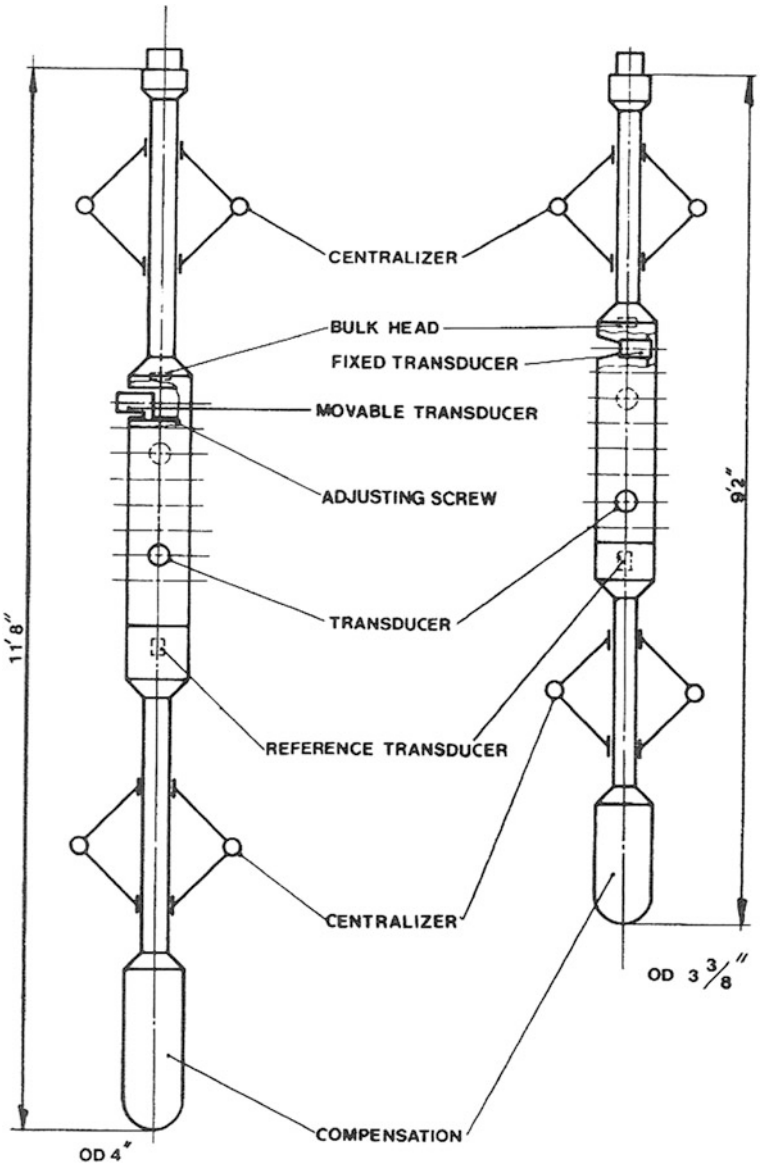

Fig. 3.33 Schlumberger CET tool

Additional information is sometimes displayed to aid log interpretation. The relative bearing of the tool is usually recorded to assist in defining the geometry of channels in the cement. Formation and gas flags are sometimes displayed. Figure 3.34 shows a typical Ultrasonic imager log presentation.

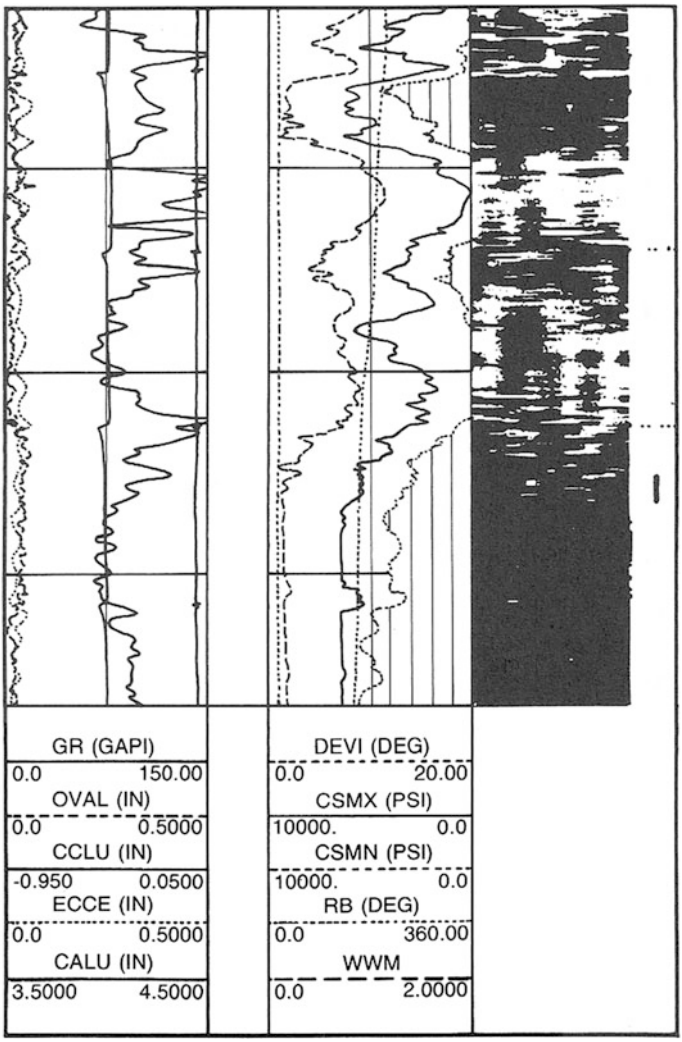

Fig. 3.34 Ultrasonic-pulse-echo log display

Ultrasonic Imager Log Examples

The following examples illustrate the use of Ultrasonic imager logs.

Example 1—Alternating Good and Poor Cement Quality. Figure 3.35 shows a typical Ultrasonic imager log in a section of well that has regions of apparently good bonding separated by regions of poor bonding. The good bonding is indicated by the solid black response from all eight transducers and by high minimum compressive strength (>1,000 psi [>6.9 MPa] where shaded). In the poor bonding regions, some or all of the eight tracks exhibit light shading, which indicates poor bonding around much of the pipe circumference.

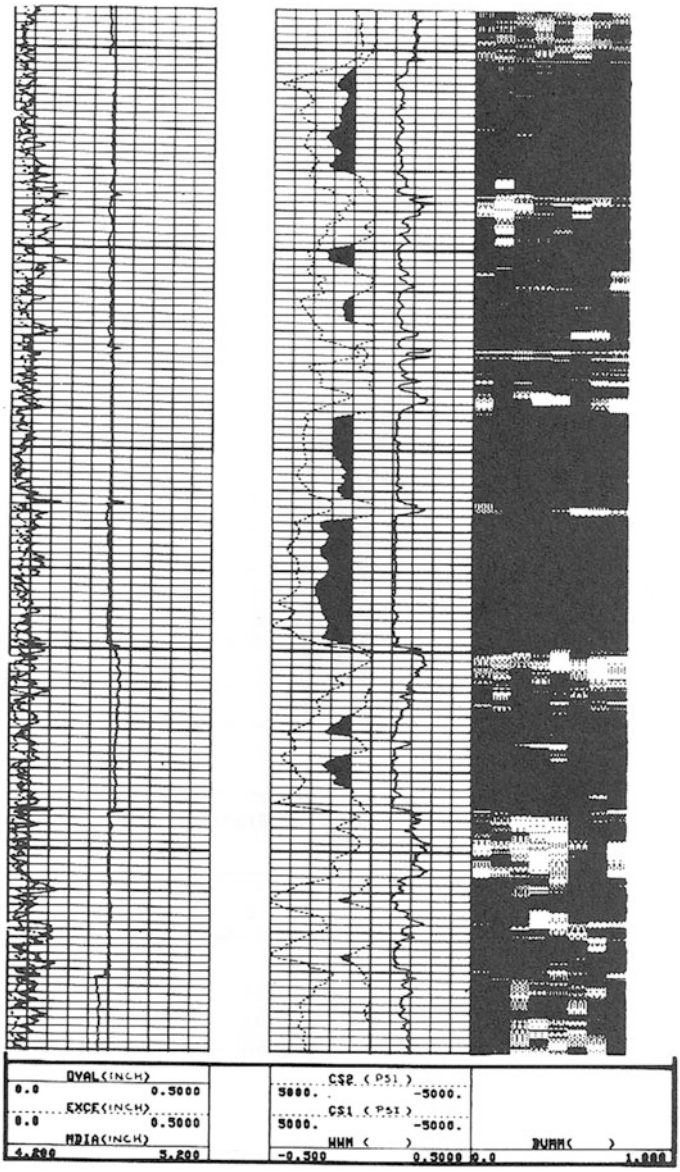

Fig. 3.35 Ultrasonic-pulse-echo log in regions of good and poor bonding

Example 2—Channeling. A primary advantage of the Ultrasonic imager log is that it can identify unsupported sections of the pipe circumference because it measures bonding conditions at eight positions circumferentially around the pipe. Figure 3.36 shows a typical response to a channel, with a few of the tracks showing poor bonding, while good bonding is indicated around the rest of the pipe. The

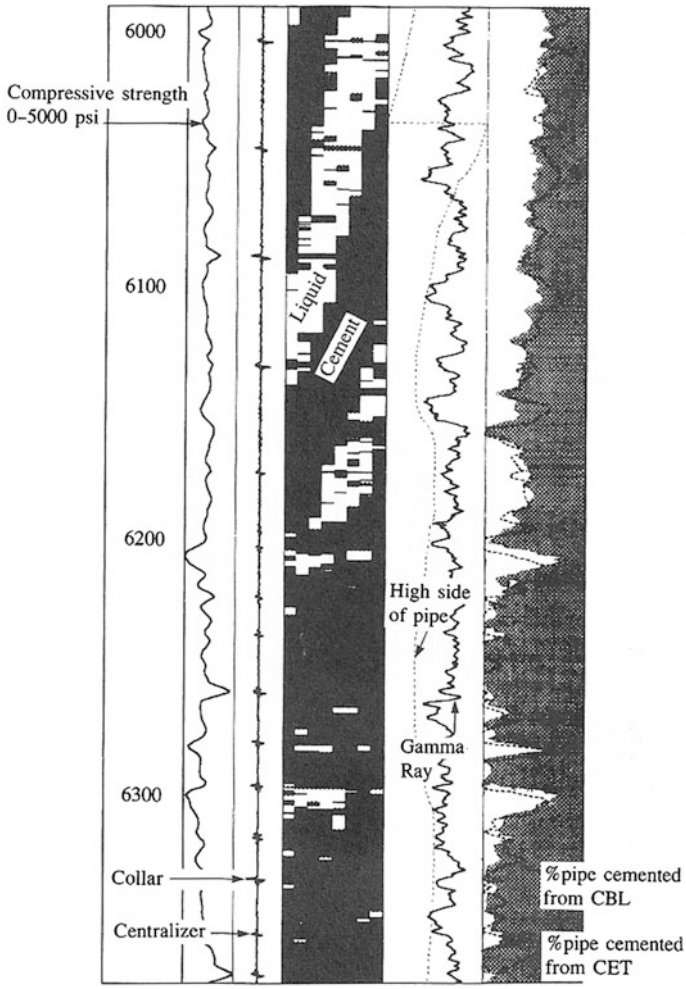

Fig. 3.36 Ultrasonic-pulse-echo response to channel

channel appears to be spiraling around the pipe; however, the relative bearing recording indicates that the tool was slowly rotating as the log was run, which means that the channel is consistently on one side of the pipe.

Example 3—Presence of Gas in Cement. The presence of gas, whether in a micro-annulus or dispersed as bubbles in the cement, causes an Ultrasonic imager log to give an overly pessimistic measure of cement bonding conditions. Figure 3.37 illustrates a case where the Ultrasonic imager log shows very poor bonding, while relatively good bonding is indicated by the cement bond log. This section of the well is opposite to gas-bearing formation, and independent tests found good zonal isolation by the cement, confirming the validity of the cement

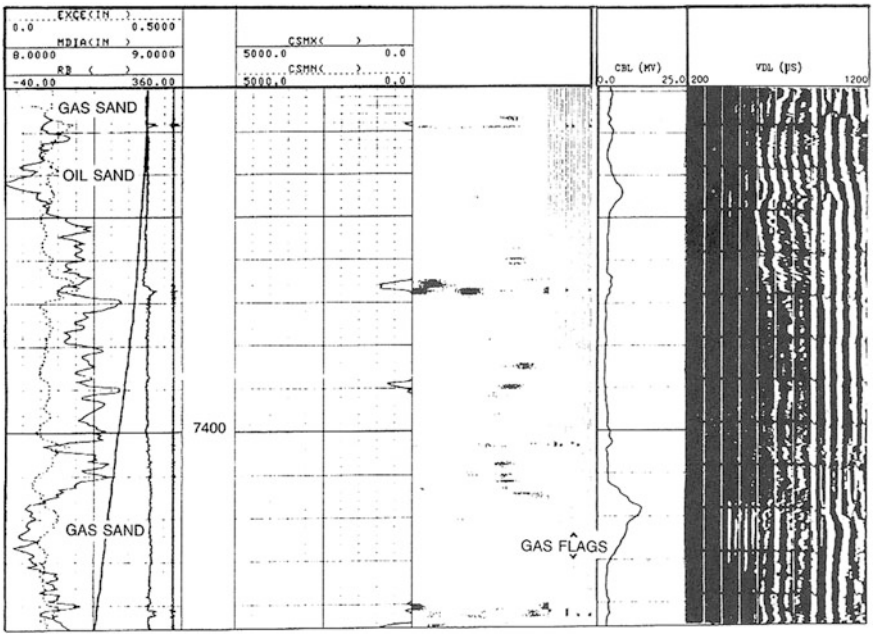

Fig. 3.37 Ultrasonic-pulse-echo log shows poor bonding because of presence of gas in cement

bond log. Gas in the cement was a possible cause of the erroneous Ultrasonic imager log. Because the cement bond log does not show weak cement, it is also possible that the gate settings were incorrect on the Ultrasonic imager log.

3.5 UltraSonic Borehole Imager (UBI)

3.5.1 Introduction

Tool principle

The sonde includes a rotating transducer subassembly, which is available in different sizes to log all standard sizes of open boreholes as shown in Fig. 3.38. The direction of rotation of the subassembly controls the orientation of the transducer—counterclockwise for the standard measurement mode (transducer facing the borehole wall) and clockwise to turn the transducer 180º within its subassembly (transducer facing a reflection plate within the tool) to measure downhole fluid properties (Fig. 3.39).

Selecting the most suitable transducer subassembly to reduce attenuation in heavy fluids and to maintain a high signal-to-noise ratio optimizes the distance traveled by the ultrasonic sound pulse in the borehole fluid. The transducer is both a

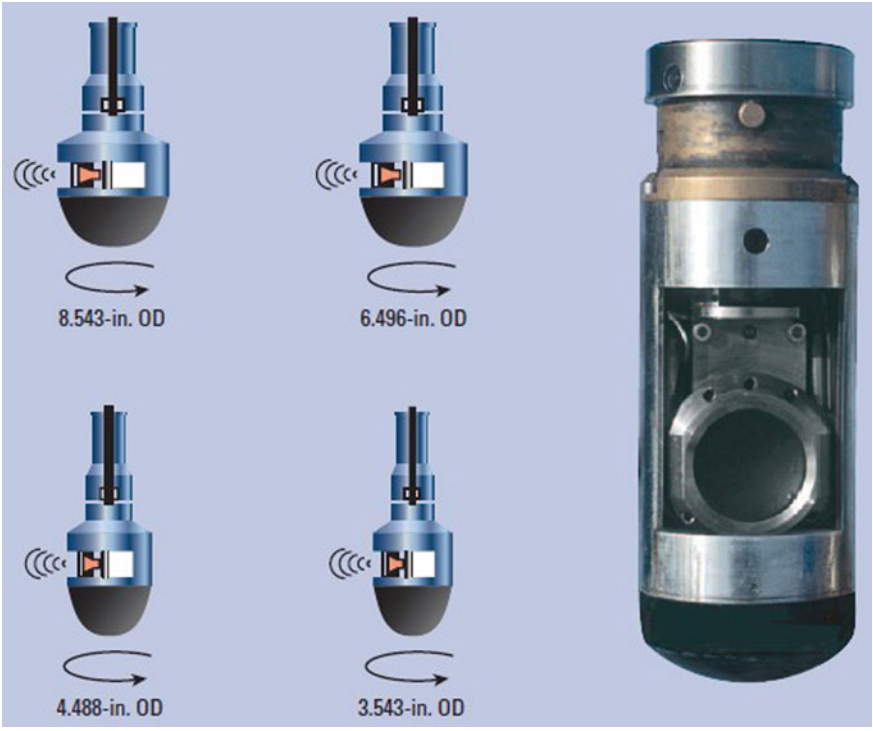

Fig. 3.38 The rotating transducer subassembly is available in different sizes to provide optimum standoff from the casing or borehole

transmitter and a receiver, transmitting an ultrasonic pulse and receiving the reflected pulse. The mud weight and type influence the manual selection of either 250 or 500 kHz for the transducer frequency.

Tool measurement

The UBI tool accurately measures both amplitude and transit time. The processing technique provides improved accuracy, avoids cycle skips, and reduces echo losses. The tool operates on two frequencies (250 or 500 kHz); the higher frequency yields higher image resolution, while the lower frequency provides a robust measurement in highly dispersive muds. The image resolution mode is selected in correspondence to the logging environment—such as mud type and density—and the resolution requirements. The standard resolution at an operating frequency of 250 kHz is already considered very high; the higher resolution, obtained at a slower logging speed, offers the next level of quality.

The tool is relatively insensitive to eccentralization up to 1⁄4 in. Even in highly deviated wells, the UBI centralization system is reliable, enabling the tool to provide clear images.

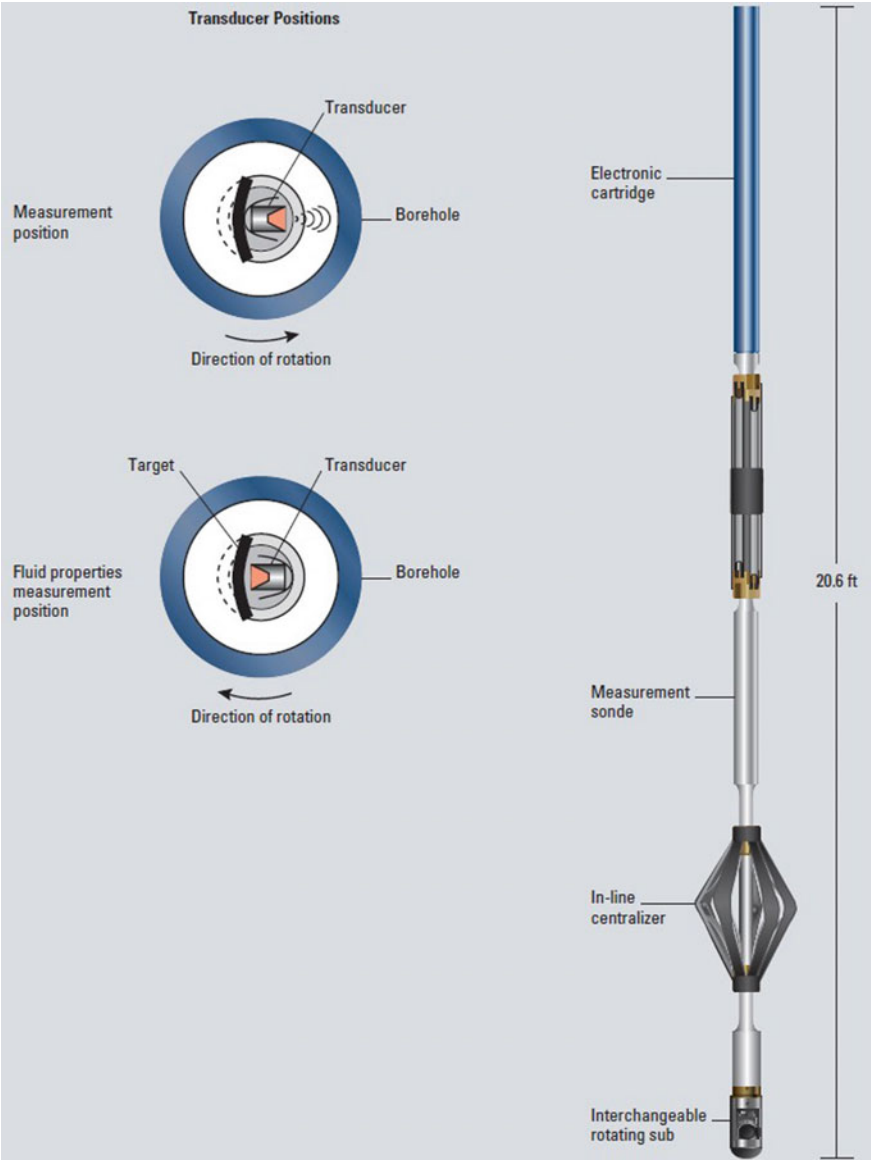

Fig. 3.39 The direction of rotation of the transducer subassembly controls the transducer position

3.5.2 Image Presentations

A typical UBI presentation consists of an amplitude image on the left and a borehole radius image on the right, on a 1:40 depth scale. Dynamic normalization, usually over a 1-m interval, is applied to both images to highlight the features of the

borehole. Dark colors represent low amplitude and large radii, indicating borehole rugosity, enlargements, and attenuation material. Two scales—on the far left for amplitude and on the far right for radii—depict the relationship between the dynamic color scale and absolute value. Three additional curves indicate the minimum, average, and maximum values of the measurement around the borehole. These curves are used to rapidly identify intervals with borehole enlargements.

Images can be oriented with respect to north or with respect to the high side of the borehole in the case of a deviated well. If oriented with respect to the high side of the hole, any casing damage caused by pipe friction appears at the center of the image and is therefore easily identified.

Cross-sectional displays

Cross-sectional displays at specific depths are essential for interpreting borehole deformation. The interpretation program fits a circle through the cross-sectional diagram to highlight places where deformation occurs.

A diagnostic listing is produced to help identify hole deformation caused by keyhole, breakout, or shear sliding. Pseudo-three-dimensional plots can be generated to give a perspective view of the borehole from the top looking down.

Spiral plots

The spiral presentation shown in Fig. 3.38 is a presentation of several successive levels of acoustic radius information, such as a stack of cross-sectional displays at adjacent levels. The impression of looking along a section of borehole helps the interpreter to visualize any borehole deformation and envision how reaming may have modified the initial deformation. Such deformation is difficult to discern from images or from a few cross-sectional plots.

3.5.3 Interpretation

Processing software available both in the MAXIS* Multitask Acquisition and Imaging System surface units and at Data and Consulting Services centers can further enhance the UBI images by correcting amplitude and transit time information for the effects of logging speed variations and tool eccentralization, and also by filtering noise.

Transit times are converted to borehole radius information using the velocity of the ultrasonic signal in mud, measured by the tool on the way down. Images are oriented by combining inclinometry data from the GPIT* General Purpose Inclinometry Tool with the UBI information. The data are then enhanced by dynamic normalization and displayed as an image for visual interpretation (Fig. 3.40).

Amplitude and radius image data can be loaded onto a geological workstation for analysis and interpretation using the FracView* fracture characterization program, and major events can be automatically extracted from the radius data evaluation of wellbore stability.

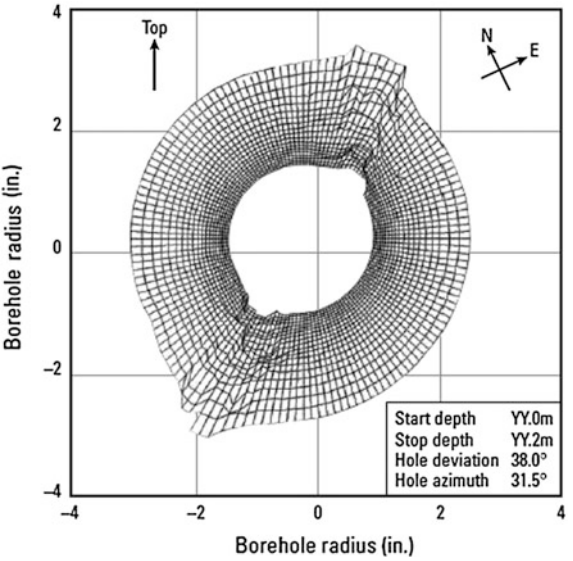

Fig. 3.40 A spiral plot of the acoustic radius information gives the visual impression of looking along a section of the hole

Comparison with electrical images

Schlumberger services such as the FMI* Fullbore Formation MicroImager, OBMI* Oil-Base MicroImager, and ARI* Azimuthal Resistivity Imager perform imaging through an array of high-resolution measurements of the formation resistivity. Typical formations show easily measurable variation in resistivity at even the slightest change in lithology. Therefore, these tools are ideal for discerning bedding and structural dip. As the measurements of these tools are made at a finite radial depth in the formation, the effects of borehole surface rugosity are minimized. These tools can also discern fractures from the surrounding matrix by the resistivity differences caused by fluid or minerals that fill the aperture.

The UBI tool measures attributes of an ultrasonic wave reflected at the borehole wall. The impedance ratio between the formation and the mud has a slight effect on the amplitude of the reflected signal; however, rugosity of the borehole wall has a much greater effect and dominates the reflection amplitude. UBI images are therefore strongly sensitive to surface variations in the borehole wall but not to variations in lithology.

The resolution of any ultrasonic imaging tool is inadequate to detect "pure" fractures unless they are very wide. However, since the drilling process tends to chip and break the formation at the edge of a fracture, the UBI tool can often discern fractures by associated surface rugosity.

Drilling-induced fractures normally open only after the drill bit has passed, so their edges are better preserved than the edges of natural fractures that existed when the interval was drilled, and the fracture is less likely to be visible on acoustic images.

As shown in Fig. 3.41, UBI images are compared with FMI and ARI images recorded in water-base mud. The FMI image on the left indicates that the formation is fractured. The ARI image shows some of the stronger features with reduced resolution. From the UBI image we can distinguish most of the major features that appear on both FMI and ARI images (X38–X39 m-deep open fractures) and some features that are seen only by the FMI tool (X39–X39.5 m-shallow fractures).

Some features that are quite clear on the FMI images are invisible or barely detectable with the UBI images. These are mostly subvertical. They may be drilling-induced fractures (X45–X49 m) that are not deep enough to influence the ARI images and they may not have enough associated surface rugosity to show up on the UBI images.

The rugosity seen by the UBI tool at X42–X42.4 m is not detected at all by the other two tools. It is probably a small stress-induced breakout.

Effect of mudcake

Mudcake also influences the ultrasonic image. It absorbs some of the signal, thereby reducing the amplitude, and it slightly decreases the measured radius. The difference in measured radius does not represent the actual mudcake thickness, but rather reflects the reduced transit time through the "faster" mudcake. This effect may make formation layering visible on the UBI images even in the absence of rugosity.

3.5.4 Applications

The UBI tool was originally developed from the USI* UltraSonic Imager to provide imaging capabilities in nonconductive oil-base muds and to provide an acoustic imaging alternative to FMI microresistivity images. Experience with high-quality UBI images has revealed some exciting new applications such as borehole stability determination and stress analysis.

Fracture detection

Because openhole borehole televiewer data are often acquired for use in fracture evaluation, the resolution of the UBI tool makes it suitable for this application.

At times, shear sliding along a fracture plane can be detected with the help of UBI radius measurements and cross-sectional plots, which provide strong evidence of both unbalanced tectonic stress and open fractures.

UBI tool can also use to improve fracture analysis in oil-base muds and analyze borehole stability and stress.

Keyhole wear

In deviated wells, the rotating drill pipe rests on the low side of the borehole, gradually wearing a smooth ovalization or keyhole shape. Often clearly visible on cross-sectional plots (Fig. 3.42), the keyhole appears as a dark band in the middle of the image, corresponding to the low side of the hole as shown in Fig. 3.43. The other dark band on the high side of the hole results from incorrect calculation of the

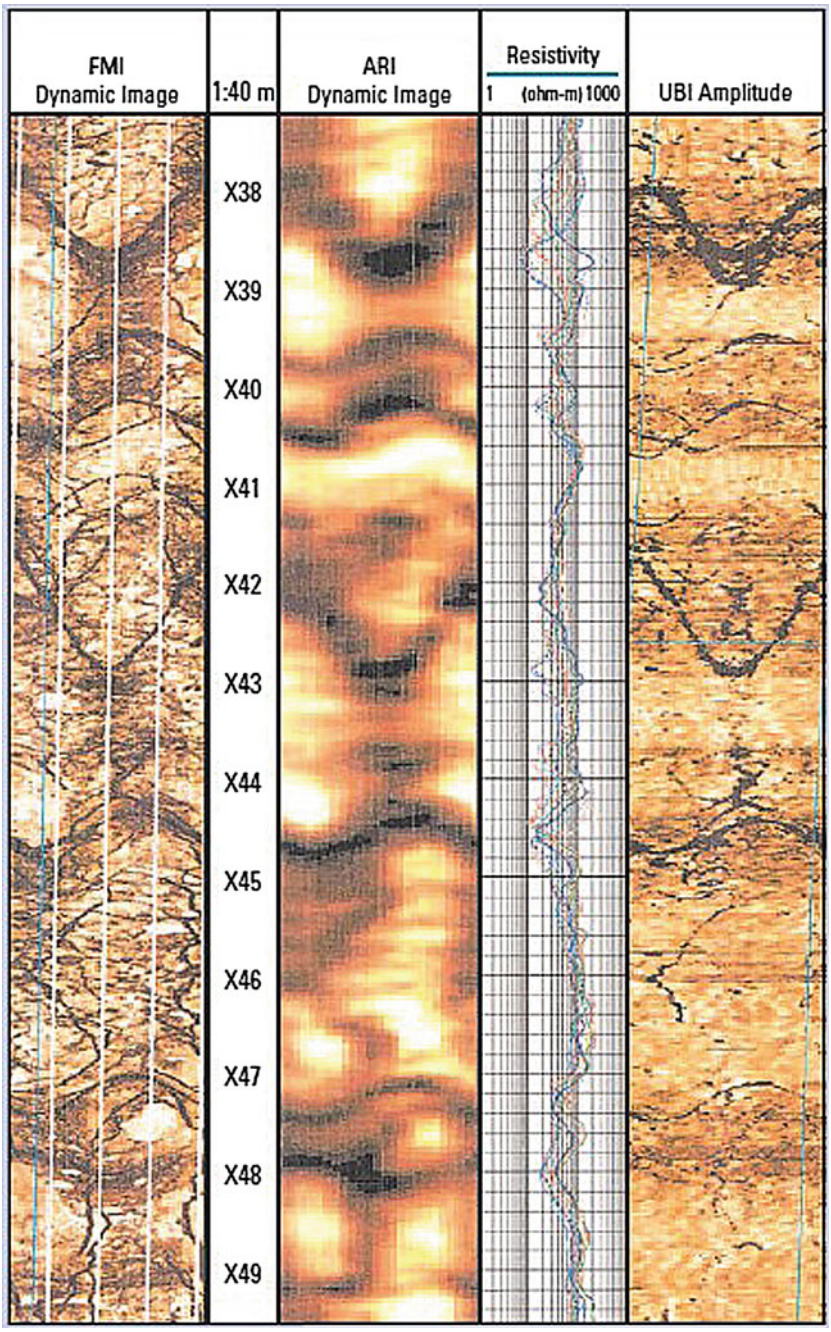

Fig. 3.41 FMI, ARI, and UBI images in water-base mud show different fracture attributes, often allowing discrimination between open and closed fractures, deep and shallow fractures, and even between natural and hydraulically induced fracture

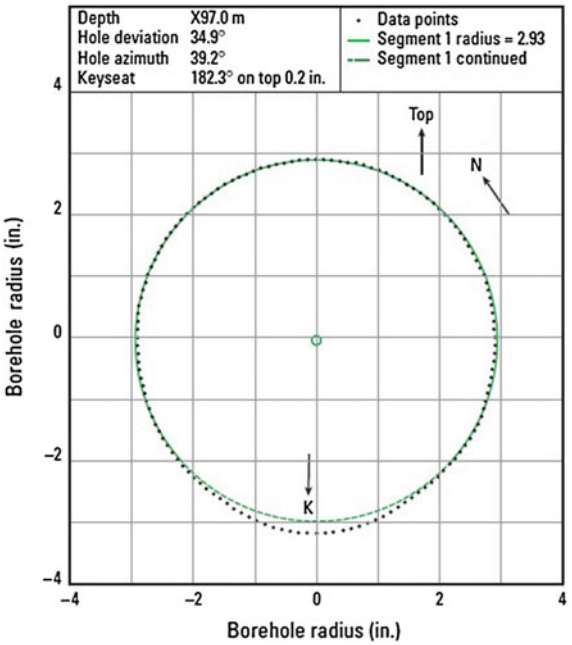

Fig. 3.42 The cross-sectional plot of the borehole in Fig. 3.43 clearly shows some keyhole wear on the low side of the hole (X97 m)

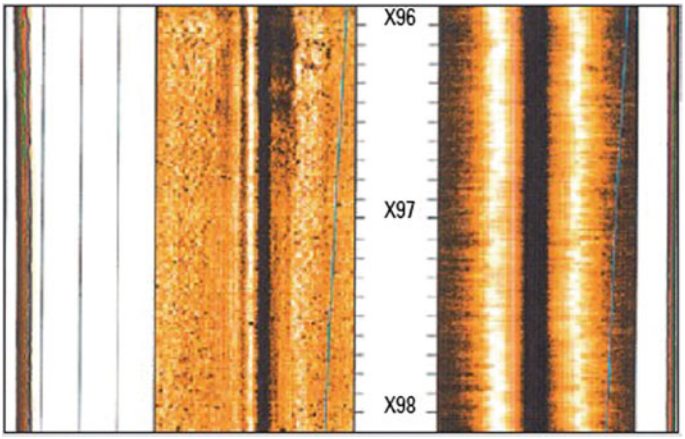

Fig. 3.43 Illustration of keyhole wear from openhole image of UBI

center of the hole caused by the existence of the keyhole. Cross-sectional plots can be used to automatically diagnose borehole anomalies such as keyholes and determine their severity and orientation. Keyhole wear inside a borehole can become a drilling hazard when the size of the enlargement is sufficient to

accommodate the drill pipe or drill collars but not the stabilizers or the bit, and it can cause the drill string to become stuck while tripping out of hole.

Breakouts

Horizontal stresses in the formation are rarely uniform. They are nearly always compressive and are usually greater in one horizontal direction than another because of tectonic forces and faulting.

If the maximum horizontal stress is in a northwest-southeast direction, the formation near the southwest and northeast sides of the borehole wall experiences a higher tangential compressive stress than before, but still in a northwest-southeast direction. The increased stress may be enough to cause compressive failure of the formation, and rock fragments may break off, causing caving on opposite sides of the well (Fig. 3.44). These oval enlargements are known as breakouts.

Shear sliding

Amplitude (left) and borehole radius (right) images in Fig. 3.46 provide an indication of shear sliding. The UBI cross-sectional plot in Fig. 3.47 more clearly shows borehole distortion that includes breakout-like enlargements and a narrowing of the hole. The smooth parts of the borehole are the shape of borehole-size circles, one slightly displaced from the other. This shape is caused by the formations on opposite sides of an extensive fracture sliding with respect to each other along the fracture plane.

The UBI images in Fig. 3.48 show borehole displacement along a fracture, which appears as a dark horizontal band on the radius image. Sometimes the dark band is not continuous, but the interpretation is usually unambiguous. A cross-sectional plot at the depth of the dark band clearly shows the slip (Fig. 3.49).

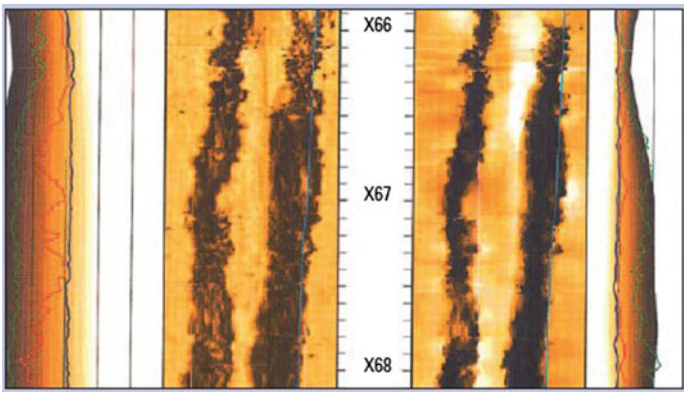

Fig. 3.44 Borehole breakout is recorded in this UBI image

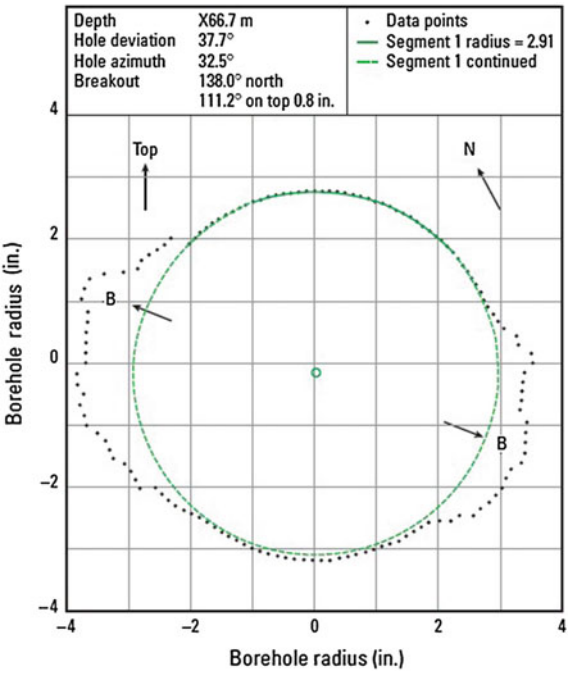

Fig. 3.45 Cross-sectional plot of the borehole in Fig. 3.44 showing the breakout on opposite sides of the hole

Shale alteration

Some shales hydrate and swell on contact with water-base mud. The altered shales may then collapse in the hole causing washouts and other borehole enlargements. Debris accumulation or clay balling caused by further hydration in the mud may constitute a drilling hazard.

UBI images usually show this alteration as a featureless hole enlargement and a very rugose borehole wall. The effect is common in soft shales, especially those containing smectite. The solution usually consists of changing to a potassium chloride, polymer, or oil-base mud to minimize hydration.

Horizontal stress determination

Displacement along a fracture plane, as measured by the UBI tool, is a function of the stress field. If the displacement is known at two fractures with different orientations, the stress direction and the ratio of maximum to minimum horizontal stress can be computed. The stress ratio can even be obtained from the displacement at a single fracture if the direction of the maximum horizontal stress is known (for example, from breakout orientation).

Horizontal stress information is an important parameter for mechanical properties evaluations such as predicting breakout and perforation stability in unconsolidated sands.

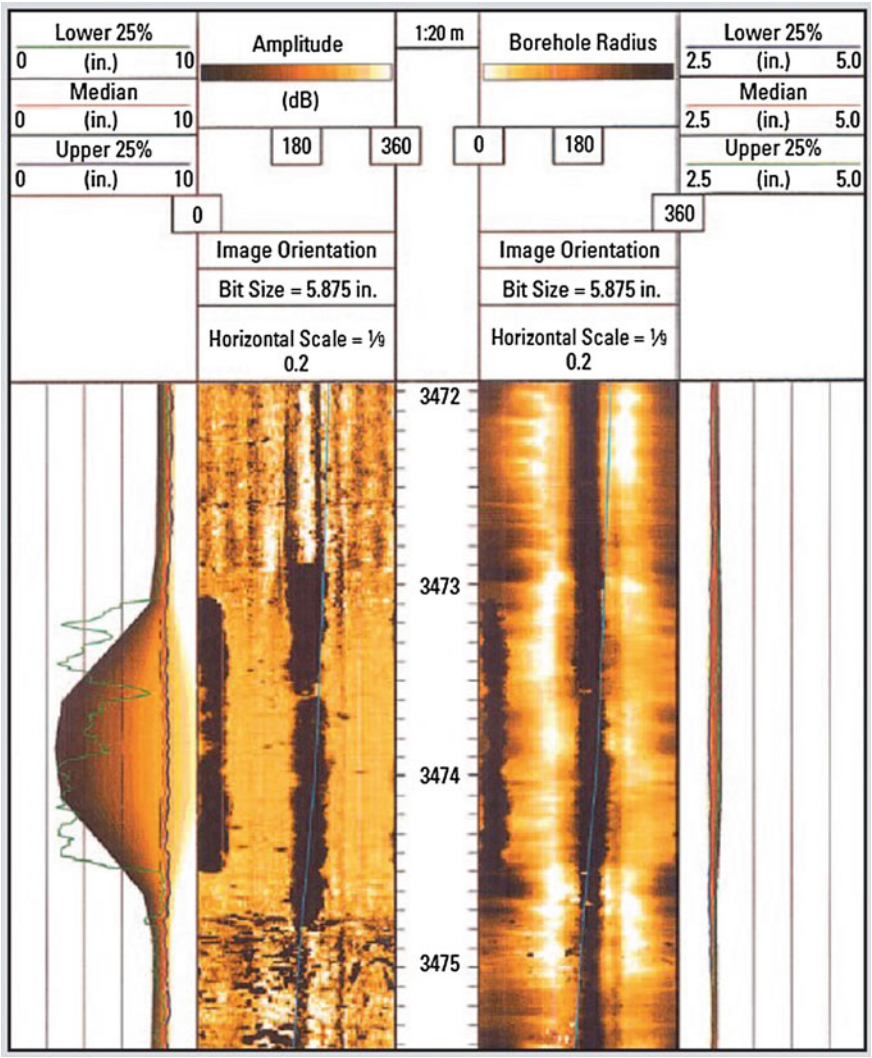

Fig. 3.46 Dynamic normalization is applied to both images to highlight the features of the borehole. *Dark colors* represent low amplitude and large radii, and indicate rugosity, enlargements, and attenuation materials. *Three additional curves* indicate the minimum, average, and maximum values of the measurement around the borehole

Automatic hole-shape analysis

An automatic analysis of the hole shape from cross-sectional information can be performed by Schlumberger Data and Consulting Services. Breakouts, keyhole wear (or keyseats), and shear displacement (or slip) are detected and flagged on a radius image log (Fig. 3.50).

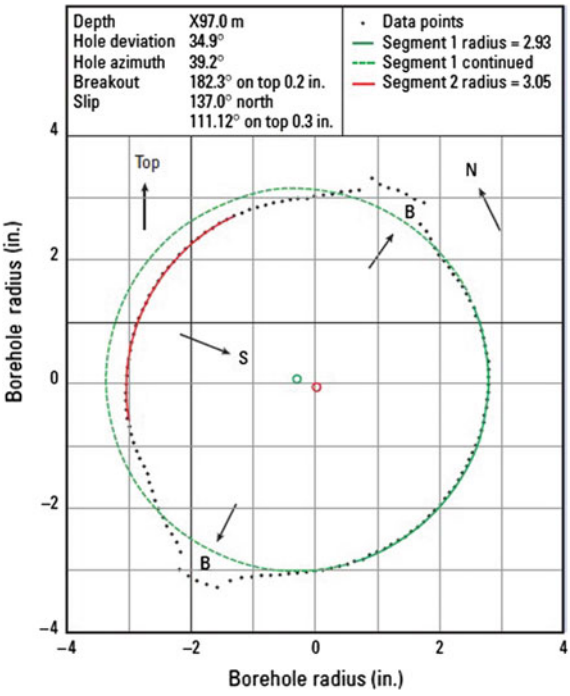

Fig. 3.47 The plot depicts the hole narrowing at the depth of slippage (3774 m) in Fig. 3.45

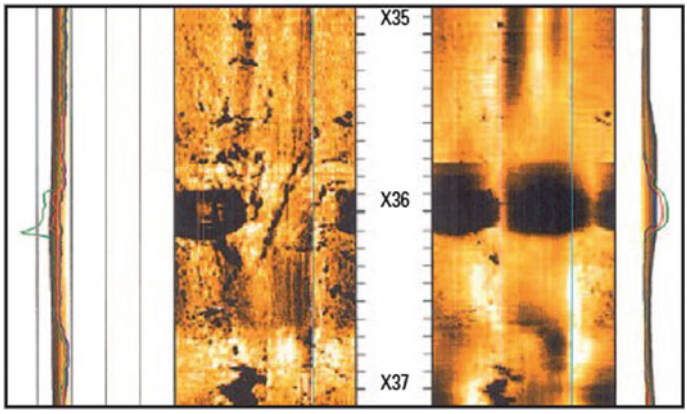

Fig. 3.48 The image shows a section of borehole with slippage at a fracture

Sometimes hole deformation cannot easily be classified as one of these three types, either because there is a combination of different deformations or because the borehole is rugose and irregular in shape. In such cases the borehole is flagged as rugose.

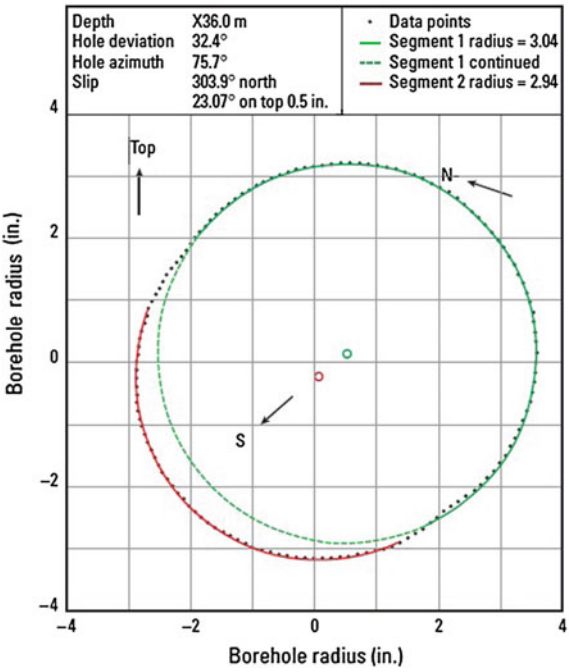

Fig. 3.49 Hole enlargement at the point of slippage in Fig. 3.47 is clarified by this cross-sectional plot

3.6 Circumferential Borehole Imaging Log (CBIL)

3.6.1 Tools

An acoustic imaging tool was first developed by Mobile in the 1960s, was further developed and improved by the oil companies Amoco and Shell and later ARCO before eventually being taken on by the service companies in the late 1980s. The tool uses a rotating rapidly pulsed sound source, a piezoelectric transducer, which both sends and receives the sound signal, that is, in pulse-echo mode (Fig. 3.51). As the tool is pulled up the hole, with the transducer rotating, a very dense matrix of data points is collected from around the borehole wall, which is then processed into an image. Early versions of the tool used photos of oscilloscope output to create the image but today images are created by the computer using measurements which have been digitized downhole. The modern service company tool will be illustrated by the Circumferential Borehole Imaging Tool (CBIL) of Western Atlas.

CBIL consists of a tool string typically approximately 12 m(40 ft) long with the rotating transducer housed in a mandrel at the bottom (Fig. 3.52). Bowsprings keep this part of the tool centered. Above this are the orientation and telemetry electronics and a spectral gamma ray sonde (Fig. 3.52). When the tool is logging, the transducer, in pulse-echo mode, turn at 6 revolutions per second, taking 250, digitized samples on each revolution, or every 1.44°. It thus acquires a tight spiral

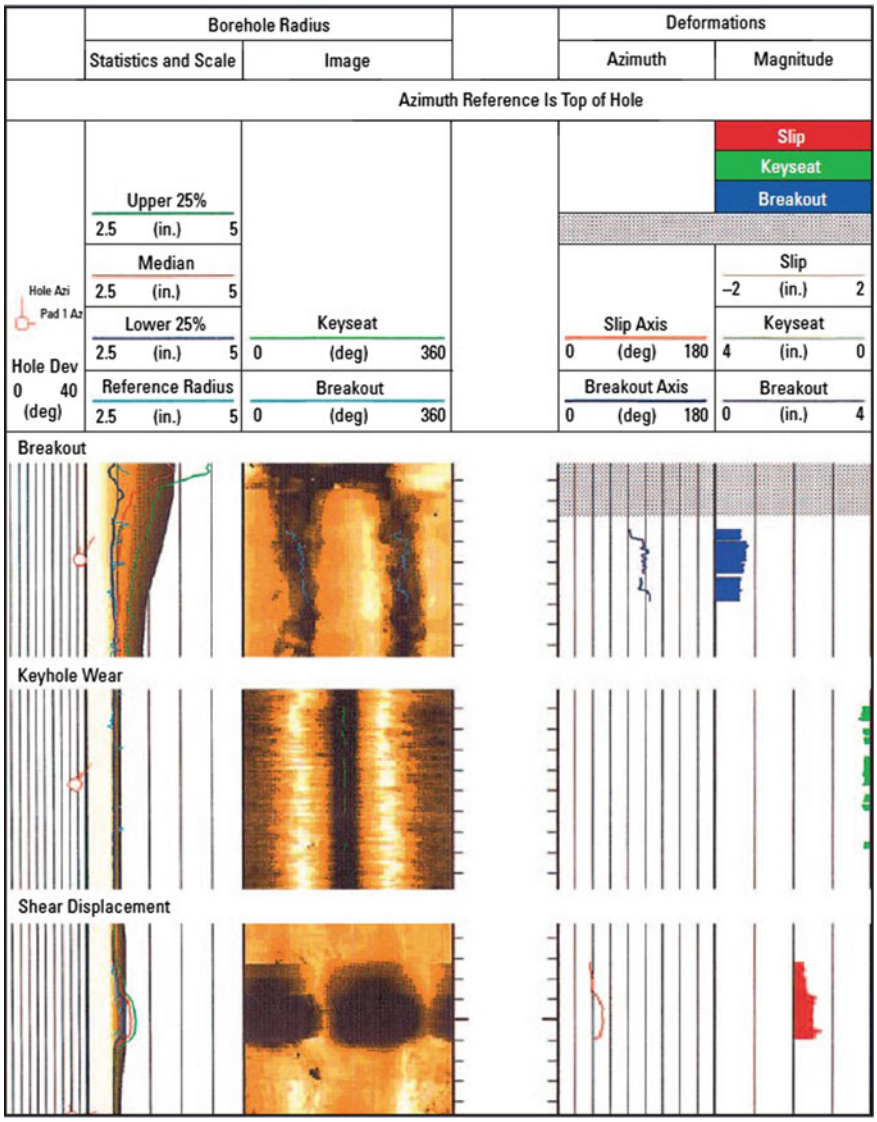

Fig. 3.50 Automatic hole-shape analysis from data and consulting services identifies breakouts, keyhole wear and shear displacement

of data points from around the entire borehole wall. When logged at a typical logging speed of 3 m (10 ft) per minute, the tool makes 1 scan of the borehole circumference each 0.83(0.33″) of depth, thus acquiring a matrix of 30,000 sample points of paired data readings (30,000 readings of amplitude and 30,000 of travel time, as explained below) for each meter of borehole logged.

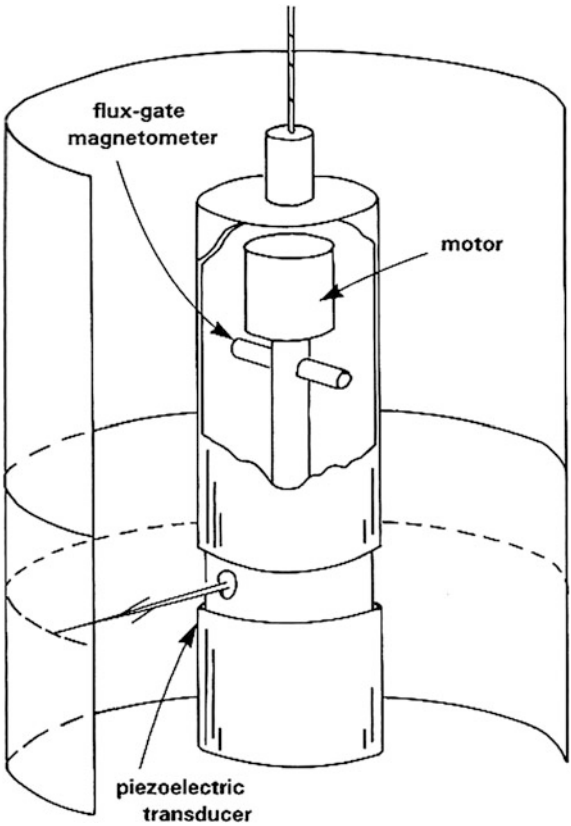

Fig. 3.51 The borehole televiewer tool (BHTV), schematic representation. A piezoelectric sonic transducer in transmit–receive mode, spins rapidly as the tool is pulled up the borehole

3.6.2 Acoustic Imaging Tool Interpretation Generalities

Acoustic imaging tools are used to provide high-quality dip and azimuth measurement, to investigate fractures, to provide information on borehole breakouts and to some extent to give information on lithological boundaries, textures, and some sedimentary features. By far the commonest used of the acoustic imaging tools to date, has been to investigate fractures. Some example of acoustic imaging tool interpretation will be explained in this section, for instance, Fig. 3.53 is the standard acoustic image.

- *Structural dip*
  Used in the simplest way, acoustic images provide a high-quality dipmeter, the dip and the azimuth taken from sine wave fitted to surfaces using the work station. This was indeed the early used to which the tool was put. The data from such a process are generally much less scattered than the comparable data from the electrical images and can be effectively used as a structural dip.

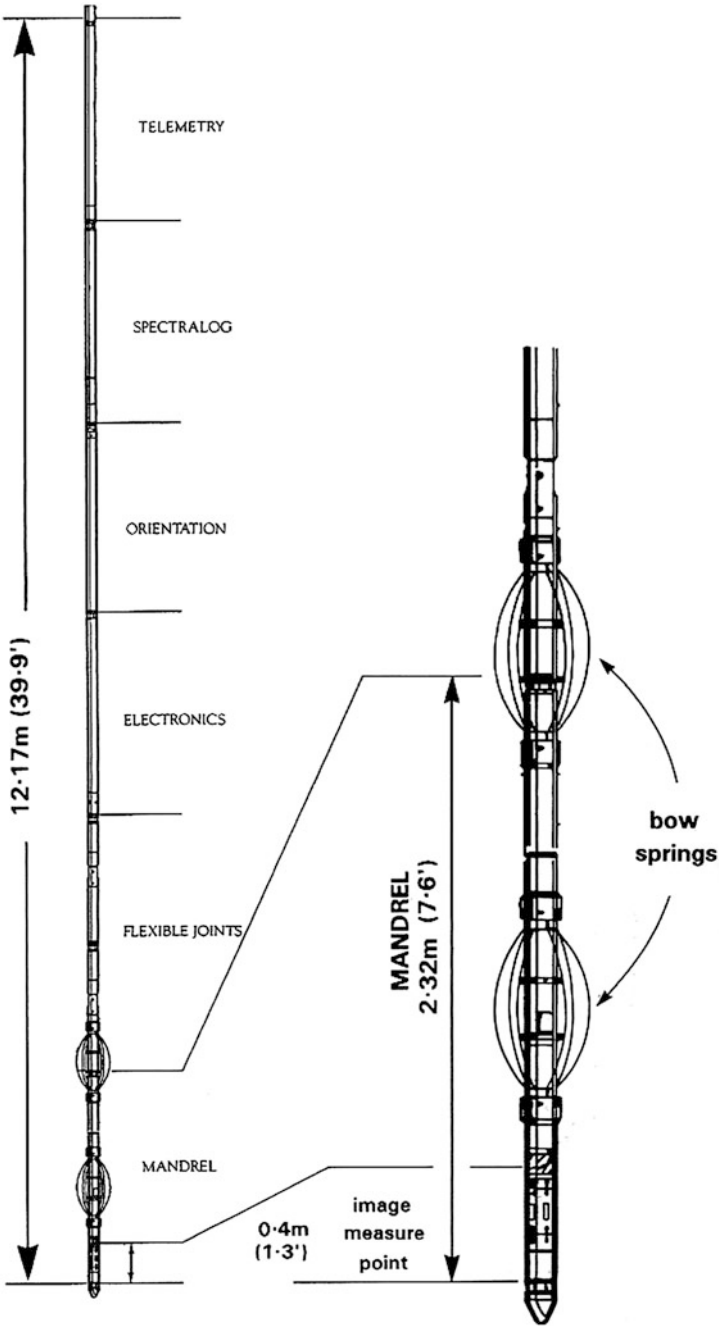

Fig. 3.52 Illustration of an acoustic imaging tool, the Western Atlas CBIL (circumferential borehole imaging log)

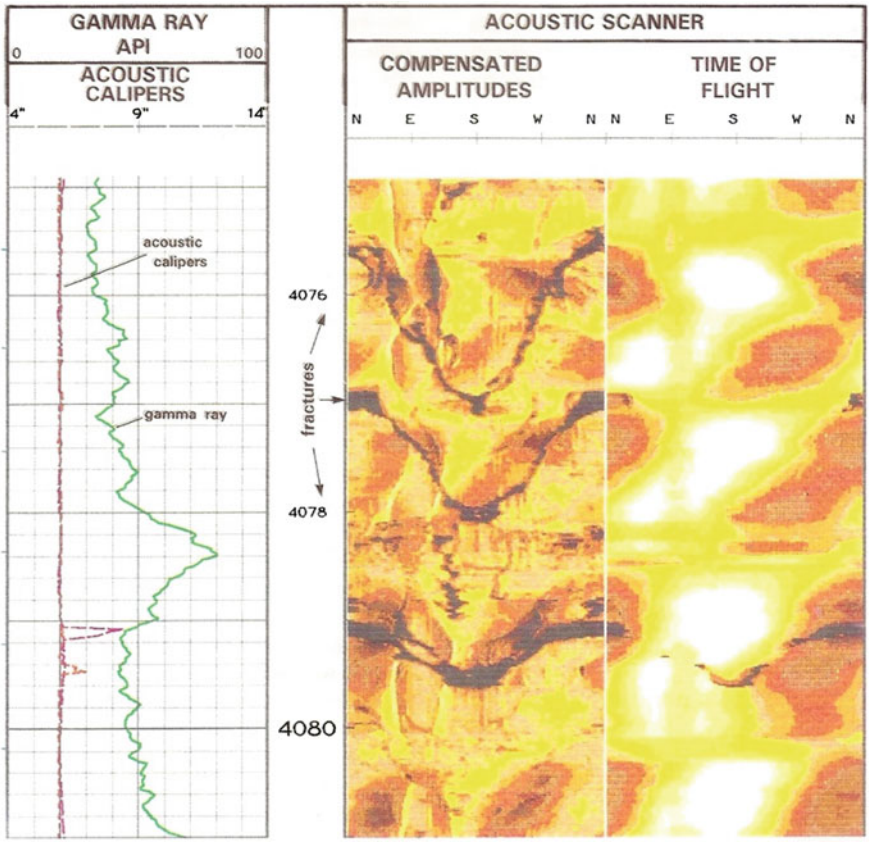

Fig. 3.53 Acoustic image presentation format. *Track 1* acoustic caliper and standard gamma ray. *Track 2* amplitude image (high = light). *Track 3* time of flight image (long = light). The lithology consists of fractured carbonates. Note the caving between 4079.10 and 4079.5 m related to fracturing (BPB Acoustic Scanning Tool)

- *Fractures*
  By far the most common use of the acoustic log is in the examination of fractures. This is as much the case in the hydrocarbon as in the non-hydrocarbon industries (water, geothermal, etc.). The advantage for all is that the images allow the identification, measurement, and recognition of fracture type in the subsurface.
- *Borehole breakouts*
  Because of its sensitivity to borehole geometry, the BHTV is an excellent indicator of breakouts. Breakouts are marked by hole enlargement in the direction of minimum horizontal stress, $Sh_{min.}$ enlargement is seen on the amplitude image log and the time of flight log as vertical stripes indicating poor reflectivity and long travel time or lost signal (Fig. 3.54). In addition to the

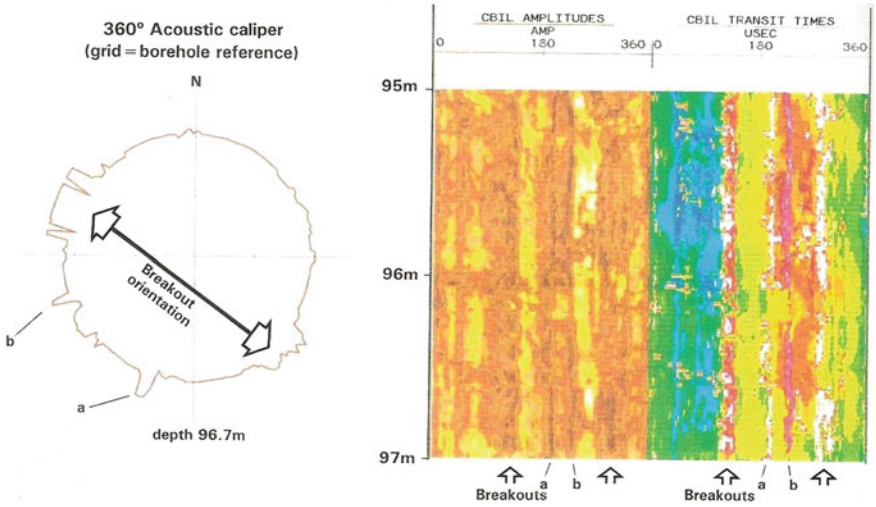

Fig. 3.54 Breakout indicated on acoustic images. The 360° caliper (from depth 96.7 m) shows the breakouts oriented approximately NW-SE. The amplitude image shows the breakouts as dark, vertical strips (*arrowed*). The transit time image shows them as well-marked light stripes (*arrowed*). **a**, **b** are additional vertical features. Western Atlas CBIL, IMAGEPRO output

images, the acoustic caliper derived from the time of flight measurements, can be used to indicate the hole circumference profile (Fig. 3.54).

As discussed above, the used of breakouts to derive present day in situ stress orientation, is an important phase in the attempt to separate natural from drilling-induced fractures. Although dipmeter calipers are traditionally used for breakout analysis, when BHTV images are available they are far more effective and more precise.

Texture, lithology, and sedimentary features

For lithological features to be seen on the acoustic images, there must be large acoustic impedance contrasts. The coal industry has long used the BHTV to localize coal seams and give accurate bed limits. However, coal seam are an exception in terms of lithology and more general lithological investigations with acoustic images are only now beginning to be used (Fig. 3.54). One of the problems with acoustic images in sedimentary sequences is that the acoustic impedance contrasts between lithologies, beds, or laminae are small. However, major bed boundaries are found to be imaged and so are tight or cemented zones, which can be identified on CBIL image, as shown in Fig. 3.55.

In the same way that lithological investigations are difficult with acoustic logs, so too are investigations of sedimentary structures. Some success in this field is beginning to be seen (Fig. 3.55) but in general electrical images are far more effective for this task.

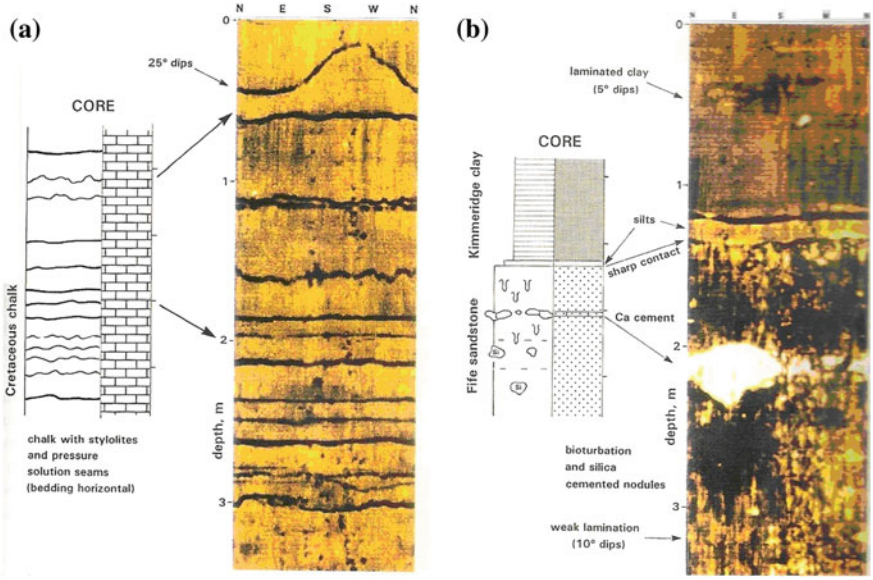

Fig. 3.55 Lithology and sedimentary features on CBIL images

Problems

3.1 Explain the elastic parameters, such as E, K, μ, σ.
3.2 Describe the mechanism of P-wave and S-wave
3.3 Derivate the formula of interval transit time for sonic logging, and how to eliminate the borehole effect?
3.4 What is the difference between Acoustic logging and Dipole shear image logging?
3.5 What are the principle and applications of CBL and VDL?
3.6 What are the advantages of CET, SBT, USI?
3.7 What is the application of UBI?
3.8 What are the principle and applications of CBIL?

Chapter 4
Nuclear Logs

4.1 Gamma Ray Logs

In the preceding chapters, electrical devices are seen to respond primarily to the fluid content of earth formations. They are not used, therefore, to obtain information about the predominant constituent of formations, the rock matrix. Nuclear measurements used in logging respond to properties of both the formation and the contained fluids. These measurements employ gamma rays and neutrons. These two types of penetrating radiation are the only ones which are able to traverse the pressure housings of the logging tools and the formation of interest and still return a measurable signal.

The gamma ray log (GR), as is evident from its name, responds to the natural gamma radiation in the formation. We distinguish between an integral gamma ray log, providing the bulk content of natural radioactive elements in the formation of interest, and a spectral gamma ray indicating the contents of individual radioactive elements separately.

This chapter including two parts, one is about GR properties and GR logs, and in this parts, GR logging, spectrum GR logging. Besides the GR logs, neutron is a powerful method to detect the inner mystery of rock. Through neutron logging, some petrophysical properties of rocks, so the other part is about neutron logging. Compensated neutron logging, compensated density logging, thermal decay logging, and C/O logging will be introduced in the second part.

4.1.1 Rudimentary of Radioactivity

There are three common types of radiation identified and named, quite unimaginatively, α, β, and γ radiation. It was subsequently discovered that α radiation consisted of fast-moving He atoms stripped of their electrons, and that β radiation

H. Liu, *Principles and Applications of Well Logging*, Springer Mineralogy,
DOI 10.1007/978-3-662-53383-3_4

consisted of energetic electrons. The gamma rays were found to be packets of electromagnetic radiation also referred to as photons. The unit chosen is known as the electron-volt (eV), which is equal to the kinetic energy acquired by an electron accelerated through an electric potential of 1 v. For the types of radiation discussed in the following sections, the range of energies is between fractions of an eV and millions of electron volts (MeV). Another convenient multiple for discussing gamma ray energies is the kilo-electron-volt (keV).

Since α and β radiation consist of energetic charged particles, their interaction with matter is primarily Coulombic in nature. This leads to atomic excitation or ionization; that is, the interactions are with the electrons of the medium. The α and β particles rapidly lose energy as they transfer it to electrons in their passage through the medium. Their ranges of penetration are rather limited and in most materials are a function of the material properties (Z, the number of electrons per atom, and density) and the energy of the particle. Consequently, they have not been of any practical importance for well logging applications. Gamma rays, on the other hand, are extremely penetrating, which makes them of great importance for well logging applications.

4.1.2 Radioactivity of Rocks

The radioactivity of rocks is due to the presence of naturally occurring radioactive elements, includes isotope ^{40}K, the parent nuclei of the three transformation series ^{235}U, ^{238}U, and ^{232}Th, as well as the multi-numerous products of their disintegration. The gamma ray from potassium are monochromatic (1.46 meV), which is shown in Fig. 4.1. The energy spectra of the uranium and the thorium series have several lines. The radioactivity level of various rocks varies with their mineral composition and its sedimentary environments. Magmatic rocks of the alkali–lime series have an increasing concentration of radioactive isotope in the succession. Higher alkalinity extrusive and intrusive formations have high radioactivity levels. Metamorphic rocks may be slightly radioactive (mafic silicate rocks) or medium radioactive (felsic gneisses, crystalline shales).

The ultra-metamorphism and the metasomatism processes contribute to the uranium and thorium contents. The radioactivity levels of sedimentary rocks vary over a wide range. Conglomerates and clays have much greater concentrations of radioactive isotope. There is a general relationship between the content of uranium and to a lesser extent, of the thorium and the granule size: the smaller the granules, the higher the content of the above radioactive elements appreciably radioactive rocks include phosphorites, potash salts, some carbonaceous and bituminous rocks, as well as sand rocks containing feldspars, glauconite, and accessory minerals. In other instance, the radioactivity level of sand rocks is low and is determined by their shale content. Carbonate rocks have a very low radioactivity level that may result from shaliness, the presence of organic materials, or bituminous. The lowest

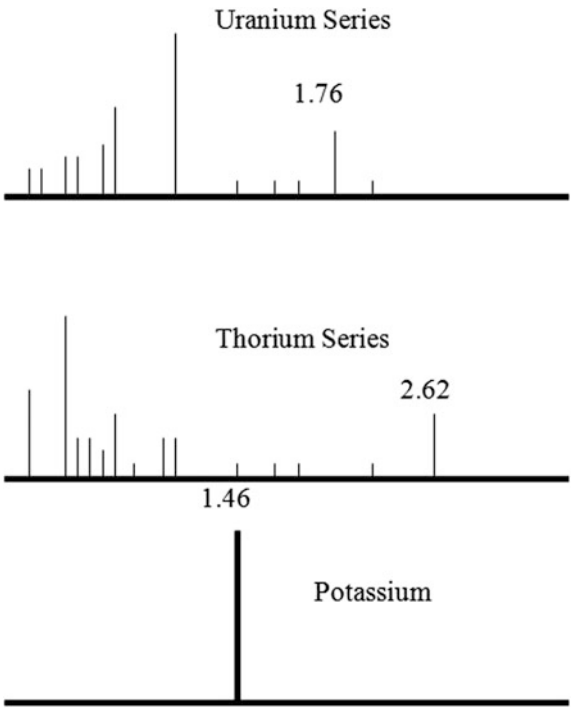

Fig. 4.1 The distribution of gamma rays from the three naturally occurring radioactive isotopes

radioactivity levels are observed in sulfates and nonpotash salts. The rough law of the radioactive intensity is shown in Fig. 4.2.

^{40}K exists in the feldspars and micas which weather easily into clay minerals. These clays, due to their ion-exchange capacity, can adsorb heavy radioactive elements from the formation water. Consequently, when there is an abundance of clay material as in shale, there generally is a high level of radioactivity observed. Carbonates are often deposited in areas with low concentrations of terrestrially derived sediments and hence, low concentrations of radioactive elements. Dolomites sometimes exhibit slightly higher radioactive levels. This is probably due to ground water (involved in the dolomitization) carrying in additional traces of radioactive isotopes in solution.

4.1.3 Interaction Between Formation and GR

Interactions classifications between the Gamma ray and atoms of rocks are depended on energy of incident gamma ray. For our purpose, there are three types of gamma ray interactions in earth formations that are of interest: the photoelectric effect, Compton scattering, and pair production. The probability of a specific gamma ray interaction occurring will depend on the atomic number of the material

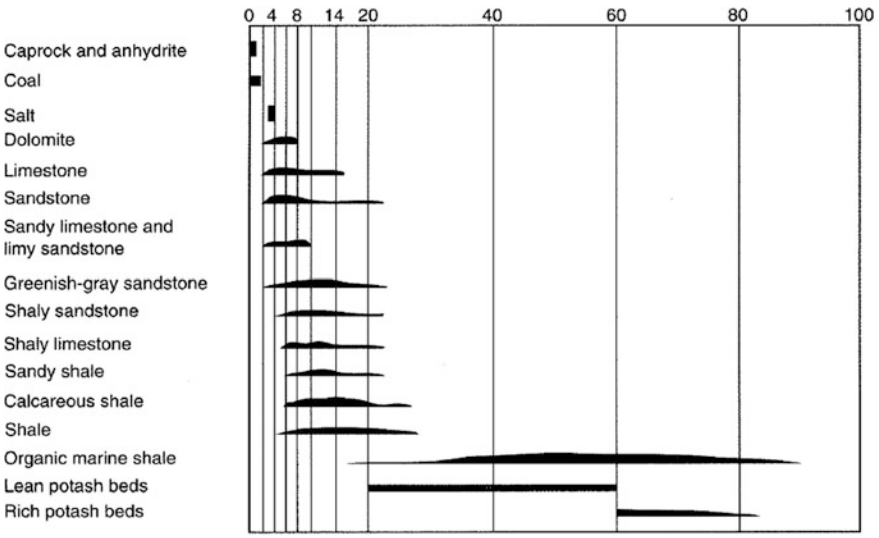

Fig. 4.2 Gamma ray strength of different rocks

and the energy of the gamma ray. The ordering of these three interactions in the following discussion reflects the change of the dominant process as the gamma ray energy increases.

4.1.3.1 Photoelectric Effect

The photoelectric effect (Fig. 4.3a) results from interaction of a gamma ray with an atom in the material. In this process the incident gamma ray disappears and transfers its energy to a bound electron. If the incident gamma ray energy is large enough, the electron is ejected from the atom and begins interacting with the adjacent material.

Normally the ejected electron is replaced by another less tightly bound electron with the accompanying emission of a characteristic fluorescence x-ray with an energy (generally below 100 keV) which is dependent on the atomic number of the material. The cross section for the photoelectric effect τ varies strongly with energy, falling off as nearly the cube of the gamma ray energy (E_γ), and the wave length of photon. It is also highly dependent on the atomic number (Z) of the absorbing medium. In the energy range of 40–80 keV, the crosssection per atom of atomic number Z is given by:

$$\tau = 0.0089 \frac{\rho_b}{A} Z^{4.1} \cdot \lambda^n \tag{4.1}$$

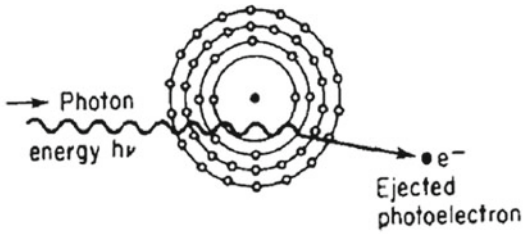

a. Photoelectron effect process

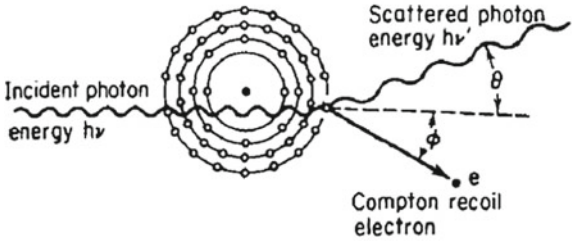

b. Compton effect process

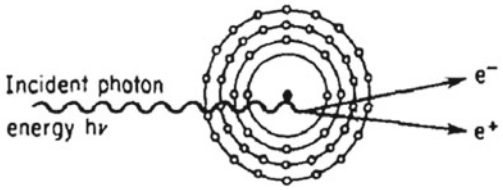

c. Electron pair production

Fig. 4.3 Interaction between gamma ray and atoms

For most earth formations, the photoelectric effect becomes the dominant process for gamma ray energies below about 100 keV. The photoelectric effect is an important process in the operation of conventional gamma ray detection devices. Also it is the mechanism by which one type of well logging tool is made sensitive to the lithology of the formation. This tool measures the so-called photoelectric absorption factor, P_e, which is proportional to the photoelectric cross section per electron. Since P_e is very sensitive to the average atomic number of the medium (Z), it can be used to obtain a direct measurement of lithology or rock type. This is due to the facts that the principal rock matrices (sandstone, limestone, and dolomite) have different average atomic numbers and thus, considerably different photoelectric absorption characteristics, and that the pore fluids play only a minor role because of their low average atomic numbers.

4.1.3.2 Compton Scattering

When the incident photon collides with an electron (Fig. 4.3b) its energy hv is divided between the kinetic energy $E = mv^2$ given to the electron ejected from its atom with initial velocity o and a photon "scattered" in a direction making an angle θ with the original incident direction.

This elastic collision between the gamma ray and an individual electron simply allows the gamma ray to proceed, deflected by its encounter, but reduced in energy. This process occurs mainly with outer electrons of the atoms. This type of reaction is called Compton scattering and it is the reaction figuring mainly in density measurements. The scattering effect is sensitive to the electron density of the formation (number of electrons per unit volume).

To appreciate the bulk effect of Compton scattering in a material consisting of atoms of mass A, and atomic number Z, one can examine the so-called linear absorption coefficient. This macroscopic cross section is just the Compton cross section σ, multiplied by the number of electrons per cubic centimeter:

$$\sigma = \sigma_e \frac{ZN_A}{A} \rho_b \tag{4.2}$$

The final factor, Z, in the equation above takes into account that there are Z electrons per atom. Consequently the attenuation of gamma rays due to Compton scattering will be a function of the bulk density ρ_b and the ratio Z/A.

4.1.3.3 Electron Pair

When the photon energy is above 1.02 meV, the interaction of photon and matter leads to pair production (Fig. 4.3c), it means the production of a negatron (or negative electron) and a positron (or positive electron), each with an energy of 0.51 meV. These two previously nonexistent electron masses appear as a result of the disappearance of the photon energy.

All of the photon energy is given up to the two electrons, with the exception of a very small amount going into the recoiling nucleus. The reaction is:

$$hv_0 \rightarrow e^+ + e^- + 2T \tag{4.3}$$

This phenomenon can only occur when the energy of the photon is higher than $2mc^2$(=1.02 meV). Requirement of conservation of energy and momentum of the system allow this process to occur only in the electric field of a nucleus. The onset of this interaction corresponds to the rest mass energy of the electron and positron. The subsequent annihilation of the positron (positively charged electron) results in the emission of two gamma rays of 511 keV each. The nuclear cross section of this process is zero below the threshold energy of 1.022 meV and rises quite rapidly

with increasing energy. It is also dependent on the charge of the nucleus, varying approximately as Z^2.

$$t = K_t \frac{N_A \rho_b}{A} Z^2 (E_\gamma - 1.022) \tag{4.4}$$

In order to observe the regions of dominance of the three types of interactions, refer to Fig. 4.4. It shows, as a function of gamma ray energy and atomic number of the absorber, the boundaries at which the linear absorption coefficients for the adjacent processes are equal. The horizontal line, corresponding to an atomic number of 16, indicates the upper limit of Z for common minerals encountered in logging as a function of energy and the atomic number, Z, of the scattering material.

4.1.3.4 Absorption Equation

If L is large enough, the intensity of the gamma rays is an exponential function of the electron density of the formation and is given by the equation:

$$I = I_0 e^{-\mu \rho_e L} \tag{4.5}$$

where:

I intensity of gamma rays measured at the detector
I_0 intensity of gamma rays at the source
ρ_e electronic density of the formation in the interval L (number of electrons per unit volume).
L detector-source spacing.

μ is, to a first approximation, a constant depending on the tool geometry, the energy of the gamma rays emitted by the source and the detector characteristics.

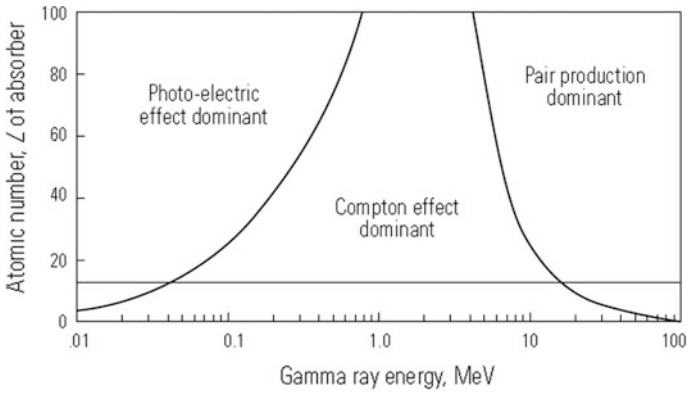

Fig. 4.4 Regions of dominance of the three principal gamma ray scattering mechanisms

4.1.4 Gamma Log

The gamma log is a measure of the natural radiation of the formation. Radioactive elements tend to concentrate in clays or shales. While shales and shaly sands are higher in radioactivity, clean sand, and carbonates exhibit low levels of radiation also. The gamma ray curve differentiates between potential reservoir rocks and shales. Thus, the gamma log can be used to determine lithology. The gamma ray log can also be used to determine volume of shale in the formation, which is shown in Fig. 4.5.

Gamma ray tools have vertical resolutions 6 in. to about 2 ft, and depths of investigation between 6 in. and 1 ft. Increased hole diameter tends to decrease the number of gamma rays observed. Mud tend to increase the background radiation because of the radioactive potassium the mud contains.

Previous log examples demonstrate that two logging measurements are reputed to respond to the difference between clean and shaly formations. One of the measurements, the SP, has been analyzed in some detail, and it is known to have a marked response to clean permeable zones. This is evident in the right track of Fig. 4.6 where the more negative potential of the zone between 8,510 and 8,540 ft is due to the simultaneous absence of clay and free communication between the borehole fluid and the formation waters. For the same well, on the left side of the figure, the gamma ray log (or GR) has a structure similar to the SP trace: a low reading in the clean zone and a high reading in an apparently shaly zone.

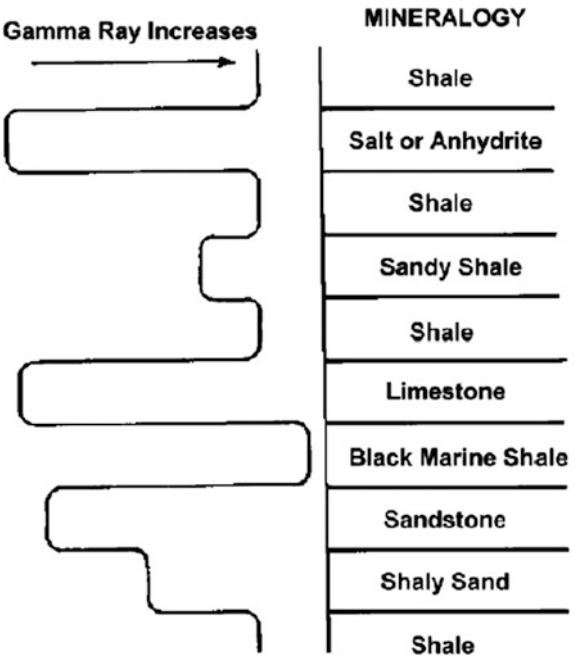

Fig. 4.5 Illustration of gamma ray curve of sedimentary rocks

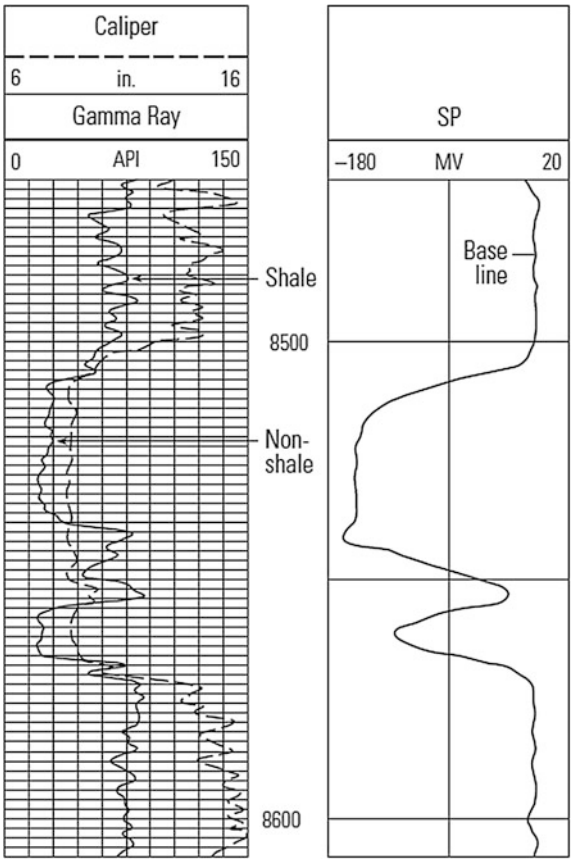

Fig. 4.6 Gamma ray curve indicates different radioactivity strength of different rocks. The GR curve shows similar changes with SP curve

4.1.5 Spectral Gamma Ray Device

One of the difficulties in the interpretation of the gamma ray measurements is a lack of uniqueness. There are nonradioactive clays, and there are "hot" dolomites. The use of spectral gamma ray devices can point out anomalies such as a "hot" dolomite or other formations with some unusual excess of U, K, or Th. They permit recording the individual mass concentrations of the three radioactive components of the total gamma ray signal. A clear example of the utility of this decomposition can be seen in Fig. 4.7. In track 2 the three components, Th, U and K, are shown in a carbonate section. In track 1 two curves are to be found. The one marked GR is the total gamma ray signal calibrated in API units as in an ordinary tool that does not employ spectroscopy. The second curve is the so-called computed GR (CGR) curve without uranium. It only consists of the sum of counting rates from Th and K converted to API units. In this way it is uninfluenced by uranium which has little association with clay minerals. It can be seen that the activity in the GR signal was

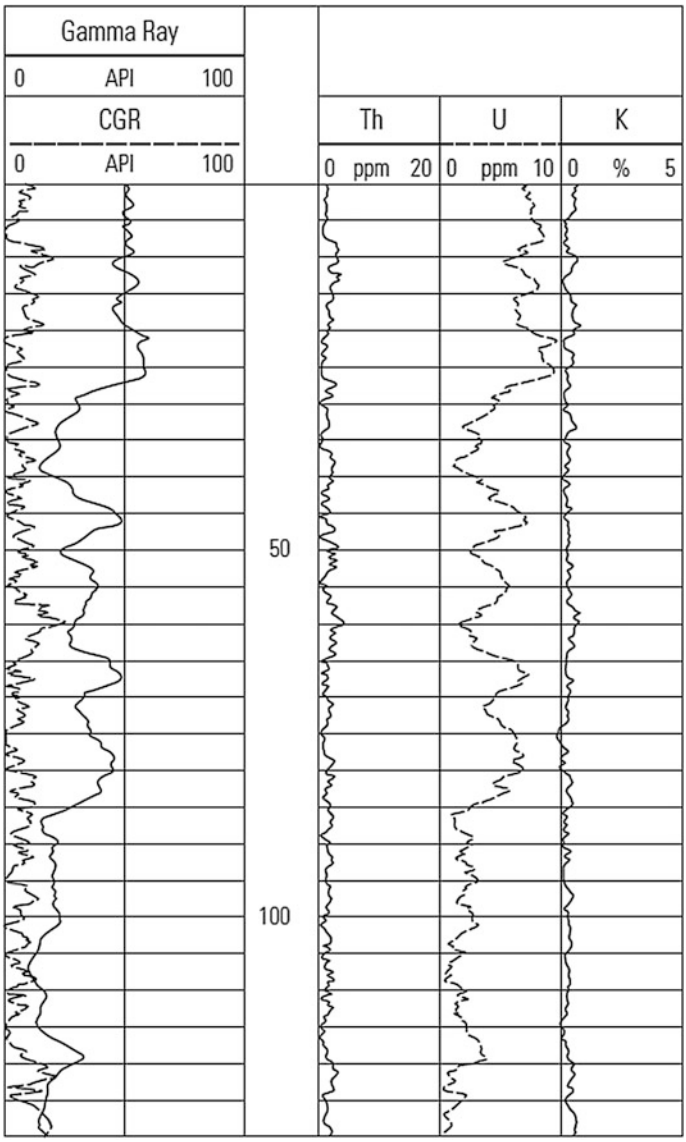

Fig. 4.7 Decomposition of the natural gamma ray activity of a carbonate section into concentrations of Th, U and K

due to uranium fluctuations. Interpreting the total GR signal for clay would have given misleading results in a zone that is essentially clay-free.

For one type of tool, the relationship between the concentration of the three radioactive components and the total gamma ray signal in API units (γAPI), which is defined as the radioactivity comes from an artificially radioactive formation,

constructed at the University of Houston facility to simulate about twice the radioactivity of a typical shale. This formation, containing approximately 4 % K, 24 ppm Th, and 12 ppm U, was defined to be 200API units.

The response of gamma ray device γAPI is given approximately by:

$$\gamma_{\text{API}} = 4\,\text{Th}_{\text{ppm}} + 8\,\text{U}_{\text{ppm}} + 16\,\text{K}_{\%} \tag{4.6}$$

when thorium (Th) and uranium (U) are measured in ppm and potassium (K) in percent by weight, and the number 4, 8, 16 are coefficient for each composition, and will be different for different device.

The use of this decomposition is to provide a total GR signal minus the uranium contribution. This can provide a uranium-free GR index which is more representative of the clay minerals in the shale, by eliminating effects of organic shales or the deposit of uranium salts in fractures. In the next example, Fig. 4.8, the GR log alone would indicate that below the lower boundary of the shale bed, at 12,836 ft,

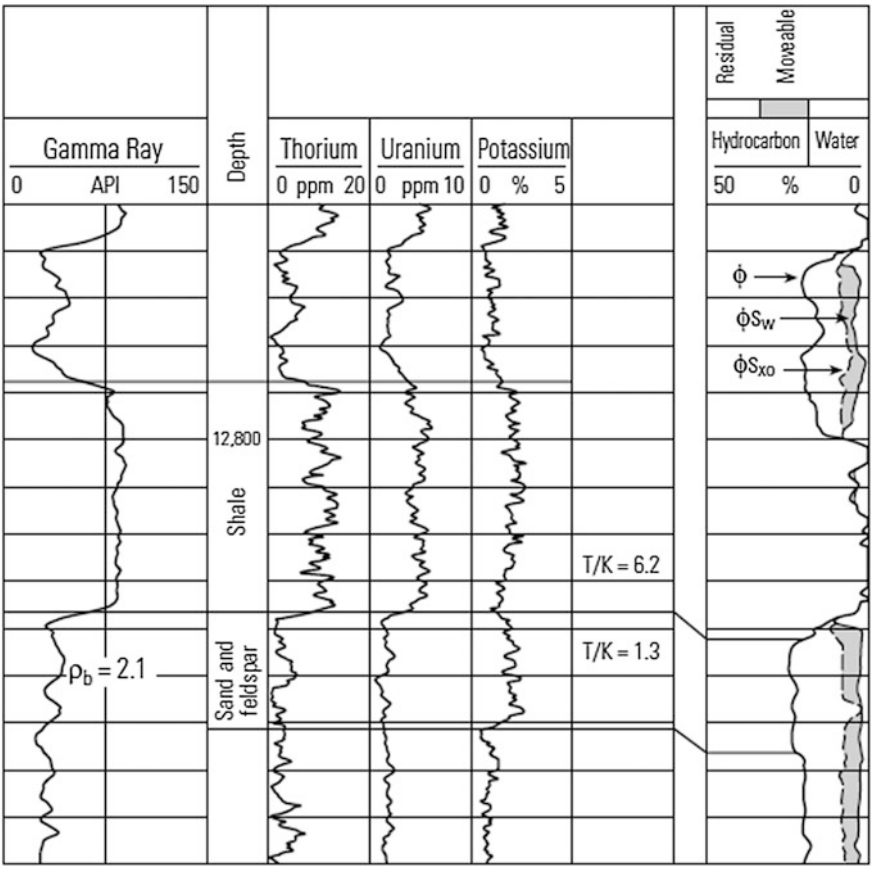

Fig. 4.8 A log showing the effect of feldspar on the spectral and total gamma ray logs

there is relatively clean sand. It can be seen, however, from the K trace that the high level of potassium in the shale zone persists below 12,836 ft. This excess potassium was found from subsequent core analysis to result from the presence of feldspar. This is an important piece of knowledge because feldspar affects the choice of grain density to be used in the interpretation of density logs.

The third example, Fig. 4.9, shows how a uranium-rich formation would be misinterpreted (in a simple gamma ray analysis) as being shale. The sudden increase in uranium content, at the indicated depth, suggests that this is not a simple shale like those at nearby depths. Core analysis showed this zone to be rich in organic material. This is consistent with the notion that U is often trapped in organic complexes.

There are two important reasons for using a spectral gamma ray measurement rather than the standard gamma ray, which is reliable only for correlation. The first

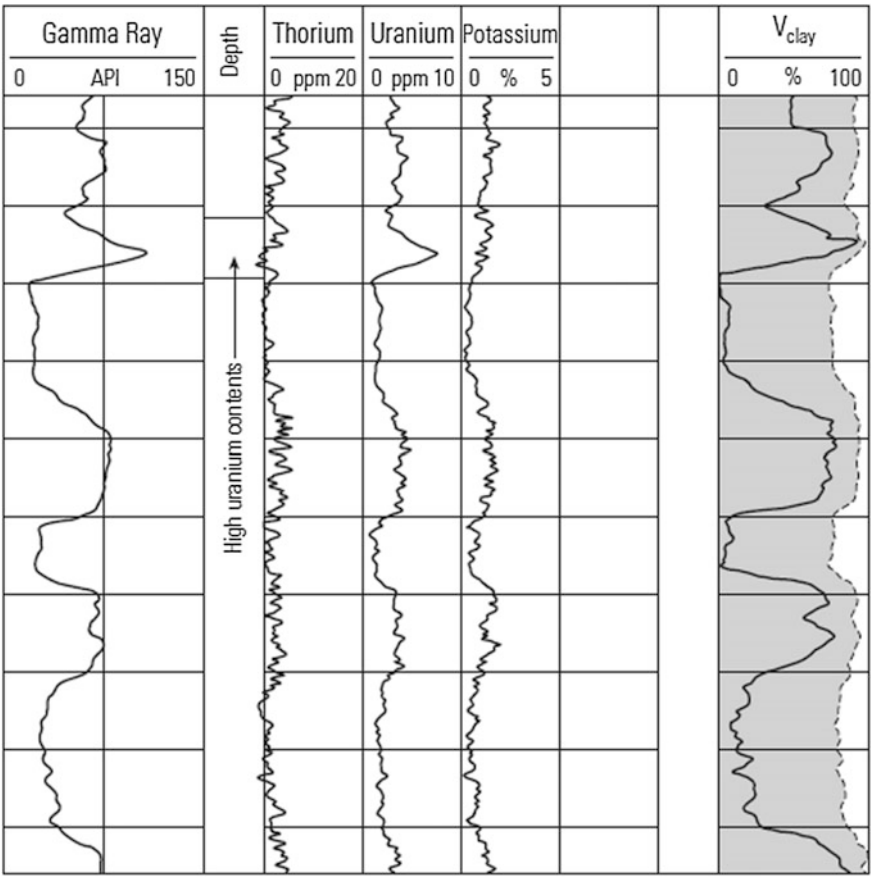

Fig. 4.9 A log showing the result of an anomaly of U. If undetected, the volume of clay in the entire zone is compromised

is for the resolution of radioactive anomalies like those described above. The second is to help identify the clay types by classifying them in terms of the relative contributions of the three radioactive components. It will become apparent in the following chapters that clay mineral identification is a task much too complicated to be attempted solely from knowledge of the associated radioactive elements.

It is based on an approximate knowledge of potassium and thorium contents of some common clay minerals, as shown in Fig. 4.10. Lines of constant clay volume should follow a parabolic shape, as indicated in the Figure. The scaling is adopted to the clay minerals present in the zones under investigation and determined from the cross plot. Quirein et al. have suggested a means to determine the presence of major clay minerals, such as illite and kaolinite, and to separate them from feldspars. The method is summarized in Fig. 4.11 and consists of an ambitious reinterpretation of the potassium–thorium cross plot.

4.1.6 Measurement of Gamma Radiation

Gamma radiation can be measured by Geiger–Mueller counters, ionization chambers, and scintillation counters.

4.1.6.1 Geiger–Mueller Counter

This is composed of a metal chamber with a central wire maintained at a positive potential relative to the cylindrical chamber wall (900–1000 V). The chamber

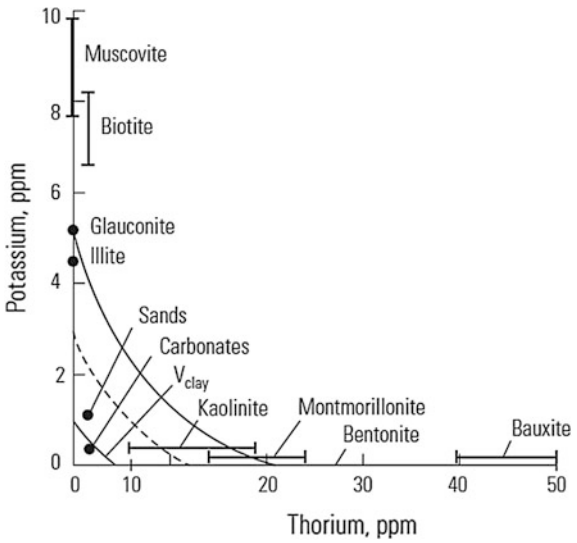

Fig. 4.10 Determination of V_{cl} for thorium and potassium distributions

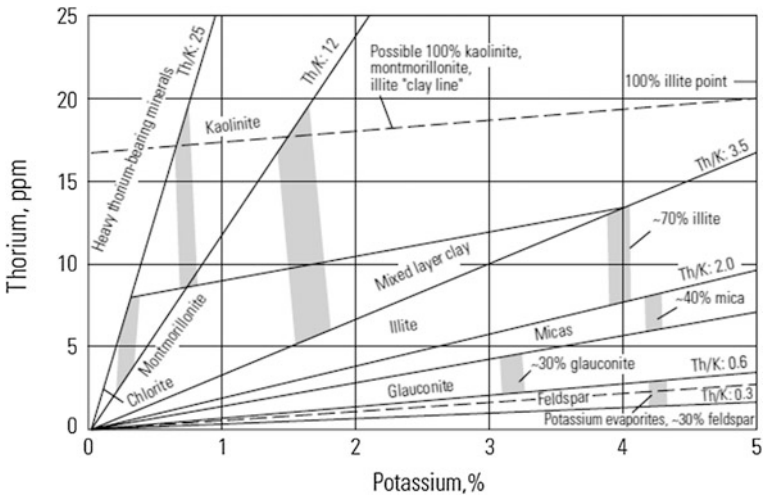

Fig. 4.11 Identification of clay minerals from thorium and potassium contents

contains gas (argon, helium, or neon) at a low pressure. Incident gamma rays cause the ejection of electrons from the detector wall into the gas. As the ejected electron is drawn toward the highly charged central wire, other collisions occur between each electron and gas atoms, thus producing additional electrons which in turn cause additional ionization by collision. This results in a multiplication of the ionization events. An avalanche of electrons arrives at the central wire for each incident gamma ray interaction with the cylindrical wall of the chamber. The dead-time is of the order of 0.1–0.2 ms.

4.1.6.2 Ionization Chamber

It consists of a gas-filled cylindrical metal chamber containing a central rod maintained at about 100 V positive to the cylinder wall. The gas is maintained at high pressure (100 atmospheres). Incident gamma rays interact with the wall material and cause the ejection of electrons. The electrons drawn to the central rod produce additional electrons in the collisions with gas atoms. The electrons moving to the central rod constitute a minute flow of electrical current, proportional to the number of gamma ray interactions.

4.1.6.3 Scintillation Counter

This consists of both a crystal detector, often called phosphor, and a photomultiplier to produce countable pulses. Gamma rays entering the crystal produce light flashes. The flash produced strikes the sensitive surface of a photocathode in the

photomultiplier, causing the emission of a number of primary electrons by photoelectric effect. These electrons are attracted to the first of a series of anodes (general 9–11), each of which is maintained at a successively higher positive potential by a voltage source and a potential divider. Each anode surface emits several electrons (4–8) when struck with a single electron of sufficient energy. The anodes are shaped and arranged so that each secondary electron moves toward the next anode, accelerated by the higher positive potential. Thus a 10-anode tube with a gain of 6 per stage has an overall gain of 10^5–10^6. The last anode is connected to the positive voltage supply through a series of resistances. A flash of light on the photocathode will result in the appearance of a pulse of electrons at the anode, which will produce a negative output pulse because of the voltage drop across the load resistor. This negative pulse can be transmitted to the recording circuits through capacitance *C*. The resulting pulse is proportional to the energy of the incident gamma ray.

This last type has an efficiency of some 50–60 % (compared with 1–5 % for the others) and crystals some 4–8 in. in length can be used (compared with 30 in. or more), giving good vertical resolution (Fig. 4.12).

4.1.7 Applications of GR

4.1.7.1 Determine V_{sh} from Gamma Ray

The gamma ray log can be used to determine the volume of shale in a formation. Volume of shale can then be used to correct the apparent porosities found by the sonic, neutron, and density logs. This method of finding V_{sh} will generally yield good values in common formations. If, however, the formation is unusually radioactive, this method will not work.

In order to determine V_{sh}, the gamma ray index (I_{sh}) must be found from:

$$I_{sh} = \frac{GR - GR_{min}}{GR_{max} - GR_{min}} \tag{4.7}$$

$$V_{sh} = \frac{2^{GCUR \times I_{sh}} - 1}{2^{GCUR} - 1} \tag{4.8}$$

where GCUR is Hill index, for tertiary formation, GCUR = 3.7, and for older formation is 2. V_{sh} is then found from a graph such as that shown in Fig. 4.13.

GR_{min} is minimum reading of GR curve, which is always found from the cleanest sand formation. GR_{shale} is found in thick shale zones near the zone of interest. This will normally be the highest reading gamma ray.

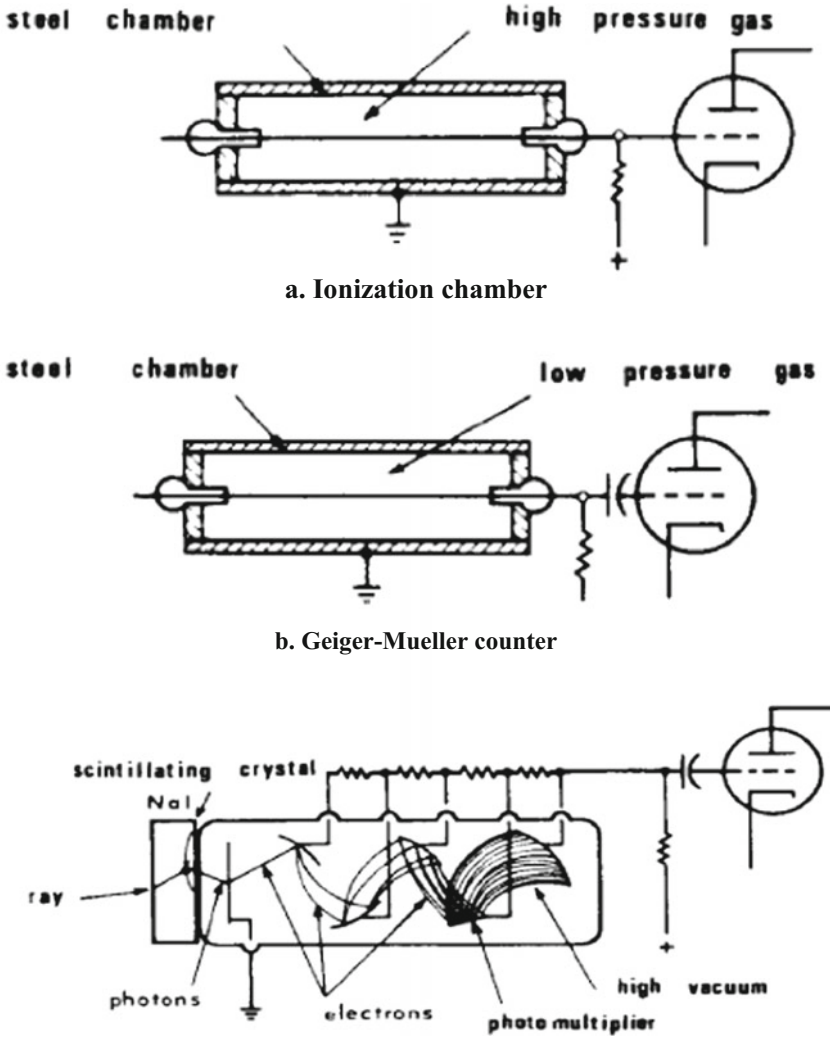

Fig. 4.12 The three types of gamma ray detectors and their principle of measurement

4.1.7.2 Other Applications

The gamma ray log is the most suitable log for prospection and exploration for deposits of uranium, thorium, potassium-containing resources, and other minerals exhibiting a higher level of radioactivity. As a glance at the Figure shows, the gamma ray log provides more precise values, compared with the drilling data. Occasionally, the gamma ray log is used to detect mineral resources with a

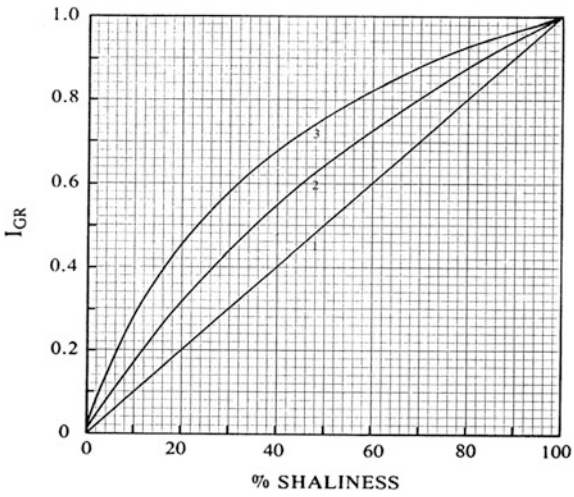

Fig. 4.13 Shale content versus gamma ray index (Courtesy of Dresser Atlas)

radioactivity level lower than in the surrounding beds. For example, coals usually display minimal intensities in the gamma log response. Lower amplitudes are also sometimes related to sulphites.

Sometimes, gamma ray log curves help to define lithology and to correlate sections.

This applies primarily to shaly varieties and coals in sedimentary rocks.

The gamma ray log is important in the prospection and exploration for hydrocarbon fields. In this application, it identifies shales and shaly formations surrounding hydrocarbon reservoirs and evaluates parameters correlated to the radioactivity level, primarily shaliness in terrigenous sections and insoluble residue content in carbonates. In certain instances, the gamma ray log indicates permeability.

The spectral gamma ray log measures the contents of uranium, thorium, and potassium in the formation separately. This information is of prime significance in the evaluation of equilibrium uranium–thorium ores; delineation and correlation of barren zones; prospection and exploration for deposits of bauxites, phosforites, rare earths, and gold, where uranium and thorium build up together with the major elements and act as geochemical indicators.

The spectral gamma ray log is important in the prospection and exploration for hydrocarbon occurrences. In this application, it evaluates the shaliness of polymictic sediments, identifies reservoirs composed of glauconite and other radioactive sandstones which could be confused in the integral gamma ray log as high-clay varieties, differentiates clay-containing carbonates from carbonates whose radioactivity level is due to bituminosity, establishes the mineral composition of clays, and quantifies the shale content and parameters of reservoirs whose reservoir properties are dictated by the type of shale and degree of shaliness.

4.2 Interaction Between Formation and Neutron

Besides the GR logs, neutron logging is another radioactivity logging method. The interaction between formation and neutron is the physical foundation for neutron logging, and its behavior depends on the energy when the neutron emitted from the source. The interaction, after the neutron entering into the formation, has four variable types with changing of the energy of neutron. These are fast inelastic scattering, fast neutron activating, fast elastic scattering, and thermal neutron diffusion and capture.

There are several types of fast neutron interaction, broadly classified as follows:

4.2.1 Fast Neutron Scattering

4.2.1.1 Inelastic Scattering

Some of the incident neutron energy imparted to the target nucleus excites it to a higher bound-state. The excited state lasts less than a microsecond, and the ensuing prompt return to ground-state results in the emission of radiation. Excitation half-life is 3.8×10^{-14}s, and a gamma ray of energy 4.44 meV is produced. In fact, this is the only emission peak observed from ^{12}C. Reaction: an important example is the neutron-induced alpha emission from ^{16}O, which results in the production of a ^{13}C isotope and the annihilation of the neutron. The ^{13}C nucleus may be already at ground-state, or it may be excited, in which case a gamma ray is promptly emitted at 3.09, 3.68 or 3.86 meV.

4.2.1.2 Activation of Atom

The target nucleus is transformed to an unstable intermediate isotope which decays with a relatively long half-life to the final nucleus. If this is in an excited state, a prompt emission of gamma radiation accompanies the return to ground-state.

The common elements currently detected by inelastic spectrometry include: carbon C; oxygen O; silicon Si; calcium Ca; iron Fe; sulfur S; (chlorine C1, an almost negligible yield).

4.2.1.3 Slowing-Down Phase

Following the fast neutron phase, the neutrons are rapidly slowed down by elastic collisions with nuclei. The energy lost at each encounter depends on the angle of incidence with, and the mass of, the target nucleus. Slowing-down length (L_s) is introduced to depict this procession, which is defined that length before the fast

neutron ultimately reaching thermal neutron with energy decreased from 2 to 0.025 meV. The mechanics of elastic collisions predict that the maximum energy will be lost when the target nucleus has a mass equal to that of the incident neutron. The decayed energy (ΔE) can be calculated by the following equation:

$$\Delta E = \frac{2A}{(A+1)^2} E_{n0} \tag{4.9}$$

where

ΔE the average energy loss of fast neutron;
A number of target nucleus
E_{n0} initial energy of fast neutron

The time of elastic scattering of fast neutron mainly depends on the number of target nucleus. The more nucleuses with little number are there in the mass, the shorter time of the elastic scattering time. As seen in the Table 4.1, hydrogen has the smallest nuclear number, hence it most strongly slow down the fast neutron. So the scattering time and slowing-down length depend on the content of hydrogen.

Thus it is that neutron slowdown is most strongly affected by hydrogen atoms (H), the single proton of the nucleus having very nearly the mass of a neutron. The average energy lost in collisions involving ^{12}C. For instance, is only 14 %, while for ^{16}O is 11 %.

The probability of a collision occurring with a particular element depends, obviously, on the number of its atoms present in a given volume of formation, i.e., the atomic concentration per cm. However, another parameter must be considered: the elastic interaction cross section. This is a characteristic of each type of atom. It has the dimensions of area and can be considered as the effective surface area presented by the nucleus to the oncoming neutron.

Since, at moderate porosities, hydrogen is relatively highly abundant, and its atoms are at least a factor of 10 more effective at slowing-down neutrons than the other common elements, it follows that the slowing-down phase is very dependent on the concentration of hydrogen or the hydrogen index (H_x). H_x is the ratio of the amount of Hydrogen atoms with that of same volume of water.

Neutrons continue to be slowed down until their mean kinetic energies are equal to the vibration energies of the atoms in thermal equilibrium. Thermal energy is 0.025 eV at 25 °C, corresponding to a mean velocity of 2200 m/s. There are only 18 collisions required for hydrogen to slow a neutron down from 2 meV to thermal

Table 4.1 Slowing-down length and diffusion length for clean sandstone

Porosity (%)	Slowing-down length (L_s, cm)	Diffusion length (L_d, cm)
3	17.8	13.1
11	13.7	8.5
23	11.5	6.6
34	10.5	4.2

energy, while other common elements require several hundred. The entire slowing-down phase requires of the order of 10–100 ms, depending on conditions.

4.2.2 Thermal Neutron Interaction

The important chlorine capture interaction is:

$$^{35}\mathrm{Cl} + \mathrm{n} \rightarrow ^{36}\mathrm{Cl} + \gamma$$

Its half-life is of the order of 10^{-20} s.

The neutron is absorbed, or captured, and the excited nucleus decays to ground-state with the emission of a gamma ray, in this case at 7.42 or 7.77 meV among others. Not all elements produce gamma rays, and some are outside the range of detection of the logging equipment. Common elements currently measured by capture spectrometry include: chlorine C1; hydrogen H; silicon Si; calcium Ca; iron Fe; and sulfur S.

Capture events generally occur at highest probability when neutrons reach thermal energy, and the term "thermal neutron capture" is used commonly for this class of interaction. The mean free path of 14-MeV neutrons down to thermal energy is, not surprisingly, larger than that of the fast neutron phase.

4.2.2.1 Diffusion

A cloud of thermal neutrons forms around the source. It is unevenly distributed in space because of the inhomogeneous nature of the borehole and formation. Collisions between the vibrating neutrons and nuclei continue and there is a general spreading or diffusion of the cloud outwards into the formation, where the concentration of thermal neutrons is low. Some diffusion of neutrons back towards the borehole may also occur.

4.2.2.2 Capture

Occasionally, during this diffusion phase, a nucleus will capture a neutron, resulting in its total absorption. The nucleus becomes momentarily excited and on returning to its ground-state, emits one or several gamma rays, or some other radiation. A number of common elements are compared in Table 4.2. In much the same way as for elastic interactions, each element has its thermal capture cross section (c in the Table). Note that, for capture, hydrogen is only moderately important, while chlorine ranks as the most effective of the common elements. Gadolinium, boron, and lithium occur infrequently as trace elements in formation water, and boron is often found in shales. Its proportion is related to the type of clay mineral and the

Table 4.2 Capture cross section and scattering cross section common elements

Element (atomic number)	Element	Average impact times (2–0.025 meV)	Micro capture cross section (b)	Micro scattering cross section (b)
1	H	18	0.3	20.0
6	C	115	0.0032	4.8
8	O	150	0.0002	4.1
14	Si	261	0.13	1.7
17	Cl	329	31.6	10.0
48	Cd	1028	2500	5.3

salinity of the depositional environment (Fertl 1973). The significance of their presence can be appreciated from Table 4.2.

4.2.2.3 Measurement Principles

Neutrons of energies between 4 and 6 meV are emitted continuously from a chemical source. The neutrons travel initially at some 10,000 km/s and have a high penetrating power. They interact both inelastically and elastically with atomic nuclei in the formation and the borehole surrounding the source. The life of these neutrons can be divided into four phases: fast, slowing down, diffusion, and capture.

Spatial Distribution of Thermal Neutrons and Capture Gamma Rays

Consider a point source of neutrons surrounded by an infinite homogeneous medium. High-energy neutrons are continuously emitted in all directions. The lifetime of these neutrons (from emission to capture) averages less than a millisecond in general.

A balance is rapidly established between the influx of "fresh" neutrons from the source and the absorption of thermal neutrons by capture, resulting in a spherical cloud of thermal neutrons whose spatial extent is primarily a function of the hydrogen concentration.

The thermal neutron density is constant over the surface of any sphere centered about the source, and decreases with distance from the source according to Fig. 4.14. Note that near to the source (the "short spacing" region) the thermal neutron density increases with hydrogen concentration, while farther out (the "long spacing" region) the opposite occurs. In the intermediate "cross-over" region there is almost no dependence on hydrogen concentration.

Since the number of gamma rays being emitted by capture is proportional to the number of thermal neutrons being captured, the preceding comments apply, with the difference that the gamma rays are able to penetrate further into the formation.

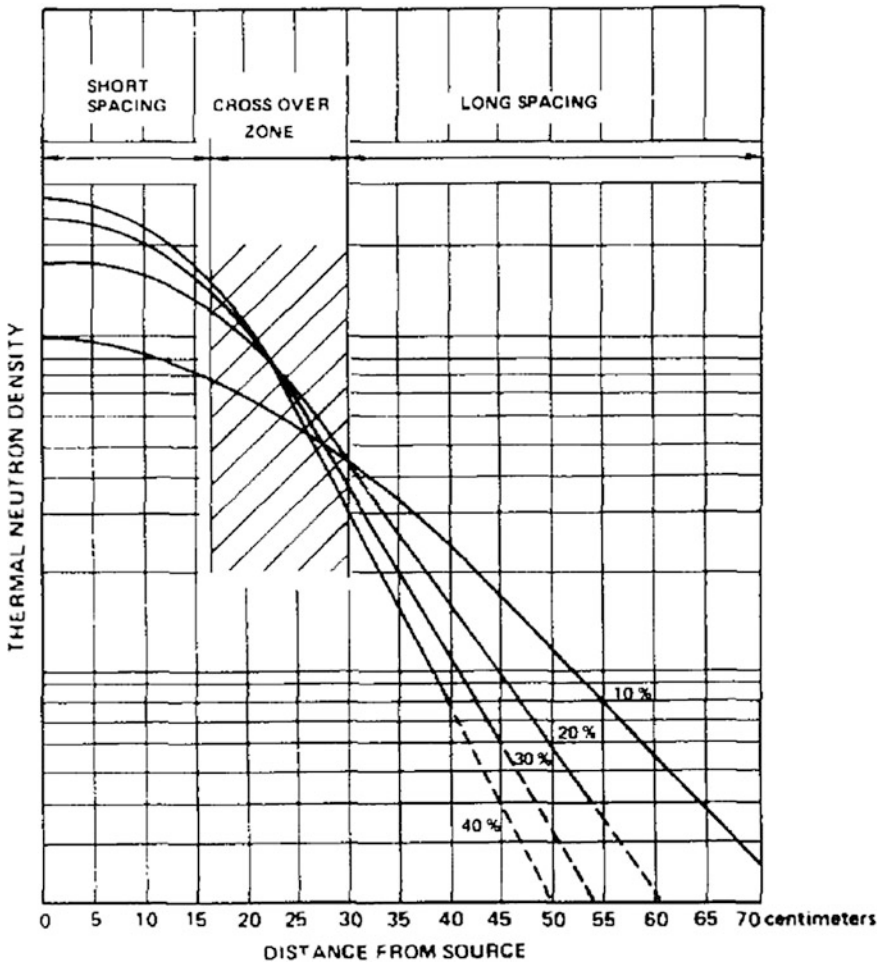

Fig. 4.14 Thermal neutron density with distance from a point source

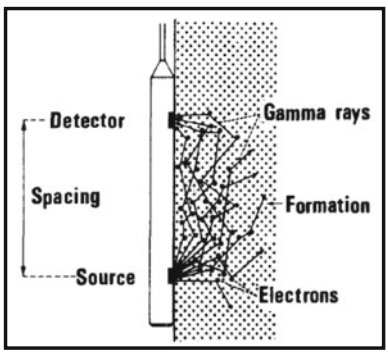

Fig. 4.15 Schematic of the one detector density tool

4.3 Basic Definitions for Neutron Logging

4.3.1 Bulk Density (ρ_b)

The bulk density, ρ_b, as we have learned in physics, is the mass gravity per cubic centimeter, sometimes this physical quantity is referred as mass density.

For normally encountered formations, it is generally between 2.65 and 2.87 g/cm^3, depending on the lithology. For values of fluid density, it is necessary to know the type of fluid in the pores. The fluid density for hydrocarbon ranges from 0.2 to 0.8 g/cm^3. Salt-saturated water (NaCl) density may be as high as 1.2 g/cm^3, and with the presence of $CaCl_2$, values even as great as 1.4 g/cm^3 may occur. It is fortunate that the uncertainty that can be tolerated in ρ_f is much greater than that for ρ_{ma}.

4.3.2 Electron Density (P_e)

The bulk density (p_b) of the formation is what we seek to determine. This is related to the electron density (p_e) by the following:

$$n_e = \frac{N_A \rho_b Z}{A} \tag{4.10}$$

where:

Z atomic number
A atomic mass
N Avogadro's number (6.02×10^{23}).

For the majority of elements and constituents of rocks (Z/A) is very close to 0.5 except for hydrogen for which it is almost 1.

$$(\rho_e)_i = \frac{2\rho_e}{N} \tag{4.11}$$

As the tool is calibrated in a freshwater-saturated limestone the apparent global density pa is linked to $(\rho_e)_i$ by the equation:

$$\rho_a = 1.07(\rho_e)_i - 0.1883 \tag{4.12}$$

For sand, limestones, and dolomites (liquid saturated), p_a, is practically equal to p_b. For some substances or for gas-filled formations corrections have to be made.

4.3.3 Photoelectric Absorption Index (P_e)

Though the photoelectric absorption cannot be easily described at the level of the electron, it has been found convenient, by analogy with the Compton effect, to define a parameter P_e the photoelectric absorption index, proportional to the "average cross section by electron", σ_e/Z:

$$P_e = \frac{1}{K}\frac{\sigma_e}{Z} \tag{4.13}$$

K is a constant coefficient characteristic of the energy E_γ, where the photoelectric absorption is observed.

The energy dependencies of σ_e and K cancel out and P_e is a parameter which does not depend on the energy. For the range of energies and minerals currently encountered P, is well approximated by:

$$P_e = \left(\frac{Z}{10}\right)^{3.6} \tag{4.14}$$

is expressed in barns/atom *. P_e is expressed in barns/electron.

4.3.4 Bulk Photoelectric Absorption Index (U)

Introducing $U = P_e p_e$, the volumetric photoeelectric absorption index:

$$\mathrm{U} = \sum_i V_i U_i \tag{4.15}$$

These equations can be generalized for a molecule with several atoms or for a mineral made of different components, i being the subscript of each individual atom or component.

4.3.5 Hydrogen Index (H_x)

The hydrogen index of a material is defined as the ratio of the concentration of hydrogen atoms per cm in the material, to that of pure water at 25 °C(75 °F). According to the definition, pure water therefore has an HI of 1.0. Although this concept is simple, the details arising from practical applications can become complicated.

Table 4.3 lists the hydrogen indices of a number of reservoir fluids and minerals. The HI of hydrocarbons covers the whole range from nearly zero (low pressure gases) to close to 1.0 (heavier oils), depending on molecular type, temperature and

Table 4.3 Hydrogen contents of some materials

Material	Experiment conditions	Number of hydrogen atoms per cm^3 ($\times 10^{23}$)	Hydrogen index
Water pure	60 °F, 14.7 psi	0.669	1
Water pure	200 °F, 7000 psi	0.667	1
Water salted	60 °F, 14.7 psi	0.614	0.92
Water salted	200 °F, 7000 psi	0.602	0.9
Methane CH_4	60 °F, 14.7 psi	0.001	0.0015
Methane CH_5	200 °F, 7000 psi	0.392	0.49
Ethane C_2H_6	60 °F, 14.7 psi	0.0015	0.0023
Ethane C_2H_7	200 °F, 7000 psi	0.493	0.74
Natural gas (mean)	60 °F, 14.7 psi	0.0011	0.0017
Natural gas (mean)	200 °F, 7000 psi	0.363	0.54
N-octane C_8H_{18}	60 °F, 14.7 psi	0.667	1
N-octane C_8H_{19}	200 °F, 7000 psi	0.639	0.96
N-nonane C_9H_{20}	60 °F, 14.7 psi	0.675	1.01
N-nonane C_9H_{21}	200 °F, 7000 psi	0.645	0.97
N-decane $C_{10}H_{22}$	60 °F, 14.7 psi	0.68	1.02
N-decane $C_{10}H_{23}$	200 °F, 7000 psi	0.653	0.98
N-undecane $C_{11}H_{24}$	60 °F, 14.7 psi	0.684	1.02
N-undecane $C_{11}H_{25}$	200 °F, 7000 psi	0.662	0.99
Coal, bituminous 0.84(C) 0.056(H)		0.442	0.66
Carnalite		0.419	0.63
Limonite		0.369	0.55
Ciment		0.334	0.50env.
Kernite		0.337	0.5
Gypsum		0.325	0.49
Kainite		0.309	0.46
Trona		0.284	0.42
Potash		0.282	0.42
Anthracite		0.268	0.4
Kaolinite		0.25	0.37
Chlorite		0.213	0.32
Kieserite		0.21	0.31
Serpentine		0.192	0.29
Nahcolite		0.158	0.24
Glauconite		0.127	0.19
Montmorillonite		0.115	0.17

(continued)

Table 4.3 (continued)

Material	Experiment conditions	Number of hydrogen atoms per cm^3 ($\times 10^{23}$)	Hydrogen index
Polyhalite		0.111	0.17
Muscovite		0.089	0.13
Illite		0.059	0.09
Biotite		0.041	0.06

pressure. The hydrogen content of most pure rock grains (quartz, calcite, etc.) being zero, their slowing-down power is weak, and it follows that the neutron log is a porosity measurement, provided the HI of the pore-fluid is equal to 1.0. We will see below how fluid characteristics and rock type must be taken into account, if we wish to estimate porosity in nonideal conditions.

4.4 Nuclear Logging

4.4.1 Borehole Compensated Density Tools

The first tools used only one detector. Although pushed against the borehole wall by a spring, the measurement suffered from the effects of mudcake, its type, thickness, and density. To eliminate mudcake effects service companies now offer two-detector systems in so-called compensated tools (Fig. 4.16). The corrections

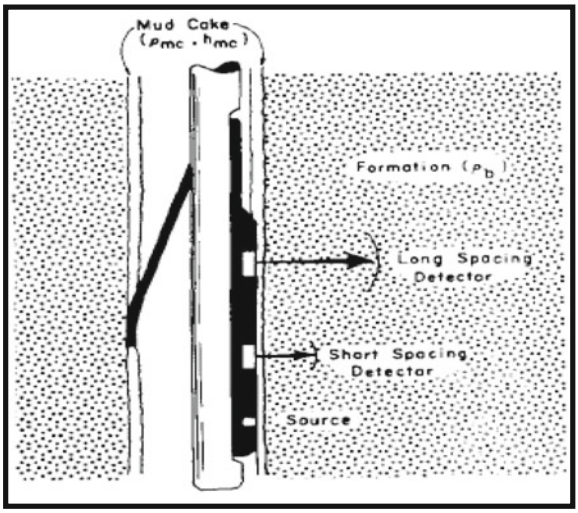

Fig. 4.16 Schematic of dual-spacing density log

are made within the surface equipment as a function of the readings from the two detectors (Fig. 4.15).

4.4.2 Litho-Density Tool

This measurement has been proposed by Schlumberger since 1977. This is a new generation of density tool which provides additional lithology information, through the measurement of the photoelectric cross section, and an improved density measurement.

4.4.3 Physical Principle of the Tool

As previously seen when the formation is submitted to a gamma ray flux, gamma photons interact with matter in different ways. Only two of them are of practical interest since the energy of the gamma rays given by the 137 Cesium source is 662 keV. These interactions are:

(a) Compton scattering of gamma rays by electrons.
(b) Photoelectric absorption of gamma rays by electrons.

The probability that a gamma ray is involved in one of these two reactions is measured by the characteristic cross section of the reaction. The cross section can be compared with the area of a target under the fire of a person shooting at random: the larger the target, the more often it is hit.

Qualitatively, the gamma ray spectra observed with a logging device equipped with a window nearly transparent to low-energy gamma rays (such as Be) is shown in Fig. 4.17. As the average atomic number, Z, of the formation increases, the lower energy portion of the spectrum is progressively reduced. Thus a measurement of this spectral shape at low GR energies should yield the photoelectric absorption properties, and thereby the Z of the formation.

4.4.4 Applications

The applications of formation density logging and lithology density logging can be concluded by the following aspects:

(a) The measurement of density is of interest itself in geophysical studies. It can help in interpretation of gravity measurements and by association with the speed of sound in formations of different density it permits an interpretation of seismic profiles passing by the wellbore.

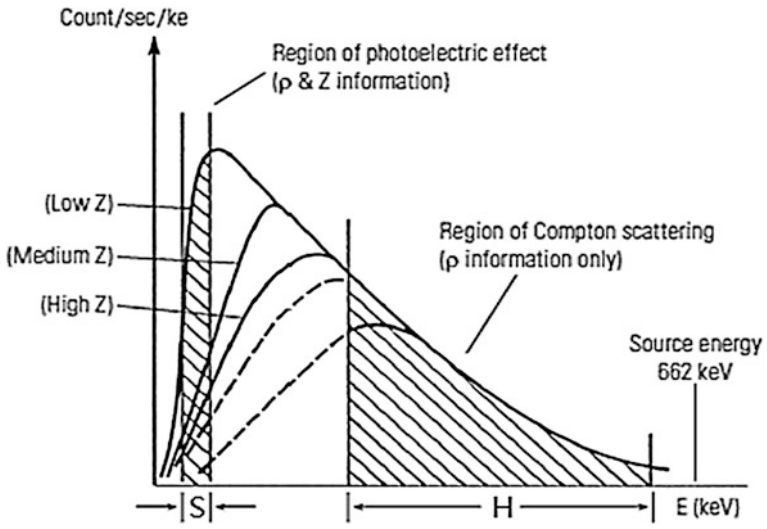

Fig. 4.17 A schematic representation of the detected spectral variation of gamma rays

(b) The porosity can be calculated directly if the density of the mineral component (matrix) and fluid are known, or, if not, by combination with the neutron log.
(c) The density provides a base log for the determination of mineral component either on its own in the case of nonporous formations or in combination with other logs, (LDT, CNL, NGS) for porous reservoirs.
(d) Comparison of density, neutron, and resistivity logs allows a fast and accurate identification of reservoir fluids and of gas–oil, gas–water, oil–water contacts.
(e) The density is used in the definition of electrofacies.
(f) Finally the density curve can be used for correlation of facies.

Porosity Determination

As shown in Fig. 4.17, the right track plots the density curve. The corrected bulk density of a formation can be converted to a porosity in the same manner as the sonic Δt. Just as before, the fluid density and matrix density must be known. With this information we solve for porosity.

$$\phi = \frac{\rho_{ma} - \rho_b}{\rho_{ma} - \rho_f} \tag{4.16}$$

Hence, as ρ_{ma} and ρ_f are known, Φ can be obtained directly from a measurement of ρ_b. Common values of ρ_{ma} are:

Shale = 2.55 g/cm^3
Sand = 2.65 g/cm^3
Limestones = 2.71 g/cm^3

Dolomites = 2.87 g/cm^3
Anhydrite = 2.92 g/cm^3.

When high salinity fluids are present in the pores, a fluid bulk density of ρ_f = 1.1 gm/cc may be required. A ρ_f of 1.0 gm/cc is appropriate where the fluid is very fresh. For flushed gas or oil reservoirs even lower ρ_f values should be assumed, depending on hydrocarbon density and residual saturation. If a ρ_f value is usually used for the entire log, porosities will be optimistic. In some applications, hydrocarbons are indicated by the presence of abnormally high log porosities.

It should be noted that if oil-based mud ($\rho_f > 1.0$) is used in drilling a well, porosities will appear optimistic in some beds if there is a lower fluid density in the invaded zone.

$\Delta\rho$ is proportional to the product of mudcake thickness, t_{mc}, and the density contrast between the mudcake, ρ_{mc}, and the formation density.

An example of the use of the $\Delta\rho$ curve as a quality control is shown in the log of Fig. 4.17 taken from the shaly sand portion of the simulated reservoir model. Portions of the $\Delta\rho$ curve are highlighted, as well as the corresponding smooth portions of the caliper. In these cases the $\Delta\rho$ curve shows negligible correction, which is probably indicative of little or no mudcake. In the very rough sections of the borehole, the value of $\Delta\rho$ is seen to be quite large, because of poor pad contact with the borehole wall (Fig. 4.18).

Shaly Formations

The density-to-porosity equation generally suffers from the same problems as the sonic equation. In shaly sands, either the ρ matrix must be changed to accommodate the mixture, or porosity must be adjusted for shale content.

For laminated shales:

$$\phi_e = \phi_D - (\phi_{sh} \times V_{sh})$$

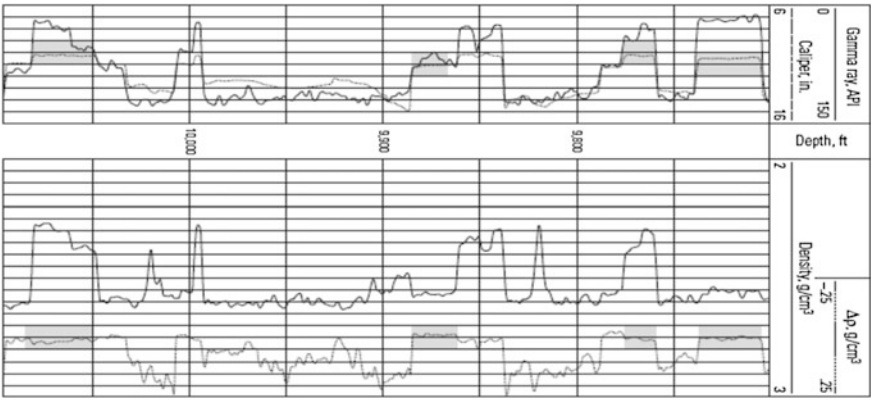

Fig. 4.18 A sample density log showing the qualitative nature of the $\Delta\rho$ curve for identifying smooth sections of borehole

where in nearby shale $\phi_{dsh} = \frac{\rho_{ma} - \rho_{sh}}{\rho_{ma} - \rho_f}$

For dispersed shales:

$$\phi_e = \phi_a - V_{sh}\phi_{sh}$$

As in all calculation procedures, the accuracy of the resulting values of Φ_e will be limited by the accuracy of the input variables (ρ_b, ρ_{ma}, ρ_f, ρ_{sh}, V_{sh}). In addition, Φ_e is affected in shaly zones by the way in which the shales are distributed. The effective porosity in a dispersed shaly formation will always be less than that in a laminated shaly formation with the same V_{sh} and Φ_a. This can be visualized very easily. In a laminated shaly sand with V_{sh} = 30 %, 70 % of the formation is filled with clean sand, having its original porosity, while 30 % of the formation is filled with shale. In a dispersed shaly sand with V_{sh} = 30 %, the entire formation is filled with sand containing intergranular volume Φ_a. However, most of this intergranular volume is filled with shale. If, for example, Φ_a = 30 %, all intergranular volume would be filled with shale, in which case Φ_e = 0 %.

Shale zones, unlike most formations, will expel water (and hence increase the density) as a function of increasing overburden pressure, time, and tectonic forces. Therefore, unlike limestone, sandstone, and other competent rocks, no one density (ρ_{sh}) can be attributed to shale. Shallow, recently deposited shales (actually clays) may have $\rho_{sh} < 1.8$ gm/cc, whereas very old shales which have undergone complete diagenesis and lithification can have $\rho_{sh} > 2.6$ gm/cc. Probably the best way to estimate ρ_{sh} for use in density log calculations is to take the ρ_b read from the log in 100 % shale formations near the zones of interest. The value of ρ_b becomes ρ_{shale}. This method of estimating ρ_{shale} will probably be more accurate in laminated shaly beds than in dispersed shaly beds, where ρ_{shale} is often hard to determine.

For structural shales:

$$\phi_e = \phi_a$$

This is simply due to the fact that structural shales are part of the matrix itself and occupy no pore space.

4.4.5 Fluid Effects

When residual hydrocarbon saturations are fairly high, calculated porosity values will be greater than the true porosity, and should be corrected for this effect. Specific values for the fluid density are often difficult to obtain. Corrected porosity values may be approximated with the following equations:

$$\text{For oil zones} : \phi = 0.9 \times \phi_a$$

$$\text{For gas zones} : \phi = 0.7 \times \phi_a$$

4.4.6 Schlumberger Neutron Tools

The earliest Schlumberger neutron logging tool was a neutron–gamma type called the GNAM, scaled in cps.

At present, four neutron porosity tools are widely available.

(a) GNT (Gamma-ray/Neutron Tool): a single detector tool which measures gamma rays of capture. Cadmium fins, part of the detector, smooth out salinity variations to some extent by capturing thermal neutrons, and converting them to gamma rays. The log is in API units.

(b) SNP (Sidewall Neutron Porosity Tool): measures epithermal neutrons. The source and single detector are mounted in a pad which is applied to the hole-wall (Fig. 4.19). The log is scaled directly in limestone porosity units, converted from the detector count rate (Fig. 4.20).

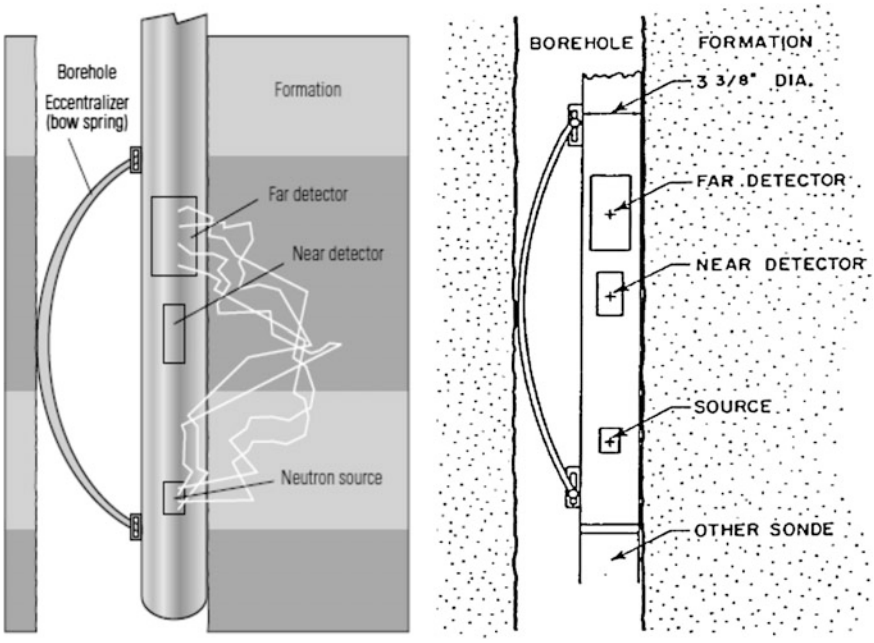

Fig. 4.19 A generic neutron logging tool

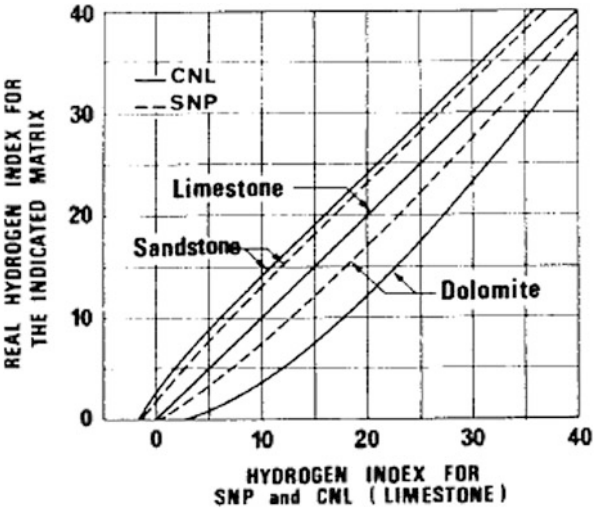

Fig. 4.20 The relationship between real and apparent (measured) hydrogen indices for three lithologies (Courtesy of Schlumberger)

(c) CNL (Compensated Neutron Log): The use of a dual-detector system reduces borehole effects. The tool is usually run eccentric as shown in Fig. 4.19. The CNL-A detects thermal neutrons. The ratio of the count rates at the near and far detectors is converted to porosity units by the surface equipment, according to the algorithms shown in Fig. 4.21 (the API test pit readings are also shown). The CNL-G consists of two dual-detector systems, measuring both thermal and epithermal neutrons. The epithermal measurement has the advantage of

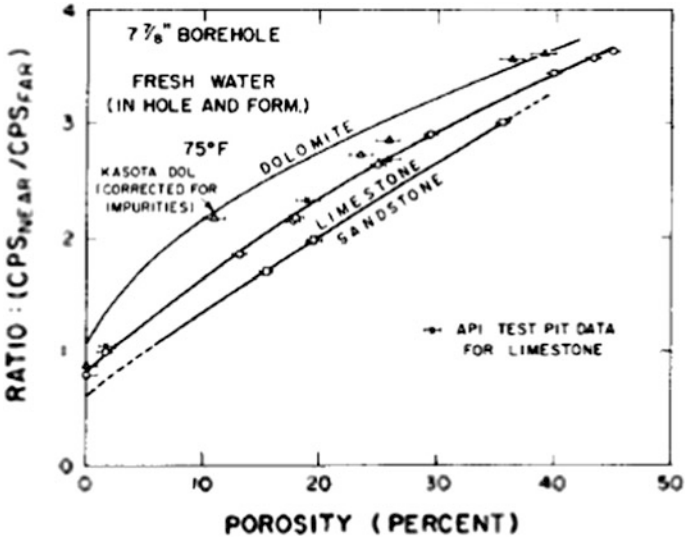

Fig. 4.21 Matrix characteristics of CNT-A

being insensitive to the presence of strong thermal neutron absorbers which perturb the thermal neutron response.

Typical Log Presentation

Figure 4.22 displays the "standard presentation." Perhaps it should be called a traditional presentation: with the computing and graphics capabilities within reach of most logging engineers and petrophysicists, there may no longer be a "standard." Why is the porosity curve, NPHI, labeled "sand," and why does the scale for NPHI seem to be presented backwards?

In Fig. 4.22, the neutron and density traces are found in track 3 in a compatible scale overlay. The particular scheme shown assumes that the lithology is expected to be predominantly sandstone. The idea behind the overlay is to adjust the gain and offset of the two traces so that they agree, or overlay, when the formation is water-filled sandstone. For this reason, the neutron curve is denoted "sand." It will be seen that there are two other common lithology outputs, "lime," and "dolomite." Presumably, when the tool measurement is presented in the selected units, the readings will agree with the porosity of the water-filled rock of the type selected.

Returning to the gain and offset, it has been traditional to present a dynamic range of 1 g/cm^3 on the density trace across the full track (or sometimes two tracks). It is easy to show that a change in bulk density of 1 g/cm^3 in a water-filled formation corresponds to a porosity change of about 60 units (p.u.). Consequently, the neutron trace is usually shown with a dynamic range of 60 units p.u. across the density track. The offset simply shifts the zero point on the neutron track to the density of the matrix; in this case of quartz sandstone, 2.65 g/cm^3. The density is also shifted so that the scale runs from 1.9 to 2.9 g/cm^3. In this scheme, the 0 p.u. point is two and a half divisions from the right hand of the track. The consequence of accommodating the 60 p.u. swing of the neutron makes it range from-15 p.u. on the right edge to 45 p.u on the left hand of the track.

The limestone compatible scale (which may be a standard, or may depend on locale) will be seen in another example. For that case, the density scale generally runs from 1.95 to 2.95 g/cm^3. The matrix density of limestone is 2.71 g/cm^3 so the neutron scale (but it is in limestone units—more about that later) remains at 45 to −15 p.u. for an approximate match at 0 p.u. Another scale, common in the Gulf of Mexico, where the apparent neutron porosity generally is high, has the neutron running from 60 to 0 p.u. and the density from 1.65 to 2.65 g/cm^3.

4.4.7 CNL Log as a Gas Locator

The sonic and density tools do not respond in the same way as the neutron tool in a gas zone. The sonic tool will have an apparent porosity greater than the effective porosity in a gas zone. The reason for this is the increased travel time caused by the gas. The density tool behaves in the same manner. The neutron tool is affected by the amount of hydrogen in the formation. Since gas is much less dense than either

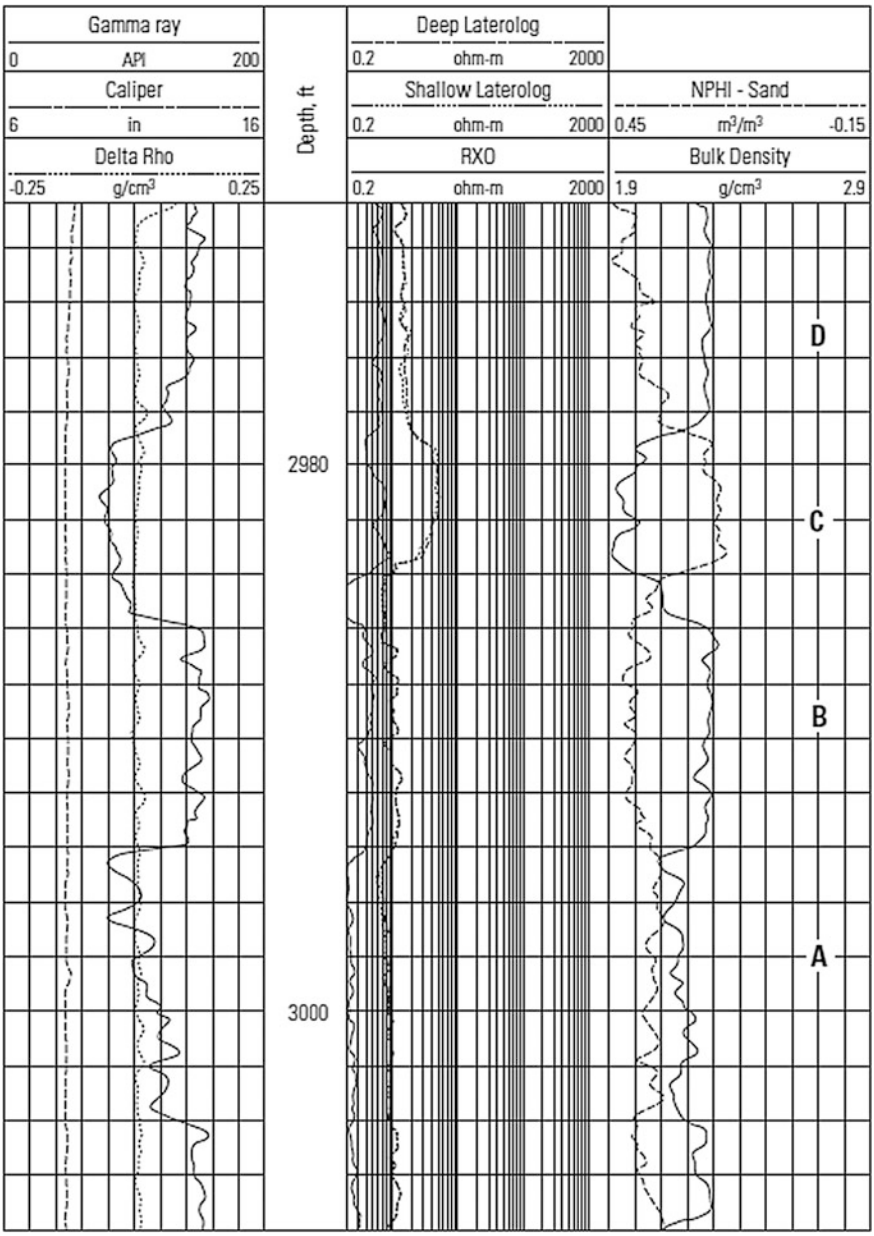

Fig. 4.22 A "typical" neutron-density presentation is shown in track 3. The neutron porosity, indicated to be in "sand" units, is scaled from 0.45 to −0.15 v/v, increasing to the *left*. The density scale is from 1.9 to 2.9 g/cm^3, increasing to the *right*

water or oil, it has fewer hydrogen atoms in a given volume. Because of this, the neutron tools tend to read too low of a porosity in a gas zone. When the neutron porosity and either sonic or density porosity are compared, any large differences in which the neutron porosity reads low and the sonic or density porosities read high, is an indication of gas (this separation is commonly known as the "football effect;" see Fig. 4.23).

This relation may not always hold true for the following reasons. The neutron tool tends to read shale as high in porosity. This will offset the effects of gas, which tends to lower the apparent porosity. A shaly gas zone could read as a clean water zone. Also, invasion may displace gas away from the borehole beyond the depth of investigation of the neutron tool. Thus, even if the zone contains gas, the neutron tool could read mostly filtrate.

Neutron-Density Patterns

The patterns made on Fig. 4.24 (left) represent the density–neutron curves on a sandstone matrix.

1. Shale
2. Shaly water sand
3. Shaly gas sand
4. Invaded low-porosity gas sand
5. Low-porosity gas sand with little or no invasion

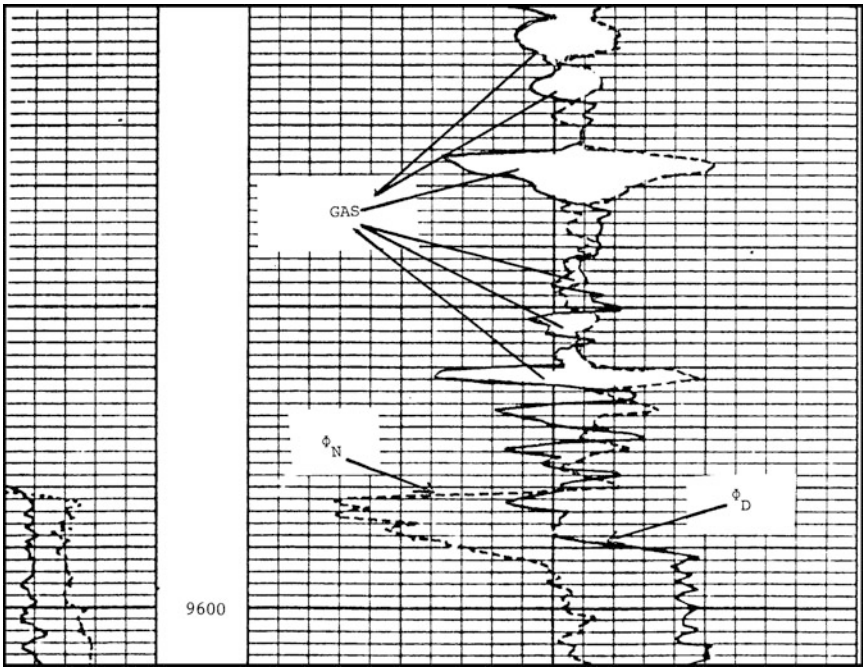

Fig. 4.23 The effect of gas on the DEN-CNL curves

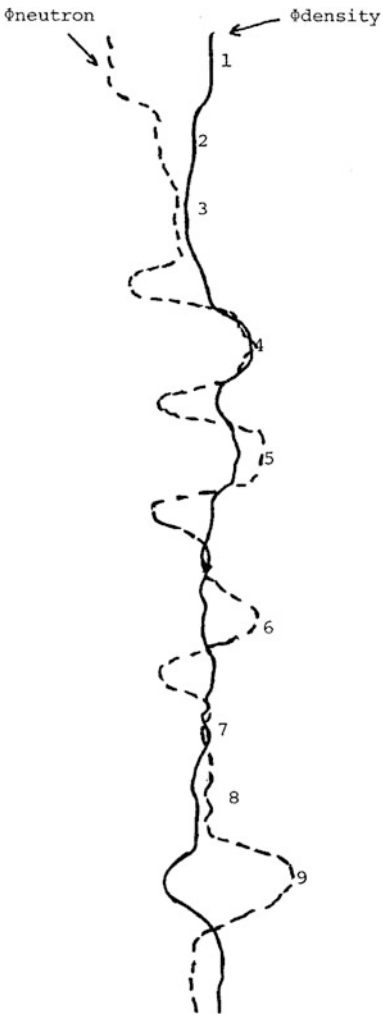

Fig. 4.24 Neutron-density patterns for sandstone (*left*) and limestone (*right*) matrix

6. Invaded high-porosity gas sand
7. Clean water sand
8. High-porosity oil sand
9. High-porosity gas sand.

The neutron-density pattern of Fig. 4.22 (right) was made using a matrix of limestone.

1. Lithology change
2. Gas effect in thin zone or possibly shale
3. Lithology/porosity change

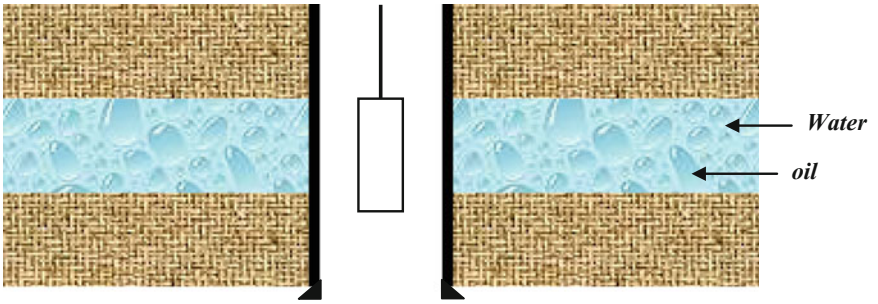

(a) with formation at residual oil log with PNC(Σ_{w1})

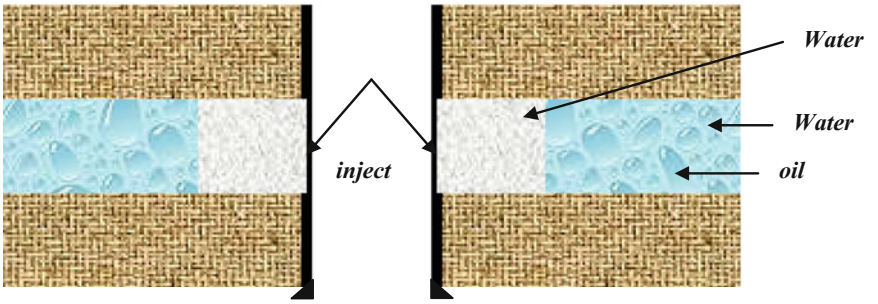

(b) inject a contrasting salinity water and log again(Σw1)

Fig. 4.25 Diagrammatic summary of PNC log-inject-log waterflood technique (open or cased hole)

4. Lithology change
5. Gas "football" effect
6. Water-saturated limestone with statistical variations on the curve.

4.5 Thermal Neutron Decay Time Logs

4.5.1 Introduction

The pulsed neutron capture (PNC) log has been found particularly desirable for measuring residual oil, since it can be used through casing. Because of the nature of the measurements, most of the effects of the borehole, casing and cement can be eliminated. Although it is a more complicated tool than the resistivity log, the PNC log is widely available commercially. Atlas, who developed this tool in 1963, called Neutron Lifetime Log (NLL), Schlumberger's version is known as the Thermal Neutron Decay Time Log (TDT).

The PNC tool employs a neutron generator that repeatedly emits pulses of high-energy neutron. After these neutrons are slowed down to the thermal state, they are captures by nuclei of the various atoms surrounding the tool. With each capture a corresponding emission of a gamma ray occurs, which can be detected a short distance from the source. The thermal decay time is primarily related inversely to the capture cross section of the surrounding nuclei. A smaller part of the decay is due to neutron diffusion or migration.

The total or bulk capture cross section (Σ) of the formation is sum of the component cross section of the rock (matrix) and the fluids (water and hydrocarbon) within the pores of the rock. This may be expressed as:

$$\Sigma = \Sigma_{ma}(1-\phi) + \Sigma_w S_w \phi + \Sigma_h (1-S_w)\phi$$

Σ is made from the apparent capture cross section read from the logging tool plus correction factors that account for neutron diffusion and borehole effects. The capture cross sections of the component fluids, water Σ_w and hydrocarbon (Σ_h), can be estimated from laboratory chemical analysis and published data or, preferably, by measuring the capture cross section directly in special cells. The difficulties of applying the proper corrections to arrive at Σ from the log reading, the uncertainty of the component variables, especially Σ_{ma}, precludes using this relationship for residual-oil measurements. A typical example indicated the uncertainty in residual-oil saturation is more than 10 % (0.10 fractional pore volume), to overcome the effect of these uncertainties, special logging procedures were developed.

4.5.2 Measurement Principle

A neutron generator in the TDT sonde repeatedly emits pulses of high-energy neutrons. Following each burst the neutrons are rapidly slowed down in the borehole and formation to thermal velocities. They are then captured by nuclei with a corresponding emission of gamma rays. Relative changes in the thermal neutron population in the media are sampled by gamma ray detectors placed at a short distance from the source. During the period of measurement the thermal neutron population decreases exponentially. This decrease is due to either neutron capture or neutron migration (diffusion).

At every point in the formation, a certain fraction of the thermal neutrons locally present is absorbed per unit time. This fraction is $v\Sigma$, where v is the neutron velocity and Σ is the macroscopic absorption (capture) cross section in the medium. Σ is the summation of the cross sections of all the individual atomic nuclei in a unit volume of formation for a mean thermal neutron velocity of 2200 m/s (corresponding to a temperature of 77 °F). For most chemical elements of interest in logging, Σ is inversely proportional to the neutron velocity. Thus, the quantity $v\Sigma$ is a constant which characterizes the formation. Since Σ varies inversely, and v varies directly with the square root of temperature, the quantity $v\Sigma$ is independent of temperature.

Consider, now, the thermal neutron density at a point in a formation. Let NO be the thermal neutron density after a delay time, t_0, following the neutron burst. Let to be long enough to permit the neutrons to reach thermal equilibrium. Then if neutron capture is the only process occurring, the neutron density, N, decays according to the equation:

$$N = N_0 e^{\frac{-t}{\tau_{\text{int}}}}$$

where t is the time measured from t_0. If capture were the only process by which neutrons disappear, the measured decay time would be equal to the intrinsic decay time, τ_{int}. The τ_{int} of a formation is related to its capture properties by:

$$\tau_{\text{int}} = \frac{4.545}{\Sigma}$$

However, neutron capture is not the only process occurring. The neutron diffusion effect is an important aspect in the actual measurement. In a homogeneous medium, the diffusion of neutrons arises from spatial variation in the neutron density. Therefore, the apparent decay time of the local neutron population contains both intrinsic decay time and diffusion time components. Without correction, the measured decay time is shortened below τ_{int}. This effect will be greater at low porosities. The methods used to handle the diffusion component will be covered under the tool sections.

Figure 4.26 shows schematically how the gamma ray count rate might typically vary with time after a fast neutron burst. At the extreme left, there is a rapid decay due to high absorption rates in the borehole fluid and casing. Next, there is a practically straight line position corresponding to the region of formation decay of the neutron density. Finally, at the right, the curve flattens out; the readings here correspond to induced radioactivity in the formation and the sonde.

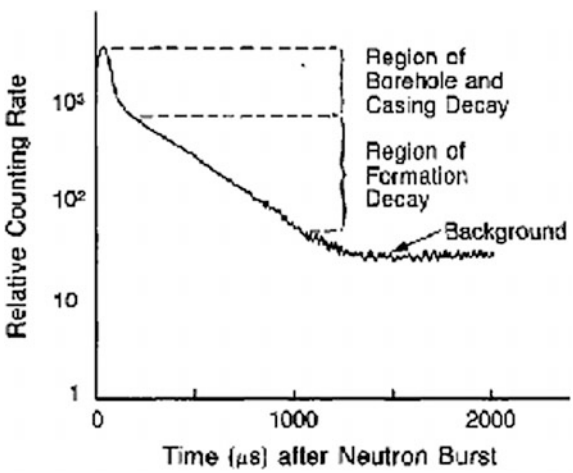

Fig. 4.26 Decay of capture gamma ray counting rate

4.5.3 Log-Inject-Log

One technique suggested by Richardson and Wyman in early 1971 is simple in concept; it allows the elimination of two variables, Σ_h, and the troublesome Σ_{ma} This technique has now been extensively field-tested. The procedure is to log with the natural formation water (Σ_{w1}),* to inject a contesting-salinity water (Σ_{w2}), and then to log again (Fig. 4.25). For this technique, the contrast in salinity should be as great as possible (Fig. 4.26).

There is no problem in determining directly from samples in a neutron absorption cell the capture cross section of the formation water Σ_{w1}, and the injected water Σ_{w2}. if the porosity can be obtained with reasonable accuracy from cores or from logging data, then good to excellent values of S_{or} can be determined.

There are two thermal decay time tools currently in use. The new Dual–Burst TDT* tool and the TDT-K tool which has been the industry standard for many years. Both tools have 11 % 6 in. diameters for through-tubing operations. The Dual–Burst TDT tool uses a diffusion model to analyze the decay of a burst of fast neutrons in the downhole environment. This method uses a better approximate solution to the neutron diffusion equation than the exponential decay model used by the TDT-K tool. The principle of operation for both tools will be covered later.

The Thermal Decay Time (TDT) log records the thermal neutron capture cross section of the formation by measuring the thermal neutrons' rate of decay. Because chlorine is by far the strongest neutron absorber of the common earth elements, the response of the TDT log is determined primarily by the chlorine present (as sodium chloride) in the formation water. Since the effects of water salinity, porosity, and shaliness on the thermal neutron decay rate are similar to those on resistivity logs, the TDT log resembles the usual openhole resistivity logs and is easily correlated with them. But the TDT differs in that it can be run in cased holes. Consequently, when formation water salinity permits, TDT logging provides the means to recognize the presence of hydrocarbons in formations which have been cased, and to detect changes in water saturation during the production life of the well. The TDT log is thus useful for the evaluation of old wells, for diagnosing production problems, and for monitoring reservoir performance.

As in the case of the resistivity log, the most important parameter values needed for quantitative interpretation are porosity and water salinity. Information is also required on shaliness, lithology, and the nature of the hydrocarbon. Modern openhole logging programs and crossplot techniques usually provide such information.

4.5.4 Log Presentation

An illustrative log from this tool is shown in Fig. 4.21. Some of the data provided for formation evaluation are:

Σ, which is the thermal neutron capture cross section. The measurement is derived from the count rates of the near detector:

$$\Sigma_{\log} = \frac{4.545}{T_{\mathrm{LOG}}}$$

a Ratio curve, which is computed from near (N) and far (F) count rates of the two detectors:

$$\mathrm{Ratio} = \frac{N_1 - \frac{N_3}{3}}{F_1 + F_2 - F_3}$$

The TDT-K ratio and Σ data can be used in charts such as those in Fig. 4.22 (***Tcor***-3, -4 or -5) to obtain an apparent porosity (ϕ_{K}) and an apparent water salinity. A count rate display, which is a recording of the counting rates, N_1 and F_2, from Gate 1 of near and far detectors.

N_1 and F_1 are uncorrected for background. The two curves are scaled to facilitate direct comparison. In some cases, as will be discussed, this display is useful for detecting gas.

4.6 C/O

The ability to measurement hydrocarbon directly in any salinity environment through casing, without the need for special injection schemes, has long been sought by the industry. The carbon/oxygen (C/O) log is a tool designed to meet these objectives by measuring relative amounts of certain elements such as carbon and oxygen. Since oil is composed largely of carbon, a measurement of this element provides a basis for direct evaluation of oil in a formation. Although the concept for such measurements has been known since 1950s, the tool has become commercially available only within the last few years. A prime use in the industry has been to detect oil in the presence of fresh water or water of unknown salinity behind casing.

The tool is similar to pulsed neutron capture tools in that it utilizes a pulsed 14 meV neutron source and a gamma ray detector. However, it is optimized for production of desired prompt gamma rays from inelastic scattering of neutrons by carbon in the formation. Energies characteristic of other elements are also measured. Because an observed change in the carbon/oxygen ratio can be caused by a change in oil saturation, or a change in lithology, a ratio of calcium/silicon (Ca/Si) is also recorded to help identify lithology changes such as a change in carbonate content.

For tools with an emphasis on the C/O measurement there have been two issues. First is that of detectors. In trying to separate the carbon and oxygen inelastic gamma rays it is necessary to have a detector with two distinct qualities. It needs to be of high spectroscopic quality and of good photoelectric efficiency. It must also

be able to register pulses arriving in close proximity to one another, implying a characteristic light-decay curve that is very short to permit the extremely high instantaneous counting rates which are typical during the neutron burst.

Regardless of the type of detection system or spectral processing technique there is a fundamental difficulty in processing the C/O ratios in the varied environments in which they are employed. Variables that affect the simple interpretation of the fan charts are the specific lithology, the porosity, and the borehole size, casing size, cement thickness, and borehole fluid.

One of the biggest concerns in the interpretation of C/O measurements is the contribution from oil in the borehole, in a producing well for instance. For this reason, one variety of tool, made in a slightly larger diameter than the usual $1^{11}/_{16}$ in. diameter, includes a second detector shielded from the formation to enhance its measurement of C/O in the borehole. By combining the apparent C/O from this shorter borehole focused detector with a longer spaced detector which sees the combination of the two it is possible to get information on the borehole oil holdup (the relative volume fraction of oil) and the formation water saturation.

An example of a C/O log in a borehole with oil in it is shown in Fig. 4.27. In the second track the C/O ratios for the two detectors are shown along with the oil holdup interpretation generated from a plot. Using the porosity information from the open hole logging shown in track 1, the interpreted oil saturation is displayed as oil and water volume in track 3. Using the measured Σ, shown in track 4, allows a further segregation of the "mixed water" volume of track 3 into connate water and injection water.

Another example is shown in Fig. 4.28, in the track 1, C/O and Si/Ca curves indicate the upper formation is water flooded.

Logging procedures are probably the most widely used of the various methods for obtaining reliable profiles of residual oil. However, the degree of accuracy usually required calls for special procedures that involve injection of fluids.

Why do we need to consider such a variety of logging techniques—why not just run the "best" one and forget the rest? Unfortunate y, there are trade offs that need to be considered. Basically, these trade offs involve complicated and extended field tests (which generally means more expense) in exchange for the ability to neglect some uncertain variables and hence obtain greater accuracy.

The most accurate logging method uses the Nuclear Magnetism Log (Chap. 8). This tool measures the residual oil directly, after deadening the water signals with paramagnetic ions. However, it must be run in open hole, as is the case with resistivity tools. Resistivity tools may have advantages because they can investigate deeper than the other tools.

In cased holes the most accurate technique is the waterflood log-inject-log procedure using the modified pulsed neutron capture tool. By injecting a contrasting-salinity water, uncertainties are eliminated in the capture cross section measurement of rock matrix and residual oil. Other schemes for using the pulsed neutron capture log which include removing all oil from the vicinity of the borehole have been proposed. Although they may have attractions such as eliminating the

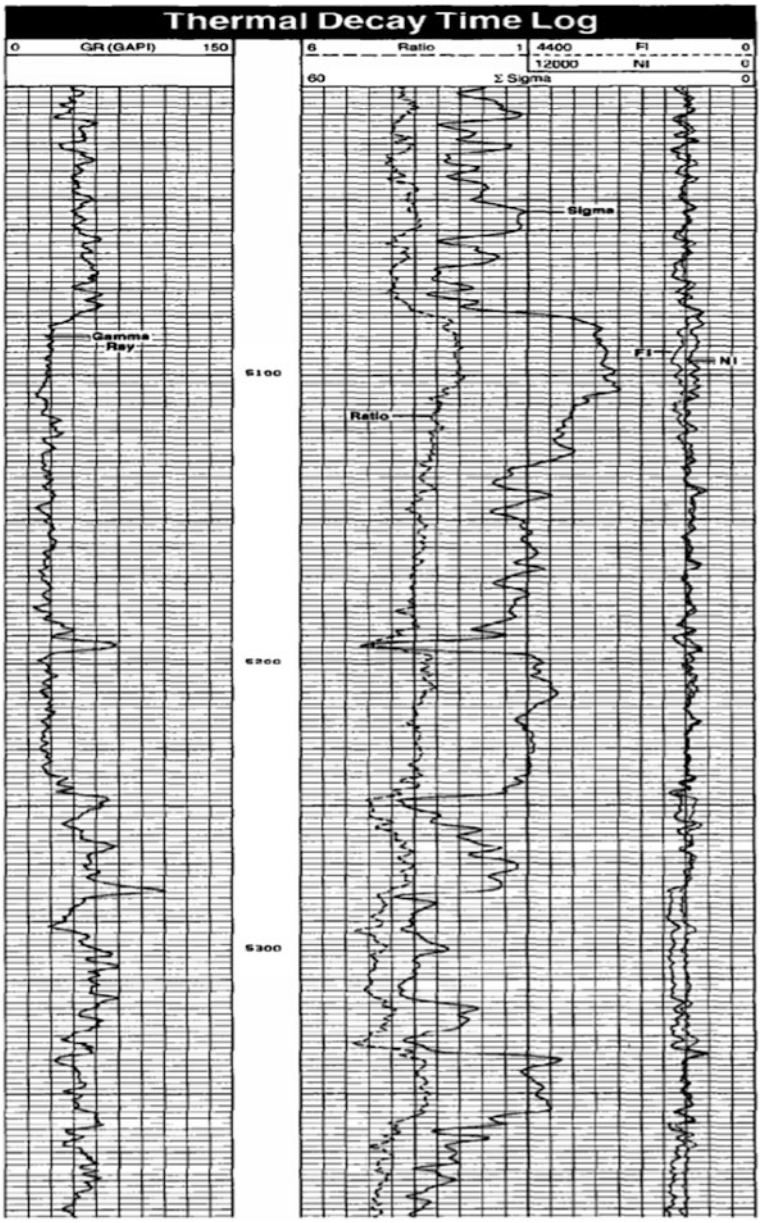

Fig. 4.27 A typical TDT-K log presentation

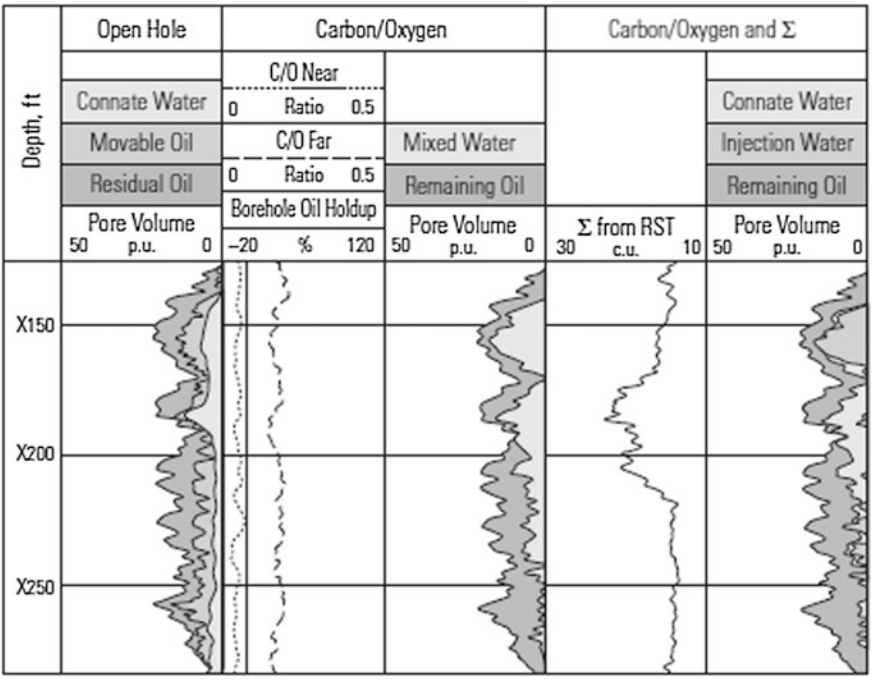

Fig. 4.28 Example of the use of a dual-detector PNG tool for interpreting the oil saturation (from C/O) and progress of water flooding by including C/O and open hole porosity

need to know porosity, they suffer from additional uncertainties in determining true capture cross section values.

Although the carbon/oxygen log can also measure oil saturations through casing, the present tools do not have the stability to achieve the precision that is required even when repeated measurements are made. Other techniques continue to be developed and are currently being tested.

Because the most accurate logging techniques require some form of water injection, special precautions must be taken so that injection procedures do not reduce the saturation of residual oil below that normally left by waterflood. Such precautions include maintaining a low rate of injection, avoiding the addition of chemicals that would alter the interracial tensions, and injecting no more than is needed to account for the radius of tool investigation plus the allowance for expected drift of the water within the formation.

All the accurate logging procedures require careful attention in planning, in execution, and in analysis of data. By giving the necessary attention, excellent profiles of residual-oil saturation can be achieved.

Problems

4.1 What is the characteristics of GR radioactivity of those common lithology?
4.2 Classify the interactions between GR with atoms of rock.
4.3 What are the applications of GR logs?
4.4 Explain the definition of bulk density ρ_b, Electron density pe, and photoelectric index P_e, Bulk photoelectric absorption index U, Hydrogen Index H_x.
4.5 Classify the interactions between the fast neutron with atoms of rock.
4.6 How to calculate the decayed energy ($\triangle E$) of neutron when they interact with atoms?
4.7 Describe the principle and applications of CNL and DEN logging.
4.8 What is the principle of thermal neutron decay time logs?
4.9 What is the principle and applications C/O logging?

Chapter 5
Nuclear Magnetic Resonance

In this chapter, the nuclear magnetic resonance phenomenon and its principle are first introduced, and then the applications, including determining the porosity, permeability, and how to discriminate fluid type by using NMR logging, which are important in this chapter.

5.1 Fundamental of Nuclear Magnetic Resonance (NMR)

In its simplest representation, one can consider the nucleus or proton as a tiny magnet with a north and a south pole like any magnet, which spins along its axis. As shown in Fig. 5.1, these tiny tissue magnets, which are called spins, are normally oriented randomly (Fig. 5.2a), but when brought close to a strong magnet they align parallel to or antiparallel to the direction of the external magnet field (Fig. 5.2b). The parallel orientation is slightly favored over the antiparallel, resulting in a small excess of spins along the parallel direction. These excess spins are the only ones that will eventually yield a signal that can be detected (Fig. 5.2c).

In 1938, Isidor Isaac Rabi (1898–1988), an American physicist, first detected magnetic resonance when he found a phenomenon where a nucleus absorbs electromagnetic radiation of a specific frequency in the presence of a strong magnetic field. Since then, magnetic resonance has been applied to the detection of light atoms, such as hydrogen in hydrocarbons.

In fact, the nuclei spin at a constant rate, they behave like spinning magnets (Fig. 5.3a), but their polarities are tanglesome. After the spin aligned to the direction of the external magnetic field (Fig. 5.3b), the nuclei with the spin axis exactly coincide with the line between the north and south poles. They interact with externally applied magnetic fields, they behave like a gyroscope, producing measurable signals. If the external magnetic field oscillates at exactly the natural frequency of the nuclei (i.e., hydrogen nuclei.), biggest signal will be produced and this frequency is called the Larmor frequency (λ_0). Obviously, if the frequency of

H. Liu, *Principles and Applications of Well Logging*, Springer Mineralogy,
DOI 10.1007/978-3-662-53383-3_5

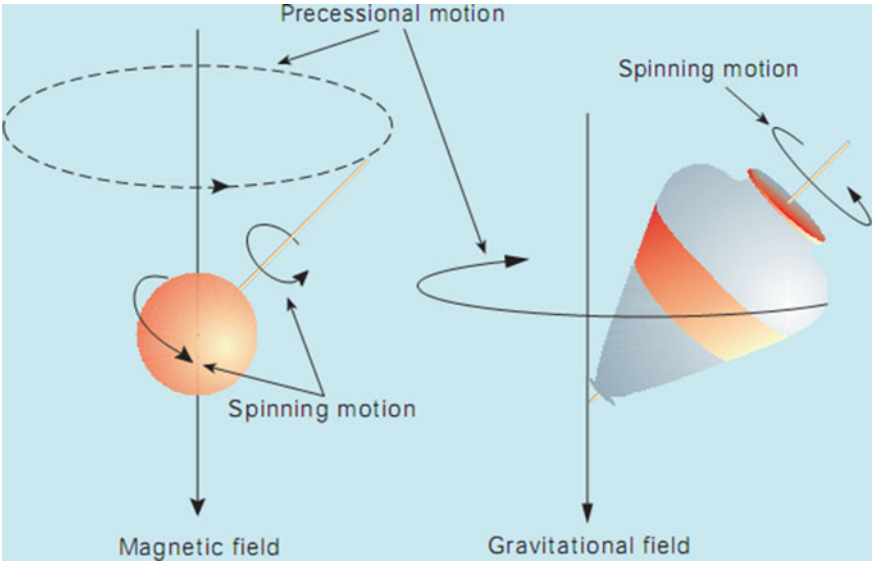

Fig. 5.1 Moment of nuclei in the magnetic and gravitational field

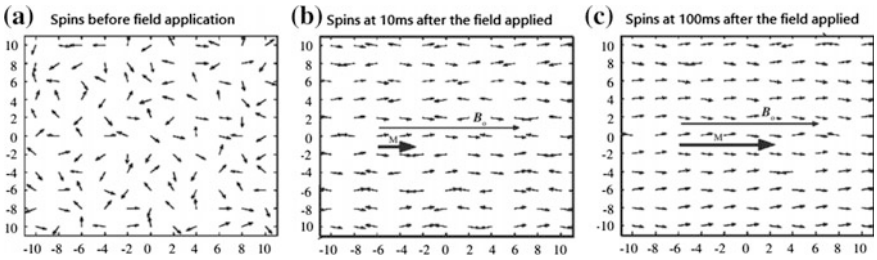

Fig. 5.2 **a** Spins are randomly oriented in the absence of an external magnetic field. **b** In the presence of an external magnetic field B_0, the spins align parallel or antiparallel to it. **c** The difference between the parallel minus the antiparallel spins represents the spins that will create detectable magnetic resonance signal

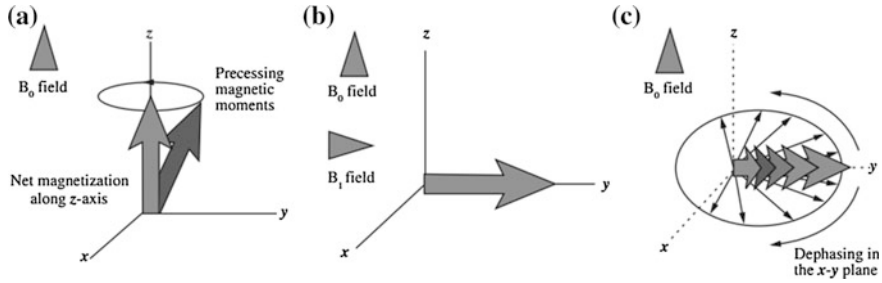

Fig. 5.3 Nuclear spinning and dephasing under the external magnetic field. **a** Precessing magnetic moments, **b** The atomic spin aligns to the external field direction. **c** Dephasing in the x–y plane after the external magnetic field turn off

the magnetic field does not match the natural frequency of the hydrogen nuclei they will not move.

Once the second magnetic field is turned off, as shown in Fig. 5.3c, the nuclei will lose its energy and relax, and slowly return to equilibrium state, in which the nuclei stop emitting radio waves, and the spins will line up with the first magnetic field. During the process, the relaxation time is a most important parameter. The time that nuclei relaxation takes for a system to return equilibrium can give us useful information.

For most elements the detected signals are small. The hydrogen nuclei, however, have a relatively large magnetic moment and are abundant in both water and hydrocarbon in the pore space of rock. By tuning NMR logging tools to the magnetic resonant frequency of hydrogen, the signal is maximized and can be measured.

5.1.1 Longitudinal Relaxation, T_1

The application of a magnetic field produces an induced magnetic moment in the sample which is proportional to the applied field strength B. The mechanism behind this induced magnetic moment is the redistribution of the protons between higher and lower energy states. But how quickly is this redistribution of states achieved?

To examine this process qualitatively, let us define n as the difference between the number of spins per unit volume in the up state with higher energy and those in the down state with lower energy:

$$N = N_{\text{up}} - N_{\text{down}} \tag{5.1}$$

We now assume some probabilities, P_+ and P_-, which give the probability per unit time that a nucleus will make an upward or downward transition. These two probabilities, yet undefined, can be shown to be unequal. If P is the absolute difference between the up and down probability, we can get the following equation:

$$\frac{\mathrm{d}n}{\mathrm{d}t} = \mathrm{P}_+ - P_- = -2P\left(N_{\text{up}} - N_{\text{down}}\right) = -2Pn \tag{5.2}$$

The solution of (5.2) is as follows:

$$n = n_0 \mathrm{e}^{-2Pt} + C = n_0 e^{-t/T_1} + C \tag{5.3}$$

where the time constant T_1 is referred to as the spin–lattice or longitudinal relaxation time.

T_1, the spin–lattice relaxation time characterizes the time taken by magnetic field to align the spins in the direction of the field, which can be computed from the imposed transition probabilities. However, in general, the parameter T_1 quantitatively

describes the observed rate of change of magnetization in a sample, which can only occur as the nuclei give up or absorb quanta of energy from the surroundings. This might result from fluctuating magnetic fields arising from protons in other molecules in thermal agitation. The surrounding molecules which can absorb or transmit this energy via a fluctuating magnetic field are collectively called the lattice, since the earliest workers in this field were solid state physicists. The value of the longitudinal or spin–lattice relaxation time, T_1, varies considerably with the type of nucleus and environment. To understand the measurement of T_1, it is useful to introduce the concept known as the rotating frame, and a technique of magnetic field pulsing for manipulating the polarized spins. The discussion will lead naturally to another important relaxation time constant known as T_2.

5.1.2 Transverse Relaxation, T_2, and Spin Dephasing

Now we come to another relaxation time of interest, T_2, which is called transversal or spin–spin relaxation time. T_2, the spin–spin relaxation time characterizes the time taken by the ordered spins in a magnetic field to become randomly oriented. T_2 is shorter than T_1.

T_2 time is related to the dephasing of the nuclear spins that are the result of local field inhomogeneity, among other things. The sources of this widely quoted relaxation mechanism are best examined by returning to the situation after the magnetic vector M has been rotated by 90°.

One source of this apparent decay comes from the behavior of the individual spins that contribute to the rotated vector M, they should all be rotating together at the Larmor frequency. However, for one reason or another, they do not rotate at exactly the same frequency. Thus in time they begin to noticeably get out of phase. In other words, as time goes by, the spins will acquire a different rotational angle (or phase) relative to each other because of their slightly different rotational speeds (or frequencies). This is called dephasing, and it is the result of increasing randomness (or increasing entropy). In doing so, the magnitude of the vector M will decrease with time. Alteration of the spin precession frequency can come from the mutual interaction (spin–spin) of the proton spins, or local field inhomogeneities. The apparent decay time will be composed, in part, of the spin–spin interactions (T_2), as well as a component due to local field inhomogeneities.

5.1.3 Spin Echoes

Once the proton spins have been tipped into the transverse plane (perpendicular to the polarizing field Bo), they precess at the Larmor frequency, but they are seen to dephase with time. This is the situation depicted in panels (a) and (b) of Fig. 5.4. To make a measurement of T_2 that reflects the spin relaxation rate caused by the spin–

spin interactions of the protons arising from other fluid molecules or molecules at the pore surfaces, it is necessary to remove from the measurement any reversible dephasing. The type of reversible dephasing described earlier was directed to spatial inhomogeneities in the polarizing field B_o. For this purpose, a number of pulsing sequences have been developed. By applying another pulse of about twice the duration of the 90° flipping pulse, the entire arrangement of proton spins can be flipped around their position on the transverse plane so that now the slower precessing protons will lead, and the faster ones will follow. This concept is illustrated in panels (c) and (d) of Fig. 5.4.

In time the spins, in their precession around the polarizing field B_o, will coincide (before smearing apart again) to create a local maximum of coherent magnetic field called a "spin echo." After the smearing out has occurred, at a time T_e after the last pulse, another flipping pulse can be applied starting the process over again. The procedure can be repeated many times if the echo spacing, T_e, is small compared to the T_2 of the sample. The appearance of the detected wave train is shown in Fig. 5.5. This pulse sequence is referred to as the CPMG pulse train after its inventors Carr and Purcell, and Meiboom and Gill.

As can be seen from the figure the echo amplitudes decrease with time because there are sources of relaxation that are not reversible, like the random interactions with the spins of other molecules in the fluid or nearby surfaces. The spin echo

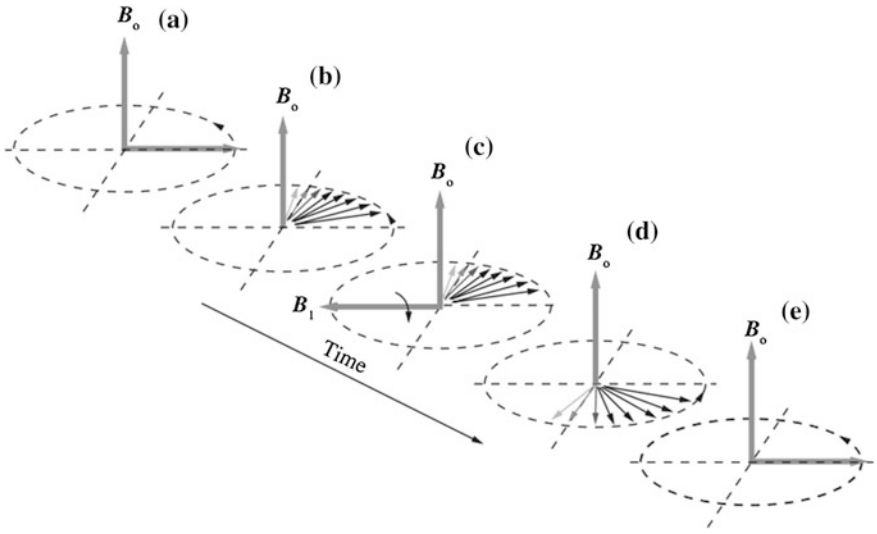

Fig. 5.4 A visualization of the Carr–Purcell pulsing scheme to defeat reversible dephasing of the protons in a slightly inhomogeneous field. In panels (**a**) and (**b**), the spins begin to dephase. In panel (**c**), a field is applied of sufficient magnitude and duration to rotate (precess) the fanned-out spins by 180° ← so that they appear in reverse order in the longitudinal plane. In frame (**e**) the spins have rotated to produce a local maximum, since the fastest have caught up with the slowest. It is this configuration of spins that produces the "pulse-echo." Courtesy of Schlumberger

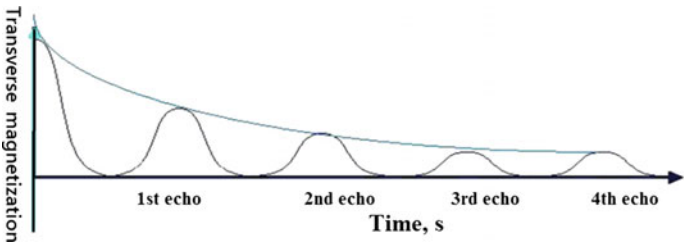

Fig. 5.5 Irreversible dephasing (T_2) described by the CPMG echo-train

technique just takes care of small magnetic field inhomogeneities. It is the time constants associated with the decreasing echo amplitudes that will reveal a wealth of information regarding the pore geometry and its contents.

The signal loss over time that is seen in the echo waves is dependent on T_2 relaxation, and it follows an exponential decay:

$$M(t) = M_0(1 - e^{-\frac{t}{T_2}}) \tag{5.4}$$

Equation 5.4 states that the magnetization observed at time zero ($M_{X\ Y}(t = 0)$) on the transverse plane will decay exponentially according to the elapsed time t and a time constant T_2 (Fig. 5.5).

5.1.4 Relaxation and Diffusion in Magnetic Gradients

Now we take a moment to explore the ramifications of, not the random inhomogeneities of the polarizing field but the presence, deliberate, or otherwise, of a strong spatial gradient in the polarizing field. To facilitate discussion the sample is considered to be a bulk liquid. If there is a magnetic field gradient in the sample volume, then after the 90° flip of the CPMG pulse sequence, some of the protons will migrate to some new position where a slightly different magnetic field is present and their frequency will shift slightly, in proportion to their displacement. To keep the random field effects in check, the CPMG sequence was developed to flip the magnetization vector and produce the spin "echoes," as shown in Fig. 5.6. However, for particles that have been displaced by diffusion to a new field value, their Larmor frequency will change and as time progresses, the smearing, despite the 180° flips, will continue to grow, reducing the number of available spins for a coherent signal. This is an instance of a nonreversible relaxation and it will add to the so-called T_2 decay rate, decreasing the amplitude of the magnetization in the transverse plane:

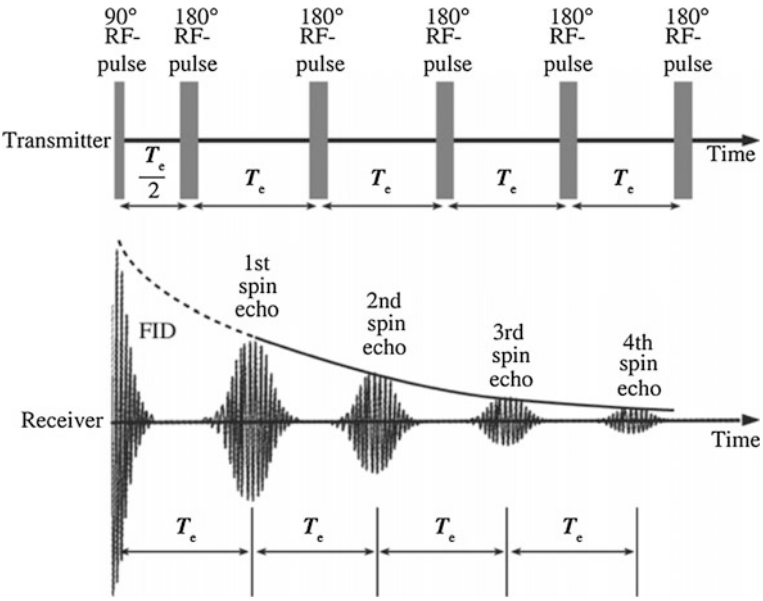

Fig. 5.6 A representation of the sequence of operation of a logging tool utilizing the CPMG sequence. The first pulse, in the top frame, rotates the spins to the transverse plane, where they are seen to decrease in magnitude in the free induction decay mode. Then, in the *upper panel*, a pulse is emitted to flip the spins by 180° that is shortly followed by a build-up and decay, in the *lower panel*, of the spins in the "echo." The application of the 180° ← pulse is then repeated at regular intervals for up to thousands of times. The maxima of the spin echo amplitudes decays with the time constant T_2. Courtesy of Schlumberger

$$\frac{1}{T_2} = \frac{1}{T_{2B}} + \frac{1}{T_{2D}} \tag{5.5}$$

where $1/T_{2B}$ is the decay rate associated with the bulk fluid and $1/T_{2D}$ is the decay rate associated with the magnetic field gradient. As shown in the Appendix, this additional decay rate is proportional to the square of the gyromagnetic ratio (γ) and the gradient (G) and the product of the diffusion coefficient (D) and the square of the time T_e (known as the echo spacing) between the 180° CPMG pulses. We will see later how this effect can be exploited to measure the coefficient of diffusion, which might be related to the viscosity of the fluid, and how its time evolution can be used to learn more about the geometric shape of the pore structure.

5.2 A Brief History of Nuclear Magnetic Resonance Tool

NMR was first discovered in 1946 independently by two different research groups, and it took only a little bit more than a decade to build the first NMR wireline logging tool. Nuclear Magnetic Resonance (NMR) was first investigated as a petrophysics tool by Turk Timur, at Chevron research, in 1954. The first truly commercial NMR tool, NMT-CA, was introduced in 1978; followed by NMT-CB, an updated version, almost a decade later. But because of its limitations, the tool never caught on. The invitation of MRIL-B, which marks the beginning of modern pulsed NMR logging until 1992, and then followed by MRIL-C, the first multi-frequency NMR logging tool; later by CMR (Combined Magnetic Resonance), the first truly combinable NMR logging tool. Overall, the progress in wireline logging technology has been dazzling: the latest generation wireline logging tools, such as MRIL-Prime, MRX (Magnetic Resonance eXpert) and MREX, are all capable of making very complex measurements designed for advanced applications. Nor has LWD NMR been left out of this rapid technology development. MRIL-WD, the first LWD NMR logging tool, was introduced into service in 2001; only a decade after the MRIL-B. Such a short development time, from wireline to LWD, is truly remarkable by historical standards, considering the typical lag time of the LWD implementations of other wireline measurements. With the introduction of ProVision in 2003, and MagTrak in 2005, all major service companies now offer LWD NMR logging services in the range of 8.5–10.5 in. borehole sizes.

5.3 LWD NMR

NMR has been taken into the industry service less than a decade, after the introduction of modern pulsed NMR wireline tools, to offer commercial LWD NMR services. This is a very short time by historical standards, and the short lag is even more impressive, considering the technical challenges associated with making a very sensitive measurement in the harsh drilling environment. One of the main challenges in LWD NMR is dealing with tool motion (mostly lateral, rather than vertical), especially during a measurement. The motion problem can be dealt in several ways, as evidenced by the innovative but different approaches adopted by the service companies.

A very effective solution is to use T_1 logging, instead of T_2. There are additional LWD-specific advantages associated with T_1 logging, involving downhole power, battery life, and data size. A more straight forward approach involves the application of motion corrections to T_2 data, by making additional motion-related measurements. The third technique is based on making T_2 measurements in a very low-gradient magnetic field. Two of the methods meet the conditions and the method satisfies the requirement in most cases. First of all, logging speed is much less of an issue in LWD NMR. In most cases, the drilling rates do not surpass the

maximum logging speeds specified by the manufacturers. Indeed, the drilling rates are slow enough to allow more frequent sampling of the formation properties, usually in excess of the industry standard sampling rate of two data points per foot. Naturally, with denser sampling comes higher SNR with good vertical resolution, an indirect, but critical improvement.

Making NMR measurements while drilling presents additional challenges related to the motion of the drill string during this not so gentle procedure. Although development of LWD versions of the tool began in the early 1990s, it was nearly a decade before commercial services were offered.

The design of one of these instruments (see Fig. 5.7) shows the symmetric device containing opposing dipole magnets. These long magnets produce a resonant zone that resembles a shell about 6 in. long with a diameter of 14 in. which means that it extends nearly 3 in. away from the tool surface. One of the tools can measure both T_1 and T_2, simultaneously or separately, but as usual, the statistical repeatability of the T_2 is greatest. Its generally faster decay allows many replicate measurements to be made in the time interval necessary to make a single determination of the decay time of the lengthier T_1 distribution. For the real-time application, the data must be transmitted by the mud-pulse telemetry so the raw measurements must

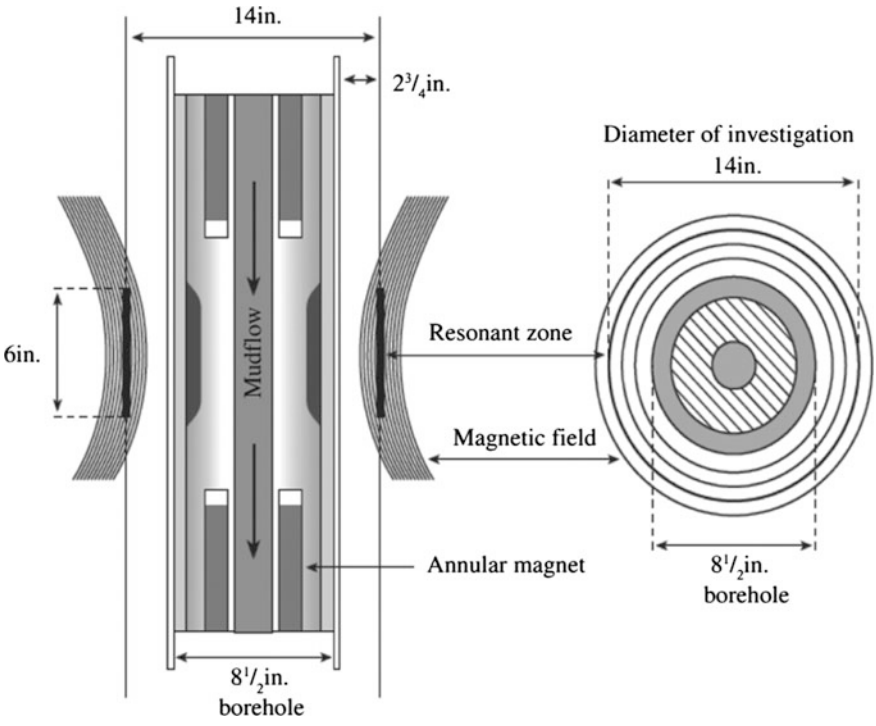

Fig. 5.7 Cross section of an LWD NMR device. This centered tool utilizes a pair of annular magnets to establish a gradient field with a nominal measurement diameter of 14 in.

be processed downhole by appropriate algorithms. Only a few important petrophysical measurements such as the total porosity, and bound fluid porosity, and the logarithmic mean of the T_2 distribution are sent to surface.

5.4 Applications of Nuclear Magnetic Resonance

For hydrogen nuclei, there are a number of factors that affect the relaxation time including the fluid molecules bumping into each other and into solids, because the relaxation time is related to the size of the pores. Larger pores mean more permeability and increased oil flow. Relaxation times depended on pore size. For example, small pores shorten relaxation time, and the shortest relaxation time corresponds to the clay-bound and capillary-bound water. In contrast, large pores allow long relaxation times and contain the most producible fluid. Therefore the distribution of relaxation times is a measure of the distribution of pore sizes. So, the important measure is to detect the distribution. NMR signal, which is proportional to the number of hydrogen nuclei present, and the energy decay responds to the relaxation time.

Usually, two relaxation times and their distributions can be measured during an NMR experiment, which are longitudinal relaxation time T_1, and transverse relaxation time T_2. Laboratory often measure T_1 and, T_2 distribution, while borehole instruments make the faster measurements of transverse relaxation time T_2. The distribution of T_2 time spectrum shows a good correspondence to the different existence of hydrogen atoms. Generally, for the bounded hydrogen atom, it shows a short T_2 relaxation time, and for the freedom one, it shows a relatively long T_2 relaxation time. Producible fluids have the much longer relaxation time, which are shown in (Fig. 5.8).

Comparing with conventional logging, NMR has solved many challenging petrophysical problems. The development of NMR well-logging technology has been motivated by the unique set of answers that NMR can provide. In particular the benefits include:

(1) Lithology-independent porosity measurement. NMR tool can give total porosity independent of lithology since it responses only to hydrogen in the fluids. The neuron log, unlike NMR, responses to all hydrogen in the formation including those in the pore and matrix. Another advantage of NMR is there is no need for environment corrections.
(2) Continuous producibility/permeability estimates. Based on the NMR logging data, permeability can be estimated qualitatively, if not quantitatively, while not anyone of the conventional logging methods do.
(3) NMR logs can directly provide bound fluid information, whereas most of conventional logs cannot.
(4) Viscosity. The NMR logging data response to viscosity, hence, it can give knowledge of the parameter, which is very important for the producibility.

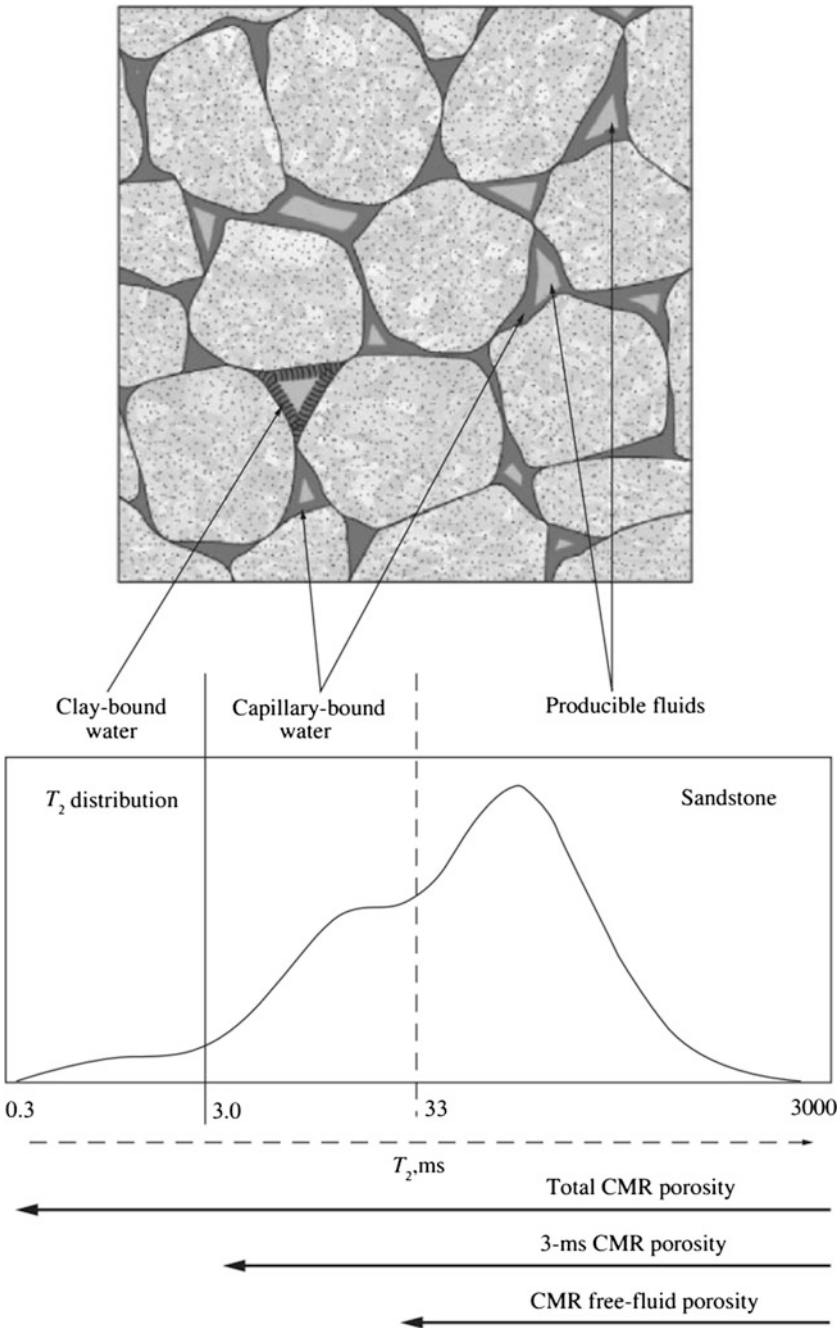

Fig. 5.8 T_2 relaxation time distribution. Courtesy of Schlumberger

In addition, the T_2 distribution has several petrophysical applications:

(1) T_2 distribution mimics pore size distribution in water-saturated rocks
(2) the area under the distribution curve equals total porosity
(3) permeability is estimated from logarithmic mean T_2 and porosity
(4) empirically derived cutoffs separate the T_2 distribution into areas equal to free fluid porosity and irreducible water porosity.

In porous media, T_2 relaxation time is proportional to pore sizes (Fig. 5.9). At any depth in the well, the NMR tool probes a rock sample that has a range of pore sizes. The T_2 decay is the sum of T_2 signals from hydrogen protons, in many individual pores, relaxing independently. The T_2 distribution graphically shows the volume of the pore fluid associated with each value of T_2, and therefore the volume associated with each pore.

Free fluid porosity is determined by setting a "Cutoff Time" value to the T_2 distribution curve. This value must be measured in laboratory from a large number of water-saturated core samples. For most of clean sandstone, the T_2 cutoff time equal 33 ms, as shown in Fig. 5.10. NMR logging curves are shown in Fig. 5.12, based on the T_2 data, we can learn about the pore sizes and the permeability of the formation.

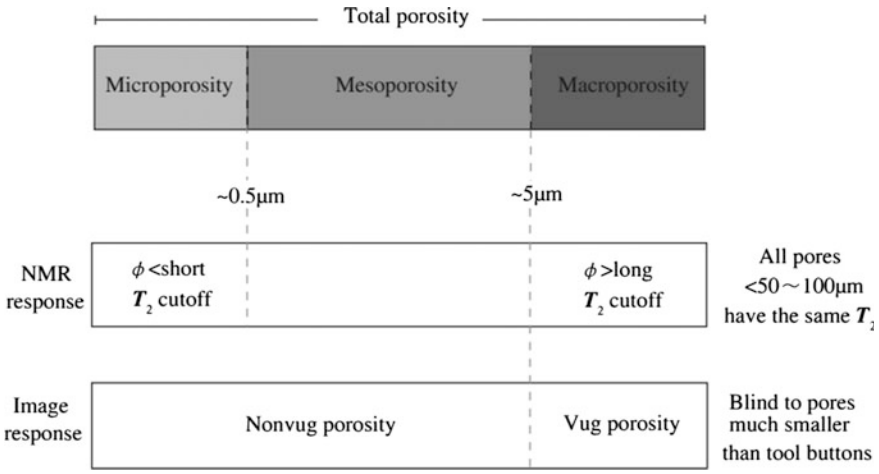

Fig. 5.9 The proportions of different pore type within the total porosity (From www.slb.com/carbonates)

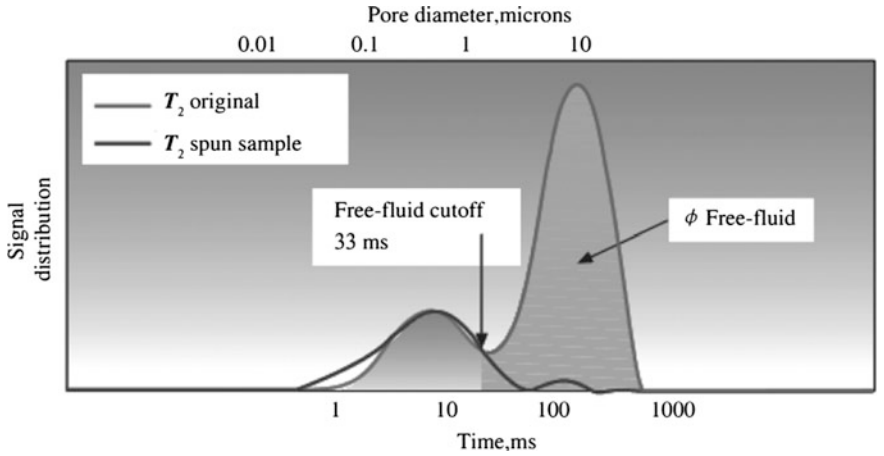

Fig. 5.10 T_2 cutoff time and its distribution (From www.slb.com/carbonates)

5.4.1 Porosity and Free Fluid Porosity

One of the claims for using NMR is to obtain a lithology-independent porosity. However, this minimizes the complications from having to know, accurately, the HI of the pore fluids and underemphasizes the ability of NMR to determine the irreducible water saturation. The irreducible water saturation, intimately related to the so-called water-cut, helps to establish the production potential of a zone: whether it will flow hydrocarbons, or a mixture of hydrocarbons and water, or just water. This most valued petrophysical parameter is the result of a rather remarkable finding made by Straley that the T_2 distributions can be used to determine an estimate of producible porosity in the manner done earlier for T_1. The technique is based on the principle that producible fluids reside in larger.

Pores with longer T_2 times, and the capillary and clay-bound fluids are associated with the smaller pores and thus shorter T_2 values. Integrating a properly normalized or calibrated T_2 distribution gives total porosity. To obtain the bound fluid volume, a cutoff value of T_2 was determined by finding the lower limit of the integration of the normalized distribution to match the fractional volume of fluid obtained by centrifuging the sample at a 100 psi air-brine equivalent capillary pressure. Figure 5.11 shows the measured T_2 distribution fully saturated and again after desaturation by centrifuging. From this graph a cutoff of 33 ms was established. It is remarkable how well this value seems to work for clastic reservoirs around the world. In a similar set of measurements, it was established that clay-bound water corresponded to T_2 values less than about 3 μs. A summary of the situation for the interpretation of water-wet clastics is shown in Fig. 5.11. These considerations then provided the basis for the most typical NMR logging presentation, an example of which can be seen in Fig. 5.11.

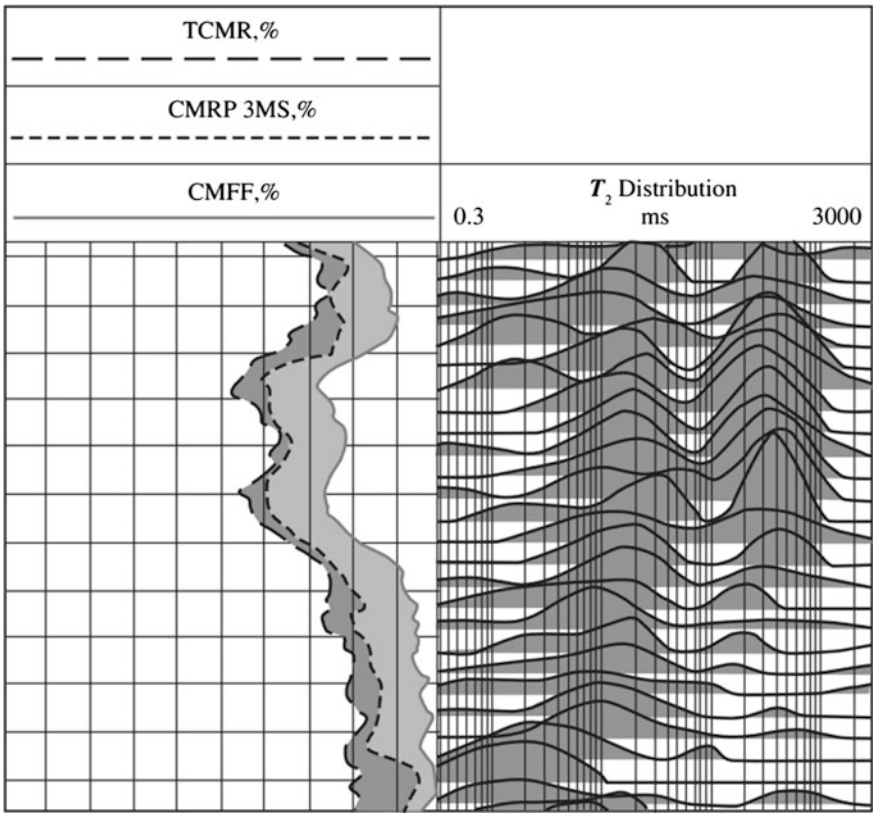

Fig. 5.11 Two tracks of a CMR display. The track on the *right* displays a representation of the T_2 distributions as a function of depth. The track on the *left* shows three version of porosity on a scale of 0–30 %. The lowermost curve corresponds to the sum of amplitudes greater than the 33 μs cutoff—the free fluid porosity. Between this lower limit and the *dotted line*, *shaded in grey* is the additional contribution between 3 and 33 μs that corresponds to capillary-bound (irreducible) water and the *dark shaded region* beyond that corresponds to the fastest component with T_2 less than 3 μs

Additional measurements made on a small sample of carbonates indicate that a cutoff value of 93 μs produces the best agreement between NMR porosity and the centrifuged volume. This latter value has not been as universally applicable in carbonates because of variability of the density of paramagnetic sites in carbonate rocks, and because the pore geometry tends to be much more complex than what is typically found in clastic environments.

The log of Fig. 5.12 compares the NMR porosity estimates with the conventional neutron and density estimates in a sand and shale sequence. In the third track is a representation of the T_2 distributions on a semilogarithmic grid. The shale zone is clearly identified by: (1) the elevated gamma ray in track 1 above ×540 ft and (2) by the clustering of the T_2 distribution around 3 μs. These low values, below the

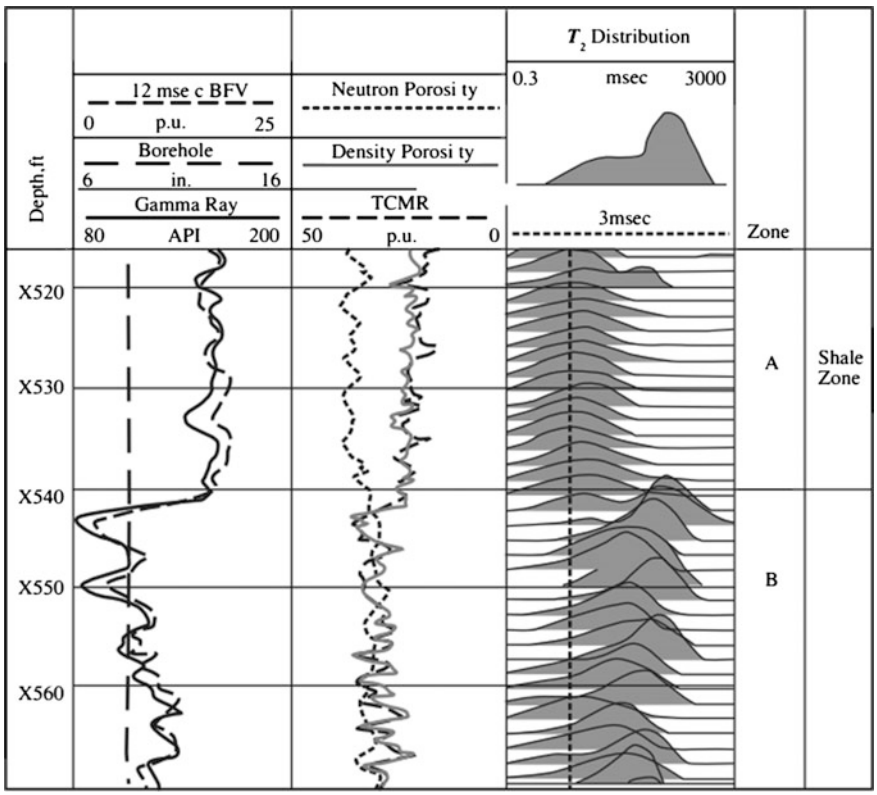

Fig. 5.12 The NMR total porosity compared to neutron and density estimates. In the sand *zone B*, the three estimates agree. In the shale *zone A*, the neutron porosity overestimates because it is sensitive to the hydroxyls in the clay minerals. In the first track, an estimate of the bound water fraction is made by comparing the fraction of the NMR signal below 12 μs to the total NMR porosity. It tracks the GR signal as an alternative indication of shale

bound fluid cutoff, signal fluid that is intimately in contact with the rock matrix or other surface with paramagnetic sites or with very tiny pore sizes. An estimate of the volume is made by comparing the portion of the signal below 12 μs to the total NMR porosity. With this special choice of cutoff, it is seen to follow the GR curve as an alternative indication of shale.

Note also that the three estimates of porosity all agree in the water-filled section below ×540 ft. However, above ×540 ft, the total CMR porosity (indicated as TCMR) agrees with the density porosity estimate. The neutron porosity is reading much higher because it is sensitive to the hydroxyls associated with the clay minerals in the shale.

5.4.2 Pore Size Distribution and Permeability Estimation

The messiness of carbonate rocks or their inherent heterogeneity, compared to clastics, is one source of interpretation difficulties for NMR measurements in these rocks. Traditional interpretation of T_2 distributions in clastics is based upon a reasonably strong correlation between pore size and the observed T_2 values. This is a result of a fairly constant surface relaxivity value in sandstones, and a lack of interaction between pores in a system of somewhat regular definition. In contrast, carbonates can contain pores on three major length scales; from extremely small micropores in the grain-like material that supports some sort of intermediate-sized porosity, to the very large and often hydraulically isolated vugs. Despite the existence of pores on these large scale difference, T_2 distributions rather than being bimodal are often only uni-modal. Several studies of these phenomena indicate that this type of behavior is caused by an interplay between surface relaxivity and communication by diffusion between the small and larger pore systems. The upshot is that in carbonates, it is often difficult to establish good T_2 cutoff values to use for free versus boundwater determination or to make permeability estimates. By contrast, the situation with clastics is much more rosy.

Estimating permeability of porous rocks from NMR measurements has had a long history extending from the early works of Seevers and Timur to much more recent contributions from Kenyon et al. All of the relationships that have been developed are based on a combination of theoretical relationships and experimental measurements.

The physical basis comes from the notion that permeability, the coefficient that links the flowrate through a porous sample to the pressure drop, depends most strongly on the size of the pore throats of the medium. The casual link to NMR is that some measure of the T_2 distribution (such as the log mean value) is related to a typical pore dimension. The next seemingly weak link is that the pore size dimension is also related to the throat size. This latter link is more reliable among sandstones than carbonates. At present, there are two general transforms in widespread use to estimate the permeability. The first, referred to as the Coates–Timur relationship is given by:

$$K = a'\emptyset^4\left(\frac{\mathrm{FFI}}{\mathrm{BFV}}\right)^2 \tag{5.6}$$

where FFI is the free fluid index, or moveable fluid volume, and BFV is the bound fluid volume. The term a' is a formation dependent constant about 1×10^4 mD for sandstone. The constants above need to be validated by laboratory measurement. However, once established they can be used within a particular formation with high degrees of confidence.

The second is the so-called SDR relationship:

$$\mathrm{K} = a\emptyset^4(\overline{T_{2,\log}})^2 \tag{5.7}$$

where $T_{2,\log}$ is the logarithmic mean value of the measured T_2 distribution. For both approaches, the constant may need to be adjusted to local conditions or perhaps the exponents on porosity (4) or on the NMR parameter (2) might be adjusted to give a

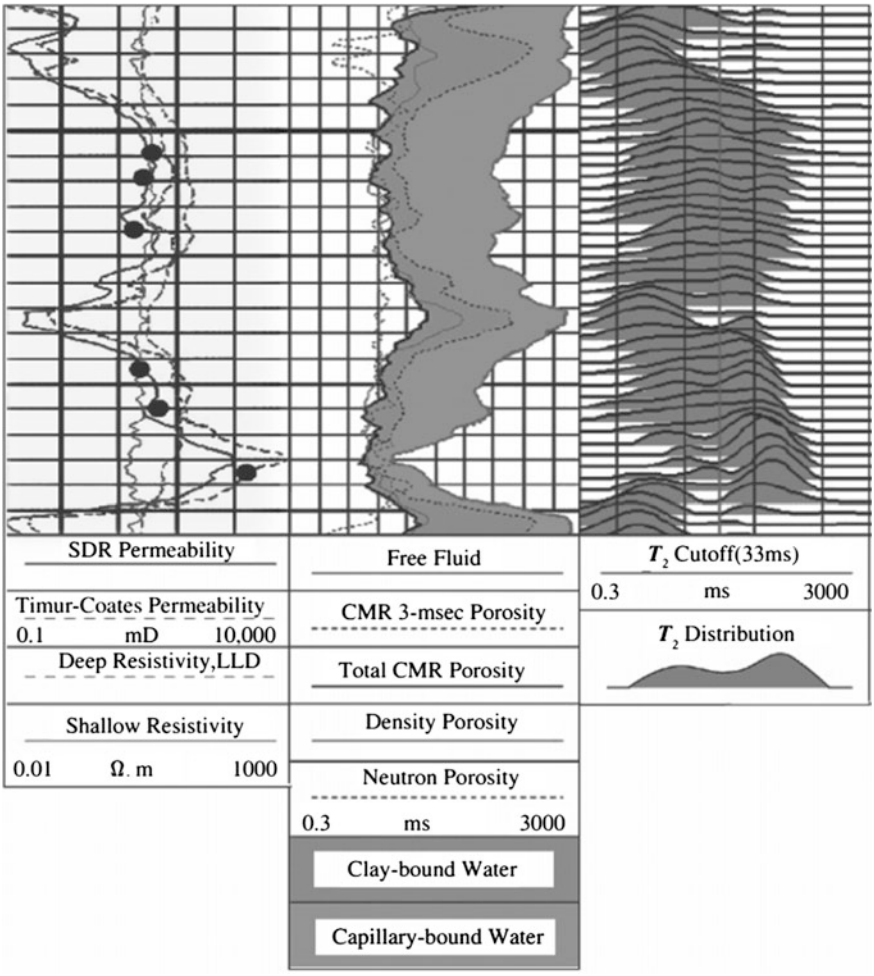

Fig. 5.13 The comparison of two estimates of permeability from the NMR measurements with that derived from a downhole sampling device is shown in the first track. The partition of porosity from the NMR measurement is shown in the middle track for the T_2 distributions displayed in track 3

better fit to known values of permeability determined on core samples or by other means.

Figure 5.13 shows an example of a continuous NMR estimation of the permeability compared to core measurements.

5.5 Summary

To understand the basis of NMR logging, we have had to learn how hydrogen acts as a magnetic gyroscope, and then enter into the details of nuclear induction and the relaxations that accompany it. These details are complicated, but it is because there are several different types of relaxation that the NMR signal contains so much information. One type of relaxation, spin dephasing, depends on variations in the magnetic field and not the formation, but can be removed by using a clever pulse sequence. The other types of relaxation longitudinal and transverse, and the effects of fast, slow or restricted diffusion lead naturally to the NMR properties of fluids and porous media.

We have seen how these properties could not be fully exploited by the earliest logging devices, but that the concept of inside-out magnets allowed resonance methods to be applied downhole and caused a renaissance in nuclear magnetic logging. The basic data acquired by an NMR measurement is a plot of relaxation times at each depth level. More information can be acquired by separating out the effects of diffusion, which can be done by recording with different polarization times and echo spacing. If there was to be only one nuclear particle in the earth that could be easily detected by nuclear induction, nature was kind to make it hydrogen. There is no other particle that can give us so much information about the microscopic properties of rocks, and in particular about the fluids in them. And we have seen the extent to which this has been exploited.

NMR logs give us information on the total amount of fluids, their distribution among different pore sizes, and the fraction that is likely to be producible. Furthermore, we are now able to distinguish between different fluids and to say something about their properties. Nature was not so kind in making rocks such complex bodies, so that unraveling the conflicting effects is not easy. In carbonates, for example, it remains difficult to extract useful information because of their relatively weak relaxation. However, one big advantage of NMR is that the downhole measurement is almost identical to that made on core samples in the laboratory. While other measurements have to be made on inconveniently large blocks of formation, or else studied with computer models, NMR laboratory results can be applied directly to the logging measurement. There is therefore good reason to hope that as new discoveries are made in the laboratory, NMR signals will reveal more information useful for unraveling the properties of reservoirs.

Problems

5.1 Give a brief explanatory of nuclear magnetic resonance
5.2 What is spin–lattice relaxation time (T_1)?
5.3 What is spin–spin relaxation time (T_2)?
5.4 What are the advantages of LWD-NMR?
5.5 How to discriminate different porosity based on the T_2 distribution?
5.6 How to calculate permeability from T_2?

Chapter 6
Production Logging (PL)

6.1 Definition Production Logging

Production logging traditionally encompasses a number of well logging techniques that run on completed injection or production wells, with the goal to evaluate the well itself or the reservoir performance. In recent years, however, the role of production logging has expanded to include applications that start at the early stages of drilling and that last throughout the life of the well. The purpose of production logs is to evaluate fluid flow inside and outside pipe or, in some cases, to evaluate the well completion directly. The most common application of production logging is the measurement of the well's flow profile, the distribution of flow into or out of the well-bore. Wade et al., referring to production wells, state that production logging is used to answer the question "How much of what fluid is coming from where."

The primary logging methods that will be considered are temperature, radioactive-tracer, and spinner-flowmeter logs for single-phase flow; temperature, fluid-density, fluid-capacitance, and flowmeter logs in multiphase flow; and noise, cement-bond logs as applied for well completion evaluation.

Major Applications of Production Logging Include:

(1) evaluating completion efficiency
(2) detecting mechanical problems, breakthrough, coning
(3) providing guidance for workovers, enhanced recovery projects
(4) monitoring and profiling of production and injection
(5) detecting thief zones, channeled cement
(6) single layer and multiple layer well test evaluation
(7) determining reservoir characteristics
(8) identifying reservoir boundaries for field development.

H. Liu, *Principles and Applications of Well Logging*, Springer Mineralogy,
DOI 10.1007/978-3-662-53383-3_6

A family of production logging tools, designed specifically for measuring the performance of producing and injection wells, is available. The sensors now included are:

(1) thermometer
(2) fluid-density (manometer, nuclear)
(3) hold up meter
(4) flowmeter spinners (continuous, full borehole, diverter)
(5) Manometer (strain gauge, quartz gauge)
(6) caliper
(7) noise (single frequency, multiple frequency)
(8) radioactive tracer.

Many of these sensors can be combined into one tool and recorded simultaneously to measure fluid entries and exits standing liquid levels, bottom hole flowing and shut-in pressures, pressure losses in the tubing, and the integrity of the gravel pack and hardware assemblies. Since the measurements are made simultaneously, their correlation is less affected by any well instability that might cause down hole conditions to vary over a period of time. The tool string also includes a casing collar locator and a gamma ray tool for correlation and depth control. Figure 6.l shows a schematic of the sensors in a typical production logging tool string.

Production logging can be a powerful tool for evaluating the performance of a well or reservoir, but also can be a waste of time and resources when applied poorly or in inappropriate circumstances. An understanding of the capabilities and limitations of the various production logging measurements available and of the types of problems that can be addressed with production logs is essential to the efficient use of these services. This chapter summarizes the applications of production logs throughout the life of a well by discussing the well or reservoir problems usually investigated with production logs and by showing the logs applicable in each case.

Reservoir performance monitoring, well completion evaluation, and planning and evaluation of well workovers are the most common applications of production logging. Production logs are sometimes run as part of a regular reservoir surveillance program; they are used more commonly to diagnose a problem implied by a well's performance. Surface conditions or a comparison of a well's behavior with that of nearby wells often suggests problems that can be pinpointed with production logs. Production logs can be useful diagnostic tools from the time a well is being drilled to its abandonment.

Though production logs traditionally have been thought of as for use in completed injection or production wells, they are increasingly being applied as a well is being drilled or completed. From the start of drilling operations, production logs can be used to locate lost-circulation zones or to find underground blowouts or the source of kicks. Virtually all completion operations—including cementing, gravel packing, perforating, and well stimulation—can be evaluated with production logs.

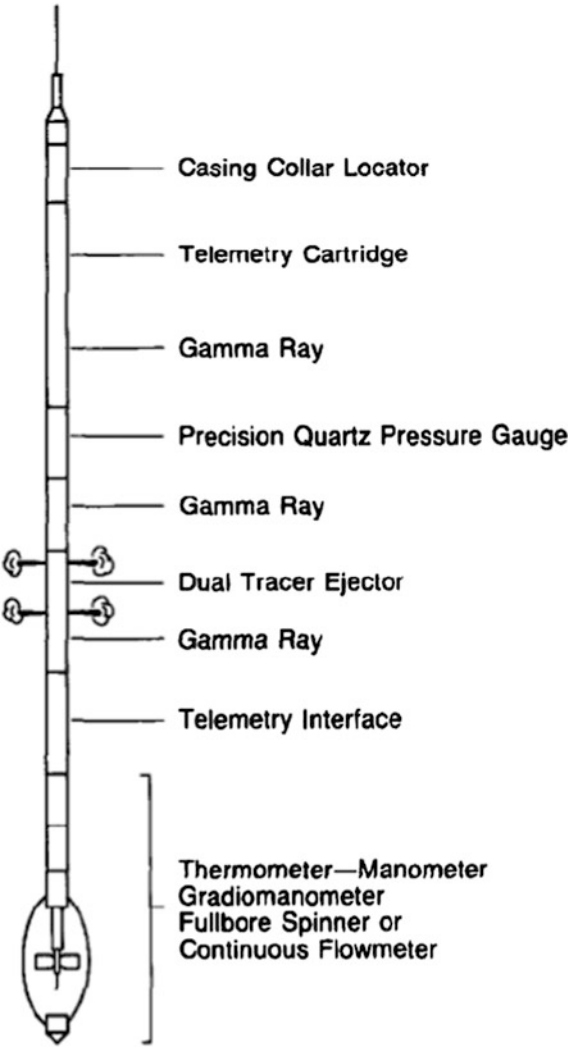

Fig. 6.1 PLT, simultaneous production logging tool

6.2 Spinner Flowmeter Logging

A spinner flowmeter is an impeller that is placed in the well to measure fluid velocity in the same manner that a turbine meter measures flow rate in a pipeline. Like a turbine meter, the force of the moving fluid causes the spinner to rotate. The rotational velocity of the spinner is assumed linearly proportional to fluid velocity, and electronic means are incorporated into the tool to monitor rotational velocity and sometimes direction. A significant difference between a spinner flowmeter and a turbine meter is that the spinner impeller does not span the entire cross-section of

flow whereas the turbine meter impeller does, with a small clearance between the impeller and the pipe wall.

A properly run spinner-flowmeter log should yield a reliable flow profile in single-phase flow in a constant-diameter well-bore. The spinner-flowmeter, however, is susceptible to mechanical problems, and the quality of the log depends strongly on the logging procedure and the care taken in running the log. If the well-bore cross-sectional area is variable, such as in an open-hole completion, a caliper log is needed to interpret a spinner-flowmeter log. In multiphase flow, a spinner flowmeter is often a very poor log, though in some instances it will perform well.

This chapter treats spinner flowmeters in single-phase flow. It begins with descriptions of the types of spinner flowmeters in common use. Procedures for running spinner flowmeters are then presented, followed by a section on the theory of spinner-flowmeter responses. This is followed by a discussion of spinner-flowmeter log interpretation methods and a description of some special types of spinner flowmeters.

Two designs of spinner flowmeters–the helical and the vane-type–are prevalent. The more common is the helical spinner, such as Gearhart Industries' spinner flowmeter and Schlumberger multiple sensor spinner (Fig. 6.2). Helical spinners are typically longer than they are wide, with a varying blade pitch. The spinner blade is housed in an open cage that extends from the main body of the tool to allow fluid flowing past the tool to impact the spinner. The spinner blade is usually suspended between jewel bearings to allow rotation with little friction.

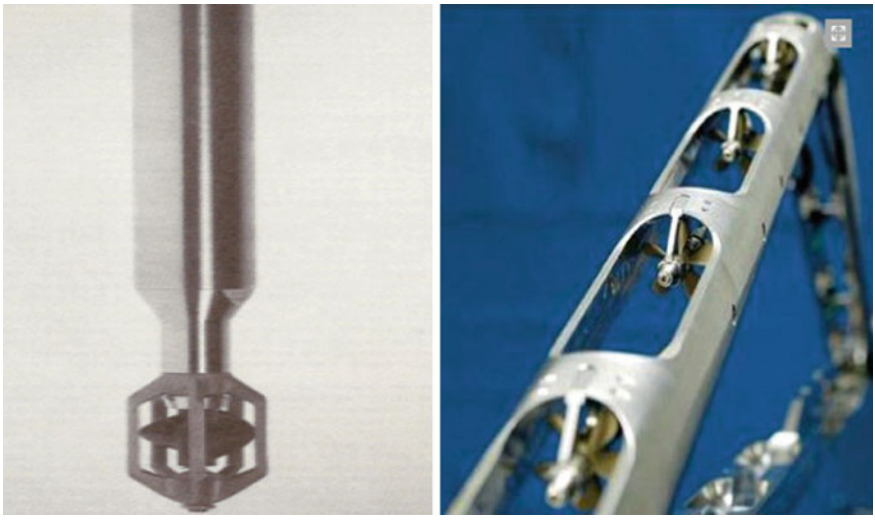

a. Gearhart helical spinner **b. Schlumberger Multiple spinner**

Fig. 6.2 Spinner flowmeters

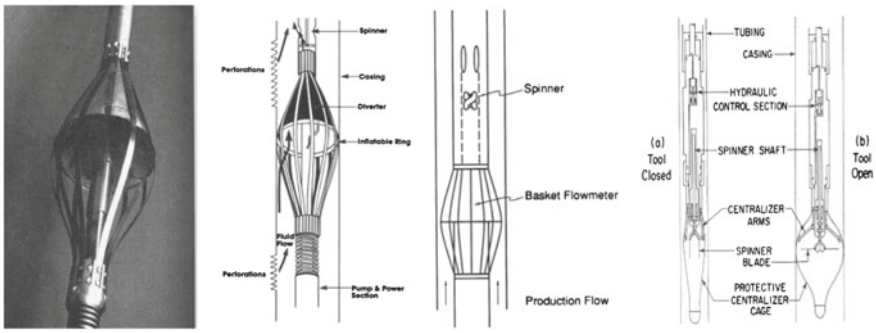

a. basket of Atlas **b. inflatable of slb.** **c. basket of Gearhart** **d. Full borehole of slb.**

Fig. 6.3 Different flowmeters

The Schlumberger Full borehole Spinner a vane-type flow meter, has four metal blades that mechanically retract to a tool diameter of l1 or 16 in. for running in the tubing. When the tool enters a larger diameter, a spring action extends the blades and the centralizer bands open, making the tool ready for operation. By this mechanism, the Full borehole Spinner is able to sample a larger portion of the well-bore than a helical spinner, whose size is restricted by tubing size.

Figure 6.3 shows different flowmeters, which have a funnel or some other device to direct the flow past the spinner located inside the tool. Deflector flowmeters have advantages over standard spinner flowmeters in low flow-rate wells and in certain multiphase flow applications.

One common method to measure the rotational velocity is to embed a small magnet in the impeller shaft; electronic pulses are generated as the magnet passes switches that surround the impeller shaft. Three to eight pulses are generated by each rotation of the spinner and are counted by surface electronics to give spinner speed. Some spinners are also able to indicate direction of rotation, discriminating direction either by pulse height (amplitude) or by polarity. In a normal, single-phase-flow situation, direction sensing, when not required, is helpful in log interpretation. In multiphase flow, where fluids can be moving up and down simultaneously, and in certain special instances, such as logging to detect crossflow in a shut-in well, the ability to sense the direction of rotation of the spinner and hence the direction of fluid flow can be very important to the log interpretation (Fig. 6.4).

The Effective Velocity

Based on the conservation of moment of momentum and rotation law, the function of the flowmeter responding to the flow rate is the following:

$$N = k(v - v_a) \tag{6.1}$$

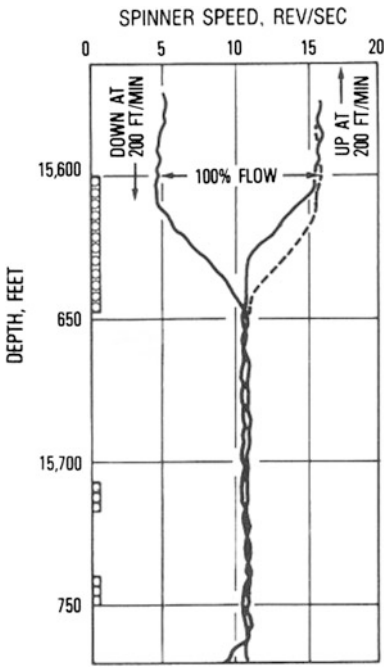

Fig. 6.4 Depth offset of spinner *up* and *down* passes

where

N rotation rate of turbine *v/s*
k tool constant depending on the materials and structure of tool, and affected of by properties of fluid
v relative velocity of fluid to the tool
v_a threshold value of rotation speed of turbine, and has relationship with turbine velocity and it is friction.

All spinner-flowmeter log interpretation is based on the spinner response being a linear function of fluid velocity. In dynamic runs, it is further assumed that the fluid and tool velocities are additive, so that the spinner responds to an effectives are additive, and then the spinner responds to an effective velocity, v_e, given by the following equation:

$$v_e = v_f + v_T \tag{6.2}$$

where v_f—fluid velocity and v_t—tool velocity. A sign convention is needed with this equation. We will assume that v_f is positive. v_t is also position when v_f and v_t are in opposite directions and is negative when the tool and the fluid are moving in the same direction.

Spinner response to effective velocity will be linear for high enough values of v_e. At lower velocities, the actual spinner response will drop until, at some velocities,

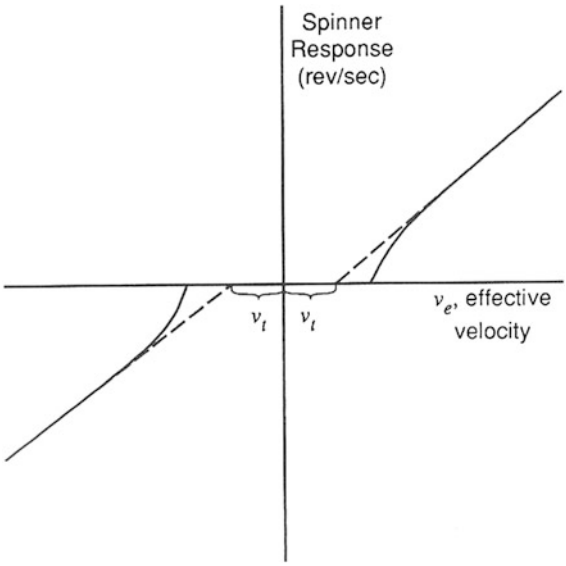

Fig. 6.5 Spinner response to effective velocity

the spinner ceases, turn, as shown by the solid line in Fig. 6.5. In spinner-log interpretation, the linear portion of the response curve is extrapolated to the zero spinner-response line; the intercept of the extrapolated line on the effective velocity axis is called the threshold velocity, v_t. Threshold velocity is sometimes referred to as bypass velocity and is a hypothetical minimum velocity required to start spinner rotation, if response is completely linear. Incorporating the threshold velocity, the spinner response can be written as

$$f = m_p(v_e - v_t)\,(v_e > v_t) \tag{6.3}$$

and

$$f = m_n(v_e + v_t)\,(v_e < -v_t) \tag{6.4}$$

where m_p and m_n—slopes of the response curve for positive and negative spinner responses, and v_t—a positive number. The two slopes, m_p and m_n, are not generally equal.

6.3 Fluid-Identification Logs

In a two-phase flow, a log that can measure the in situ fraction of the wellbore occupied by each phase is needed. Two types of measurements are commonly used for this purpose: fluid-density and fluid-yielding.

6.3.1 Fluid-Density Logs

Two types of tools are used to measure fluid-density—those based on gamma ray densitometer and gradiomanometer.

The most common type of fluid-density tool is the gamma ray densitometer. This tool is based on the fact that gamma ray absorbance is inversely proportional to the density of the material through which the gamma rays are passing. The device consists of a gamma ray source, an open space through which wellbore fluids can pass, and a gamma ray detector. Figure 6.6 shows a schematic of Atlas Wireline Services' density tool.

A gamma ray densitometer has several inherent limitations, including the statistical nature of the measurement, small sampling size, and low sensitivity in oil/water flow.

As in any nuclear measurement, there will be statistical fluctuations in gamma ray densitometer readings because the gamma ray source does not emit radiation at a constant rate. This effect can be minimized using a strong gamma ray source and by averaging the tool response over a finite time period.

6.3.2 Gradiomanometer Tool

The gradiomanometer tool uses the pressure differential between two bellows to infer the density of the fluid between the sensors. A schematic of the bellows tool is shown in Fig. 6.7. The bellows compress with pressure and a rod moves in proportion to the difference in compression between the two sets of bellows. A magnetic plunger on the end of the rod generates a signal proportional to the rod movement in a transducer coil. The coil output is calibrated in terms of fluid-density. In deviated wells, the gradiomanometer reading must be multiplied by the cosine of the deviation angle to correct the hole deviation effect.

$$\Delta\rho = \rho g \Delta h = \rho g d \cos\theta \tag{6.5}$$

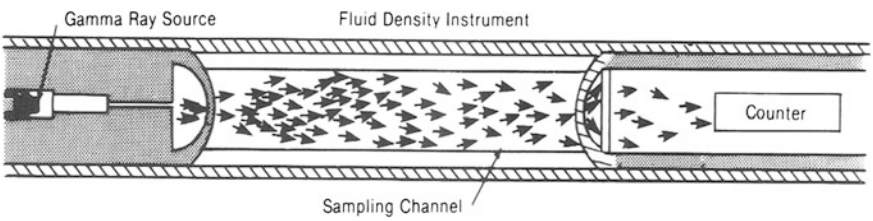

Fig. 6.6 Atlas wireline services gamma ray density tool

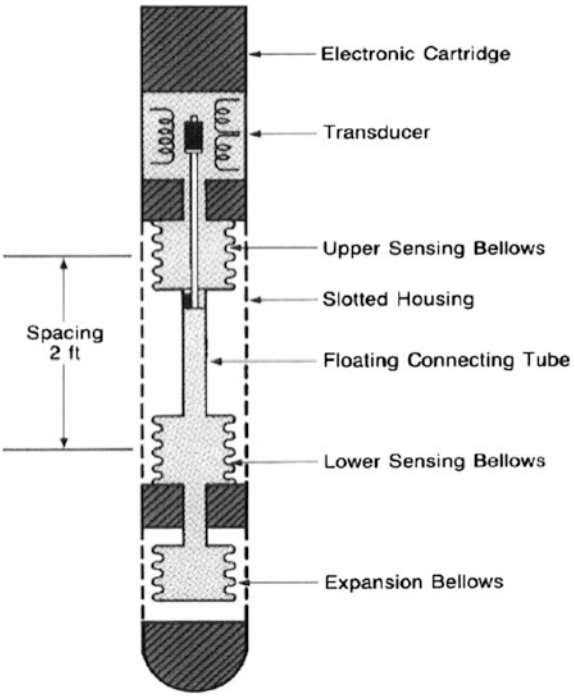

Fig. 6.7 Gradiomanometer fluid-density tool

where d, spacing between the bellows, θ, deviation from vertical, Δh, vertical height between the bellows, g, acceleration of gravity

Under the hydrostatic condition, that the pressure gradient in multiphase flow can be written as

$$\Delta\rho = \Delta\rho_{HH} + \Delta\rho_{f} + \Delta\rho_{E_k} \tag{6.6}$$

where $\Delta\rho_{HH}$, hydrostatic head of the flow stream, $\Delta\rho_{f}$, frictional pressure gradient, and $\Delta\rho_{E_k}$, pressure gradient resulting from kinetic energy change. Assuming that $\Delta\rho_{E_k}$ is negligible and that $\Delta\rho_{f}$ is small compared to compared to $\Delta\rho_{HH}$, then $\Delta\rho$ can be given by Eq. (6.5)

6.3.3 Nuclear Fluid-Density

The Nuclear Fluid-Density tool operates on the same principle as open hole density tools. A gamma ray source is positioned with respect to a gamma ray detector so that the wellbore fluid acts as an absorber. Figure 6.8 illustrates the measurement principle. A high count rate indicates a low fluid-density and a low count rate indicates a high fluid-density.

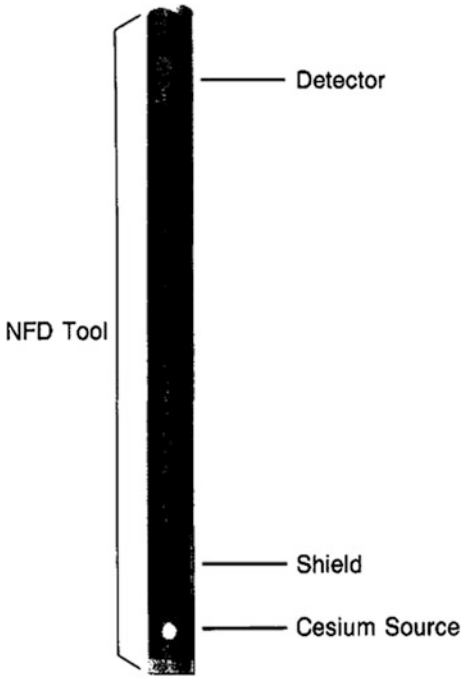

Fig. 6.8 Nuclear fluid-density tool

The advantage of the Nuclear Fluid-Density tool over the gradiomanometer tool is that the measurement is not affected by wellbore deviation or friction effects. However, since the tool relies on radioactive decay, the readings are subject to statistical variations. It should also be noted that the measured value is the average density of the flowing mixture. Therefore, it is subject to the same hold up effects as the gradiomanometer measurement.

6.3.4 Temperature Tools

The varying electrical conductivity of a thin wire that accompanies changes in ambient temperature is the basis of most temperature tool measurements. The common temperature tools include general temperature meter, vertical differentiate temperature meter, and radial differentiate temperature meter. A tool schematic is shown in Fig. 6.9.

The temperature log has many applications, particularly when run in combination with other sensors. Some of these applications are the following:

detection of gas production via the cooling effect of expanding gas (in or behind casing);

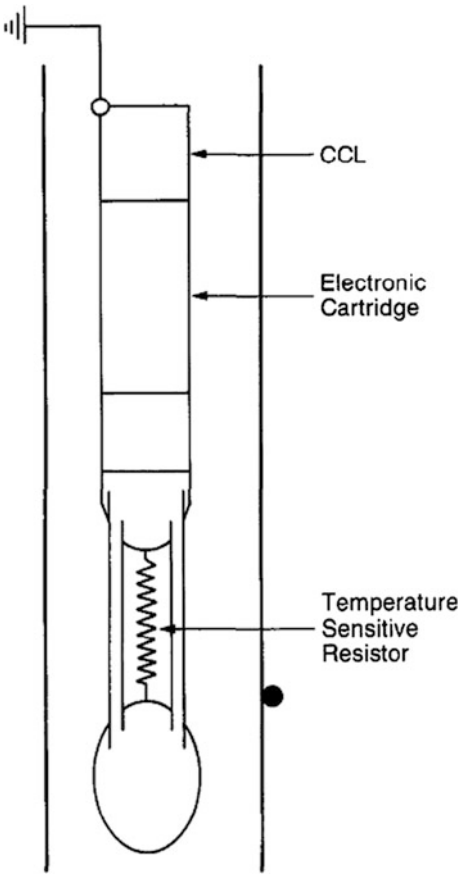

Fig. 6.9 Schematic of temperature tool

qualitative evaluation of fluid flow as indicated by departures from the geothermal gradient;
temperature (T) information for PVT equations and charts. Temperature information is critical to the determination of gas expansion/compression, GOR, and oil shrinkage from downhole to surface conditions and vice versa; evaluation of fracture treatments; and evaluation of the mechanical integrity of a completion.

Temperature log interpretations can also be used to determine flow rates; however, other sensors generally provide better results. The thermometer responds to temperature anomalies produced by fluid flow either within the casing or in the casing annulus, and is thus useful for detecting the latter. Figure 6.9 illustrates the temperature log response in four different situations: liquid flow, liquid flow behind casing, gas flow, and gas flow behind casing.

The temperature logs shown in Fig. 6.8 were run on a well that was completed as an oil well but soon started producing with a high GOR. Pressure,

gradiomanometer, and flowmeter logs were run with the temperature log to determine if the gas breakthrough was in the completed zone or channeling down behind casing. Both shut-in and flowing passes were recorded. The flowing gradiomanometer log indicated a drop in density at the top of the perforations and the flowmeter showed a large increase, pinpointing the gas entry into the casing. The temperature pass run with the well flowing on 24/64-in. choke shows that the gas was channeling down from 3931 m, and possibly from as high as 3923 m as indicated by the temperature slope changes (Fig. 6.10).

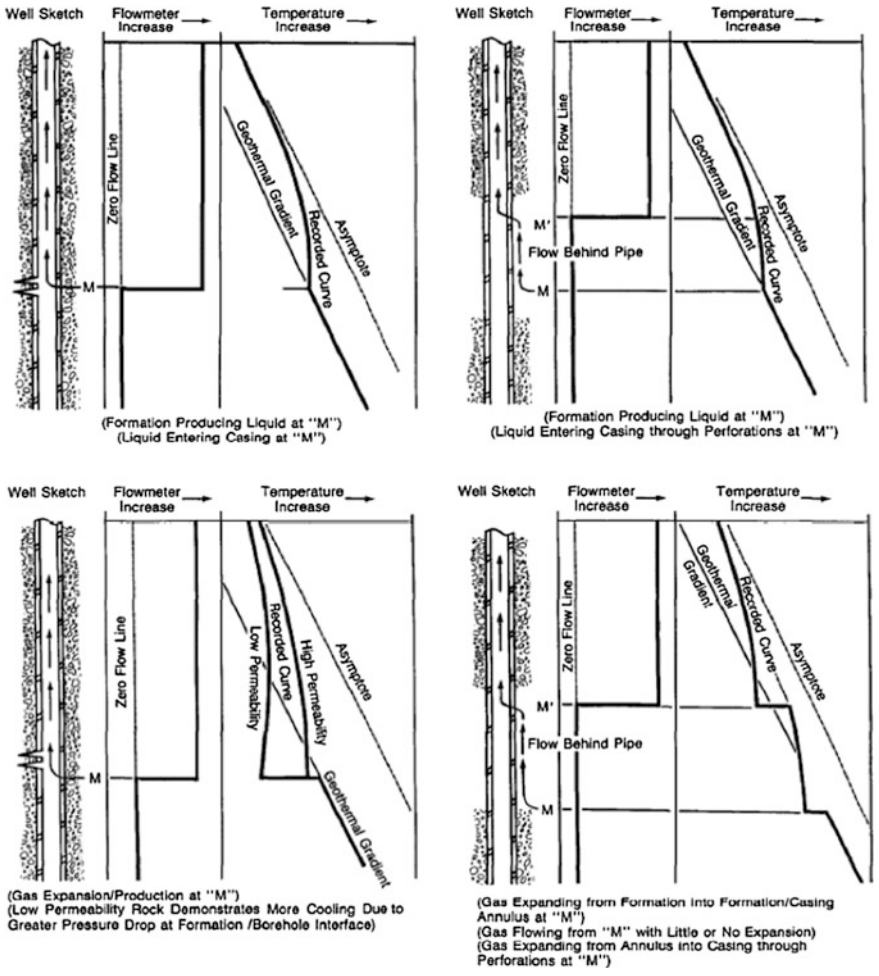

Fig. 6.10 Temperature log response

6.3.5 Capacitance Logs

To overcome the problems inherent in the ability of fluid-density tools to distinguish between oil and water, another class of tools was developed to measure water fraction more accurately in multiphase flow. The devices are based on an electrical-capacitance measurement and are sometimes referred to as hold up meters or water-cut meters.

Capacitance tools are essentially coaxial capacitors. By application of a voltage potential between a central electrode and the outside of the logging tool, the capacitance of the device is determined. Because the measured capacitance is a function of the dielectric constant of the fluids in the sample chamber, the capacitance tool provides a measurement of dielectric constant. Liquid hydrocarbons have dielectric constants on the order of 2–6, while water has a dielectric constant of about 80. Thus a dielectric constant measurement distinguishes easily between hydrocarbons and water. Because the dielectric constants of gases are near one, the capacitance log does not discriminate well between oil and gas.

6.3.6 Radioactive Water-Hold up Log

Radioactive water-hold up tool detects bottom fluid hold up of water and missed fluids based on absorption of low energy gamma ray. The principle of this tool is similar to that of gamma ray densitometer.

6.4 Radioactive-Tracer Logging

6.4.1 Introduction

One of the most common logging methods being used today for quantitatively evaluating injection profiles is radioactive-tracer logging. Radioactive-tracer logging methods can be placed in two broad categories: (1) a tracer material is injected from the surface and (2) a radioactive tracer is ejected from a logging tool in the well-bore. The first category includes such techniques as injecting radioactive proppant during a fracture treatment. Running a gamma ray detector after treatment gives some indication of the fracture location. Another application in the first category is tagging cement with a radioactive tracer. Again, a subsequent gamma ray survey locates the tagged cement. Because logs in the first category are generally self-explanatory and are discussed in detail elsewhere, we will focus on logs from the second category. These logs are generally run to evaluate injection profiles.

Obtaining injection profiles from radioactive-tracer logs is based on the ability of the tracer, which is miscible with the well-bore fluids, to disperse rapidly and then to travel with the well-bore fluids. If the tracer moves with the well-bore fluid, monitoring the velocity or loss of tracer from the well-bore should mirror the distribution of velocity or fluid loss of the injected fluid. In addition, because the gamma radiation emitted by the radioactive tracer can penetrate through casing and cement, a radioactive-tracer log can, in some instances, be used to detect channels behind casing, though other logs, such as temperature or noise logs, often identify channels more conclusively.

6.4.2 Tools and Operations

Figure 6.11 shows a typical instrument used for radioactive-tracer logging. A solution of radioactive tracer material is loaded on the surface into a chamber in the tool. A motor then ejects tracer whenever it is activated by an electrical signal from the surface. One or more commonly, two gamma ray detectors—either scintillation counters or, more often, Geiger–Muller tubes—are incorporated in the tool.

The tracers used are radioactive isotopes that emit gamma rays as they decay. The most commonly used isotope in tracer logging is iodine 131, which decays to stable xenon (^{131}Xe) through the emission of five beta particles and six gamma ray photons of various energies. Iodine ^{131}I has a half-life of 8.1 days. In a typical water-injection well application, the radioactive tracer will be contained in a dilute aqueous solution to ensure miscibility with the well-bore fluids. Oil- or gas-soluble radioactive tracers are also available for logging in those media. Generally, about 5×10^{-6} C_i of radioactive material is placed in the tool.

In any radioactive-tracer logging, centralizing the logging tool is always a good practice if the well completion will allow. With the tool decentralized, tracer may be ejected against the casing wall, leading to poor mixing of the tracer in the injection stream. Because of small tubing size, to allow more rapid tool movement, or simply for ease of operation, radioactive-tracer tools are often run without centralizers. In this case, the operator should be aware of the possible poor mixing of the tracer with the well-bore fluids and should rerun the log when an unusually dispersed tracer profile indicates poor tracer distribution.

Two radioactive-tracer logging methods-tracer-loss (timed-slug) and velocity shot are commonly used today. In the tracer-loss method, a single slug of tracer material is ejected into the well-bore above all zones of fluid loss. The tracer concentration is then measured as a function of depth by passing a gamma ray detector repeatedly through the tracer as the tracer slug moves down the well-bore. The tracer-loss method was developed for open-hole completions with irregular well-bore diameters. The velocity-shot method consists of measuring the transit time of a slug of tracer between two points (usually between two gamma ray detectors, but sometimes between the ejector and one gamma ray detector).

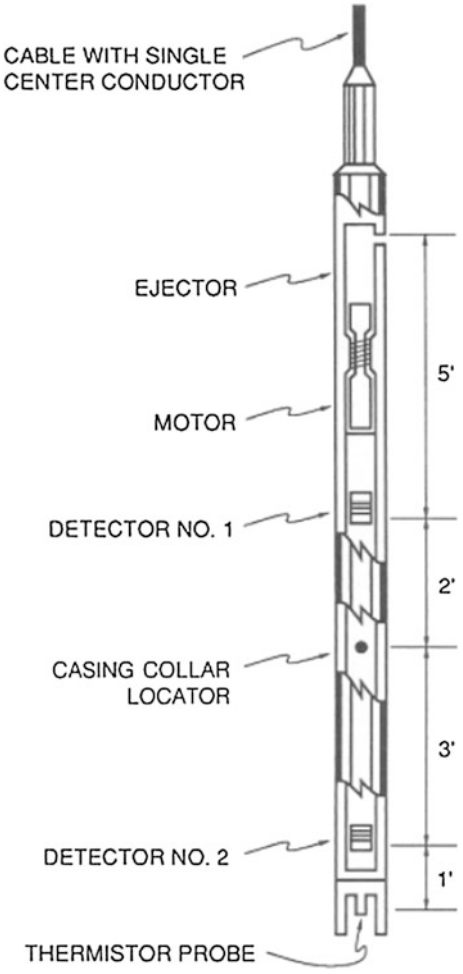

Fig. 6.11 Radioactive-tracer logging tool

Velocity-shot measurements are repeated at various locations in the well-bore. We will consider these two methods of injection-profile logging in detail in the next two sections.

6.4.3 Running a Tracer-Loss Log

Running a tracer-loss log begins when the baseline gamma ray intensity is recorded throughout the well before any tracer is ejected. The baseline gamma ray log is preferably run with high sensitivity to help judge tracer movement behind pipe. Though its gamma ray levels are usually quite low compared with the levels

measured in the tracer slug, this baseline log must be subtracted from the subsequent measurements of the tracer slug. Next, a fairly large slug of radioactive tracer is ejected into the well-bore above all zones of fluid exit. The tracer will ideally be ejected well below (20–30 ft) the tubing tail and a similar distance above the first perforated interval. After ejecting the tracer, the operator will often move the tool rapidly up and down through the tracer slug, attempting to mix the tracer thoroughly with the injection water. The logging tool is then dropped below the tracer slug, and gamma ray intensity is measured with a gamma ray detector as the tool passes back up through the tracer. It is important that this first measurement of the tracer slug be made before any of the tracer reaches a fluid exit location. If there is sufficient distance between the tubing tail and the top of the perforations, making several passes through the tracer before tracer reaches the perforations is helpful. This provides a measure of the accuracy of the tracer response in the maximum flow-rate portion of the well.

Procedure consists of repeatedly lowering the tool through the tracer slug and then measuring gamma ray intensity while logging back up through the tracer slug. These measurements are made as rapidly as possible to enhance depth resolution as the tracer slug moves down the wellbore. Logging continues until the tracer slug has ceased moving appreciably or is no longer detectable. The resultant log will consist of a series of plots of gamma ray intensity versus depth and the time each peak concentration was recorded, the tracer slug diminishes in intensity, spreads in extent, and slows as it moves down the wellbore because of turbulent dispersion and fluid exiting.

Because the movement of the tool through the tracer slug tends to spread the tracer longitudinally, the number of passes that can be made is limited, with 15 being a typical maximum. Thus, in a well with a long injection interval, the tool may be moved at a slower rate to obtain data over the entire injection zone before the tracer has become too dispersed. In any case, the logging passes made up through the tracer slug should be made at a high cable speed to minimize slug distortion caused by tool motion.

6.4.4 Tracer-Loss Log Interpretation

To determine an injection profile from a tracer-loss log, we must first relate the measured gamma ray intensity to tracer concentration. The gamma rays emitted by the disintegrating isotopes travel in random directions and can travel 1–2 ft before being absorbed. The gamma rays are scattered and absorbed by all the materials in the tracer surroundings, e.g., the tool, water, casing, and formation. Thus, much of the radiation emitted by the tracer will never reach the detector. Furthermore, the number of gamma rays incident on the detector will vary inversely with the square of the distance of the source from the detector. The overall effect is that the gamma ray detector is influenced primarily by tracer that is near the detector, i.e., the tracer inside the casing. Because the number of disintegrations is proportional to the

number of radioactive atoms, the gamma ray intensity measured by the detector should reflect the mass of tracer in the wellbore. Bearden et al. show that in full-scale tests, the gamma ray intensity measured does "map" the amount of tracer present. Thus, the first fundamental basis of the tracer-loss method is that gamma ray intensity measured by the detector is proportional to tracer mass. It is also convenient to assume that gamma ray intensity is proportional to tracer concentration, which implies uniform mixing of the tracer across the wellbore cross section.

As the tracer slug moves down the wellbore, some of the tracer will be carried into the formation with the wellbore fluid in regions of fluid exit. If the tracer is uniformly mixed with the wellbore fluid, tracer should be lost to the formation in the same proportion as fluid is lost to the formation. If, for example, the tracer slug passes a zone taking 30 % of the total injection, 30 % of the tracer should exit the wellbore. A logging pass through the slug after it has passed the fluid exit would show 30 % less tracer in the slug than was measured with a logging pass through the tracer slug before it reached the fluid-loss zone. This proportionality between tracer loss and fluid loss is the second fundamental basis for the tracer-loss log.

6.5 Other Production Well Logging

This unit discusses a few less commonly applied techniques for measuring fluid movement or the competency of the completion behind casing. These techniques include the use of pulsed-neutron logs for flow profiling, application of the radial differential temperature log for channel detection, and the use of the unfocused-gamma-ray-density log for gravel-pack evaluation. Though these logging methods may not be considered production logs in the classic sense, they are used to obtain the same sort of information as traditional production logs.

6.5.1 Pulsed Neutron Logs for Flow Profiling

The pulsed-neutron log is a commonly applied cased-hole log for formation evaluation that measures primarily the water saturation in the formations surrounding the well-bore. The log is sometimes used, however, as a means of obtaining a qualitative flow profile, and in this application plays the same role as such traditional production logs as temperature, spinner, or radioactive-tracer logs. This section reviews the theory of pulsed-neutron logging and presents examples of its use for flow profiling.

1. **Theory**

The basic principle of a pulsed-neutron log is that thermal neutrons traveling through a material will be captured by the atoms of the material and will emit gamma rays when captured. The capacity of elements to capture neutrons, called

the capture cross section, varies, with chlorine having a high capture cross section compared with other elements commonly found in formation rocks and fluids, e.g., hydrogen, carbon, oxygen, and silicon. Thus, the pulsed-neutron log can measure the relative amount of chlorine (salt water) in the formation near the well-bore. The radiation emitted by neutron capture events is proportional to the number of events (and thus is proportional to the number of live or uncaptured neutrons) and can be measured with a gamma ray detector.

A pulsed-neutron tool emits a short burst of neutrons, then monitors their decay by measuring the gamma rays emitted. The number of thermal neutrons decreases exponentially. Because the gamma radiation emitted is proportional to the number of live neutrons. Through measuring gamma ray intensity, pulsed-neutron tools can detect the number of living thermal neutrons.

The macroscopic capture cross section, Σ, is a simple average of the capture cross sections of the individual elements composing the medium. Thus, if the capture cross sections of the brine, oil, and rock and the porosity are known, the water saturation can be calculated from the macroscopic capture cross section. Table 6.1 lists the capture cross sections of some common reservoir constituents.

2. **Flow Profiling**

The injection profile in a well can be estimated by running a baseline pulsed-neutron log in a well, injecting a fluid with a higher capture cross section than that of the normal injection fluid, then repeating the pulsed-neutron log. The portions of the formation receiving injected fluid are identified by their higher capture cross section after injection of the high-Σ fluid. The capture cross section of the fluid is typically increased by addition of boron, which has a very high-Σ, or by raising the salinity.

This method does not provide a quantitative measure of the injection profile because once the high-Σ fluid has penetrated the formation beyond the depth of investigation of the pulsed neutron tool, typically about 1 ft, no further change in the measured capture cross section takes place. All zones that received this amount of fluid appear similar, regardless of the rate at which fluid was injected into the different zones. The pulsed-neutron log for flow profiling is most valuable in completions where spinner or radioactive-tracer methods cannot be used with accuracy.

Here a case where the completion prevented the use of conventional production logging tools for detailed flow profiling. In the field considered, water was being

Table 6.1 Macroscopic capture cross section of materials

Material	H	C	O	Si	Cl	Cd	Shale
Σ(c.u.)	0.3	0.0032	0.002	0.13	31.6	2500	35–55
Material	Matrix sandstone	Fresh water	Formation water		Oil	Gas	Methane
Σ(c.u.)	8–12	22	22–120		18–22	0–12	6–9

injected into three different zones, with the water injection regulated by tubing mandrels with packers separating the zones. If a spinner-flowmeter or radioactive-tracer log was run in the tubing, the gross injection into the tubing mandrels could be measured, but no detail about the distribution of injection in a particular zone could be obtained.

6.5.2 Repeat Formation Tester

The Modern sampling devices are the RFT and the MDT. The former of these has the ability to take multiple pressure tests and recover up to two samples of fluids. The MDT can be configured in a number of ways, but the main advantages are its ability to flow between probes and to recover multiple fluid samples as well as multiple pressure tests.

Formation test tools are used extensively in modern drilling operations and they provide a fast, safe and economical method of testing. Pressures can be recorded at the surface, and formation fluids can be recovered by using one or two chambers. Depth control is obtained by correlation with the SP log or with the GR log in cased holes. The main advantages in using wireline formation testers are:

(1) The well is under complete control.
(2) An average test can be completed under 4 h.
(3) Selection of zones to test can be made after logs have been analyzed.
(4) The complete cycle of tool operation is recorded on film at the surface.

The tool basically comprises, a surface controlled actuating mechanism, the hydraulic system formation seal pad and backup shoe with the snorkel tube, and the sample chamber. The sample chamber capacity is usually 3 or 6 gallons. For the Repeat Formation Tester, or RFT, two sample chambers can be attached for recovering fluids from different zones, and any number of pressure readings can be taken.

For unconsolidated sands the formation seal pad is fitted with a snorkel tube, but for tighter formations where the tube may become clogged or bent, the snorkel screen is used. For testing consolidated formations and cased holes, the seal pad can be fitted with a dual gun block, which fires two shaped charges into the formation.

6.5.2.1 Sample Procedure

The tool is run into the well to the depth required, which is recognized by comparing the gamma ray readings from a gamma ray sensor attached to the tool with previously taken logs. In this way an accurate depth may be fixed. Initially the tool takes a reading of the drilling mud pressure. The tool is then attached securely to the wall of the borehole, by a jacking device known as a backshoe on one side of the

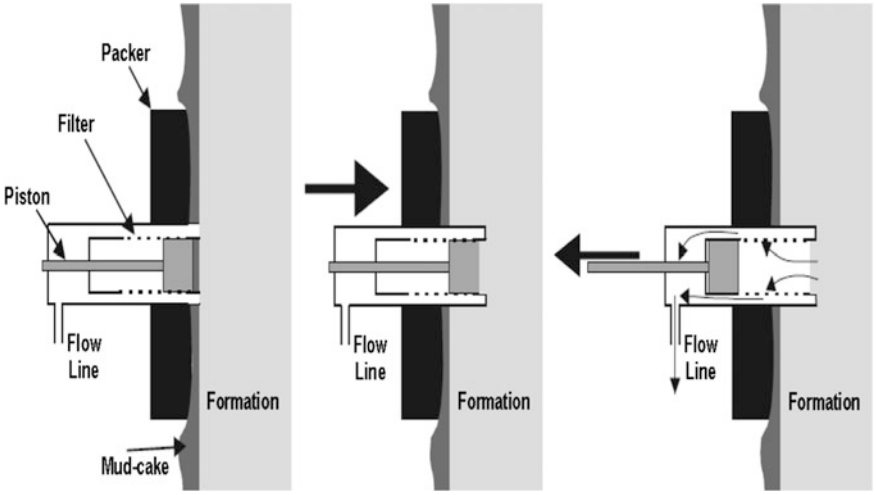

Fig. 6.12 RFT operation

tool. Opposite the backshoe is the measurement and sampling head. This consists of an annular seal or packer surrounding a sampling probe which contains a piston. The packer seals the sampling head from the drilling mud and mud cake surrounding the tool (Fig. 6.12a). The probe containing the piston is then pressed through the mud-cake into the formation (Fig. 6.12b). The piston is withdrawn, allowing fluids to pass from the formation into the tool (Fig. 6.12c). This fluid is made to enter a chamber (first pre-test chamber) through a special valve that limits the flow rate to about 60 cm^3/min. The sampling pressure is measured. When the first chamber is full, it is closed-off and a second pre-test chamber is filled at a higher rate (150 cm^3/min), while measuring the fluid pressure. When this chamber is full the flow-line fluids are at the same pressure as the fluids in the formation, and this pressure is measured. Figure 6.13 shows the internal piping of the tool.

Up to now, only pressures have been measured, and there are two pre-test samples in the pre-test chambers. The measured pressures give an indication of the productivity of fluids from the test depth. Since, there are only two main sampling chambers in the tool for operational samples, these samples are precious. It may therefore be decided that the tool should not take an operational sample, but move on to another depth. If this is the case, the pre-test chambers are emptied into the borehole, the backshoe is retracted, the drilling mud pressure is re-recorded, and the tool moves on to another depth. If an operational sample is required, one of two valves to two chambers is opened so that fluid flows into a chamber. The fluid sample is commonly between 5 and 20 l. Once the sampling chamber is full, the valve is closed. Note that the fluids are sealed in the sampling chamber at reservoir pressures. If another sample or more pressure data is required from further depths, the pre-test chambers are emptied and the tool progresses. Finally, the tool is

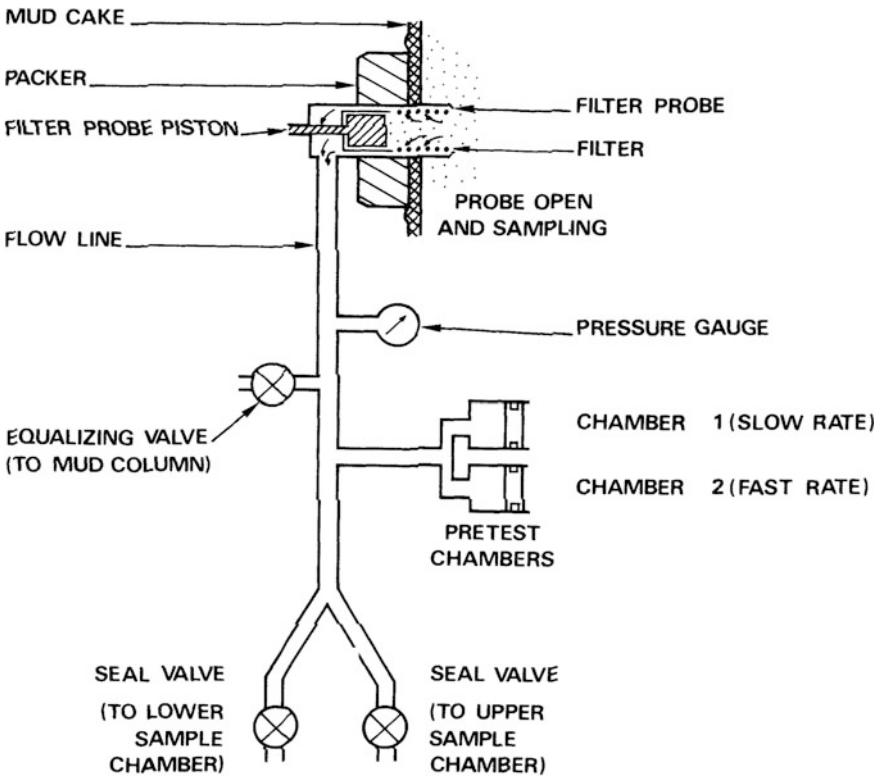

Fig. 6.13 Structure of repeat formation tool

removed with both its sampling chambers full, and having taken a number of pressure readings at sampled or unsampled depth points.

The samples are usually sent to a specialist laboratory where the compositions, physical properties and relative volumes of oil, gas, mud filtrate, and formation water can be measured.

6.5.2.2 Analysis of Pressure Measurements

A typical RFT recording of pressures from one depth is shown in Fig. 6.14. The hydrostatic pressure is that of the drilling mud, and is recorded while the tool is at the required depth, but has not been pressed against the wall by the packer (A). This is constant for a given depth in the borehole, and depends upon the weight of the column of mud above it. As the mud density is generally known, this value can be calculated and compared with the measured value.

When the probe penetrates the mud-cake, some mud is compressed between the probe and the formation wall, leading to a transient pressure increase (B).

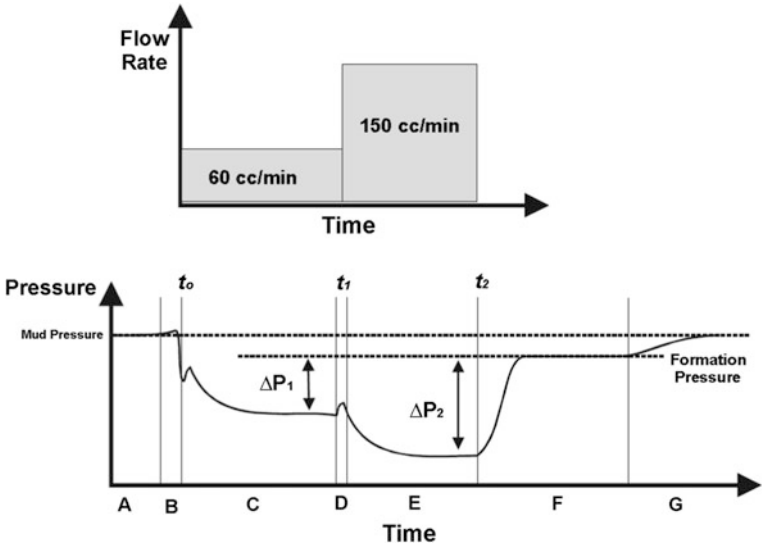

Fig. 6.14 Pressure changes during the RFT operation

The piston is open, and fluid flows into pre-test chamber 1 at 60 cm^3/min. The pressure drops because an additional volume has been added to the system (the chamber). The pressure pushing the fluid into the chamber is P_1 (C).

There may be some variations in the pressure behavior here as the flowing fluid is a mixture of mud-cake particles, mud filtrate, and formation fluids of different flow characteristics. When the chamber is approaching full the measured pressure begins to increase towards the formation pressure again (D).

However, the second chamber is opened up, and the pressure once again drops because fluid now flows at 150 cm^3/min into the second chamber. The pressure pushing the fluid into the chamber is P_2 (E).

When both chambers are full the measured pressure increases toward the formation pressure, which may take some time for low permeability formations (F).

After the pressure measurement, the backshoe is retracted and the mud pressure is measured again (G).

Note that the pre-test chambers have a low volume (about 20 cm^3). Hence, the fluid flowing into these chambers is most likely mud filtrate. However, the pressure that is recorded is the true formation pressures, as this is the pressure driving the mud filtrate into the chambers.

Several problems may occur. The most common questions are the following:

A Tight Test If the sample is very impermeable the sampling pressure drops to near zero. In this case it will take too long to obtain a pressure reading and the tool may stick in the borehole.

Stuck Tool Usually when the tool has been set at a given depth for some time.

Plugging Sand grains from the formation may enter the tool and block the flow lines, especially in unconsolidated samples. This problem is reduced by the filter in the sampling probe, but fine grains may still get through.

Seal Failure If the packer fails, the drilling mud will be sampled and the mud pressure will be recorded.

6.5.2.3 Log Presentation

The pressures are given in analogue and digital form. Track 1 usually contains the analogue pressure data. Tracks 3 and 4 are divided into 4 sub-tracks that contain the pressure data in exploded form:

Subtrack 1 Pressures from 0 to 10,000 psi in 1000 psi increments.
Subtrack 2 Pressures from 0 to 1000 psi in 100 psi increments.
Subtrack 3 Pressures from 0 to 100 psi in 10 psi increments.
Subtrack 4 Pressures from 0 to 10 psi in 1 psi increments.

The sum of all four digital tracks is the same as the analogue data. A typical RFT log for one depth is given as Fig. 6.15. Note that the vertical scale is in TIME not in DEPTH.

6.5.2.4 RFT Data Interpretation

The pressure data obtained from RFT are very useful as they enable judgements to be made about the position of the free water level (FWL), oil–water contact (OWC), and the gas–oil contact (GOC). Additionally, it gives information about compartmentalization, or whether the various fluids in a reservoir are separated physically by an impermeable barrier.

If we have several (>4 say) fluid pressure measurements at different depths in an fluid-bearing sand, where the fluid is in good connection throughout the interval, we can calculate the pressure gradient in the formation fluid. All the pressures should lie on the straight line which defines the pressure at a given depth as a function of the depth and the density of the fluid.

$$P = P_0 + \rho_{\text{fluid}} g(Z - Z_0) \tag{6.1}$$

where:

P_0 the fluid pressure at depth Z_0
P the fluid pressure at depth Z
ρ_{fluid} the density of the fluid
g the acceleration due to gravity.

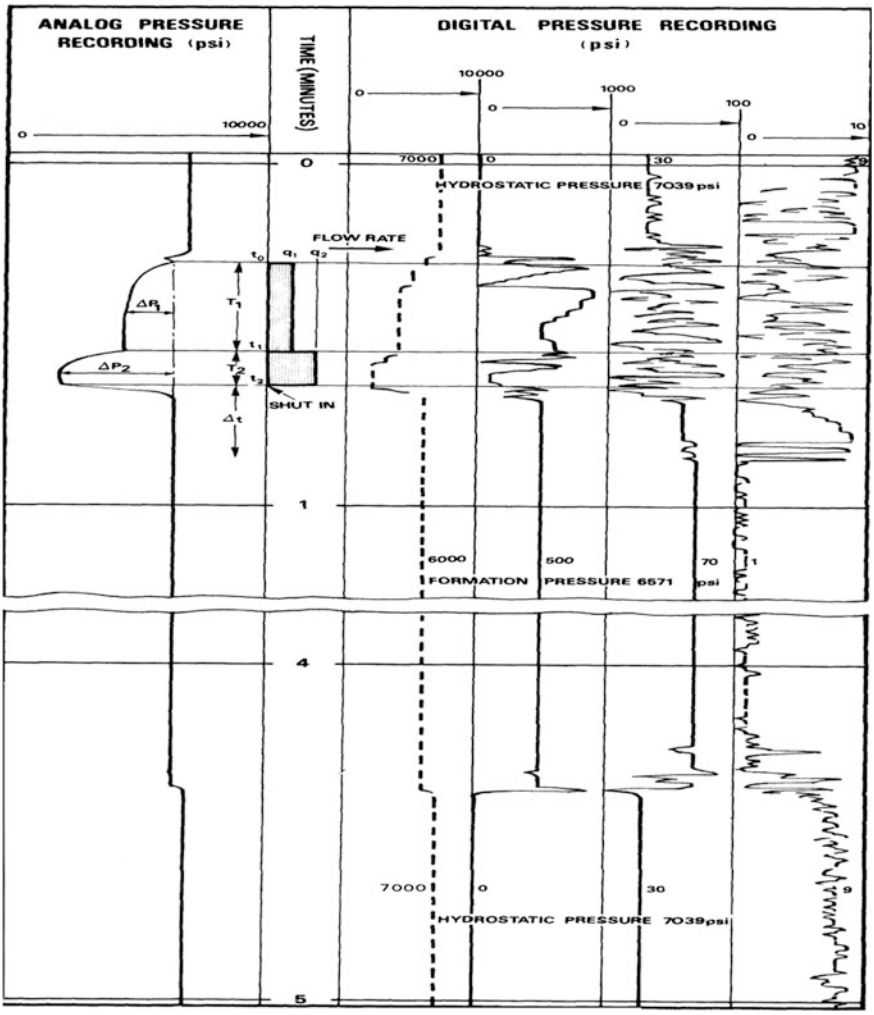

Fig. 6.15 An example RFT pressure log (Courtesy of Schlumberger)

This is applicable to all fluids (gas, oil or water) providing that the fluid in question is continuously connected throughout the interval.

A plot of pressure on the *x*-axis against depth on the *y*-axis is used to interpret reservoir pressures as shown in the following sections. This simple equation and the pressure versus depth plot allows us to examine a large range of possibilities that might occur in a reservoir. It can be seen from the pressure depth plot that the gradient of the line $G = 1/(\rho_{\text{fluid}}\, g)$, hence the density of the fluid represented by a line $\rho_{\text{fluid}} = 1/(9.81 \times G)$.

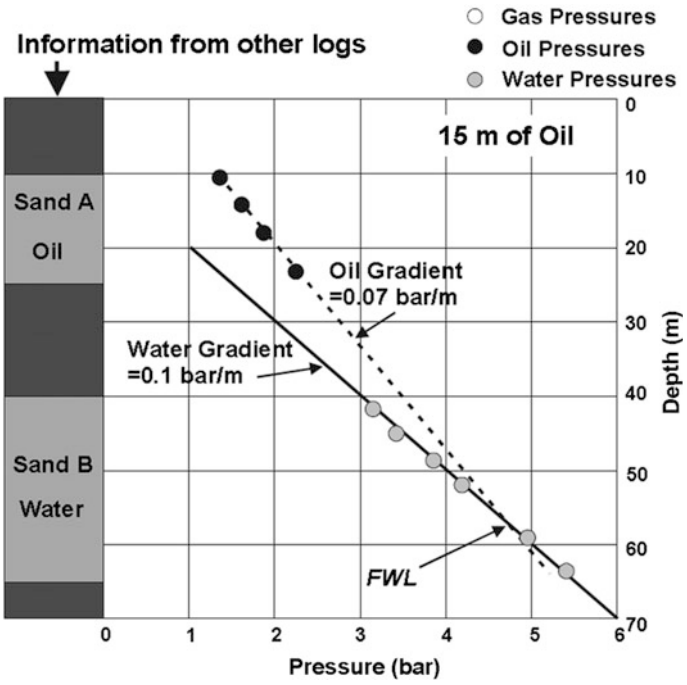

Fig. 6.16 Pressure versus depth plot 1

(1) **Oil and Water**

Referring to Fig. 6.16, the four oil pressures in Sand A determine the oil pressure line according to Eq. (6.5), and by fitting this equation to this pressure depth data, we can calculate the density of the oil. The six water pressures in Sand B determine the water pressure line according to Eq. (6.5), and by fitting this equation to this pressure depth data, we can calculate the density of the water. Note that the gradient of the lines is steeper for fluids of lower density. If one has pressure data, but does not know the type of fluid, then one may infer it from the relative gradients on the pressure/depth plot, or calculate the densities (gas very low, oil 0.5–0.9 g/cm^3, water about 1 g/cm^3). The intersection of the two lines is the likely free water level, providing Sand A and Sand B are connected. Sand B may be oil-bearing up-dip.

(2) **Gas, Oil, and Water**

Referring to Fig. 6.17, the four gas pressures in Sand A determine the gas pressure line according to Eq. (6.5), and by fitting this equation to this pressure depth data, we can calculate the density of the gas.

The data in Sand B do not form one straight line, but two. The higher is for oil and the lower for water. The densities of each can be calculated as above. The

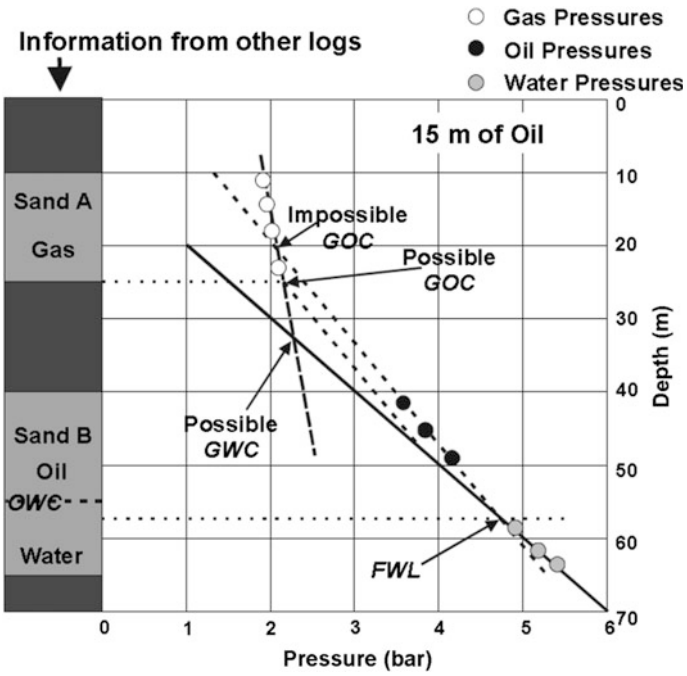

Fig. 6.17 Pressure versus depth plot 2

intersection of the water and oil lines is the free water level, as in the previous example. Note that this is about 2.5 m below the known oil water contact OWC.

If Sand A and Sand B are in communication, the intersection of the gas line with the oil line gives the gas oil contact (GOC). If they are not in communication, the GOC is controlled by the impermeable barrier, and might be anywhere between the two sands.

If oil is missing in the column, then the likely gas water contact (GWC) would be where the gas and the water lines intersect, again providing there is good communication between the two sands. If the recorded gas pressures are lower (Fig. 6.18), the assumption that the sands are in communication implies a GOC in Sand A, which is contrary to the log evaluation shown on the left of the figure. Hence, the sands are not in communication.

If the recorded gas pressures are higher (Fig. 6.19), the assumption that the sands are in communication implies a GOC in Sand B, which again is contrary to the log evaluation shown on the left of the figure. Hence, the sands are not in communication.

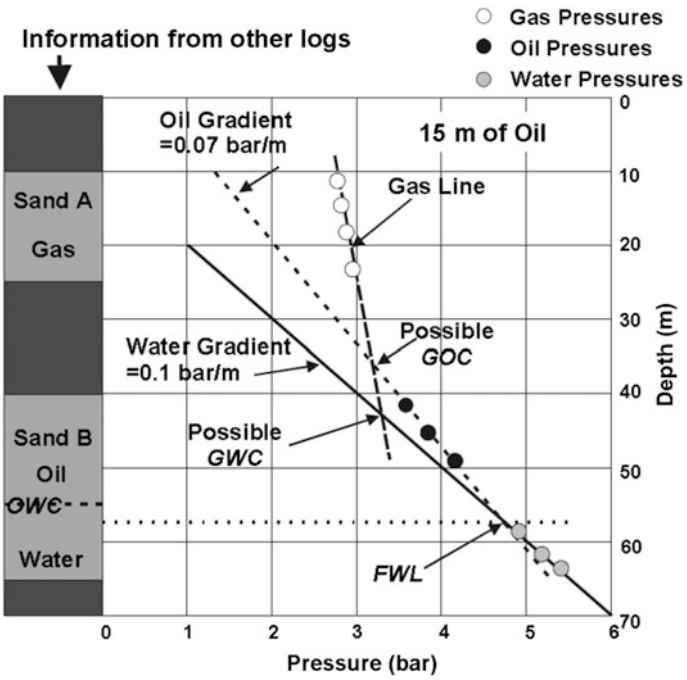

Fig. 6.18 Pressure versus depth plot 3

6.5.2.5 Estimation of Formation Permeability

The fluid gradient may have spurious data points for a large variety of reasons, such as reservoir heterogeneity, over-pressure, etc. One example is when the mud column supercharges a low permeability zone such that the hydrostatic pressure does not bleed away.

The actual tool uses pretest chambers to perform mini-drawdowns on the isolated formation. The pretest chambers are very small, only 20 cm^3 or so, but this is enough to investigate a volume out to 2 ft or so. One of the pretest chambers has a small orifice and the other a larger one in order to change the filling rate characteristics. In essence, differentiation of the pressure drawdown with respect to time and some geometrical model gives permeability. The resultant equation for the pressure drop is:

$$\Delta P = \frac{C\mu q}{2\pi r_p k_d} \Delta \left(1 - \frac{r_p}{r_e}\right) \tag{6.6}$$

where:

ΔP is the drawdown pressure, psi;
C is the geometric shape factor for flow

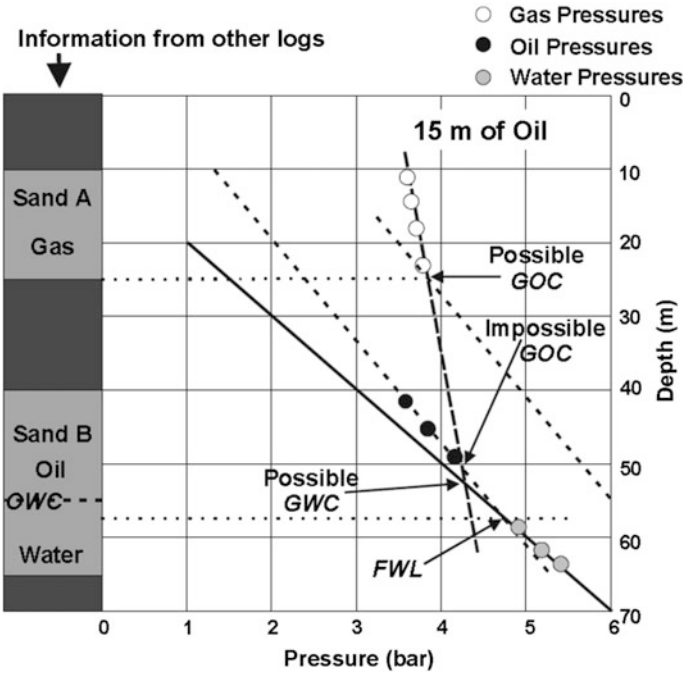

Fig. 6.19 Pressure versus depth plot 4

q is the flow rate, cm/s;
μ is the viscosity of the fluid, cp;
r_p is the effective probe radius, cm;
r_e is the outer radius of investigation of the flowing field, cm;
k_d is the effective permeability, mD
W_e can simplify the equation because r_p is very small with respect to r_e and solve it for permeability,

$$k_d = \frac{C\mu q}{2\pi r_p \Delta P}$$

Because the geometrical terms are all to do with the probe and packer sizes under pseudo-hemispherical flow, they can be grouped as a probe constant and the equation simplifies to;

$$k_d = c\Delta \frac{\mu q}{\Delta P}$$

where c is the probe constant, 5660 when the standard probe is used.

Problems

6.1 What is production logging?
6.2 Describe the methods to detect the flow rate in the cased hole?
6.3 What are the applications of temperature logging?
6.4 Comparing with spinner flowmeter, what are the advantages of the nuclear flowmeter?
6.5 Explain the process of Tracer-loss logging, and its applications
6.6 Explain the principle and applications of Repeat Formations tool
6.7 Based on the Fig. 6.14, describe the pressure changes during RFT operation.
6.8 How to estimate permeability using RFT data?

Chapter 7
Logging-While-Drilling (LWD)

7.1 What Is MWD/LWD?

The crucial element in logging that has so far been covered up, is the wellbore and the drilling process that creates it. Although it is beyond the scope of this volume to discuss drilling, there are several aspects that merit mention in their relationship to logging. To assist drillers in the complex task of a rotary drilling operation, a number of types of information like the downhole weight on bit and the downhole torque at bit are desirable in real time. To respond to this need, a type of service known as measurement while drilling (MWD) began to develop in the late 1970s. A typical MWD system consisted of a downhole sensor unit close to the drill bit, a power source, a telemetry system, and equipment on the surface to receive and display data. The telemetry system was often a mud-pulse system that used coded mud pressure pulses to transmit (at a very slow rate of a few bits per second) the measurements from the downhole subassembly. The power source was a combination of a generating turbine, deriving its power from the mud flow, and batteries. The measurement subassembly evolved in complexity from measurements of the weight and torque on bit to include the borehole pressure and temperature, mud flow rate, a natural gamma ray measurement, and a rudimentary resistivity measurement. For wells that are primarily drilled vertically, wireline logging, which relies on gravity for the descent of the tool package, is well adapted to obtaining the measurements used in formation evaluation. However, vertical wells are not always the norm. There are a number of reasons why one might wish to drill a well with some deviation from the vertical. A short list might include: drilling multiple wells from a single surface location as in the case of offshore platforms, avoiding a geologic feature, such as a salt dome, or to maximize the lateral extent of the wellbore in a reservoir by drilling parallel to the reservoir boundaries. Although a number of so-called conveyance systems (for example, coiled tubing) were innovated to "convey" wireline logging tools through the complex geometry of the non-vertical well, another technology has arisen to deal with the situation. It is

H. Liu, *Principles and Applications of Well Logging*, Springer Mineralogy,
DOI 10.1007/978-3-662-53383-3_7

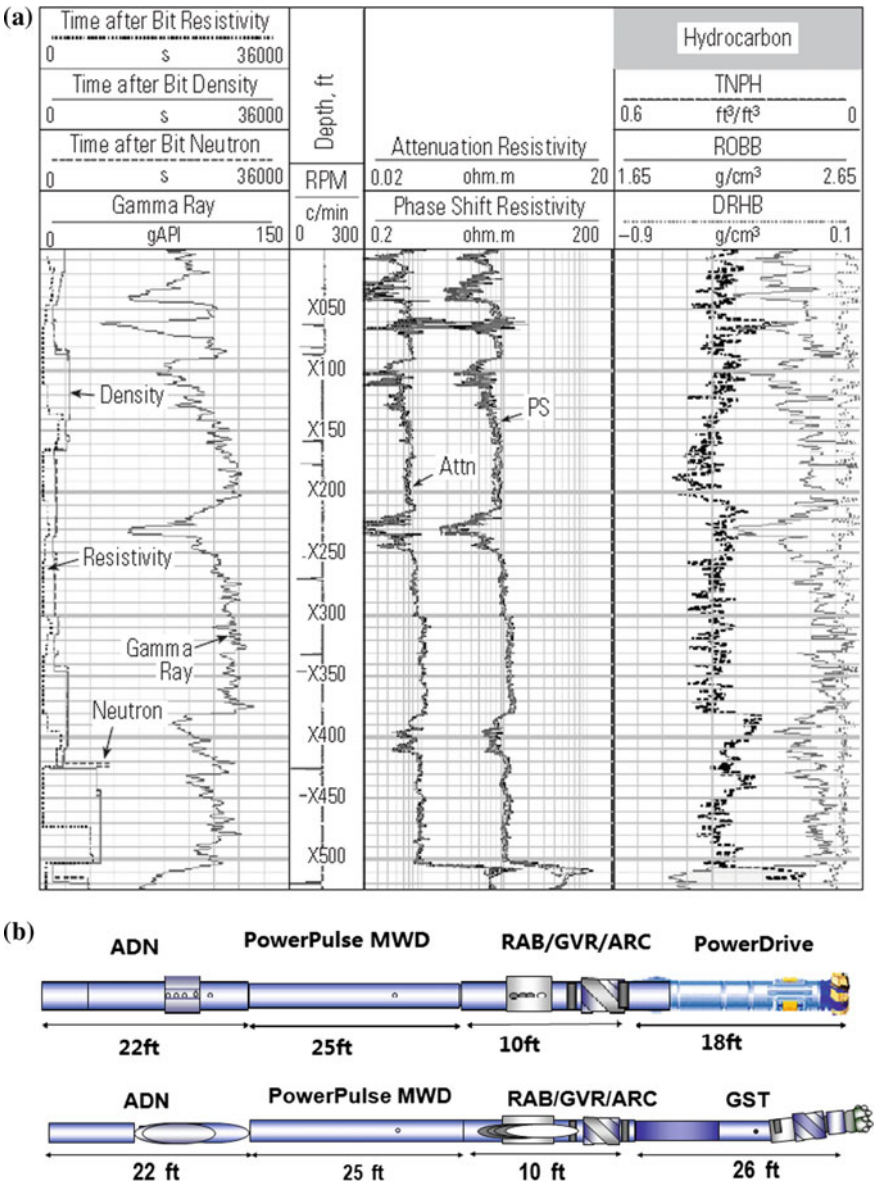

Fig. 7.1 **a** An example of an LWD log in a *horizontal well*. In track 1 is the familiar GR along with three *curves* indicating the time delay between drilling and the three types of measurements made; the tool rotation rate appears in the depth track. Track 2 contains two resistivity curves, each with multiple depths of investigation that overlay in this example. The third track contains the LWD versions of the neutron measurement (TNPH), the density measurement (ROBB), and the density correction (DRHB). **b** LWD devices containing AND, MWD, RAB, etc. measurements (courtesy of Schlumberger)

referred to as LWD and provides, in addition to drilling-specific MWD measurements, a family of measurements entirely analogous to the measurements of traditional wireline logging. The LWD tools are all built into heavy thick-walled drill collars—the special portion of the drill string used to counter buoyancy and provide stiffness to the lower segments of the drill string. Thus, like the wireline tools all the LWD resemble one another.

Figure 7.1a is an example of an LWD log recorded in a horizontal well. The basic presentation is similar to wireline logs, but some other useful curves may be included. LWD measurements are taken at regular time intervals, so that the sampling rate, in depth, depends on the rate of penetration of the drill bit. Sometimes tick marks in the depth track indicate the depth at which samples were taken for the different measurements. In this case some indication of the variable sampling density and rate of penetration is conveyed in track 1 by the three curves that show by how many seconds each measurement lags the bit position. In this example, the drilling rotation rate is shown in the depth track; for some oriented tools rotation is required for meaningful results.

Figure 7.1b shows the PowerDrive and GST LWD devices containing a AND, MWD, RAB, GVR, and ARC measurement. The upper one is PowerDrive LWD system and the lower one is GST LWD system. We will discuss several LWD instruments in the next sections.

7.2 Schlumberger Scope LWD Series

Schlumberger has introduced Scope, its new LWD system. This system consists of four new tools: LWD (Ecoscope), geosteering (PeriScope 15), telemetry (TeleScope), and formation pressure (StethoScope). The LWD and geosteering tools are of particular interest here.

7.2.1 EcoScope

The EcoScope logging-while-drilling service produces neutrons on demand with a unique pulsed neutron generator. Its design eliminates the need to use chemical sources for neutron generation and removes the risks associated with handling, shipping, and storing these sources. Measurement of formation density without the side-mounted cesium source is an option, making the EcoScope service the first to offer commercial LWD nuclear logging without traditional chemical sources.

All EcoScope measurement sensors are integrated in a single collar that can be deployed faster than conventional LWD tools, and advanced EcoScope measurements and large memory capacity enable the recording of quality data at 2 points/ft at penetration rates up to 450 ft/hr. TeleScope high-speed telemetry maximizes the real-time value of the EcoScope measurements. EcoScope sensors are integrated

into a single collar, so the measurements are made close to the bit, reducing the invasion effects. This advantage, combined with the service's deep measurements and high sampling rates, enables a comprehensive, accurate characterization of the formation.

Three levels of visual quality control indicators are associated with each EcoScope measurement, giving instant data quality verification that reduces uncertainty in interpretations and reserve calculations.

The EcoScope service delivers a comprehensive set of real-time measurements for drilling optimization, well placement, and well-to-well correlation. These measurements permit the fine tuning of drilling parameters to obtain the maximum ROP and the best hole quality. Measurements include those from the APWD (Annular Pressure While Drilling) service, which allow monitoring of hole cleaning as well as leak off-test and connection pressures.

EcoScope caliper data, from density and multisensor ultrasonic measurements, provide a visual representation of hole shape, enabling identification of over-gauge or under-gauge hole to help mitigate drilling problems. These hole measurements are also useful in calculating the volume of mud and cement needed for operations. EcoScope three-axis shock and vibration measurements indicate whether drilling energy is being dispersed in bottom-hole assembly shocks or being used to make hole. Rock typing and mineralogy information from the spectroscopy measurement allows advanced monitoring of borehole stability and facilitates risk planning. Dedicated internal diagnostic electronics record information used for EcoScope preventive maintenance, which can significantly extend drilling footage between failures and reduce nonproductive time.

EcoScope has a PNG producer, which can emit more neutrons with higher energies than a traditional chemical source, resulting in deeper and more precise measurements. It also enables several measurements that are available for the first time in commercial LWD services. Among these are neutron induced capture gamma ray spectroscopy data, which provide mineralogy, lithology, and matrix properties. Formation sigma, a salinity indicator, is also available, providing a viable alternative to resistivity for determining hydrocarbon saturation. The neutron gamma density is a measure of the gamma rays that are generated from neutron formation interactions.

Other EcoScope formation evaluation measurements include resistivity, azimuthal natural gamma ray, azimuthal cesium density, photoelectric factor, and thermal neutron porosity. The dual-frequency propagation resistivity array makes 10 phase and 10 attenuation measurements at several depths of investigation, providing invasion profiling and formation resistivity. Gamma ray detector allows the EcoScope service to provide gamma ray images in addition to the standard density and photoelectric factor images. All EcoScope measurements can be transmitted to the surface in real time using TeleScope high-speed telemetry.

EcoScope services can be delivered with the EcoView answer product, which integrates the measurements into an easy-to-use software package that offers multiple display options for the measurements. These include standard log formats, two-dimensional and three-dimensional images, and petrophysical data displays for

information, such as lithology, permeability, flow profiles, and volumetrics. In addition, EcoView software can be used for cross-plotting EcoScope well data. The EcoView answer product provides multiple means for sharing and exporting data, ranging from hard-copy prints to digital files.

Integrated sensor design, proximity to the bit, and multi-imaging capability make the EcoScope service an excellent tool for well placement. Its real-time azimuthal density and gamma ray images provide options for identifying the optimal well trajectory, and its spectroscopy and sigma measurements are available while drilling. High real-time effective data rates provided by the TeleScope service make these measurements available for fine-tuning the well trajectory.

7.2.2 PeriScope

PeriScope bed boundary mapper is revolutionizing well placement by providing the ability to see the reservoir as wells are being drilled, thereby eliminating sidetracks on wells and enhancing production. With the industry's first deep and directional electromagnetic LWD measurement, you can continuously monitor the position of formation and fluid boundaries up to 21 ft away so you can drill challenging horizontal wells entirely within the sweet spot.

1. **Drilling environments**

Since its launch in 2005, the PeriScope service has been extensively used around the world in environments, such as heavy oil, coalbed methane, and tight gas, including horizontal shale gas drilling in the US.

As advertised in Hart's E&P, the PeriScope bed boundary mapper has optimized well placement in the Permian Basin when used with PowerDrive RSS. For more of the story, read the industry article and case study.

2. **Directional and deep well placement**

The PeriScope service indicates the best steering direction, and the deep measurement range gives you early warning when steering adjustments are required to avoid water, drilling hazards, or exiting the reservoir target.

Because this technology continuously delivers deep images of boundaries around the borehole, uncertainties in structure and formation properties are significantly reduced when compared with traditional well logs in very large volumes of the reservoir. This results in more accurate reservoir models, superior reserves estimation, and improved planning of future wells. Producing previously uneconomic wells is now a reality.

7.2.3 StethoScope

StethoScope formation pressure while sdrilling (FPWD) service minimizes risk and reduces cost with real-time calibration points for pore pressure models. This service enables mud weight optimization so that drilling can continue confidently at ideal penetration rates.

FPWD measurements also improve casing point selection by offering a better understanding of the formation pressure around the planned casing point, reducing risk.

StethoScope HT services have a proven track record for high-temperature operations around the world. Our suite of best in-class HT technology and high-temperature-certified engineers includes products and services for directional drilling, MWD, and LWD. Real-time formation pressure measurements (delivered to surface by On-Demand Frame technology) eliminate time wasted drilling pressure-depleted formations and preserve virgin pressure zones scheduled for sidetrack development or completion. Pressure and mobility data help in targeting the most productive zones and determining the optimal drain length for horizontal wells. In faulted formations, rapid pressure analysis enhances effective geosteering between compartments.

(1) **Accurate data for improved formation evaluation**

In developed reservoirs, pressure profiles help to understand fluid movement. In virgin reservoirs, pressure profiles can be combined with other LWD logs to develop a static reservoir model. For pretests, TOP time-optimized technology supplies reliable data.

Using these pressure profiles to model the dynamic reservoir pressure optimizes recovery. The model enables an increased understanding of a field's production systems, leading to better completions.

(2) **Versatility for holes and settings**

StethoScope FPWD service is performed using a variety of tool sizes:
StethoScope 475 for holes with maximum OD of 5 3/4 in
StethoScope 675 for 8 1/4in and 9 7/8in holes
StethoScope 825 for 10 5/8in and 12 1/4in holes.

The StethoScope 675 and StethoScope 825 FPWD services draw from the knowledge gained from leadership in the LWD industry, as well as with wireline modular formation dynamics tester (MDT). Using an advanced crystal quartz and a strain gauge for valid data, the service is ruggedized to withstand the drilling environment. The information obtained works to optimize fluid typing, reservoir pressure, and mud weight.

7.3 LWD Technology of Halliburton

Sperry Drilling Services EWR-PHASE 4™ (Fig. 7.2) service utilizes a high-frequency LWD induction resistivity sensor. This tool comprises four radio-frequency transmitters and a pair of receivers. By measuring both the phase shift and the attenuation for each of the four transmitter-receiver spacing, eight different resistivity curves with differing depths of investigation can be provided. In addition to the standard tool sizes of 4 3/4, 6 4/4, and 8 in., there are also special large and super slim tool designs.

The 9 1/2 in. EWR-PHASE 4D™ tool is designed for logging larger holes that are up to 30 in. in diameter. This tool has extended transmitter-receiver spacing to increase the depth of investigation, minimizing borehole effects in large boreholes. For logging smaller boreholes, the 3 5/8 in. super slim tool is suitable for coiled tubing drilling, through-tubing rotary drilling and conventional rotary drilling applications in borehole diameters as small as 3 3/4 in. The EWR service has been commercial since 1983 and has established a track record of high reliability under a wide variety of formation and borehole conditions.

The multiple resistivity measurements of the EWR-PHASE 4 sensor facilitate the use of various interpretation models for evaluating invaded and anisotropic formations. The INVAMOD™ program computes R_t, $R_{xo,}$ and D_i in invaded formations, which can be particularly applicable when logging after drilling when formations may be invaded. The ANIMOD program computes the vertical and horizontal formation resistivity values (R_v and R_h) and relative dip angle when logging anisotropic formations at high relative dip angles. For geosteering applications, the forward modeling capability of the StrataSteer 3D software provides a synthetic log along the proposed well path to use as a correlation "road map." VRE (vertical resolution enhancement) processing corrects for shoulder bed and dipping bed effects, providing curves with enhanced vertical resolution.

The applications of EWR-PHASE 4 Sensor can be grouped as following:

- R_t, $R_{xo,}$ and D_i in invaded formations
- R_v and R_h in anisotropic formations
- High-resolution R_t in deviated wells and/or dipping beds
- Pre-invasion R_t measurement in deeply invading formations

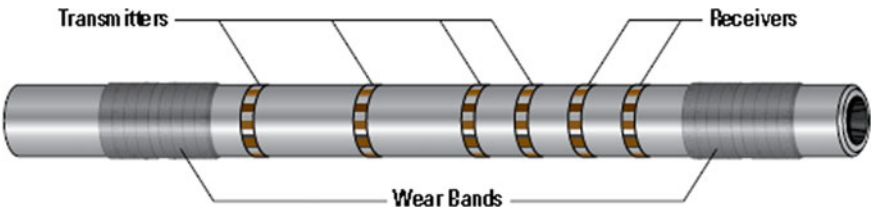

Fig. 7.2 EWR-PHASE 4™ sensor has four transmitter-receiver spacing

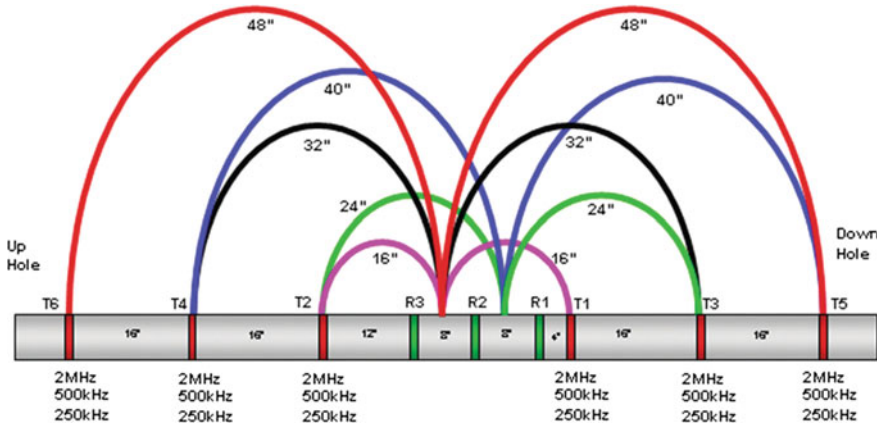

Fig. 7.3 The fully compensated geometry of the EWR-M5™ service helps to ensure accurate resistivity readings with minimal borehole influence

- Pre-washout R_t measurement in unconsolidated formations
- LWD replacement for wireline array resistivity tools.

The Sperry M5™ Integrated Logging-While-Drilling service (shown in Fig. 7.3) provides formation evaluation answers from resistivity and azimuthal gamma ray sensors and drilling optimization answers from vibration and pressure sensors. These new fully digital sensors are bundled together in one short, integrated collar, reducing the number of connections and yielding a significantly more reliable design than that of EWR-Phase 4. The service includes the new third generation EWR-M5™ resistivity sensor, from the company that first introduced the 2 MHz LWD resistivity sensor to the industry. The M5 service includes the following sensors:

- EWR-M5 Resistivity
- Azimuthal Gamma Ray
- Mud Resistivity and Temperature
- Pressure While Drilling
- Dynamic Motion Sensor
- Formation Evaluation.

The EWR-M5 resistivity sensor measures resistivity using three frequencies (2 MHz, 500 kHz, 250 kHz) and five compensated spacing. This provides very deep resistivities for bed boundary detection while geosteering as well as a greater number of resistivity measurements to cover the broadest range of applications. With both phase shift and attenuation measurements, the EWR-M5 sensor provides 30 unique compensated resistivity measurements. These curves have been characterized for depth of investigation and are utilized to generate an accurate interpretation of R_{xo} and R_t.

The AGR™ azimuthal gamma ray sensor measures the natural gamma ray activity of the formation. This helps distinguish between reservoir and non-reservoir rocks. As the AGR sensor is located only 1.8 ft from the bottom of the tool, readings are less affected by borehole degradation and therefore more accurate. With imaging capability and near-bit positioning, the AGR sensor is ideal for most geosteering and casing point determination applications. The Mud Resistivity and Temperature sensors provide the inputs to make real-time environmental corrections for other sensor measurements.

M5 Service Benefits

- Sensors are closer to the bit, helping to reduce reaction time, reduce the effects of borehole degradation and formation invasion and improve the quality of the measurement. Five compensated resistivity spacing at three frequencies, measuring both phase and amplitude, provide 30 measurements to cover the widest possible range of formations and provide input to advanced petrophysical analyses:
- Azimuthal gamma ray sensor readings produce borehole images for indicating dip and approaching bed boundaries
- Data is relayed at higher speeds so decisions can be made more quickly, in real time
- Mud weight can be optimized for managed pressure drilling (MPD) and management of equivalent circulating density for maximum ROP Critical pressure event response time is reduced through real-time PWD
- Hole cleaning exercises can be done on an as-needed basis, not according to arbitrary schedules
- Formation damage and mud losses due to swab/surge are reduced
- Rig down time associated with wireline logging can be eliminated
- Ideal for geosteering with its deep-reading capabilities.

7.4 Integrated MWD and LWD Instruments of Baker Hughes

7.4.1 AziTrak Deep Azimuthal Resistivity LWD System

The Baker Hughes AziTrak™ deep azimuthal resistivity tool is a fully integrated, measurement while drilling (MWD) and logging-while-drilling (LWD) tool. It provides real-time directional, azimuthal gamma ray, MPR™ multiple propagation resistivity, deep-reading azimuthal resistivity measurements, and downhole pressure and vibration measurements from a single sub. These measurements allow operators to deliver optimal wellbore placement and increase production in horizontal and multilateral wells.

The tool is designed to withstand challenges present in the most demanding drilling applications. Combined with a Baker Hughes downhole telemetry system and the Advantage™ surface system, the AziTrak tool delivers optimal directional control, accurate formation evaluation and borehole gamma ray imaging. The deep resistivity imaging allows a 360° peripheral vision of approaching bed boundaries in real time to achieve a more precise wellbore placement while drilling and to improve reservoir navigation capabilities by reducing sub-seismic uncertainty in the reservoir.

1. **Reservoir navigation with AziTrak deep azimuthal resistivity**

Until recently, operators were limited in the types of real-time resistivity measurements they could use for reservoir navigation. Deep-reading, omnidirectional measurements provided information about approaching contacts, but did not tie the approaching boundary to a specific azimuth. In contrast, high-resolution resistivity images provided a 360° view of the wellbore in excellent detail, but only had a depth of investigation of a few inches. As a result, the value of this data in reservoir navigation applications was typically limited.

With Baker Hughes' new AziTrak Deep Azimuthal Resistivity tool, reservoir navigation, and geosteering decisions just got easier, more precise and a lot more confident.

AziTrak azimuthal propagation resistivity subintegrates measurement while drilling (MWD) and logging-while-drilling (LWD) capabilities into one tool, using extended-range signal propagation and detection for precise, reliable navigation data. Operators know their location, can see their target and steer right to it. Despite claims, there still is no such thing as "forward-looking" drilling. What reservoir navigation with our AziTrak Deep Azimuthal Resistivity service provides is forward-looking knowledge. With deep-reading azimuthal images, one can calculate the distance and angle of the deviation several hours sooner than with conventional technology offering the ultimate in well plan flexibility.

2. **Navigating with answers while drilling**

Reservoir navigation the matching of geological and resistivity response models to predict bed boundaries in order to precisely place wells has never been more efficient and accurate than with Baker Hughes' experienced well planners, reservoir navigation supervisors and directional drillers coupled with best in-class technology. Technology such as the powerful, Auto Trak™ closed-loop rotary steerable systems and near-bit advanced MWD and LWD systems are what make real-time geosteering and precise reservoir navigation possible. With the addition of our AziTrak Deep Azimuthal Resistivity technology, this integrated real-time drilling service is more efficient and precise than ever before. The AziTrak sub is virtually a GPS system for reservoir navigation with a clarity that allows operators to visualize their location, the formation structure and the navigational heading-all in real time, for immediate answers and immediate decision-making.

3. **The GPS system for the subsurface environment**

Two key technologies give AziTrak the depth of investigation, the precision of directional and reservoir navigation data, and the visual imagery of approaching beds, boundaries, and pay zones. The first is the ring of multiple coil sensors, arranged perpendicularly and axially around the tool to offer a combined 360° view. The second is Baker Hughes' proprietary ferrite antennas. These induce a powerful electromagnetic signal that measures deep into the formation. Measuring the magnitude and amplitude of the resistivity signal determines the bed direction, azimuth and images for navigation.

4. **The instrument package**

Baker Hughes' surface system captures data from all of the downhole MWD/LWD subs via mud-pulse or wired-pipe telemetry to immediately display navigational data and memory-quality images for on-the-spot analysis-delivering valuable answers while drilling.

5. **Reservoir navigation imaging**

Data measurements and logs are key to correlating the wellbore to the predictive geological and resistivity model of the reservoir. They become the map and GPS for targeting the reservoir. Operators can see the image they have been looking for and zero in on the goal. At the surface, Baker Hughes' Reservoir Navigation experts immediately review navigational data and downhole AziTrak images for on-the-spot analysis and timely directional drilling decisions. If an approaching bed is up or down, left or right, the azimuthal image reveals it. If an operator wants to zero in on the roof of a reservoir to place their well with the precision that ensures maximum production, they not only see the target; they can drive straight to it.

7.4.2 OnTrak Integrated MWD and LWD System

On Trak integrated MWD and LWD system offers you a better understanding of the actual well position by taking measurements close to the bit. Positional certainty is increased further when MWD measurements are combined with near-bit inclination from our AutoTrak™ rotary closed-loop system, avoiding expense remedial directional work.

With reliable mud-pulse telemetry, the OnTrak MWD service offers real-time downhole measurements from a single sub.

1. **Maximize production with effective reservoir navigation**

To make steering decisions and optimally place the well, our reservoir navigation engineers identify bed boundaries and formation dips using gamma ray images. They spot approaching bed boundaries early with low-frequency resistivity measurements looking deep into the formation. With high-frequency resistivity

measurements they can see thin beds and fluid contacts in superior vertical resolution. When coupled with the AutoTrak system, steering decisions can be executed rapidly and precisely to maximize your reservoir exposure and future production.

2. **Get more real-time information**

The accelerate™ high-speed mud-pulse and wired pipe telemetry service can be combined with the OnTrak™ service and all other LWD services for a clearer picture of the downhole environment. This allows you to drill farther, faster, and safer.

Baker Hughes used its high pressure X-treme motor technology, along with OnTrak and LithoTrak LWD systems to ensure functionality in an operating environment that was planned to exceed 25,000 psi annular pressure.

The 8½ in. hole section was successfully drilled in one run with the X-treme motor and maintained directional control, delivering outstanding hole quality, and providing excellent ROP optimization for ECD management with minimal vibration.

Quality measurements were provided to determine lithology, fluid type, saturation, and porosity information at near virgin conditions minutes after being drilled-eliminating the need for additional wireline runs. Excellent borehole images were acquired while drilling, from which structural and stratigraphic dips were determined.

7.5 Resistivity Measurements While Drilling

The first resistivity measurement made while drilling was a short normal with electrodes mounted on an insulated sleeve, itself mounted on a drill collar. This was subsequently improved by the use of two guard electrodes in an LL3 arrangement that was also mounted on an insulated sleeve. Insulated sleeves are not popular in the drilling environment as they tend to wear faster than the steel collars. A much better solution was to use toroids. Toroids also offered a solution to the problem of measuring resistivity at the very bottom of the drill string, i.e., at the bit. It has always been highly desirable to measure the resistivity of the formation as soon as it is penetrated, or even beforehand. With this information it is possible, for example, to steer a highly deviated well within a reservoir or to stop drilling as soon as the reservoir is penetrated, as shown in the example of Fig. 7.4.

7.5.1 Resistivity at the Bit

The first device to measure the resistivity at the bit was the Dual Resistivity MWD Tool, which also makes a type of lateral measurement. The second device was the

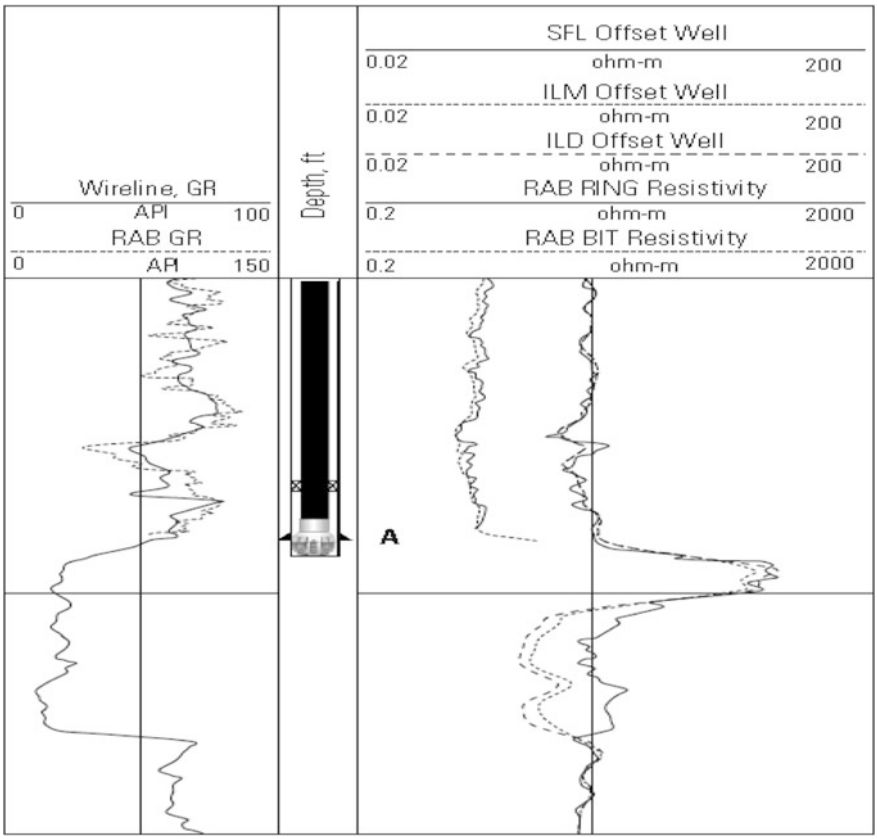

Fig. 7.4 Example of a log recorded by the RAB tool. The increase in bit resistivity at *A* indicates the *top* of the reservoir sand. This *top* can be seen in logs from the offset well (*right*). Drilling was stopped to set casing

Resistivity at the Bit Tool (RAB), which also makes a focused resistivity measurement. A removable sleeve with button electrodes can be added to the tool in order acquire data that varies azimuthally and has different depths of investigation. An improved version of the RAB is known as the GVR, geoVision Resistivity.

In both the Dual Resistivity MWD Tool and the RAB, a current is sent down the drill collar and out through the bit by a toroidal transmitter before returning through the formation (Fig. 7.5). The toroidal transmitter, shown in Fig. 7.6a, is a transformer with its coils acting as the primary, and the drill collar and return path through the formation acting as the secondary. A low (1,500 Hz) alternating voltage is applied to the coil inducing a voltage difference between the collar sections above and below the toroid. This voltage difference, which is almost entirely in the formation due to the low resistance of the collar, is equal to the input voltage divided by the number of turns in the toroid. The axial current is measured by a

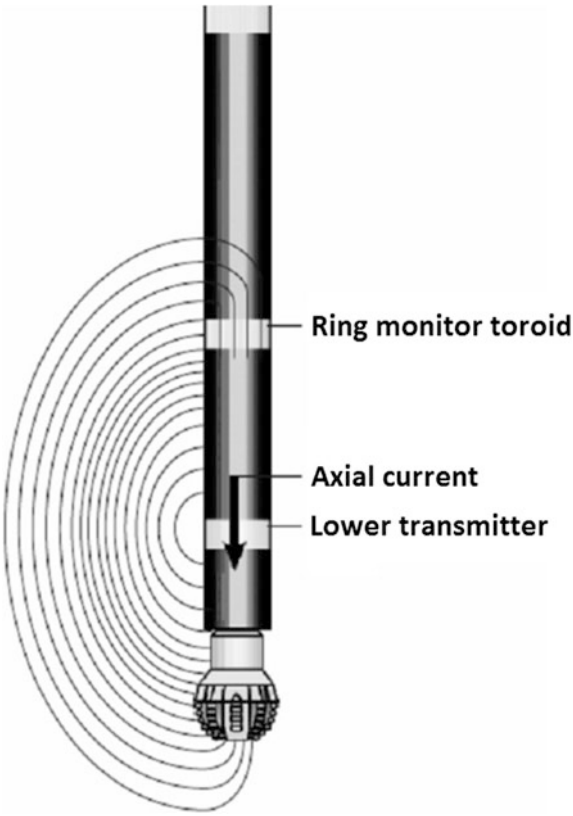

Fig. 7.5 An illustration of how resistivity is measured at the bit. The toroid transmitter sends current down the drill collar and out through the bit. The current lines that travel through the formation return further up the collar where they are measured by a monitor toroid. Courtesy of Schlumberger

toroidal monitor (Fig. 7.6b). This is also a transformer with, in this case, the drill collar and formation acting as the primary and the coils as the secondary. The current flowing in the coils is equal to the axial current divided by the number of turns.

It is important to maximize the amount of current flowing out through the bit but at the same time to place the transmitter and monitor far enough apart that the measured current flows through the formation and not the borehole. For this reason the transmitter is placed as close to the bit as possible and the monitor is placed further up the string (Fig. 7.5). Resistivity is calculated from:

$$R_p = K \cdot V_{tool}/I_{meas}, \tag{7.1}$$

where V_{tool} is the formation voltage drop measured by the toroid and I_{meas} is the current at the monitor. K depends on the drill collar geometry. The result is an unfocused device whose characteristics depend strongly on the distance between transmitter and bit. When the main purpose of the log is to measure the resistivity of the formation as soon as it is penetrated, the RAB should be placed immediately

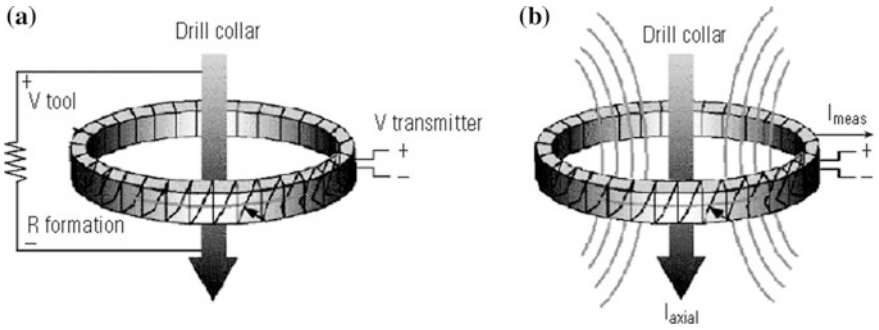

Fig. 7.6 **a** A toroidal transmitter formed by wrapping a coil around a ferromagnetic toroid. The voltage *V*tool $\Im \leftarrow V_{transmitter}/N$, where N is the number of turns in the coil. **b** A current monitor formed by connecting a toroidal coil to a low impedance circuit. The current $I_{meas} \Im \leftarrow I_{axial}/N$. From Bonner et al. used with permission

above the bit. This gives a reasonable vertical response of a few feet as well as the earliest response to resistivity changes. If the RAB tool is placed further up the tool string, the response is less well-defined and the measurement is more qualitative than quantitative.

Surprisingly, this measurement works in most oil-based muds, even though they are nonconductive. The reason is that the formation is in contact with the bit as well as with some part of the drill collar, usually through a stabilizer. There is thus a current return path. However in nonconductive mud the current returning through the monitor shown in Fig. 7.5 is unpredictable, so it is measured at another monitor placed just below the transmitter (not shown). There is no concern about current flowing through the borehole in this situation.

7.5.2 Azimuthal Measurements

The RAB buttons respond to the resistivity in front of them, so that if the drill string is rotated it is possible to record an image of the formation at different azimuths. This is a powerful feature as it allows images of formation features to be seen while drilling. Magnetometers orient the tool with respect to the earth's magnetic field. RAB images do not have the vertical resolution of electrical microscanners but do reflect bedding and structural features from which formation dip can be determined. This information can be very useful in near real time. For example, in highly deviated wells an image can determine whether a new bed is being entered from above or below, something that cannot be done with non-azimuthal measurements.

7.6 Density Measurements While Drilling

Since LWD density devices are derived from their earlier cousins, the wireline devices, their similarities are many. LWD devices also have a source and a long-spaced and a short-spaced detector. The only difference is that the LWD density devices are built into the drilling collars and are generally close to the bit. As part of the drilling string they also rotate. Consequently, the data is generally acquired as a function of time along with orientation information so that the data can be binned with respect to hole orientation. In Fig. 7.7 the data is collected in four geometric sectors (for imaging purposes many more bins may be used). In the figure on the left, the horizontal borehole is at the boundary of two formations with different densities, foreshadowing a difference in the measured density between the upper and lower quadrants. In the figure on the right, where the tool is run without a stabilizer, the density most representative of the formation corresponds to the bottom quadrant, and a significant correction should be apparent when the tool is pointed toward the top of the hole.

Figure 7.8 shows one version of the multiple-density traces that might be available from an LWD density measurement. In this example there is a fairly obvious discrepancy between the upper and bottom quadrant density estimates. This discrepancy can be caused by the wellbore lying at the intersection of beds of two different densities as indicated in the left-hand sketch in Fig. 7.7. Due to the action of gravity, in a highly deviated well, the bottom quadrant is frequently the curve with the least perturbation.

Inspection of the correction curves in the log of Fig. 7.8 confirms that the $\Delta\rho$ curve in the bottom quadrant is the least active of the four presented and is the one that is closest to zero over most of the section displayed. In an over-sized or washed-out hole, the measurements around the circumference may contain significant error if the compensation range is exceeded. Another benefit of the rotational measurement, in appropriate sized boreholes, is the possibility of deriving density

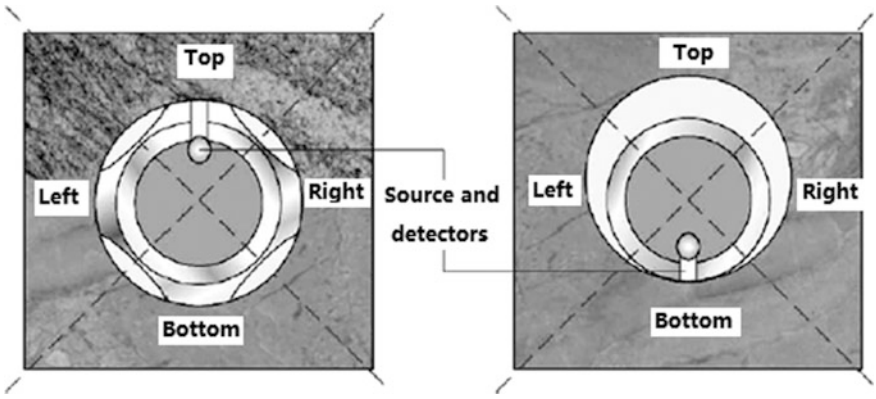

Fig. 7.7 An example of an LWD density tool is seen built into one side of the drill collar. As the pipe rotates the density is collected continuously and binned, in this example into four quadrants

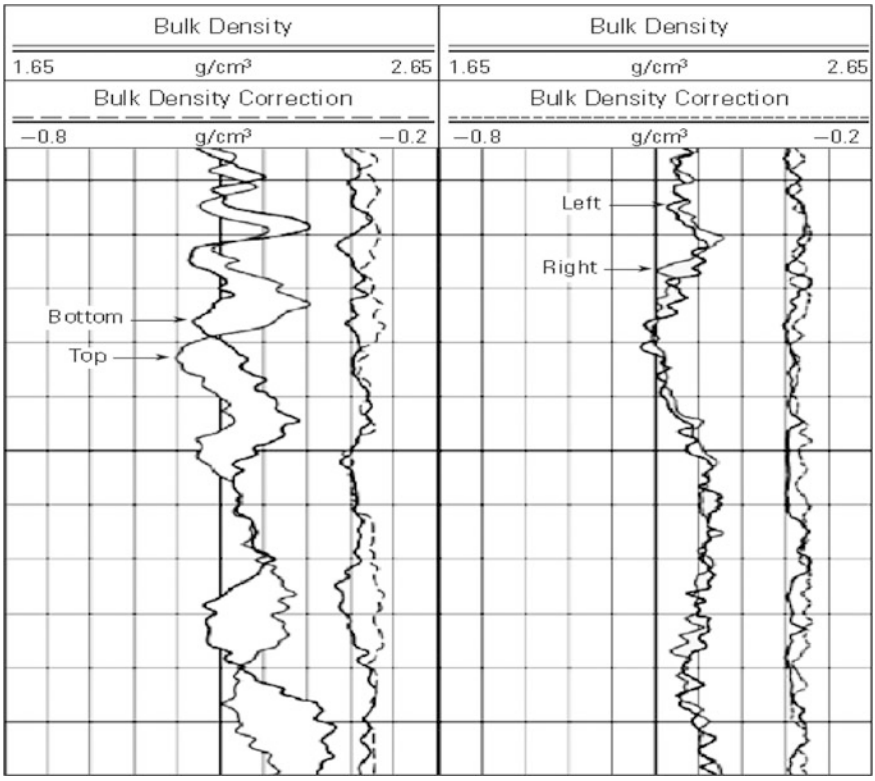

Fig. 7.8 An example of a LWD density log where the data has been collected in oriented quadrants. From Bourgois et al. 1998

or Pe-based images as an alternative method of sensing and quantifying dipping beds. Although the density measurements around the circumference may contain significant errors this information can be turned to good advantage to derive a "caliper" measurement. For this application the material in front of the pad is mainly mud, not mud cake. The mud density must be known to provide a good long-spacing detector apparent density, the standoff, unlike the compensation, can be estimated reliably up to approximately 3 in.

The great advantage of LWD density devices is their ability to measure at different azimuths. In the deviated wells the best reading is often in the bottom quadrant since it is there that the measurement is most likely to be in contact with the formation. However, several factors can complicate the interpretation: the presence of a bed of cuttings, which can cause the bottom density to read too low if it is thick; the tendency during rotation for the drill collar to ride up one side of the hole, causing some standoff on the bottom density; and the effect of invasion and of bed boundaries. An example of the latter is shown in Fig. 7.9. In zone A, the neutron–density separation indicates gas while the bottom density reads higher than the others. Since the DRHO curves indicate no standoff in any quadrant, the likely

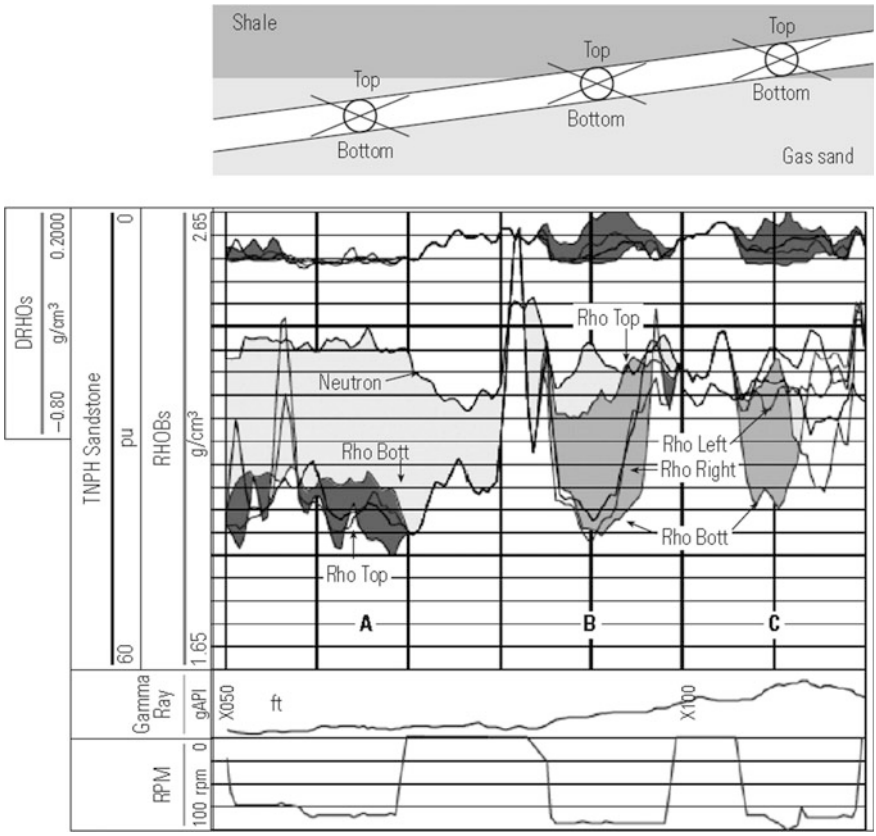

Fig. 7.9 Density and neutron logs from a HZ well with (above) an interpretation of the borehole moving up from a gas sand into a shale. *RPM* revolutions per minute of drill-string. From Holenka et al. used with permission

interpretation is that gravity has caused gas to displace the filtrate above and at the sides, with only the bottom quadrant seeing filtrate. Between A and B, the RPM log in track 1 shows a section with no rotation. The detectors are normally oriented toward the bottom when sliding, as here, and therefore see filtrate. At B the top density reads higher than the others, which is best explained by the drill collar entering a shale. By C the left and right quadrants have entered the shale, soon followed by the bottom quadrant. In this example the neutron–density separation clearly indicates the presence of gas. If there had been oil instead, the effect on the density readings would have been less, but much harder to interpret. This example illustrates the variety of factors invasion, standoff, and bed boundaries that must be kept in mind when studying the logs. Given these factors it is perhaps not surprising that several studies have shown systematically lower density readings from high angle (HA) or horizontal (HZ) wells than from vertical wells in the same reservoir. The causes of the differences could not always be uniquely identified, and therefore

could not be easily corrected. Nonetheless, in one particular case of a formation which consisted of alternating thin sand-shale sequences a satisfactory explanation for the density difference seen between logging vertical and highly deviated wells was achieved by the use of detailed tool modeling. In the case of vertical logging, the resolution of the measurement is determined by the tool vertical resolution which is on the order of the source-detector spacing. For beds of thickness much smaller than this dimension (30–40 cm) the device simply returns the average density of the beds contained within that spacing. When the tool is nearly parallel to the laminated beds, it is the depth of investigation (generally much smaller than the source-detector spacing) that controls the measurement. The tool will read the correct density of a bed of only a few inches thickness if it lies next to the HZ well bore. Thus, it can be anticipated that when the bed thickness is much less than 30–40 cm, the porosity of the sand beds estimated from the horizontal measurement will be more representative of the reservoir property than one derived from a vertical density measurement.

One of the advantages of the LWD density, with its proximity to the drilling bit, is the relatively short time between drilling and measurement. From this fact come two advantages. The first is the condition of the borehole wall that usually deteriorates with time. Thus rugosity is at a minimum. The second is the short time available for invasion to proceed. This means that the value of ρ_f must not be assumed to be mud filtrate but rather the virgin formation fluid. Hansen and Shray have documented the consequences of using an incorrect fluid density for interpreting an LWD density log in an oil reservoir containing light hydrocarbons.

7.7 Nuclear Measurements While Drilling

The most fundamental change in the nuclear tool is detector design. The first generation used a combination of ^{3}heium(He) detectors, also used in wireline tools, and Geiger–Muller detectors. Compared to Geiger–Muller detectors, ^{3}He detectors, have a broader dynamic range, do not need correction for spurious activation, are less affected by borehole salinity and have better statistics, permitting a higher rate of penetration (ROP). But they were not thought to be as rugged as Geiger–Muller detectors. Field experience proved otherwise, and since 1990 the CDN tool uses ^{3}He detectors only Older tools are being retrofitted.

The CDN tool has a 7.5-curie241 americium–beryllium neutron source and a 1.7-curie137cesium density source, both connected to a source retrieval assembly. In the first version of the tool, the sources and retrieval head were connected with a flexible titanium rod, giving more reliable retrieval and more accurate placement of the source. Also improved is the density detector shielding, which eliminates sensitivity to spurious signals from the mud.

The CDN tool uses a full-gauge stabilizer with windows cut in the blades in front of the density source and gamma ray detectors (top). When the hole is in gauge, the blades wipe away mud from in front of the sensors, thereby minimizing borehole

effects. A locking mechanism is being retrofitted on the stabilizer to increase its resistance to slippage under high torque and jarring. New stabilizers with an integrated lock are under design and scheduled for release next year. A range of stabilizer, including under-gauge sizes, has been added for use in horizontal and deviated holes.

Memory of the CDN and CDR tools was double to 1 Mb in 1991, and with the introduction of Anadrill's second-generation MWD/telemetry system in 1991, downlink to the tools can be established while they are in the hole. Previously, tool operation, such as data sampling rate had to be preset at the surface and was not adjustable once the tool was downhole. The downlink capability permits, for example, the operator to use one CDR sample rate while tripping out, or to turn sampling off in front of casing, thereby saving memory. The current generation mud telemetry system permits transmission of data at up to 3 bit/sec.

Another advance is the introduction of a downhole shock measurement transmitted to surface. This measurement enhances selection of the bottom-hole assembly (BHA) and drilling parameters, and may increase survival of MWD/LWD tools. Many failures of MWD/LWD tools result from high shock and vibration produced during drilling. Lateral vibration contains the most energy and does the most damage to downhole tools, the drill string and drill bits. Traditionally, engineers predicted a rough running drilling environment from surface torque measurement and modeling of drill-string dynamics. But this is not a direct shock measurement and therefore does not properly account for all causes of vibration and for frictional loss between the surface and BHA. Now the driller can see the downhole environment in real time and adjust rotary speed, weight-on-bit and flow rate to eliminate or reduce shocks. The drilling engineer can also use this information to design BHAs less prone to vibration.

When geosteering was introduced, the CDR (as shown in Fig. 7.10) resistivity log was used for detecting hydrocarbons and gamma ray log finding marker beds and kick off points. Because the CDR measurement has higher resolution and

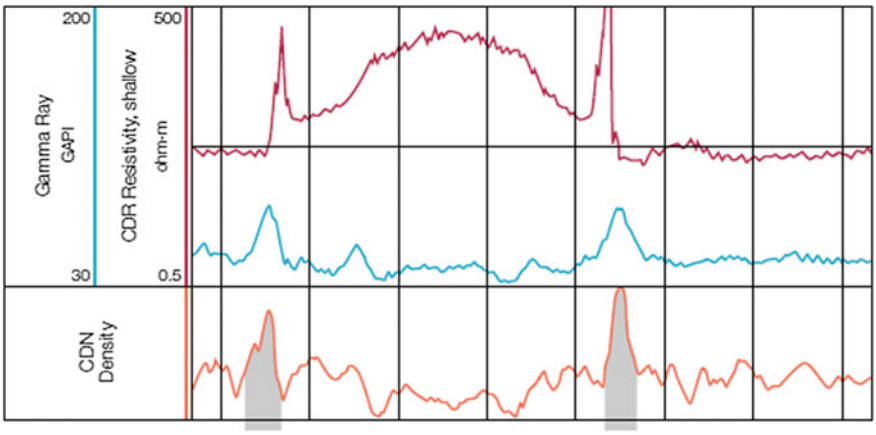

Fig. 7.10 CDR curves of LWD logging

precision than the typical MWD short-normal resistivity measurement, thin beds can be more easily identified. It is also more sensitive to boundaries between beds of contrasting resistivity indicated in a deviated well by the characteristic peak on the log curve, call horn—and has a greater depth of investigation.

Although resistivity remains the main headlight, a handful of operators have recently examined CDN density logs to see if they can contribute to geosteering. However, the CDN tool is always farther from the bit than the resistivity measurement so its contribution to steering may be as confirmation of gamma ray and resistivity logs (as shown in Fig. 7.10).

Comparison of wireline and CDN density and neutron porosity logs (Fig. 7.11) in a vertical well drilled with fresh mud. Above and below the bar, the hole was

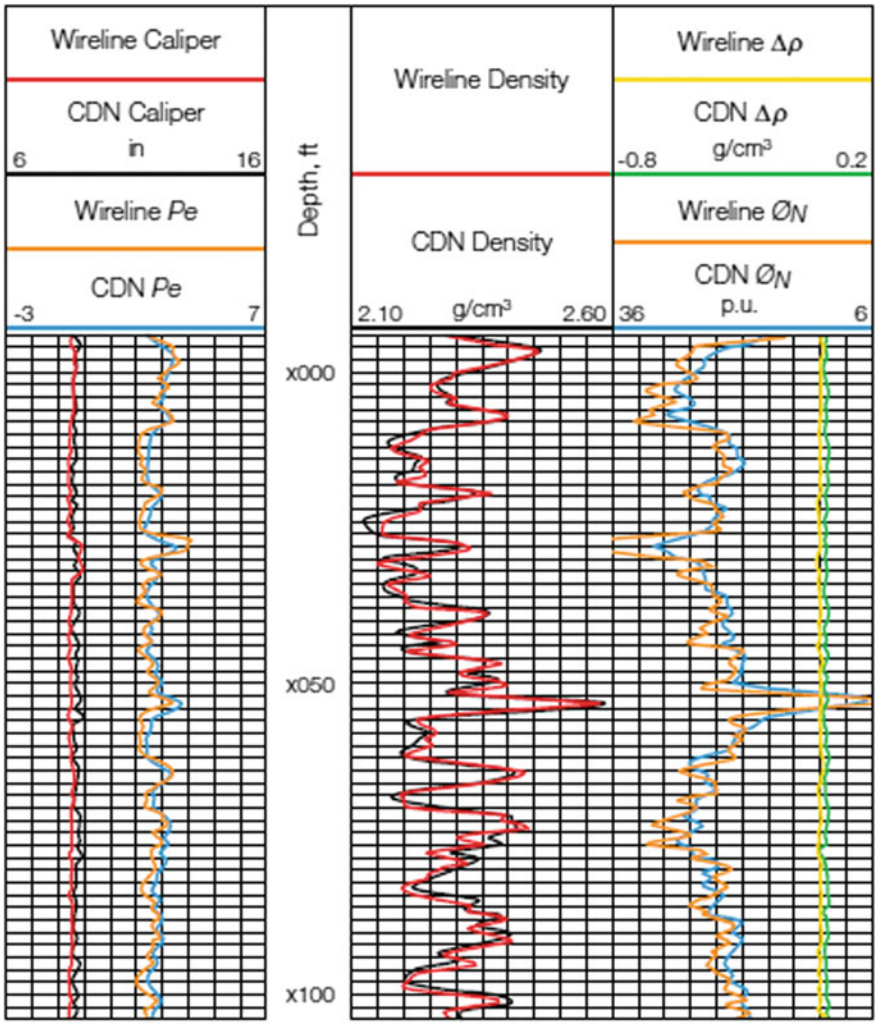

Fig. 7.11 Density and CNL curves of wireline and LWD logging

smooth and in gauge during a bit trip after being open several hours. Here, the CDN, Δp is high, consistent with a 9 pounds per gallon mud weight, and DCAL is close to zero. This combination of readings the hole was enlarged enough to prevent the CDN tool from maintaining contact with the formation. The combination of a well-stabilized BHA and lack of hole deviation produced this standoff. By wireline time, the caliper indicates mud cake had formed. Arrows mark rugose intervals where wireline density reads too high. In these intervals, the CDN measurement would be preferred, while in the zone by the bar, wireline density would be preferred.

Close agreement between wireline and LWD density logs in a North Sea well Divergence of neutron porosities is probably due to differences in the physics of wireline and CDN measurement-wireline density is a purely thermal measurement, whereas the CDN density measure a combination of thermal and epithermal neutrons.

7.8 Sonic Measurements While Drilling

The drilling environment hardly seems the best place to attempt to do acoustic logging, regardless of the anticipated benefits. It is a very acoustically noisy environment and the drill collar, which must house the instrument components, is a stiff cylindrical pipe capable of producing high amplitude arrivals to obscure the measurement. Despite these obstacles, by designing a periodic grooved structure to isolate the transmitter from the receivers in certain frequency bands and placing the receivers far from the bit, the first LWD acoustic tools capable of measuring compressional and fast shear velocities appeared in the mid-1990s. Next, it was logical to attempt to make a direct shear velocity measurement using a dipole source as is done in wireline acoustic tools. Although some devices with dipole sources were constructed, it soon became apparent that there were additional problems associated with the LWD environment. First of all, the drill collar is stiff and cannot be made as flexible as a wireline tool can, so the dipole source excites flexural waves in the drill collar that cannot be easily separated from the formation signal. Some tools have been designed with attenuators in the drill collar to reduce the energy transmitted through the tool but the dispersion of the borehole flexural signal makes it difficult to get an accurate formation shear slowness. Theoretical studies and modeling indicate that the use of a quadrupole source would provide a good possibility to couple energy to the formation while avoiding exciting the drill collar. Quadrupole wave propagation in the drill collar has a cutoff frequency so that for a given collar thickness it is possible to find a frequency below which energy is only coupled to the formation. Unfortunately, the most easily detected quadrupole-excited borehole wave has a quite different dispersion relation compared to the wireline dipole flexural wave dispersion. Rather than having an asymptote at low frequencies that gives the formation shear slowness, the quadrupole dispersion ends abruptly at some low-frequency cutoff (like the collar

behavior) making it difficult to determine the precise value of the shear slowness. Solutions to these issues are currently under development and new tools are on the horizon to exploit this type of source (and detection) for the shear velocity information.

LWD acoustic measurements have provided the possibility of detection of overpressured zones in real time. Wireline measurements can only "detect" overpressured zones from the deviations from a trend after the fact. It is of much greater utility, during the drilling process, to be able to detect the onset of an overpressured zone so that a reaction to it can be made before it gets too large.

7.9 Geosteering

The term "geosteering" means deciding the direction in which to drill from knowledge of the geology and from measurements taken while drilling. Instead of drilling to reach a preset target the course of the well is altered according to the formations encountered during drilling. At first sight this may seem simple: detecting from an LWD gamma ray device when the well has exited a sand into a shale should not be difficult. However, it is necessary to know in which direction the well has exited the sand. The basic problem is illustrated in Fig. 7.12. Has the well exited from the top or the base of the sand, or has it hit a fault? A second, practical, problem is that to do this successfully the measurements must be as close to the bit as possible, otherwise the bit will have gone too far before any change can be detected and made.

To examine this further we can consider the four possibilities: either the well enters a shale or a sand, and either from the top or from the bottom, as shown in Fig. 7.13. If the well has entered a shale, as in the left half of the figure, the well must be turned to reenter the sand. With two non-azimuthal measurements, such as a gamma ray and a propagation resistivity, it is not possible to know whether the sand is now above or below the well. With two directional measurement, either from resistivity buttons or density segments, it is possible to tell by observing whether the up measurement changes before or after the down measurement. With only one azimuthal measurement, it is still possible to separate the cases by observing whether it changes at the beginning or end of the slope on a non-azimuthal measurement.

In the other two cases, of a well entering a sand, the current course can be held, but it may be better to turn and run parallel to the sand-shale boundary. In the case of a fault, the two non-azimuthal measurements should respond at the same depth. Clearly, a measurement at a single azimuth might respond to other formation features than a boundary, for example, a nodule or a fracture. Complete images from multiple azimuthal measurements will provide a much clearer picture as to whether the well is passing through a boundary or some other feature (see the bottom of Fig. 7.13). Unfortunately not all situations are as simple as those of Fig. 7.13. There are often multiple sand-shale layers, so that it is difficult to know

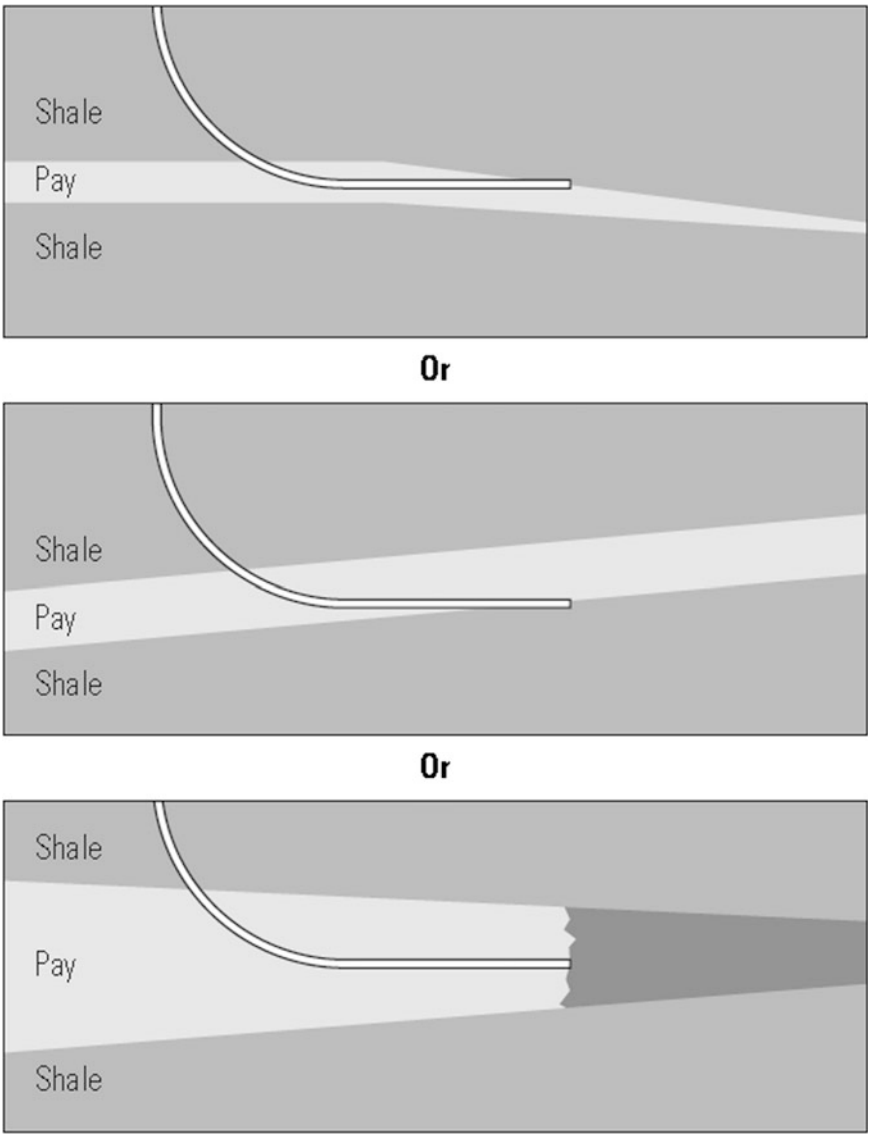

Fig. 7.12 The three possibilities when a HA well goes out of a pay zone into a shale. Courtesy of Schlumberger

which one is being penetrated. Furthermore the resistivity buttons and density detectors that make these few inches above or below the drill collar. Propagation resistivity devices see a few tens of inches away from the drill collar but are not azimuthally focused.

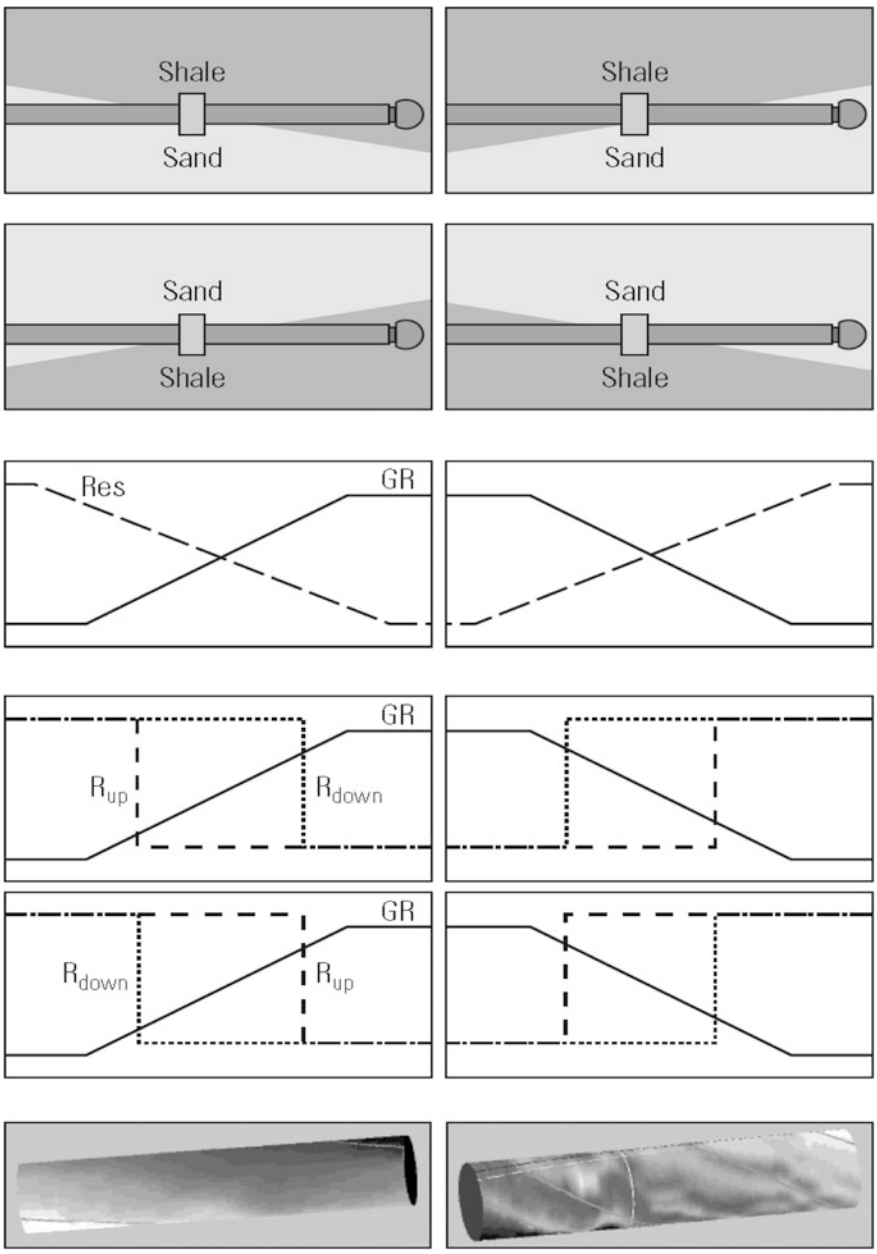

Fig. 7.13 The four possibilities when a well moves *up* or *down* from sand to shale or vice versa, showing the response of non-azimuthal measurements, focused measurements (*up* or *down*), and resistivity images (*light color* is *high resistivity*). Images adapted from Rasmus et al.

During the drilling of the well the actual recorded logs are compared with the simulated logs. Since the actual trajectory and geology may be different than planned, the simulations may need updating as drilling proceeds. If the recorded logs match the simulated logs, it is a reasonable assumption that the well is on target (although as with any modeling exercise there are no unique solutions). If a difference starts to develop, the recorded logs can be compared with the data bank of alternative scenarios to try and understand what might have happened; for example has the well exited the target into the shale above, or is it just crossing a thin stringer in the middle of the reservoir?

Problems

7.1 What are the merits of EcoScope series?
7.2 What are the applications of RAB, especially the azimuthal resistivity while drilling?
7.3 Understand the principle and applications of Sonic, Density and neutron logging while drilling.
7.4 Based on the example of Fig. 7.12, explain the definition of Geosteering, and how does the Geosteering carry on?

Chapter 8
Rock Mechanics

Rock mechanics is defined as "the fields of study devoted to understanding the basic processes of rock deformation and their technological significance." The significance of these processes to petroleum engineers is considerable. For instance, being able to predict the mechanical behavior of underground formations is a key to avoid borehole instabilities during drilling. If rock deformation results in a noticeable contraction of the wellbore due to the state of induced stress in the rock formation immediately adjacent to the wellbore, the motion of the drill bit may be restricted or the emplacement of the casing, after drilling ceases, may be hampered. If the deformation results in a large expansion of the wellbore, the rock formation may fracture and result in lost circulation. Predicting the mechanical behavior of reservoir rock is essential for well completion or stimulation programs. Reservoir compaction, which may lead to surface subsidence, is a critical factor with respect to design of the casing platforms and to the overall reservoir performance.

Rock mechanical properties, such as Poisson's ratio, shear modulus, Young's modulus, bulk modulus, and compressibility can be obtained from two different sources:

(1) laboratory measurements, which allow for direct measurements of strength parameters and static elastic behavior with recovered core material from discrete depths; and
(2) downhole measurements through wireline logging, which allow the determination of dynamic elastic constants from the continuous measurement of compressional and shear velocity.

H. Liu, *Principles and Applications of Well Logging*, Springer Mineralogy,
DOI 10.1007/978-3-662-53383-3_8

8.1 Basic Stress and Strain Analysis

8.1.1 Static Stress and Strain Relation

Poulos and Davis developed the following analytical model of the evaluation of the static stress–strain relation. Consider a cubic rock sample in a three-dimensional stress field, as shown in Fig. 8.1.

8.1.1.1 Stress Analysis

If a rock body is subjected to an external load or force, internal stresses are developed. If these stresses are strong enough, the rock deforms. Deformation refers to changes in shape (distortion) accompanied by change in volume (dilation). Three basic internal stress conditions are recognized: compressive, shear, and tensile, as illustrated in Fig. 8.2. Compressive stresses occur when external forces are directed toward each other along the same plane. If the external forces are parallel and directed in opposite directions along the same plane, tensile stress develops. Shear stress occurs when the external forces are parallel and directed in opposite directions, but in different planes.

If any plane is taken within a solid body, as shown in Fig. 8.3 along the *yz*-plane, then the internal components of stress may be resolved into normal stress (σ_{xx}) which acts at a right angle to the plane, and shear stress components, which act parallel to the plane (τ_{xy} and τ_{xz}). If the solid plane is taken along the *xz*-plane, the normal and shear stress components at point O are τ_{yx}, σ_{yy}, τ_{yz}, and in the *xy*-plane the three components are τ_{zx}, τ_{xy}, and σ_{xx}. Therefore, nine components of stress are required to fully define the forces acting on the cubic element. The stress matrix is:

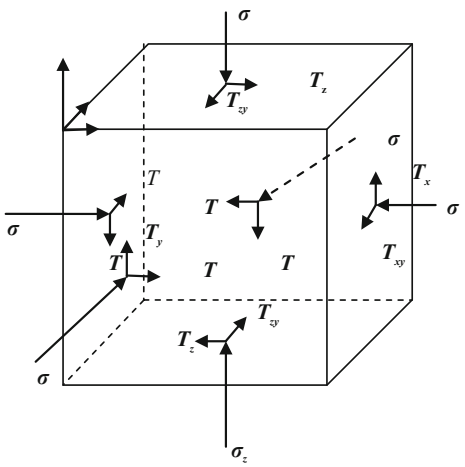

Fig. 8.1 Three-dimensional stress field of a *cubic rock*

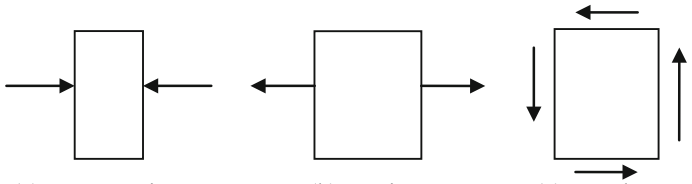

Fig. 8.2 Representation of tension, compression, and shear or couple

Fig. 8.3 Stress at point O in a plane

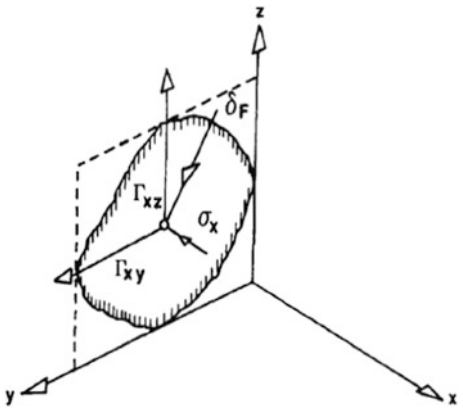

$$\sigma_{xyz} = \begin{bmatrix} \sigma_{xx} & \tau_{xy} & \tau_{xz} \\ \tau_{yx} & \sigma_{yy} & \tau_{yz} \\ \tau_{zx} & \tau_{zy} & \sigma_{zz} \end{bmatrix} \tag{8.1}$$

The notation τ_{ij} should be read as the "shear stress acting in the j direction on a plane normal to the i axis." By convention, the normal stresses σ_{xx}, σ_{yy}, and σ_{zz} or for convenience σ_x, σ_y, and σ_z are positive when directed into the plane. If the body is at equilibrium, then $\tau_{xy} = \tau_{yx}$, $\tau_{yz} = \tau_{zy}$, and $\tau_{zx} = \tau_{yz}$. In matrix operations, it is convenient to express the stress tensor as:

$$\sigma_{123} = \begin{bmatrix} \sigma_{11} & \tau_{12} & \tau_{13} \\ \tau_{21} & \sigma_{22} & \tau_{23} \\ \tau_{31} & \tau_{32} & \sigma_{33} \end{bmatrix} \tag{8.2}$$

It is possible to show that there is one set of axes with respect to which all shear stresses are zero and the normal stresses have their extreme values. The three mutually perpendicular planes where these conditions exist are called the principal planes, and the three normal stresses on these planes are the principal stresses (Fig. 8.4): σ_1 or σ_{11} (maximum or major), σ_2 or σ_{22} (intermediate), and σ_3 or σ_{33} (minimum or minor).

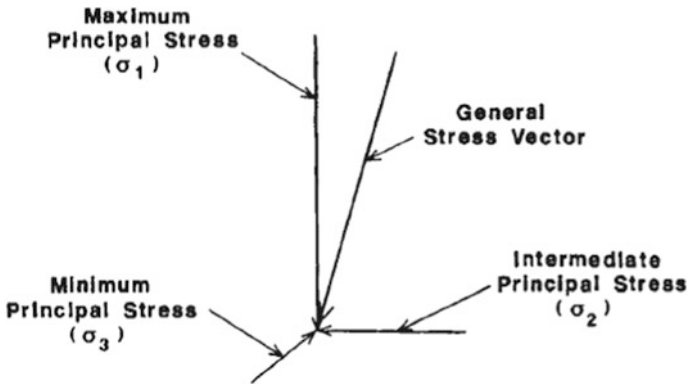

Fig. 8.4 Principal stresses acting on a point

The principal stress tensor is represented as:

$$\sigma_{\mathrm{p}} = \begin{bmatrix} \sigma_{11} & 0 & 0 \\ 0 & \sigma_{22} & 0 \\ 0 & 0 & \sigma_{33} \end{bmatrix} \tag{8.3}$$

The maximum shear stress at a point, $\tau_{\max}$, occurs on a plane at an angle of 45° with the σ_1 and σ_3 directions, and is given by:

$$\tau_{\max} = \frac{1}{2}(\sigma_{11} - \sigma_{33}) \tag{8.4}$$

8.1.1.2 Strain Analysis

Strain is defined as the compression (positive) or extension (negative) resulting from the application of external forces, divided by the original dimension. Two types of strain can be recognized: homogeneous and heterogeneous. When every part of a body is subjected to a strain of the same type and magnitude in any direction of the displacement, the strain is considered homogeneous. The strain is heterogeneous if it is not the same throughout the body. The strain is responsible for inducing body displacement, rotation, and strain. Shear strain, y, is defined as the angular change in a right angle at a point in a body and is related to the displacements in the x, y, and z directions. Assuming that a negative shear strain represents a decrease in the right angle and a positive shear strain represents an increase in the right angle:

$$\varepsilon_{xyz} = \begin{bmatrix} \varepsilon_{xx} & \frac{\gamma_{xy}}{2} & \frac{\gamma_{xz}}{2} \\ \frac{\gamma_{yx}}{2} & \varepsilon_{yy} & \frac{\gamma_{yz}}{2} \\ \frac{\gamma_{zx}}{2} & \frac{\gamma_{zy}}{2} & \varepsilon_{zz} \end{bmatrix} \tag{8.5}$$

where ε_{xx}, ε_{yy}, and ε_{zz} are the normal strains.

In matrix operations, it is convenient to use the double suffix notation and to define $\gamma_{ii}/2$ as ε_{ij}. The strain matrix is then:

$$\varepsilon_{xyz} = \begin{bmatrix} \varepsilon_{xx} & \varepsilon_{xy} & \varepsilon_{xz} \\ \varepsilon_{yx} & \varepsilon_{yy} & \varepsilon_{yz} \\ \varepsilon_{zx} & \varepsilon_{zy} & \varepsilon_{zz} \end{bmatrix} \tag{8.6}$$

The shear strains in the three principal planes of strain are zero, and the normal strains are the principal strains. The greatest and least normal strains at a point are preferably referred to as the major and minor principal strains. The principal strains are determined in a similar manner to principal stresses.

The maximum shear strain, $\gamma_{\max}$, occurs on a plane whose normal makes an angle of 45° with the ε_1 and ε_3 directions, and is calculated from:

$$\gamma_{\max} = \varepsilon_1 - \varepsilon_3 \tag{8.7}$$

where:

ε_1 maximum principal normal strain, MPa; and
ε_3 minimum principal normal strain MPa.

The principal strain tensor is represented as

$$\varepsilon_{\mathrm{p}} = \begin{bmatrix} \varepsilon_1 & 0 & 0 \\ 0 & \varepsilon_2 & 0 \\ 0 & 0 & \varepsilon_3 \end{bmatrix} \tag{8.8}$$

The sum of the principal strains is the volumetric strain or dilatation, ΔV

$$\Delta V = (\varepsilon_1 + \varepsilon_2 + \varepsilon_3)v \tag{8.9}$$

where V is the initial volume of the rock. In as much as strain is a ratio of volumes or lengths, it is dimensionless.

8.1.2 Parameters of Rock Elastic Properties

A number of methods have been used to determine the dynamic values of Young's modulus and Poisson's ratio. Hosking obtained the dynamic values of various elastic properties by determining the velocities of propagation in rock using ultrasonic pulse, v_{p}, and the sound of resonance, v_{r}. Young's modulus is obtained from:

$$E = \frac{F/A}{\Delta L/L} \tag{8.10}$$

where:

F is the force on the material, N;
A is the surface area of the material, cm^2;
L is the length of the material at the same direction with force, cm;
ΔL is the deformation of length, cm;

and Poisson's ratio from:

$$v = \frac{\Delta d/d}{\Delta L/L} \tag{8.11}$$

where:

d is diameter of the material, or length perpendicular to L, cm;
Δd is the deformation of the diameter, cm.

Deere and Miller used a similar method to derive the following relationship between compressional wave velocity (v_c), density of the rock (ρ_b), Young's modulus, and Poisson's ratio:

$$v_s = \frac{\rho_b E(1-v)}{(1+v)(1-2v)} \tag{8.12}$$

Sonic logging and wave form analysis provide the means for obtaining continuous measurements of compressional and shear velocities. These data, in conjunction with bulk density measurements, permit the in situ measurement and calculation of the mechanical properties of the rock. Table 8.1 shows the elastic moduli relationships in terms of transit times and bulk density. The units applicable to the table are: ρ_b = bulk density, g/cm^3.

Table 8.1 Parameters of rock properties

v Poisson's ratio	$\frac{\text{Lateral strain}}{\text{Longitudinal strain}}$	$\frac{\Delta t_s^2 - 2\Delta t_c^2}{2(\Delta t_s^2 - \Delta t_c^2)}$
E Young's modulus, psi	$\frac{\text{Applied uniaxial stress}}{\text{Normal strain}}$	$\frac{a\rho_b}{\Delta t_s^2}\frac{3\Delta t_s^2 - 4\Delta t_c^2}{\Delta t_s^2 - \Delta t_c^2}$
G Shear, psi	$\frac{\text{Applied stress}}{\text{Shear strain}}$	$\frac{a\rho_b}{\Delta t_s^2}$
K_b Bulk Modulus, psi	$\frac{\text{Hydrostatic pressure}}{\text{Volumetric strain}}$	$a\rho_b\frac{3\Delta t_s^2 - 4\Delta t_c^2}{3\Delta t_s^2\Delta t_c^2}$
C_b Bulk Compressibility (with porosity), psi	$\frac{\text{Volumetric deformation}}{\text{Hydrostatic pressure}}$	$\frac{1}{K_b}$

v_s = shear velocity, ft/sec
where,

a is a coefficient for unit change
Δt_s shear transit time, μs/ft
Δt_c compressional transit time, μs/ft.

Generally, dynamic elastic constants are derived from the measurements of elastic wave velocities in rocks. Equipment such as geophones and seismographs can be used to measure in situ values of wave velocities. Inasmuch as the static moduli are required for design of most rock engineering projects, however, dynamic moduli measurements are not common. Also, equations used to calculate dynamic moduli assume ideal rocks, i.e., the rock is perfectly linear elastic, homogeneous, and isotropic. Reservoir rocks, of course, are not ideal. This causes the values of static and dynamic moduli to be different. Therefore, dynamic testing techniques will provide meaningful design data if dynamic moduli values can be converted into static values. Many studies aimed at establishing a relation between dynamic and static moduli showed that the dynamic modulus of elasticity, E_d, tends to be greater than its static equivalent, E_s, and that v_d is slightly smaller than versus, such as E_s, using experimental data, the following correlation is obtained:

$$E_s = \exp\left[\frac{1.843 \ln E_d}{\sigma^{0.0724}} + 0.45 \ln (0.0266\sigma)\right] \tag{8.13}$$

where σ is the uniaxial compressive strength in MPa, and E_s is static Young's modulus expressed in G_{Pa}.

This correlation makes it possible to predict approximate values of the static Young's modulus from dynamic measurements for most reservoir pressures. Ten different types of rock materials were used to derive this correlation, including several sandstones, quartzites, and magnetite.

8.2 Natural Fracture Classification and Stress Analysis

The stress conditions at the bottom of the wellbore greatly influence the strength and ductility of the rock being drilled or fractured. A knowledge of the stress redistribution that occurs on drilling a wellbore is important in understanding (1) the causes of the reduction in the rate of penetration, (2) fluid loss problems, and (3) borehole and perforation instability problems in friable clastic formations.

8.2.1 Natural Fractures

Naturally fractured zones are important, because of the extra drainage and considerable increase in porosity and permeability they promise. Although fractures can have a very significant effect on the total permeability of a rock, they usually have very little effect on the porosity, saturations, or other petrophysical characteristics of the rock.

Natural fractures generally exhibit certain constant characteristics:

They are usually approximately perpendicular to the dip; this does not, however, exclude the possibility of horizontal fractures, although horizontal fractures are much less frequent and less extensive than subvertical fractures.

(1) They are usually oriented according to one (or more) prevailing strikes. Since fractures are often the result of tectonic stresses, the prevailing strike of the fractures generally coincides with the orientation of the faults in the region.
(2) They frequently cause small amounts of rock to be broken off from the borehole wall by the drill bit or drill string during drilling.
(3) They usually occur in compact, competent rocks where the hole would normally be cylindrical and in gauge the absence of fractures.

Only fractures that are at least partially open are useful from the point of view of production.

8.2.2 Geological Classifications of Natural Fractures

Natural fracture patterns are frequently interpreted on the basis of laboratory-derived fracture patterns corresponding to models of paleo-stress fields and strain distribution in the reservoir at the time of fracture.

1. **Classification based on stress/strain conditions** Stearns and Friedman proposed classification based on stress/strain conditions in laboratory samples and fractures observed in outcrops and subsurface settings. On the basis of their work, fractures are generally classified as follows:

   (1) ***Shear fractures*** exhibit a sense of displacement parallel to the fracture plane. Shear fractures are formed when the stresses in the three principal directions are all compressive. They form at an acute angle to the maximum principal stress and at an obtuse angle to the direction of minimum compressive stress.
   (2) ***Extension fractures*** exhibit a sense of displacement perpendicular to and away from the fracture plane. They are formed perpendicular to the minimum stress direction. They too result when the stresses in the three principal directions are compressive and can occur in conjunction with shear fracture.

(3) ***Tension fractures*** also exhibit a sense of displacement perpendicular to and away from the fracture plane. However, in order to form a tension fracture, at least one of the principal stresses has to be tensile. Since rocks exhibit significantly reduced strength in tension tests, this results in increased fracture frequency.

2. **Classification based on paleo-stress conditions** The geological classification of fracture systems is based on the assumption that natural fractures depict the paleo-stress conditions at the time of the fracturing. Based on geological conditions, fractures can be classified as in the following paragraphs.

(1) ***Tectonic fractures*** The orientation, distribution, and morphology of these fracture systems are associated with local tectonic events. Tectonic fractures form in networks with specific spatial relationships to faults and folds. Fault-related fracture systems could be shear fractures formed either parallel to the fault or at an acute angle to it. In the case of the fault wedge, they can be extension fractures bisecting the acute angle between the two fault shear directions. The intensity of fractures associated with faulting is a function of lithology, distance from the fault plane, magnitude of the fault displacement, total strain in the rock mass, and depth of burial.

(2) ***Fold-related fracture*** systems exhibit complex patterns consistent with the complex strain and stress history associated with the initiation and growth of a fold. Fracture types in fold-related systems are defined in terms of the dip and strike of the beds.

(3) ***Regional fractures*** These fracture systems are characterized by long fractures exhibiting little change in orientation over their length. These fractures also show no evidence of offset across the fracture plane and are always perpendicular to the bedding surfaces. Regional fracture systems can be distinguished from tectonic fractures in that they generally exhibit simpler and more consistent geometry and have relatively larger spacing.

(4) ***Regional fractures*** are commonly developed as orthogonal sets with the two orthogonal orientations parallel to the long and short axes of the basin in which the fractures are formed. Many theories have been proposed for the origin of the regional fractures, ranging from plate tectonics to cyclic loading/unloading of rocks associated with earth tides. As in the case of tectonic fractures, small-scale variation in regional fracture orientation of up to $\pm 20^{\circ}$ can result from strength anisotropies in reservoir rocks due to sedimentary features such as across bedding.

(5) ***Contractional fractures*** These types of fracture result from bulk volume reduction of the rock. Desiccation fractures may result from shrinkage upon loss of fluid in subaerial drying. Mud cracks are the most common fractures of this type. Syneresis fractures result from bulk volume reduction within the sediments by subaqueous or surface dewatering. Dewatering and volume reduction of clays or of a gel or a colloidal suspension can result in syneresis fractures. Desiccation and syneresis fractures can be either tensile or extension fractures and are initiated by internal body forces. The fractures

tend to be closely spaced and regular and isotropically distributed in three dimensions. Syneresis fractures have been observed in limestone, dolomites, shales, and sandstones.

(6) ***Thermal contraction fractures*** may result from contraction of hot rock as it cools. Depending on the depth of burial, they may be either tensile or extension fractures. The generation of thermal fractures is predicted on the existence of a thermal gradient within the reservoir rock material. A classic example of thermally induced fracture is the columnar jointing observed in igneous rocks.

Fractures may also result from mineral changes in the rock, especially in carbonates and clay constituents in sedimentary rocks. Phase changes such as the chemical change from calcite to dolomite result in changes in bulk volume, and this leads to complex fracture patterns.

It is clear from the above discussion that the complex stress/strain distribution in reservoir rocks results in complex fracture patterns. Fracture patterns corresponding to different geological systems have key characteristics that can be used to classify and index natural fracture networks observed in outcrops and subsurface samples.

8.2.3 Fracture Detection

Logging tools are designed to respond to different characteristics of the wellbore environment. Some tools respond primarily to lithology, some primarily to porosity, and others to fluid saturations. None, unfortunately, responds primarily to fractures although fractures, particularly open ones, may affect the response of some logging tools. The effect, however, is usually rather subtle. Thus, in the search for fractures using log measurements, it is necessary to understand both the basic tool physics and the geometry of all the measurements involved. Generally, only experience permits us to define the methods which, in a given location, will give the best results.

When looking for fractured zones on logs, the search is usually focused on are as where they are suspected for the following reasons:

(1) Local history of naturally occurring fractures.
(2) Lack of precision in seismic recordings.
(3) Extrapolation of observations on outcrops.
(4) Increase in the rate of penetration of the bit.
(5) Presence of crystals in the drill cuttings.
(6) Circulation losses during drilling.
(7) Poor core recovery.

(8) Fractured cores.
(9) Test results that are incompatible with the known or estimated porosities and permeabilities.
(10) Pressure interference between wells (production or injection).

8.2.3.1 Sonic Measurements

One of the oldest fracture indicators is the reverberation of sound waves in and around the borehole. Measurements based on sonic wave propagation respond to the mechanical properties of the rock and are little affected by the borehole environment.

In fractured zones, the appearance of the wavetrain, as recorded on the Variable Density log (VDL), shows sudden changes vague or blurred zones, chevron patterns, etc. (see Fig. 8.5). These features suggest interfaces of differing acoustic impedance between the transmitter and receiver of the sonic tool. Such propagation

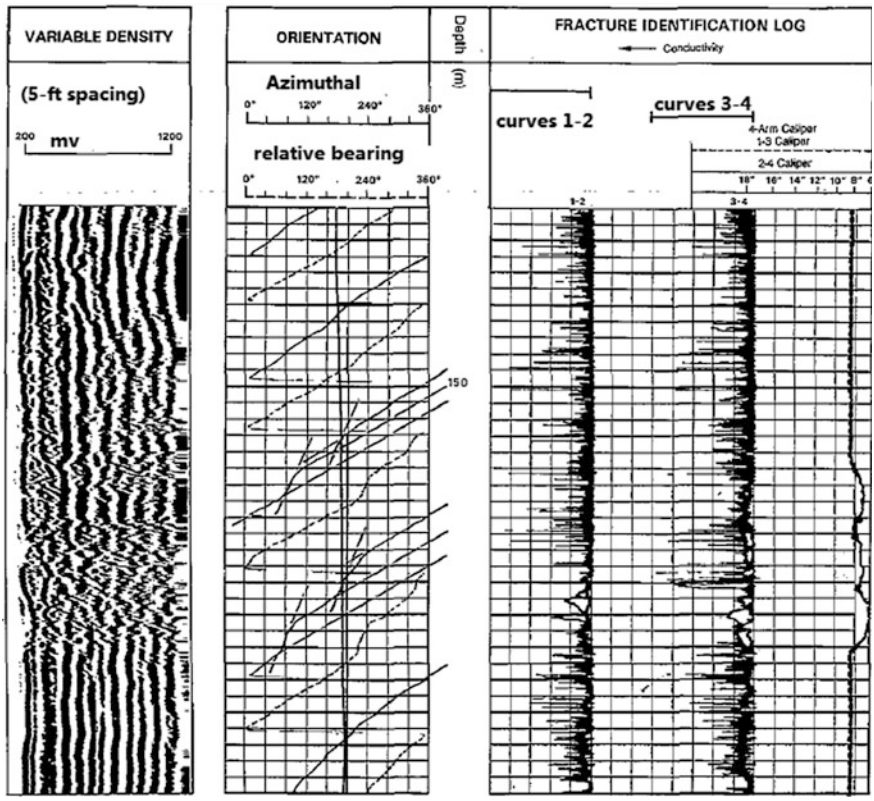

Fig. 8.5 Fracture identification with VDL display and fracture identification log

anomalies can be caused by open fractures. Unfortunately, similar anomalies can also occur with changes in the diameter of the borehole or because of thin beds of differing lithology or even a "healed" (closed) fracture system.

LSS long-spaced sonic and Array-Sonic tools have become popular for the recording of the sonic tools have become popular for the recording of the sonic wavetrain. In addition to the two travel times (shear and compressional), the energy of the compressional and shear wave packets and their respective frequency contents can also be recorded. The Array-Sonic tool emits a given amount of energy. By measuring the amount of energy that arrives at the receiver, an indication of the competence and uniformity of the formation can be obtained. High signal strength at the receiver suggests a competent rock with a low probability of fractures; very low signal strength suggests a high probability of fractures, other things being equal. Figure 8.6 is an example of a decrease of shear energy opposite a zone where fractures are suspected. At the fracture interface, some of the shear energy is reflected, some is converted to other modes of wave propagation, and some is refracted; as a result, the amount of shear energy reaching the receiver is significantly reduced.

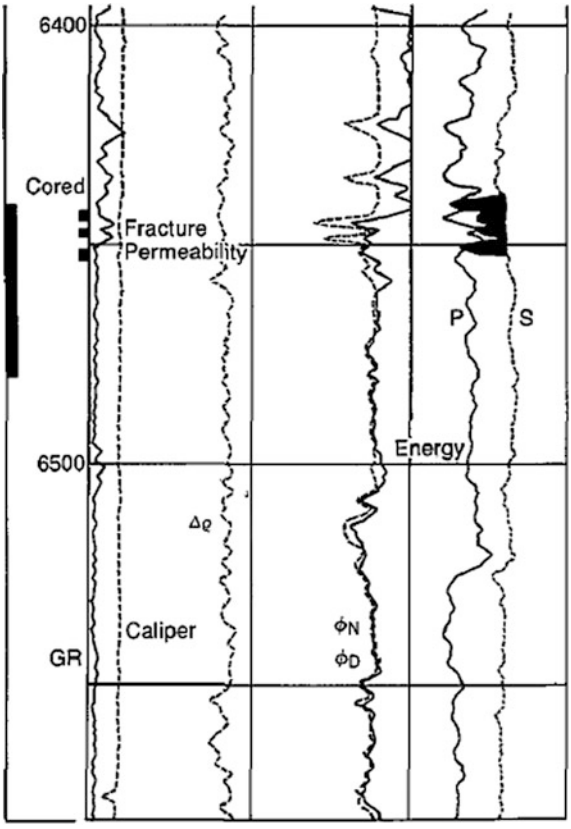

Fig. 8.6 Drop in shear energy indicates fractures

Another promising technique is a study of the mode conversion effects that take place when acoustic energy encounters fluid-filled fractures. At the intersection of the borehole and the fracture, the coupling between borehole and formation is enhanced because of the large surface area of contact. This greatly facilitates the conversion of acoustic energy from one of the formation modes to one of the borehole modes Stoneley (tube) waves and the various normal (pseudo-Rayleigh) modes or vice versa. When the transmitter or receiver is opposite the fracture, this mode conversion causes a characteristic spike in formation mode amplitude. Two such spikes separated by the transmitter–receiver spacing provide a reliable means of detecting fractures.

Figure 8.7 shows a 12-ft spacing sonic waveform in the vicinity of a large horizontal fracture. Points A and B are, respectively, the positions where transmitter and receiver are directly opposite the fracture. A sharp increase in the amplitude of the compressional and shear first arrivals can be easily seen.

Another feature, clearly discernible, is the crisis-cross patterns originating in the compressional and shear waves. However, anomalies caused by vertical fractures are more subtle. Poisson's ratio can be computed from the compressional and shear wave velocities (or transit times). Rocks with a high Poisson's ratio are more likely

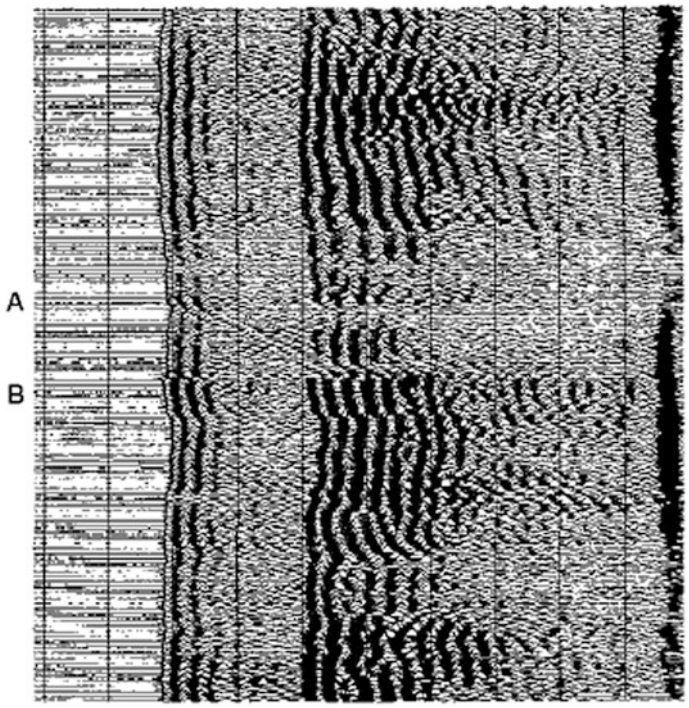

Fig. 8.7 Sonic waveform response over a large *horizontal fracture*

to have fractured zones than those with a low Poisson's ratio. Thus, some insight into the likelihood of fracturing can be obtained from Poisson's ratio.

With the advent of the Array-Sonic a sophisticated processing techniques, these sonic techniques for fracture recognition may be used in both openhole and casedhole.

8.2.3.2 Caliper Measurements

In drilling through a fractured zone, the rock edges of the fractures are often chipped away, thereby enlarging the borehole in the plane of the fracture system. Borehole enlargement and, particularly, borehole elongation in a formation expected to have an in gauge and circular borehole can indicate fractures. To detect fractures with a caliper log, a multi-arm, multidirectional caliper is preferred. The calipers recorded with the HDT high resolution diameter or Dual Diameter (SHDT) tools are examples. These four-arm calipers record two borehole diameters 90″ apart. One pair of arms is almost always aligned with the major axis of an elliptical borehole, the other pair with the minor axis. An elliptical or elongated borehole is, thereby, readily recognized.

8.2.3.3 Four-Arm Caliper Interpretation

A great deal of more information can be gained from dual caliper tools than from the simple caliper tool. As indicated above, dual caliper information is generally taken from the four-arm dipmeter tool.

Using just a single caliper, borehole shape cannot be interpreted. Data from a four-arm caliper, however, enables the shape of a hole to be much better defined. A hole can be seen to be on gauge and round (Fig. 8.8a) or enlarged by a key seat (Fig. 8.8b) or oval, washed out (Fig. 8.8c) and breakout (Fig. 8.8d). When oval, the direction of enlargement can be given. However, much more can be interpreted from borehole shape.

Three main types of elliptical borehole have been recognized, keyseats, washouts, and breakouts. Washouts develop from general drilling wear, especially in shaly zones and dipping beds. On the geometry logs, a washout has a considerable vertical extent and both calipers are larger than the drill bit size with one caliper being much larger than other. Shape changes are variable and gradual. Keyseats are asymmetric oval holes, formed by wear against the drill string at points where the borehole inclination changes (dog-legs). Both washouts and keyseats are general drilling phenomena: breakouts, however, have a special cause.

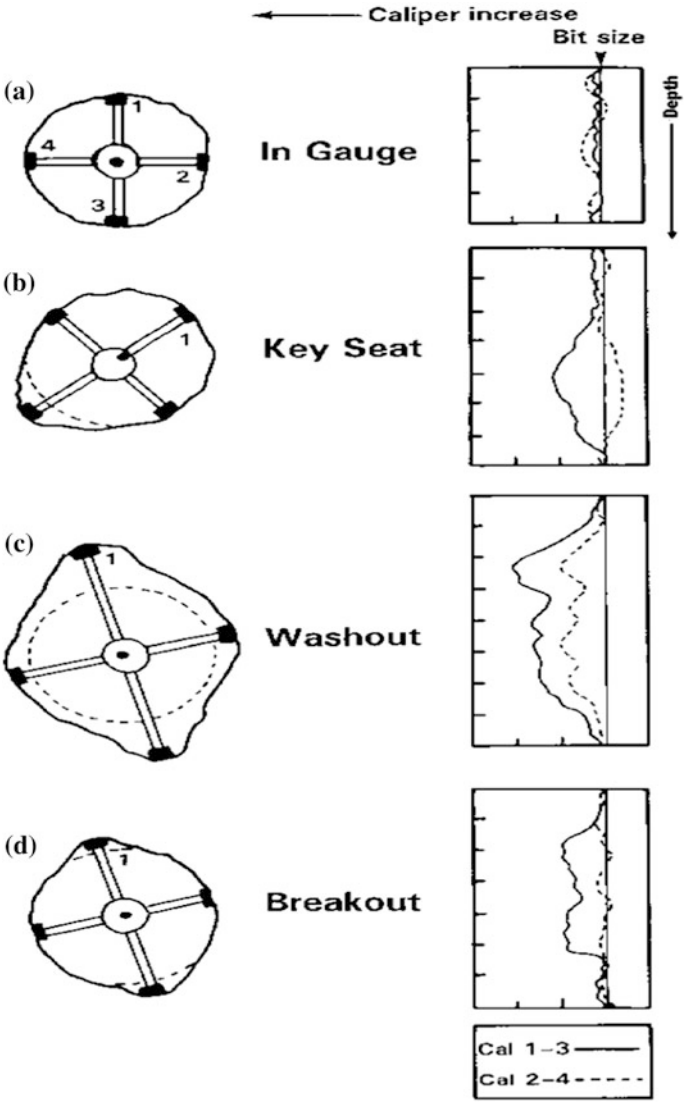

Fig. 8.8 Diagrammatic representation of types of borehole shape and profile as identified on the two-arm caliper

Breakouts are recognized using the following strict criteria:

1. The tool must stop rotating (ideally the tool should rotate before and after a breakout zone)
2. The caliper must separate to indicate an ovalhole: the larger caliper should exceed hole gauge, the smaller caliper should not be less than hole gauge and its

trace should be straight (the caliper difference should be larger than 6 mm and the zone of elongation greater than 1.5 m). The limits of the breakout should normally be well marked
3. The larger diameter of hole elongation and its direction should not consistently coincide with the azimuth of hole deviation.

Breakouts are considered to form as a result of the interaction of stresses induced by drilling and the existing stress regime of the country rock. Small brittle fractures (spalling) occur in the borehole around a rotating bit which, if there is unequal horizontal stress in the formation, form in a preferential direction of the minimum horizontal stress, Sh_{min} (Fig. 8.9a). In more precise terms, compressive shear fracturing of the minimum horizontal formation stress Sh_{min}, and is the cause of breakouts. Laboratory experiments and empirical observations seem to back up the theory. Hence breakouts indicated the present day stress-field orientation and are independent of lithology, dip, and existing fractures or joints.

Breakout studies to define in situ stress fields are now being carried out on many scales from the local to the global. On the global scale, breakout derived stress-field orientations are similar to those derived from earthquake studies and tend to indicate intra-plate tectonic stresses. On a local scale, breakout studies have an importance for field development. Natural and artificial fractures are most likely to be oriented in the maximum horizontal stress direction Sh_{max} (i.e., normal to breakouts) (Fig. 8.9b). Fracture connection between wells during field production is then more likely in this orientation. It is also possible that horizontal drilling will be more stable in the Sh_{max} (maximum horizontal stress) direction.

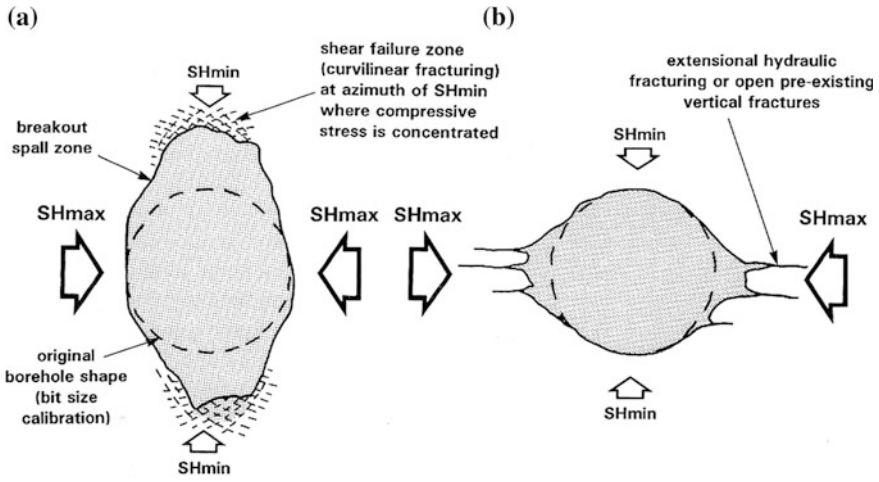

Fig. 8.9 Horizontal stress field relationship to *borehole shape*. **a** Breakout formation due to spalling during drilling, in the direction of minimum horizon stress (Sh_{min}). **b** Hole enlargement along drilling induced extensional fractures oriented in the direction of maximum horizontal stress (Sh_{max})

a. round, in gauge hole.
b. key seat hole enlargement at a dog-leg.
c. washout hole enlargement due to general drilling wear.
d. breakout, showing characteristic oval hole with abrupt vertical limits.

8.2.3.4 Borehole TeleViewer Tool

The borehole televiewer is an acoustic scanner. As it is pulled up the hole, it scans the borehole wall with a rotating transducer that emits a pulsed ultrasonic beam. A visual representation of the pattern of acoustic reflectivity off the borehole wall is displayed on a cathode-ray tube. The image shows the borehole wall as if it were split vertically and laid flat. Vertical fractures appear as straight lies, while fractures dipping between vertical and horizontal appear as sinusoidal traces.

Initial popularity of the tool waned because of the operational difficulty and environmental limitations. The results are poor in elongated, rugose, or collapsing boreholes, and these conditions are common in fractured intervals. The tool and signal processing have been improved to the point that the service is now regaining some of the lost popularity.

8.2.3.5 Other Measurements

There are several other methods that sometimes provide insight into possible fractured intervals in specific locales. These include locating radioactive streaks with the gamma ray or NGS* natural gamma ray spectrometry tools, special pulsed-neutron techniques, EPT* log response, temperature, and noise anomalies.

8.2.4 Visual Identification of Fractures

Nelson defined, for consistency, four useful terminologies to describe cracks in a rock as:

(1) **Fracture** any break in the rock;
(2) **Fissure** an open fracture;
(3) **Joint** one or a group of parallel fractures which has no detectable displacement along the fracture surface; and
(4) **Fault** a fracture with detectable displacement.
(5) All these features can be visually identified on a core or borehole electrical images. Figure 8.10 shows three types of fracture that may be visually detected:

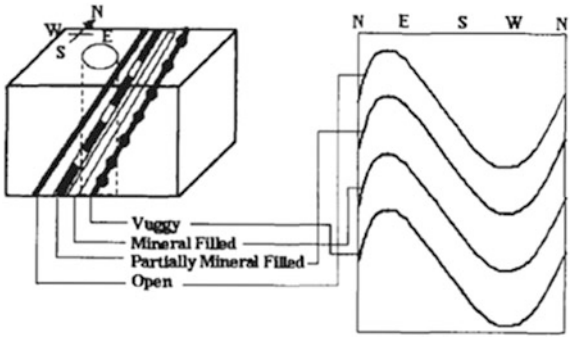

Fig. 8.10 Fracture morphology showing vuggy, mineral filled, partially mineral filled, and open fractures and their log response sequence

(a) Natural vertical fractures in a nondeviated borehole can be identified as a high-amplitude feature that crosses other bedding planes. They occur in all lithologies. Fractures may be open, mineral filled, or vuggy. Visual inspection of cores and borehole electric images may be used only as a guide for interpretation. Core flow tests and actual production tests are recommended for interpreting the morphology of natural fractures. Production and recovery efficiency in reservoirs is influenced by the angle. The angle most often used by oil companies as a criterion is 75°. Fractures with dip angles of more than 75° are treated as vertical fractures, while those less than 75° are treated as high-angle fractures. Vertical fractures are more common in sandstone rocks.

(b) Syneresis fractures have a braided appearance and are often referred to as "chicken wire" fractures. They normally occur only in carbonate formations.

(c) Mechanically induced fractures are sometimes unintentionally created during the drilling operations, or by hydraulic fracturing to stimulate the formation.

Fracture morphology can also be visually detected on cores and/or borehole images. Figure 8.10 shows four detectable fracture morphologies: vuggy, mineral lilled, partially mineral filled, and open.

8.3 Critical Pressure and Stress Relationship in the Borehole

The mechanical properties derived from testing rock samples in the laboratory, such as the measurement of the strain for a given applied stress, are static elastic constants. Dynamic elastic constants are derived from the measurement of elastic wave velocities in the material. Sonic logging and waveform analysis provide the means for obtaining continuous measurement of compressional and shear velocities. These

data, in conjunction with a bulk density measurement, permit the in situ measurement and calculation of the mechanical properties of the rock. The standard practice is to use measured values of compressional travel time (τ_c) and shear travel time (τ_s), When shear travel time cannot be measured (i.e., in soft formations or poor cement jobs), predictions based on Poisson's Ratio and elastic moduli are not recommended. However, τ_s data may be replaced with synthetic shear travel times computed from lithological models, using compressional travel times, and bulk density that have been corrected for hydrocarbon effect. It should be noted that even though the hydrocarbon corrections are applied for the lithological model inputs for synthetic τ_s computations, hydrocarbon corrections are not made when the raw data are used for the elastic properties computation.

8.3.1 Mohr–Coulomb Failure Criterion

The Mohr–Coulomb Failure Criterion (Fig. 8.11) was usually used in the sand strength analysis. In general, it differs from the 3D Griffith Model in an element on the borehole wall is examined rather than the cavity shape. δ_x and δ_y are far field total stresses, δ_x is derived as shown in the next section. δ_y is the maximum horizontal stress and is equal to δ_z multiplied by the tectonic unbalance factor, δ_x/δ_y, which will be described later. Only two principal stresses on the element in the borehole wall are noted; effective radial stress; δ'_r, and effective tangential stress, δ'_θ.

In the case of a "step" pore pressure profile, effective stresses on the element of borehole wall are

$$\delta'_\gamma = p_w - \alpha p_p \tag{8.13}$$

and

$$\delta'_\theta = 3\sigma_x - \sigma_y - p_w - \alpha p_p \tag{8.14}$$

Mohr's Circle is a graphic representation of the variation in shear stress along a plane and the normal stress across the plane, as γ (the angle that the direction of the

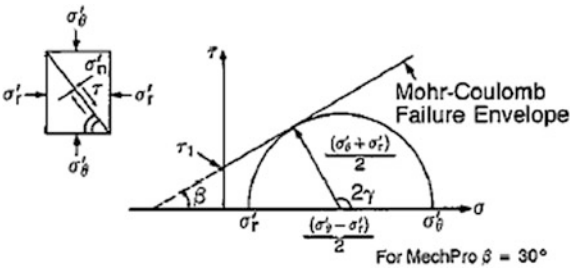

Fig. 8.11 Mohr's circle showing 30° failure envelope

normal stress makes with the greater principal stress) changes from 0° to 90° (Fig. 8.11). The shear stress is:

$$\gamma = \frac{1}{2}\left(\sigma'_\theta - \sigma'_\gamma\right)\sin\gamma \tag{8.15}$$

The normal stress is

$$\sigma'_{\mathrm{n}} = \frac{1}{2}\left(\sigma'_\theta + \sigma'_\gamma\right) + \frac{1}{2}\left(\sigma'_\theta - \sigma'_\gamma\right)\cos 2\gamma \tag{8.16}$$

The initial shear strength is derived from an empirical model based on Deere and Miller's work (1969) and elaborated by Coates and Denoo (1981):

$$\tau_i = \frac{0.026E}{C_{\mathrm{b}} \times 10^6}\left[0.008\mathrm{VSH} + 0.0045\left(1 - \mathrm{VSH}\right)\right] \tag{8.17}$$

where

E Young's Modulus in psi
C_{b} bulk compressibility in psi^{-1}
VSH the volume of clay, %.

A formation collapses due to shear failure when the induced shear stress exceeds an amount depicted by the failure envelope. If the Mohr's Circle just intercepts the failure lie, the point of contact identities both the critical shear stress and the angle y between the normal to the shear plane and the direction of the maximum stress.

The Coulomb failure line is a linear approximation of the Mohr failure envelope. It is depicted as follows:

$$\tau = \tau_i = \sigma\cos\beta \tag{8.18}$$

where β is angle of friction.

The condition of instability occurs when

$$\frac{\sigma'_\theta - \sigma'_\gamma}{2} = \left[\tau\cos\beta - \frac{\sigma'_\gamma - \sigma'_\theta}{2}\right]\sin\beta \tag{8.19}$$

By substituting σ'_θ and σ'_γ, from Eqs. (8.13), (8.14) in (8.19), a solution is provided.

The model is more representative of producing conditions by allowing for a radial pore pressure gradient from the wellbore to the far field. Critical wellbore pressure, p_{c}, using the Mohr–Coulomb Criterion becomes:

$$p_c = \frac{1.5\sigma_x - 0.5\sigma_y - 0.5\alpha p_p\left(\frac{1-2v}{1-v}\right) - 1.732\tau_i}{1 - 0.5\alpha\left(\frac{1-2v}{1-v}\right)} \tag{8.20}$$

Experience has shown that the results are pessimistic in competent sands, but closely match the Griffith results in unconsolidated formations.

In an example from a chalk reservoir in the North Sea, the well pressure desired by the operator is compared with the critical well pressure estimated to cause failure. Intervals where well pressure is lower than the critical pressure were considered susceptible to failure. Producing the well at the desired production rate would cause most of the upper oil-bearing zone to collapse, a catastrophe that had previously occurred in other wells. In this case the weak zones were sealed, zones below them were perforated, and communication was reestablished to the producing horizons through hydraulically induced fractures.

8.3.2 Stress Relationship at the Wellbore

The simple correlation, which relates the maximum tangential stress to the principal stresses at the wellbore, is given as:

$$\sigma_{\text{Hmax}} = 3\sigma_{\max} - \sigma_{\min} - P_{\text{H}} \tag{8.21}$$

where $\sigma_{\max}$ is the maximum stress, psi, $\sigma_{\min}$ is minimum stress, psi, and PH is horizontal stress, psi.

The maximum tangential stress occurs in the direction of the least principal stress. The axial stress is estimated as

$$\sigma_{\text{axial}} = \sigma_{\text{OB}} + 2v\left(\sigma_{\max} - \sigma_{\min}\right) \tag{8.22}$$

where v is the static Poisson's ratio of the formation rock. Equations (8.21) and (8.22) are valid only if the pore pressure is constant throughout the formation. To incorporate the changing pore pressure profile and the pore elastic term, Haimson and Fairhurst developed the following correlation:

$$\Delta\sigma = \alpha\left[\frac{(1-2v)}{(1-v)}\left(P_{\text{wb}} - P_{\text{p}}\right)\right] \tag{8.23}$$

where α is the Biot coefficient, and P_{wb} is the pore fluid pressure just behind the wellbore, and P_{p} is the pressure of pore.

8.3.3 Estimating Critical Borehole Pressure in Vertical Wells

1. Overbalanced Conditions

For an impermeable mud cake, the pore elastic effect does not exist. The maximum effective tangential stress is given by:

$$\sigma_{\theta\,\mathrm{max,eff}} = 3\sigma_{\max} - \sigma_{\min} - P_{\mathrm{b}} - P_{\mathrm{p}} \tag{8.24}$$

where P_{b} is the wellbore pressure.

The radial effective stress at the wellbore wall is given by:

$$\sigma_{\theta\,\mathrm{radial,eff}} = P_{\mathrm{b}} - P_{\mathrm{p}} \tag{8.25}$$

The combination of Eqs. (8.24) and (8.25) and the Mohr–Coulomb shear failure criterion, results in the critical bottomhole flowing pressure as shown by Rhett and Risnes:

$$P_{\mathrm{bfc}} = 0.5[3\sigma_{\max} - \sigma_{\min} - \sigma_{\mathrm{UCS}}](1 - \sin\theta_{\mathrm{f}}) + P_{\mathrm{p}}\sin\theta_{\mathrm{f}} \tag{8.26}$$

where P_{bfc} stands for critical wellbore pressure, θ_{f} is the internal friction angle and is a material property of the rock, σ_{UCS} is the unconfined compressive strength of the rock, psi. It is obtained from the slope of the failure line on the Mohr–Coulomb figure. The most common overbalanced conditions are encountered during drilling operations and injection projects such as waterflooding. If the calculated critical bottomhole flowing pressure is less than the pore pressure, then the assumption of overbalance is not valid.

The critical wellbore flowing pressure is a function of pore pressure, which continuously changes with depletion. The change in critical pressure with change in pore pressure is simply the derivative of Eq. (8.26), as shown by Rhett and Risnes:

$$\Delta P_{\mathrm{bfc}} = 0.5[(2 - 3\sigma_{\max} + \sigma_{\min}) + \sin\theta_{\mathrm{f}}(3\sigma_{\max} - \sigma_{\min})]\Delta P_{\mathrm{P}} \tag{8.27}$$

2. Underbalanced Conditions

The most common practice of underbalanced conditions is where wellbore flowing pressure is always lower than the reservoir pressure. Recently, drilling and perforation techniques have been frequently applied to maintain wellbore pressure in order to reduce damage to the formation. Such conditions, however, affect the effective stress at the wellbore. A useful correlation for underbalanced conditions is:

$$P_{\text{wfcu}} = (1 - v)[3\sigma_{\max} - \sigma_{\min} - \sigma_{\text{UCS}}] - P_{\text{p}}(1 - 2v) \tag{8.28}$$

Equation (8.28) requires accurate knowledge of the downhole stresses. If the estimated value of critical borehole pressure does not agree with the filed observations of the pressure at which first sand production was observed, the values of the stress can be adjusted to match the stress history of the formation.

8.3.4 Critical Pore Pressure

The only factor that reduces reservoir pressure is the primary depletion. Thus, initial effective stress, which is partially supported by the reservoir fluid, is progressively transferred to the rock matrix. The rock begins to fail if the increasing effective stress approaches the critical shear stress of the rock. Thus, any reservoir pressure value below the shear failure value of the rock matrix will cause crushing of the rock solids. Fluid movement further enhances the cavitations of the cementing material and dislodged particles are carried by the fluid toward the wellbore.

$$P_{\text{pc}} = \frac{(3\sigma_{\max} - \sigma_{\min} - \sigma_{\text{UCS}}) + P_{\text{pi}}(3K_2 - K_1 - 2)}{3K_2 - K_1} \tag{8.29}$$

For axial stress greater than the maximum tangential stress:

$$P_{\text{pc}} = \frac{\sigma_{\text{ob}} - 2v[\sigma_{\max} - \sigma_{\min} + (K_2 - K_1) + P_{\text{P}}] - \sigma_{\text{UCS}}}{1 + 2v(K_2 - K_1)} \tag{8.30}$$

Once the weight of the overburden is unloaded from the reservoir fluids and is supported by the grains, rock mass remains at the maximum shear stress evolved during the depletion. Thus, stress paths during the injection are different from the paths followed during the depletion. During the repressurization, critical pore pressure can be estimated by using the minimum values of the maximum and minimum horizontal stresses as follows:

$$P_{\text{pc}} = (1 - v)(3\sigma_{\max-\min} - \sigma_{\min-\min} - \sigma_{\text{UCS}} - P_{\text{p}}) \tag{8.31}$$

where $\sigma_{\text{Hmax}-\min}$ and $\sigma_{\text{Hmin}-\min}$ are the lowest values of the maximum horizontal stress and minimum horizontal stress, respectively. Change in critical pore pressure with changing reservoir pressure at a given stage is then given by:

$$(\Delta P_{\text{pc}})_{\text{t}} = -(\Delta P_{\text{P}})_{\text{t}}(1 - 2v) \tag{8.32}$$

where subscript t stands for any given time.

8.3.5 Porosity as Strength Indicator to Evaluate Sand Production

Petroleum production from poorly consolidated formations can be considerably hindered by the phenomenon of sand production. Gravel packs can be used to prevent sand production, but they are generally harmful to well productivity and expensive. Sarda et al. proposed tensile rupture and compressive rupture as possible mechanisms of sand failure.

Field observations indicate that the formations possessing low porosity show significant rock strength. Thus, porosity can be used as a qualitative measure of rock strength and to predict sand production. Sand production can be expected if the product $G \times K_b$ of two elastic parameters exceeds the threshold value 8×10^{11} psi^2, where the shear modulus G and the bulk modulus K_b are derived from the interpretation of acoustic and density logs. The

$$G = 1.24 \times 10^{10} \frac{\rho_b}{\Delta t_s^2} \tag{8.33a}$$

$$K_b = G(r^2 - 4/3) \tag{8.33b}$$

where r is obtained from the acoustic log and is expressed as:

$$r = \frac{\Delta t_s}{\Delta t_c}$$

where Δt_s and Δt_c are travel time of compressional wave and shear wave, respectively, μs/ft. The ratio r is related to Poisson's ratios as follows:

$$v = \frac{r^2 - 1}{2r^2 - 1} \tag{8.34}$$

The porosity is obtained from:

$$\emptyset = \frac{\Delta t_c - \Delta t_{ma}}{\Delta t_f - \Delta t_{ma}} \tag{8.35}$$

where Δt_{ma} is compressional travel time of matrix. The product $G \times K_b$ is actually the "Sand Production Indicator" or SPI:

$$\text{SPI} = G^2(r^2 - 4/3) \tag{8.36}$$

Thus, using the suggested threshold:

$\text{SPI} \leq 8 \times 10^{11}\text{psi}^2$ The formation is stable, therefore, no sand production
$\text{SPI} \geq 8 \times 10^{11}\text{psi}^2$ The formation is unstable, sand production could occur.

The sand strength limit can be estimated using the following correlation:

$$\sigma_{\text{UCS}} = 0.087 \times 10^{-6} E K_{\text{b}} [0.008 V_{\text{sh}} + 0.0054\,(1 - V_{\text{sh}})] \tag{8.37}$$

The internal friction angle, θ_{f} of the sand is assumed to be equal to 30°. Parameters such as grain form and grain strength, grain size and size distribution contribute to the frictional strength of the sand, whereas cementation, contact surface area, and pore fluid contribute to its cohesional strength.

8.3.6 *Estimation of Unconfined Compressive Rock Strength from Porosity Data*

In clean sandstones the acoustic velocities depend on porosity. Unconfined compressive rock strength can be estimated using log derived data as follows:

$$\sigma_{\text{UCS}} = f(\theta_{\text{f}}) \frac{\rho_{\text{b}}^2}{\Delta t_{\text{s}}^2} \left[\Delta t_{\text{c}}^2 - \frac{4 \Delta t_{\text{s}}^2}{3} \right] g(V_{\text{sh}}) \tag{8.38}$$

where P_{b}, Δt_{c}, and Δt_{s} depend mainly on porosity. Equation (8.38) clearly introduces porosity as a basic and implicit variable.

8.4 Rock Drillability

Various indirect measuring techniques are presently employed for estimating formation strength, which in turn is correlated to drillability and polycrystalline diamond compact (PDC) bit selection. Drillability is a measurement of the difficulty that the rock cab be drilled, which is an important parameter to describe rock strength. Usually, in engineering, the drillability is calculated by drilling time, T, as the following equations:

$$K_{\text{d}} = \log_2 T \tag{8.39}$$

where, K_{d} denotes drillability of rock, and T is drilling time, s.

Formation mechanical properties derived from conventional open-hole logs in combination with a rigorous assessment of formation shear wave velocities can be used successfully to determine drillability as it pertains to bit selection. Formation drillability is determined from unconfined compressive strength and the angle of internal friction assessment. Rock strength is found to correlate well with the overall measures of bit effectiveness. Further, the angle of internal friction, which is a subsidiary rock strength parameter, correlates with PDC bit wear rates.

Compressive strength and drillability have been linked in the laboratory and observed in the field since the early 1960s. Compressive strengths, however, need to be qualified as a function of confinement stress. The concept that compressive strength increases with confinement stress is well-understood and can be easily explained with Mohr's failure criteria. With the Mohr's failure technique, it is important to understand that inherent rock strength properties (cohesion and angle of internal friction) must be known before compressive strengths can be estimated.

A generally well-known method to determine rock strength is based on sonic log interpretation together with lithological analysis of formation data. Even if sufficiently reliable to calculate rock strength, such a methodology suffers from two main limitations:

(1) Rock strength is derived from elastic theory, relating rock acoustic responses to its hardness, i.e., it is not a direct measurement.
(2) Sonic log is recorded at the end of the section, so not available during drilling operations. An interesting solution to bypass these limits is represented by indentation technology on cuttings. The improvement compared to sonic approach is its capability to directly acquire a rock parameter related to the uniaxial compressive strength of formation.

Together with a better definition of rock behavior, indentation technique on cuttings allows a continuous, while drilling control of rock strength directly at the rig site.

Correlation between sonic logs and the formation drillability for different lithology types have been developed from in-site data. The gamma ray log was used in conjunction with drilling data to calculate the drillability. The drillability from penetration rate models is back calculated from bit design and reported field wear in conjunction with meter-by-meter operating parameters, formation type, and pore pressure. Then, this drillability was correlated with sonic logs for different lithologies as defined by the gamma ray log.

The optimization of the drillability process by the use of drilling simulator can significantly improve results with the input of proper rock properties. The unconfined compressive strength (UCS) of the rock is one of the most important properties and is also the most difficult to obtain.

The ultimate objective of well logging is to evaluate subsurface formation by providing an indirect measurement of fluid and rock characteristics. Well logging has been known to provide information on rock strength, but the usage of electric logs for calculating drillability is less common.

Onyia conducted test involving the Induction, Sonic, Density, Gamma Ray, and porosity log. Data was taken from a research test well in some area. The lithologies encountered in Onyia's study were shale, sandstone, limestone, dolomite, granite porphyry, and some mixed lithologies.

Sonic models produced the best agreement with the triaxial test results analyzed for the comparison. Onyia concluded that the sonic model may be used to develop a continuous rock strength model.

8.4.1 Technical Steps: Determination of Lithology

Experience in the areas where the wells were drilled specifies that the formations are mainly composed of shale, sandstone, and small amounts of coal. With this information known, the homogeneous lithologies of sandstone and shale were separated using a gamma ray cutoff value. Linear interpretation of the gamma ray log values was used to determine the shale fraction of the mixed lithology.

$$\rho_{\text{corr}} = \rho_{\log} - V_{\text{sh}}\rho_{\text{sh}}$$

Bulk density values below 1.1 g/cm^3 were determined to contain coal within the formations.

The rock strength was plotted versus the sonic travel time to determine the trend of the data. The correlation in Fig. 8.12 resembles the form of exponential decline. No data points for the sonic travel time were observed below 45 μs/ft; therefore, a boundary condition of 40 μs/ft was used to develop Eq. (8.40).

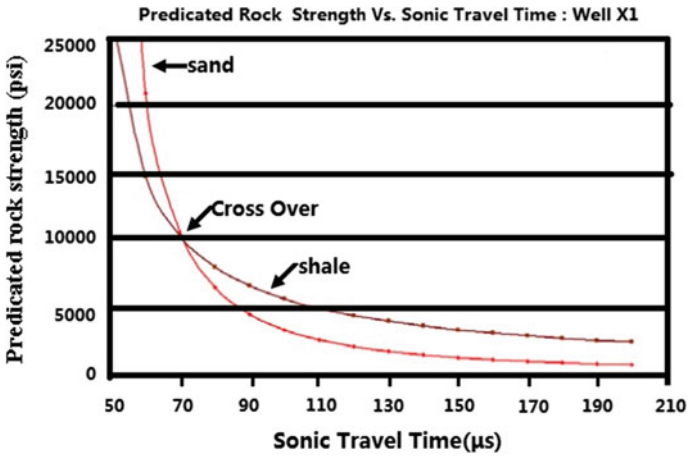

Fig. 8.12 Predicted rock strength versus sonic travel time

$$\delta = \frac{K_1}{(\Delta t_c - 40)^{K_2}} \tag{8.40}$$

An average representation of porosity was developed from a normalized rock strength (σ/σ_{max}) versus neutron porosity relationship. Neutron porosity was chosen since poor correlations were found using the density porosity from Onyia's research (rock strength is closely related to porosity and, therefore, important to include when developing a correlation). The resulting empirical relationship is given by:

$$\sigma/\sigma_{max} = 1 - \varphi^{1.8} \tag{8.41}$$

As a rock compacts, the grain contact area and contact stress increase which cause the bulk and shear modulus to increase. Rock compaction also reduces the porosity, in effect increasing the density and reducing the sonic travel time. Further compaction is resisted by either stiffness in the rock frame or by increases in the pore pressure.

Sonic, density, and resistivity logs of a normally pressured formation will generally increase with depth of burial. At surface levels shale has higher porosity than sandstone. As depth increase and rock compacts, the porosity is reduced and the density increases due to the greater overburden pressure. Since shale is normally composed of softer minerals, the compaction is greater within this lithology.

Figure 8.12 shows the predicted rock strength from Eq. (8.40) versus sonic travel time. A modified model correlation of depth versus porosity for sandstone and shale was used to determine a relationship between sandstone and shale compaction. Equation (8.42) combines the sonic equation with the porosity and compaction terms.

$$\delta = \frac{K_1(1 - \emptyset^{1.8})f}{(\Delta t_c - 40)^{K_2}} \tag{8.42}$$

Rock strength information is crucial when analyzing the safe mud weight window for assessing the stability of the wellbore, selecting mud weights, and designing casing programs. Strength information is also used for completion and hydraulic stimulation design. However, there are other areas, especially in drilling, where rock strength information is applicable, but still underutilized. To obtain the rock strength along the wellbore, logs, rock mechanical tests, or even drilling data can be used.

The rock mechanical parameter that is most important when conducting drilling analysis is unconfined compressive rock strength (UCS). The UCS can be determined from Mohr–coulomb failure criteria. The Mohr–Coulomb failure criterion in terms of peak loads is given as:

$$S_v = \text{UCS} + S_h \tan \alpha$$

where S_v is vertical effective stress, S_h is horizontal effective stress, and α is failure angle. Effective stress are defined the difference between total stresses and pore pressure.

$$S_v = S_v' - P_p \tag{8.43}$$

S_v' is the total stress and P_p is the pore pressure.

There are several methods to obtain UCS along the wellbore. In most cases, the availability of data determines which methods to choose. Obtaining UCS from logs are describe below.

8.4.2 Rock Strength from Sonic Log

The use of sonic velocity logs to determine elastic properties of rock is well established. There is several correlations between rock strength and sonic travel time. Sonic travel time measured on cores can be correlated with unconfined compressive strength derived from failure compressive test on sandstone and shale cores. The sonic versus UCS were analyzed using Eq. (8.44).

$$\text{UCS} = \frac{1.0}{k_1(\Delta t_c - k_2)} + k_3 \tag{8.44}$$

where Δt_c is travel time (μs/ft), UCS is unconfined compressive strength (MPa) and k_1, k_2, k_3 are experimental constants. In Fig. 8.13, the shale and sandstone data are

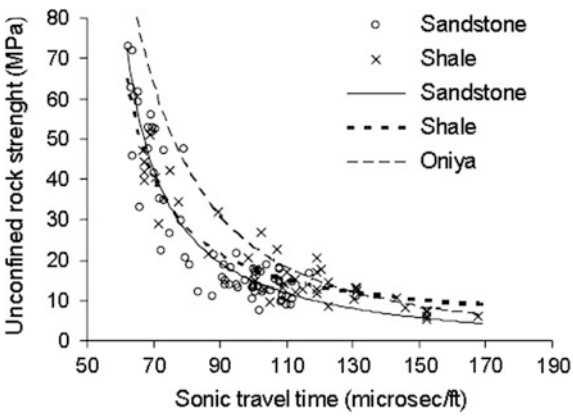

Fig. 8.13 Correlation of UCS versus sonic travel time for shale and sandstone

Table 8.2 Experimental constants for rock strength correlation based on sonic logs

Lithology	k_1	k_2	k_3	R^2
Sandstone	0.0011	50	3.42	0.9
Shale	0.0013	50	−2.66	0.9
Combined	0.0012	50	0.22	0.9

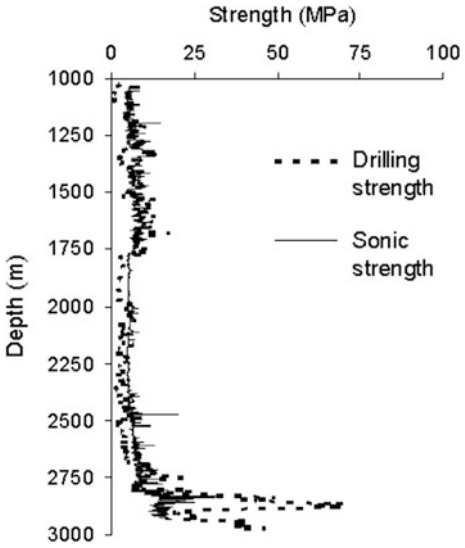

Fig. 8.14 UCS from sonic logs and ROP model strength

plotted with a best curve fit for the sandstone, shales and both lithologies combined. The best fit experimental constant for Eq. (8.44) are given in Table 8.2. When sonic logs are available these data can give a continuous strength profile along the wellbore as shown in Fig. 8.14. In Fig. 8.15, UCS derived from triaxial tests is also included. The match between the rock mechanical tests and the velocity trend is good. However, this approach will only give indicative results since there are no strength variations within the specific formations.

Neutron density logs can be used for deriving rock strength from logs. Porosity information can be obtained along with the well bore neutron density logs.

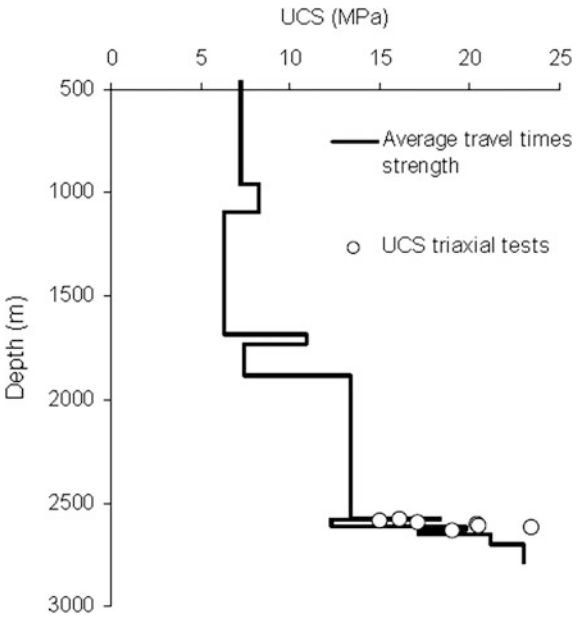

Fig. 8.15 Rock strength estimated based on seismic travel times

8.5 Borehole Stability

The borehole wall must support the loads resulting from the outlying earth stresses and the pressure of the wellbore fluid. Failure can enlarge, reduce, or collapse the hole, or fracture the formation (Fig. 8.16), depending on the rock strength, stress on the bore wall, drilling fluid pressure, and formation pore pressure.

Fracturing can occur when the mud weight exceeds the effective tangential stress, by an amount sufficient to overcome the rock's tensile strength. The rock's pore pressure, p_f, is assumed to be close to the borehole fluid pressure. This type of failure is prevented by reducing the effective mud weight.

Some rocks fail in a brittle manner when the borehole stress exceeds the rock's compressive strength. Because borehole stress can vary circumferentially, such failure can result in an out-of-round hole and very rugose hole walls. This type of failure is controlled by increasing the mud weight.

Some rocks fail by plastic flow when their compressive strength is exceeded. Flow failure is most likely in salts, shales, and unconsolidated sands, and is recognized by hole sizes that are smaller than the bit-size-minus-mudcake thickness. Obviously, a partly collapsed hole is a hostile environment for logging. This instability is controlled by increasing the mud weight.

The borehole's angle and direction can also affect its stability, depending on the natural stress field, and mud weight. Bradley found that in areas where the principal horizontal stresses are equal, hole direction does not affect stability; inclination from the vertical does. An example from this study (Fig. 8.17) shows that

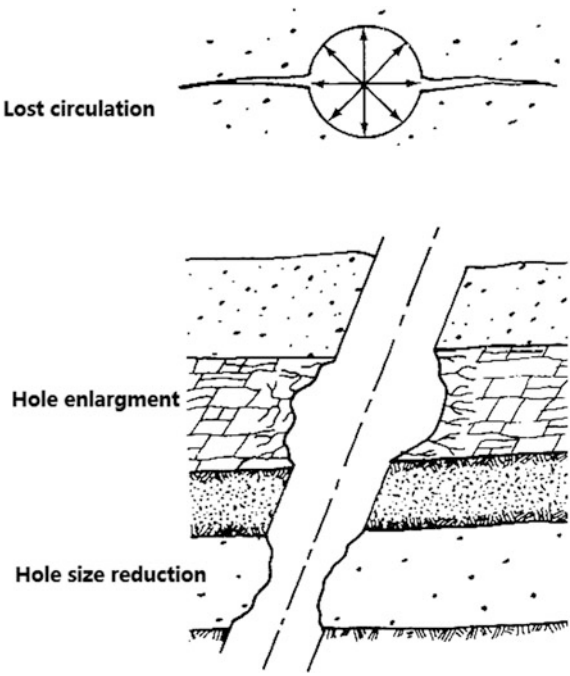

Fig. 8.16 Types of borehole failure (modified after Bradley)

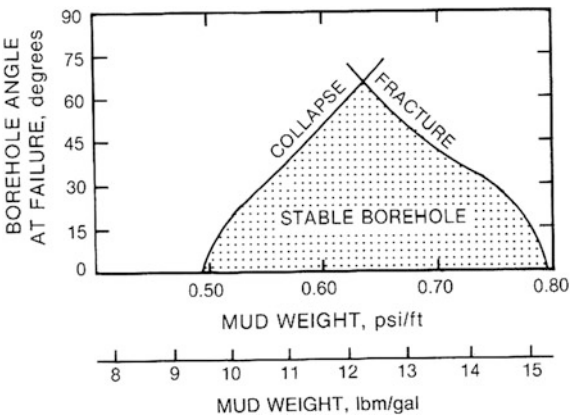

Fig. 8.17 Effect of borehole angle on hole stability (after Bradley)

increasing the borehole angle from 0° to 60° requires reducing the mud weight from 15.3 to 12.5 lbm/gal to prevent fracturing the formation; but the same change requires increasing the mud weight from 8.5 to 12.0 lbm/gal to prevent collapse. The shaded region represents the combinations of mud weights and hole angles at which the hole will be stable for the conditions in this example.

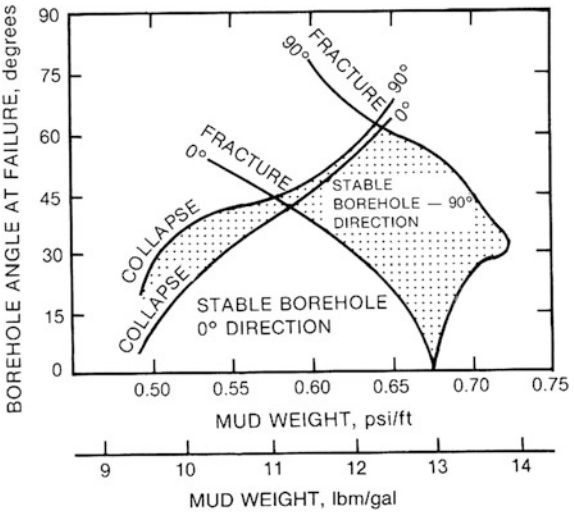

Fig. 8.18 Effect of borehole direction on hole stability (after Bradley)

In areas where principal stresses are not equal, Bradley states that borehole stability depends on the relative orientations of the hole and the regional stress field. Figure 8.18 shows the stability/instability fields for two borehole orientations.

Problems

8.1 Explain the mechanics parameters, such as Young's modulus, Poisson ratio, Bulk modulus, and shear modulus. And write out its formulas, respectively.
8.2 What are the classifications and its characteristics of natural fractions?
8.3 How to discriminate facture by logging methods?
8.4 Based on the Fig. 8.11, clarify the meaning of Mohr–Coulomb failure criterion.
8.5 How to estimate the rock stress?
8.6 What is drillability of rock and how to calculate?
8.7 Based on the Fig. 8.17, explain the relationship between the stability and the borehole angle and mud density.

Chapter 9
The Advanced Well Logging Technology

This chapter will present some advanced well logging system, which mainly includes the so-called image logging, such as Eclips-5700 of Baker Hughes, Exell-2000 of Halliburton, these two systems are briefly introduced. In Sect. 9.3, Sondex system is presented in order to let students familiar with a newest production logging technology. And the last Sect. 9.4, introduces Schlumberger's cased-hole formation resistivity tools, which is utmost important for Chinese oilfields, especially the over-matured fields, who have a large amount of residual oil and flooded zone under the earth, which cannot be clearly interpretated by conventional logging method.

9.1 Eclips-5700

9.1.1 Eclips-5700 Well Logging System

Baker Hughes Inc. is a leader in oilfield services in the world. Baker Atlas is a subsidiary company of Baker Hughes. Baker Atlas offers a complete range of downhole well logging services for every environment, including advanced formation evaluation, production and reservoir engineering, petrophysical, and geophysical data acquisition services. ECLIPS-5700 well logging system, which is manufactured by Baker Atlas, is a set of advanced system in the world (shown in Fig. 9.1).

ECLIPS is the abbreviation of Enhanced Computer Logging Interpretation Processing System. ECLIPS-5700 well logging system can provide data acquisition and processing of the conventional logging and the imaging logging. Menu drive and "help" function are introduced into ECLIPS-5700 well logging system, which is convenient for operation. ECLIPS can offer abroad diagnostic program, for example the diagnostic program of Power and Telemetry system and the diagnostic

H. Liu, *Principles and Applications of Well Logging*, Springer Mineralogy,
DOI 10.1007/978-3-662-53383-3_9

Fig. 9.1 ECLIPS-5700 instrument truck (Courtesy by Sichuan Oilfeild)

program selected by the user. ECLIPS can monitor the quality of the well logging by the real-time display of curve and data processing.

In logging the well, ECLIPS-5700 well logging system uses four main types of equipment: the downhole instrument (which measures the data), the computerized surface data acquisition system (to store and analyze the data), the cable or wireline (which serves as both mechanical and data communication link with the downhole instruments), and the hoisting equipment to raise and lower the instruments. In this unit, we will mainly introduce the downhole instrument. We will introduce the conventional logging instrument in this passage, and we will introduce the imaging logging instrument in the next passage.

ECLIPS-5700 well logging system is compatible with the conventional logging instruments of 3700 series. Five kinds of the conventional logging instruments of ECLIPS-5700 well logging system have been upgraded to measure the downhole formation more accurately. These five kinds of instruments are

- 1329 spectrum logging tool
- 2228 lithology density logging tool
- 1680 digital acoustic logging tool
- 2446 compensate neutron logging tool
- 1239 dual lateral logging tool.

Hostile environmental conditions often exist in the well, contributing to the difficulty in acquiring these downhole data. Temperatures can exceed 400 °F, and

pressures can exceed 20,000 psi. Pulling the tools through the well can subject them to high shock and vibration. In spite of these conditions, we must offer high standard of service and can still offer data with more reliability and more accuracy. Meeting these specifications requires the integration of highly trained personnel and advanced technology. New-generation instrument just can do it.

9.1.2 Eclips-5700 Imaging Logging Instrument

In recent years, Baker Atlas has delivered new-generation technologies and developed new type imaging logging instrument to help oil and gas producers evaluate and access reservoirs more efficiently and reliably. Imaging logging instruments mainly include the types listed below:

MRIL, CBIL, STAR, MAC, SBT, HDIL

MRIL For distinguishing between producible fluids and irreducible water and providing permeability estimate on a foot-by-foot basis, Baker Atlas introduces an innovative approach in providing reservoir descriptions using the Magnetic Resonance Imaging Log (MRIL) service. The Magnetic Resonance Imaging Log (MRIL) service uses the principle of nuclear magnetic relaxation to provide formation evaluation, petrophysical data including porosity, irreducible water saturation, permeability, and grain-size and pore-size distribution.

The measurement of the MRIL service primarily responds to the hydrogen protons in the pore space of the formation. This allows a measure of porosity. MRIL porosity, in contrast to compensated neutron porosity, does not include the hydrogen bound in the matrix of the rock, thus providing a lithology- and clay-independent porosity value.

From the nuclear magnetic relaxation measurement (T2), bulk volume irreducible (BVI), and moveable (BVM) fluids can be determined. By comparing these results with conventional open-hole log data analysis, a more accurate prediction of producible fluids is made. Permeability and grain- and pore-size distribution are also derived from the MRIL T2 data.

Benefits

Accurate shaly sand and low resistivity pay evaluation

Improved reserves and volumetric estimates (identification of net pay and oil saturation)

Quantification of producible fluids (movable versus bound)

Improved reservoir quality estimate (permeability, pore- and grain-size distribution)

Direct hydrocarbon typing (differentiate between gas, oil, and water)

CBIL The Circumferential Borehole Imaging Log is an acoustic device that produces images of the borehole wall. These images can be used for formation evaluation and borehole inspection in both clastic and carbonate environments. The instrument can also be run in cased holes for casing inspection applications.

The images that are recorded are the variable density representation of reflected acoustic waves. These waves result from the activation of a rotating transducer that emits focused beams of high-frequency acoustic energy towards the borehole wall. The images can be oriented to magnetic north by a flux-gate magnetometer that senses the earth's magnetic field.

Applications

- Present a complete 360° borehole image
- Provide orientation and correlation of whole cores
- Dip determination
- Detect fractures
- Determine sand/shale ratios in thin-bedded intervals
- Provide high-resolution acoustic caliper data
- Provide borehole geometry
- Supply detailed borehole images in fresh-, salt-, and oil-based muds
- Locate and evaluate internal casing corrosion, mechanical wear, defects, and perforations.

STAR The Simultaneous Acoustic and Resistivity (STAR) service is another member of the Baker Atlas family of new-generation technologies.

The STAR Imager service integrates high-resolution resistivity and acoustic imaging sensors into one instrument, enhancing reservoir evaluation in geological environments ranging from soft, thinly laminated clastics to highly indurated and complex carbonates.

The STAR Imager service combines the full coverage of the acoustic imager with the wide dynamic range of the resistivity imager, resulting in detailed geological and petrophysical information. Combining the two imaging devices also extends the operating environment beyond that of conventional systems. The resistivity imager functions best in water-based drilling fluid systems, while the acoustic imager works well in all water-based and oil-based drilling mud systems. The resulting high-resolution borehole images can be used to identify geological and borehole features such as structural dip, faults, and borehole geometry, as well as for analysis of fracture systems, depositional environments, borehole stability.

MAC Full waveform acoustic logging tools measure formation velocities by transmitting and receiving pressure pulses. The Multipole Acoustic (MAC) tool provides measures of both the body-wave compressional and shear velocities and the guided Stoneley waves. The tool was especially designed to preferentially excite low frequency acoustic waves. From the decay or attenuation of the low frequency pressure pulses, it is possible to estimate the permeability. Compressional and shear wave velocities and attenuation data are obtained from the conventional full waveform and dipole data. The Stoneley (or tube) wave, a guided wave traveling in the borehole, is ideally suited for permeability estimation.

SBT The SBT instrument quantitatively measures the cement bond integrity in six angular segments around the casing. The acoustic transducers are mounted on six pads positioned in contact with the interior casing wall and provide

compensated attenuation measurements. These measurements are insensitive to heavy mud or gas-cut borehole fluids, fast-formation effects, and moderate tool eccentricity, all of which significantly degrade conventional and reflectance-type measurements. The SBT service also provides improved Variable Density Log (VDL): measurements and tool orientation for identifying the low side of the borehole.

HDIL A new digital full-spectrum induction device for determining accurate formation resistivity with enhanced diagnostics and data integrity verification-application of the improved resistivity data acquired with the HDIL service results in better reservoir description, improved Sw and more accurate reserves estimates. The HDIL service provides better vertical resolution in thin beds and a detailed description of the drilling fluid invasion profile.

The HDIL subsurface instrument is a multi-receiver, multi-frequency, fully digital array-type induction device that provides an order of magnitude more information than a conventional induction tool.

Multiple receivers provide six depths of investigation, ranging from 10 to 120 in., for determining R_t and invasion profile.

Multiple frequency acquisition allows for more accurate skin-effect corrections and improved data quality.

HDIL data are well suited for advanced processing methods.

Feed-through wiring allows flexible subsurface hardware combination options.

The array-type HDIL instrument uses selectable software focusing that can be adjusted to choose the response characteristics best suited for the problem at hand. This is made possible by the powerful ECLIPS acquisition system, eliminating previous dependence on inflexible hardware focused induction tool designs.

9.2 Excell-2000 Well Logging System

Halliburton developed the Excell 2000 logging system, as shown in Fig. 9.2, a state-of-the-art integrated logging platform that consistently delivers accurate, high-quality data, and provides powerful post-processing workstation capabilities. The system enables greatly improved wellsite performance and provides a standard platform from which new logging tools and software currently in development can be more efficiently operated. And the most important, it allows critical formation data to be at the right place, at the right time to help ensure correct decisions are made about your well.

The Excell 2000 is a new-generation logging system. This platform unites a family of data acquisition systems to provide a broad spectrum of real-time geophysical data acquisition system. Systems can be optimized based on the services required at each site. Each configuration uses the same operator interface, thus providing the same “look and feel” to each system.

Fig. 9.2 Excell-2000 instrument truck (Courtesy by Sichuan Oilfield)

9.2.1 System Software

Operating system: The Excell 2000 uses the UNIX operating system as part of the open architecture. The UNIX operating environment allows the host computer sub-system to be upgraded as new technology emerges. This system provides true multitasking and multiuser capabilities.

Logging software: Excell 2000 incorporates UNIX-based CLASS software. The logging software is a second-generation CLASS logging program. This proven, time-tested system is currently operating in hundreds of logging units worldwide. The CLASS logging program is a mature logging environment that stresses ease of use. It also runs in the Computing Center to replay logs from the raw data.

Powerful processing software: Desktop Petrophysics (DPP) is fully integrated into the Excell 2000 system. It allows the operator to manage and manipulate log data for further evaluation and interpretation, utilizing a common desktop environment. Desktop Petrophysics is an integrated software package that converts, stores, and analyzes log data. This powerful package is available in our processing centers, worldwide, and at the wellsite. Excell 2000 supports our most advanced data processing applications:

(1) Acoustic full waveform processing.
(2) Thin bed processing routines.
(3) Dipmeter processing
(4) Production logging analysis.
(5) Image processing for fracture and sedimentological identification.
(6) Excell 2000 supports specialty services such as the EMI, CAST, and MRIL service.

9.2.2 System Configuration

The system has three main sub-systems. The Tool Power Sub-system provides the cable interface and the AC and DC voltages that are necessary to operate the tools. The Tool Interface Sub–system provides the different telemetry interfaces to communicate with the various tool strings. The Processing Sub-system processes the data from the various tool interfaces (along with other surface sensors) to provide calibrated logs for display and output. It also provides the storage needed to evaluate the petrophysical properties of the well.

9.2.3 System Features

1. *Faster and More Powerful Capabilities*

   The Excell 2000 unit contains state-of-the-art technology for increased power and speed during data acquisition and processing. This means more tool combinations for specific well conditions and faster logging speeds throughout the job.

2. *Multitasking Versatility*

   The powerful processing capabilities of the Excell 2000 system allow multiple applications to run simultaneously. For example, the field engineer can perform post-processing routines, such as SHIVA, on acquired data while the tool is still logging.

3. *Global Data Transmission*

   Excell 2000 is fully compatible with HalSat, Halliburton's new satellite data transmission system. HalSat allows wellsite data to be transmitted to the computing center and computed products to be transmitted back to the wellsite. Data can be transmitted in real-time or at the end of logging runs.

4. *Dual-System Flexibility*

   Fully redundant and independent dual-surface systems allow two major functions to be done simultaneously. For example, one system can calibrate a tool string while the other system is logging or processing data.

5. *Modular Design*

   Individual panels in the Excell 2000 system are modular in design. This flexibility allows each unit to be easily upgradable to accommodate increases in speed or memory.

9.2.4 Applications

The Excell 2000 logging system is a full service data acquisition system. It supports all standard logging, processing, and utilities within a common environment. This benefits the wellsite logging engineer and saves the client rig time since it is not necessary to change programs for processing, tool function checks and calibrations, or to merge and edit data tapes. The system has full service capabilities for cased-hole applications as well.

(1) Complete open-hole logging service.
(2) Complete casehole logging service.
(3) Production logging.
(4) Real-time display of borehole images via the EMI, CAST, and MRIL-P service.
(5) Completion services including setting packers and bridge plugs, perforating, pipe recovery.

9.3 Sondex Production Logging System

9.3.1 Flowmeter

This section will introduce several flowmeters, including Caged Fullbore Flowmeter (six-arm CFBM, shown in Fig. 9.3), Continuous Flowmeter Spinner (CFSM), Diverter Basket Flowmeter (DBT), Continuous Flowmeter Jewelled (CFJM), In-line Spinner Flowmeter (ILS).

1. *Caged Fullbore Flowmeter (six-arm CFBM)*

The Caged Fullbore Flowmeter is run at the bottom of a production logging tool string. The spinner blades and cage assembly collapse down to tool diameter, enabling it to pass through tubing restrictions without damage.

The tool has a six arm, spring-loaded cage that centers the spinner in the middle of the flow and supports tool weight in deviated wells. The signal from the sensors is converted into a flow rate measurement. The low mechanical threshold of the tool enables it to be used in low flow rates; normal output is 10 pulses per revolution with directional indication.

Fig. 9.3 Six-arm CFBM flowmeter

Features

- High deviation and horizontal well logging.
- Injection and production flow profiling.
- Measurement of low flow rates.
- Leak and cross-flow detection.
- Interchangeable mechanical sections to match casing sizes from 4½ to 9 5/8 in.
- Combinable with other UltrawireTM PL Tools.
- Connects to either a Spinner Electronics (CFBE) or a Capacitance/Temperature/Flow Tool (CTF).

2. *Continuous Flowmeter Jewelled (CFJM)*

The Jewelled Bearing Continuous Flowmeter, as shown in Fig. 9.4, is designed for logging in high fluid velocity wells, such as gas wells. The tool can be used in sand producing wells.

The Jewelled Bearing Continuous Flowmeter is run at the bottom of the production logging string in combination with a Capacitance/Temperature/Flow tool or CFJ Electronics cartridge. The tool has low friction jeweled bearings to reduce the mechanical threshold of the spinner and improve sensitivity to fluid flow. The spinner is an ideal design for use in high velocity wells.

3. *Diverter Basket Flowmeter (DBT)*

The Diverter Basket Flowmeter Tool (DBT) is designed to provide accurate measurements of total flow rate in low multiphase flows in vertical or deviated wells at stations along the borehole.

The DBT operates as part of an Ultrawire™ toolstring and has a motor-controlled, patented fabric basket to divert well bore flow through a modified in-line spinner, which allows for accurate measurement of the flow rate of all the fluids flowing along the well bore at the position of the skirt (Fig. 9.5).

The basket effectively reduces the flow cross-sectional area, allowing measurements in very low fluid velocities. In multiphase fluids, the tool minimizes the segregation effects. For more accurate holdup measurements, a shroud may be fitted

Fig. 9.4 CFJM flowmeter

Fig. 9.5 DBT flowmeter

to the exit of the in-line spinner housing to redirect flow through a radioactive Density tool.

5. *In-line Spinner Flowmeter (ILS)*

The Sondex In-Line Spinner Flowmeter is a compact flowmeter which can be run in combination with other PL tools. The tool may be used in areas where fullbore spinners may be closed due to restricted diameters (as shown in Fig. 9.6).

The ILS allows for production profiling in tubing and casing within one logging run and is less susceptible to the effects of jetting (high velocity fluid entry from perforations) than a fullbore spinner. The ILS has a shroud that protects the spinner blade as the tool moves through well restrictions. A combination of ILS and CFB provides a continuous optimized flow profile.

Precision roller bearings allow the spinner to rotate with minimal friction. As fluid moves past the spinner rotation is detected by zero drag Hall effect sensors. The spinner blade has been optimized to have a very low mechanical threshold and is ideal for low flow rates. The signal from the Hall-effect sensors is converted into a flow rate measurement with direction indication (up or down flow).

Features

- Production flow profiling,Leak detection.
- Additional spinner measurement in high deviation/horizontal wells.
- Flow measurement inside sand screens/slotted liners.
- Surface readout or memory operation.
- High-temperature polymer spinner blade.
- 11 1/16 in. tool body available with 11 1/16 in. or 2 1/8 in. spinner shroud.

Fig. 9.6 ILS flowmeter

9.3.2 Single Gauge Quartz Pressure Tool (QPS)

The Single gauge Quartz Pressure Tool (QPS) is used to provide a continuous log of borehole fluid pressure and to record reservoir

pressure draw-down and build-up data during flowing tests.

The Sondex Quartz Pressure Tool measures pressure and gauge temperature using an industry standard precision quartz crystal pressure transducer.

A Quartzdyne® pressure gauge, with removable bellows to isolate the quartz crystal from well fluids, is fitted to the lower tool body. An open pressure port with wire mesh filter allows well pressure into the gauge. A second (flushing) port is plugged whilst running in hole.

The crystal resonance frequency depends on pressure and temperature, hence the gauge incorporates a second "temperature" crystal, thermally coupled to the first which is not subjected to well pressure.

A 7.2 MHz clock, used to down shift the pressure and temperature crystal frequencies is output as a time reference for frequency measurement. Drift of this clock is included in the calibration algorithm, resulting in accurate calculation of temperature and pressure. Gauge output pressure and temperature frequencies lie in the range 15–60 kHz.

Features

- Pressure gradient measurement.
- Draw-down and build-up pressure transient Analysis.
- Fast response to small changes in fluid pressure.

9.3.3 Platinum Resistance Thermometer (PRT)

The Platinum Resistance Thermometer (PRT) tool measures the borehole fluid temperature, which can be used for finding fluid entry, gas leaks, and injection zones. It is also useful in finding cement tops. The tool plays a critical role in PL interpretation and is an integral piece of equipment in any production logging string.

The PRT measures downhole temperature by measuring the resistance of a platinum resistance element. The probe is contained in a pressure tight Inconel® needle, protruding into an open slot through which borehole fluid can flow. The measurements from the low mass probe result in high-resolution data with fast temperature response.

Features

- Fluid, gas leak detection.
- Location of production and injection zones.
- Cement top identification.
- Location of fluid movement behind pipe (Fig. 9.7).

Fig. 9.7 PRT thermometer

9.3.4 Enhanced Capacitance Water Holdup Tool (CWH)

The Enhanced Capacitance Water Hold-Up (CWH) Tool measures the dielectric constant of the surrounding borehole fluid to determine the water holdup.

Borehole fluid enters a hollow tube that surrounds an insulated rod at the centre. The tube wall and the insulated rod form the electrodes of a capacitor. As hydrocarbons and water have different dielectric constants, the capacitance is a function of the dielectric constant of the fluid between the rod and wall of the tube. This capacitance is incorporated in the frequency determining circuitry of an oscillator. The frequency of the oscillator is therefore a function of the type of fluid that is present in the borehole.

The dielectric constant of water is 80, oil is around 10, and air has a value of 1. Salinity has minimal effect on tool measurement. The enhanced measurement has improved response characteristics particularly at water holdup values greater than 50 %. The improved design also minimizes the "watering out" effect that can, under certain circumstances, result in the tool continuing to read water even though the surrounding fluid has been replaced by hydrocarbons.

Features

- Improved response compared with earlier generation capacitance sensors
- Two phase production profiling
- Water Hold-up calculations
- Qualitative Analysis of high GOR wells (Fig. 9.8).

9.3.5 Fluid Density Radioactive (FDR)

The FDR (see Fig. 9.9) uses low-energy gamma rays to determine the downhole fluid density during a production log. It provides a safe and reliable measurement that is unaffected by well deviation and flow rates.

Gamma rays are emitted from an Americium-241 source at one end of a measuring cell and are detected at the opposite end by a scintillation detector and photomultiplier. Well fluid flows through the cell and attenuates the received count

Fig. 9.8 CWH water hold-up tool

Fig. 9.9 FDR fluid density radioactive tool

rate in an inverse logarithmic function of the average fluid density. The detector is temperature stabilized and matched to the gamma energy of the source.

The tool can be calibrated in air and fresh water using Sondex supplied multipliers to derive calibration values applicable to oil and saltwater densities.

Features

- Americium 241 gamma ray source.
- Shielded detector highly resistant to radioactive scale interference.
- Multiphase production profiling.
- Fluid identification.
- Used in all well deviations.
- Density measurements in a range of fluid flow rates.
- Protective radiation shield (type A rated) can be locked on the tool so that the source can be left in place between jobs.

9.3.6 Multifinger Imaging Tool (MIT 60 Finger)

The 60 finger MIT (see Fig. 9.10) is used to detect very small changes to the internal surface condition of tubing or casing with a high degree of accuracy. The tool may be run with extended length fingers to increase the measurement range.

The MIT is available in a range of diameters to suit varying casing/tubing sizes. The number of fingers increases with the diameter of the tool to maintain maximum surface coverage. When the tool is run in hole, the fingers are closed to prevent damage. Once at logging depth, a motor is activated from the logging system or by the memory tool and the fingers open. A continuous measurement of the pipe's surface condition is made as the tool is logged up. The tool has an inclinometer to indicate the finger positions relative to the high side of the pipe, so that features can be orientated correctly during data processing. MIT data can be used to generate 3D images of pipe condition using Sondex's visualization software Well Integrity Visual Analysis (WIVA). Well Integrity Processing, Evaluation and Reporting

Fig. 9.10 MIT-60 multifinger imaging tool

(WIPER) software can also be used to make a statistical analysis of the pipe condition.

Features

- Available in 24 or 40 finger versions.
- Surface Readout or Memory options.
- 3D data analysis using WIVA software.
- Statistical analysis using WIPER software.
- Suitable for all well deviations.
- Extended finger lengths available for all tools (optional).

9.4 Cased-Hole Resistivity Measurements (CHFR)

The ability to measure water saturation through casing is highly desirable, mainly in old wells to monitor changes with depletion and identify zones that still have producible oil. It has been done for many years using pulsed neutron devices. However these have relatively shallow depths of investigation and do not always give satisfactory answers. At first sight it, would seem impossible to measure resistivity through the highly conductive casing, but the method has been recognized for years, with the first patent being filed in the 1930s. The main difficulty is the extremely small electrical potential that must be measured, but this was overcome in two devices that appeared in the late 1990s: the Through Casing Resistivity Tool and the Cased-Hole Formation Resistivity Tool.

Both tools work on the same basic principle (see Fig. 9.11). In the current leakage mode, current is sent between a downhole injection electrode and the surface. This current flows down the casing past three voltage-measuring electrodes A, B, and C, each 2 ft apart. Although most of the current stays within the casing, a small fraction leaks into the formation (ΔI). This leakage is seen as a progressive reduction in current flowing in the casing, which leads to a different potential drop from A to B than from B to C. This difference also depends on the casing resistance from A to B and B to C. If it is the same then $V_2 - V_1$ is a direct measure of ΔI, but since we are dealing with very small voltages any small difference in casing resistance is important. This difference, ΔR_c, is therefore measured in a second "calibrate" mode, in which the current is returned downhole instead of to the surface. In this configuration, the leakage current is found to be negligible so that $V_2 - V_1$ is a direct measure of ΔR_c.

The signal to noise ratio is low enough that measurements must be made with the tool stationary. Logging speed is therefore slow, so there have been several efforts to speed it up. By adding a fourth electrode and duplicating circuits it is possible to make measurements at two depths, 2 ft apart, during one station. In a recent tool the two modes are performed at the same time. This is achieved by a voltage generator that feeds back current around the calibrate path during the current leakage mode so as to cancel the voltage V_2. The computation now no

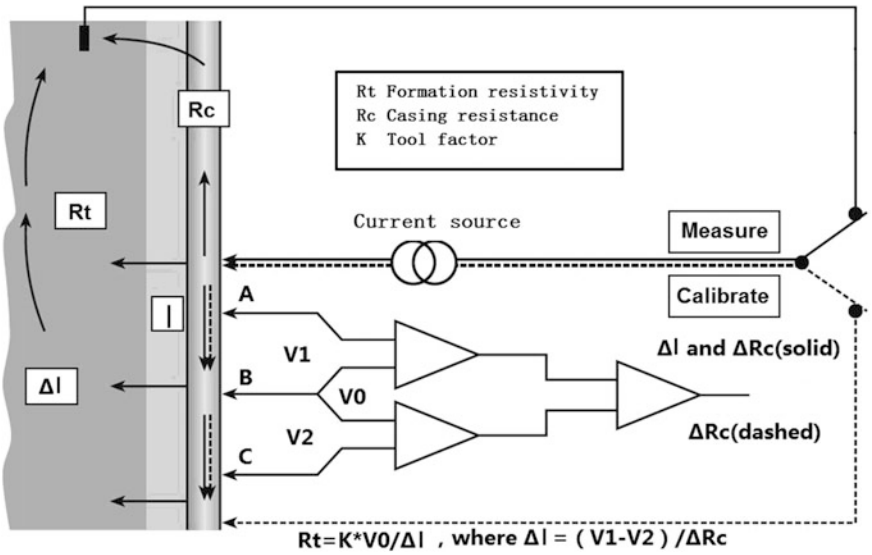

Fig. 9.11 The basic principle of measuring resistivity through casing. The formation current, ΔI, and the variation in casing resistance between AB and BC, R_c, are measured in two steps, labeled Measure and Calibrate. In some later tools more complex circuitry allows this to be done in one step

longer depends on ΔR_c but on V_1 and the R_c between A and B. The latter can be measured at the same time as, but with a different frequency than, the current leakage.

The result is a reduced sensitivity to measurement errors and a one-step, faster, recording. With the formation current ΔI known, R_a can be calculated from Eq. 9.1 with the voltage on the casing at the electrodes, V_0, and a K-factor. V_0 is measured by sending current as in the current leakage mode and measuring the voltage between the downhole voltage electrodes and a surface reference (not shown in Fig. 9.11).

$$R_a = K\frac{V_{tool}}{I_{meas}} \tag{9.1}$$

where V_{tool} is the formation voltage drop measured by the toroid and I means is the current at the monitor. K depends on the drill collar geometry.

Although V_0 varies slowly with depth it is not easy to measure accurately because it is small (less than 100 mV) and because of problems with the surface reference electrode: for example, it may not be possible to place the electrode far enough from the casing to be considered at zero potential. In practice, cased-hole resistivity logs may need to be shifted to match openhole logs in a shale or other zone where formation resistivity should not have changed with time. Any such shift

needs to be adjusted near the bottom of the casing where voltage changes fast with depth.

Understandably there are some limitations to the through-casing measurement. First we should appreciate that formation resistivity is typically nine orders of magnitude larger than that of the casing. However the formation presents a much larger area than the casing, so that the ratio of resistances and hence of leakage current to total current is around $10 - 4$. This current is measured through a casing resistance that is a few tens of micro-ohms, leading to a differential voltage $V_2 - V_1$

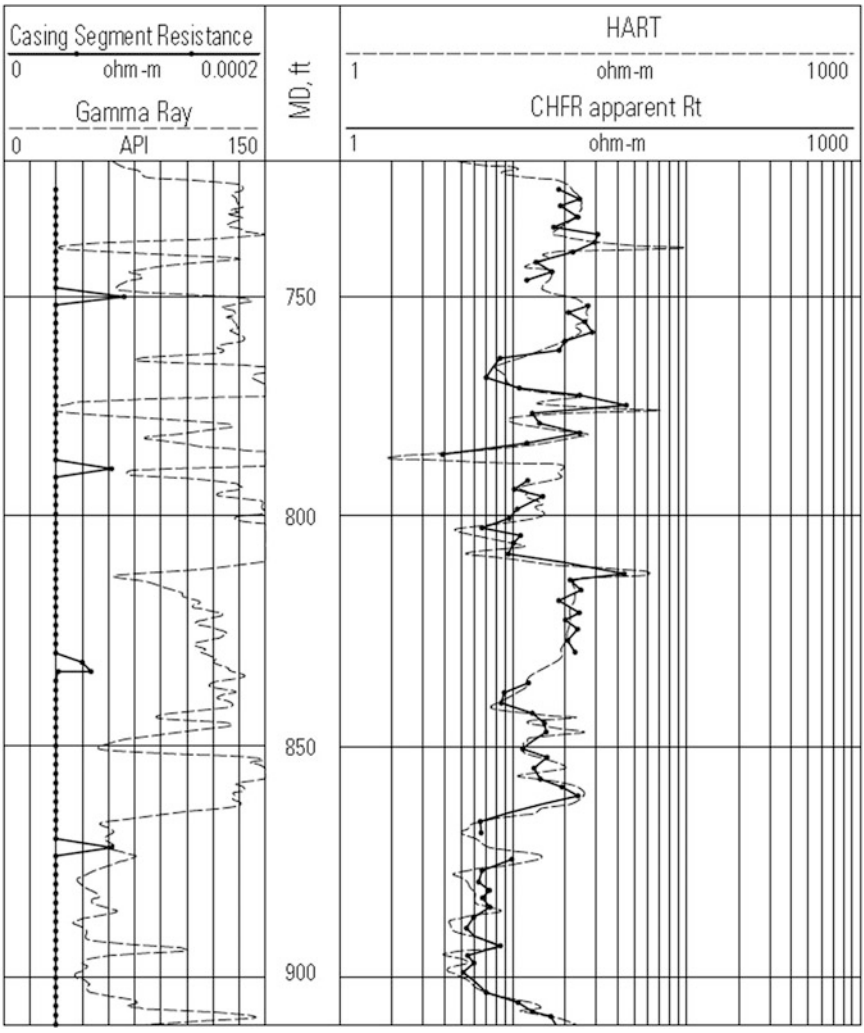

Fig. 9.12 A cased-hole formation resistivity log in a newly cased well versus a laterolog previously recorded in the open hole

that is in nanovolts. In order to achieve sufficient signal to noise, this small voltage must be measured over a period of time with the tool stationary. The measurement frequency is no more than a few Hz: at higher frequencies the skin depth in the casing would be reduced, confining even more of the current within the casing and further decreasing the leakage current, while a direct current would polarize and drift.

For the time being, the tool works best in the formation resistivity range 1–100 Ωm. Below 1 Ωm, the measurement becomes sensitive to the cement resistivity and thickness, neither of which is well known. As resistivity increases, the formation current drops. This can be partially overcome by repeating the measurement for a longer period at each station, but there is a practical limit on how much this can be done. The good agreement that can be obtained within the 1–100 Ωm range between cased-hole resistivity and an open-hole laterolog can be seen in Fig. 9.12. Once measured, the resistivity through casing has some appealing features. The casing acts as a giant guard electrode so that the leakage current is particularly well focused. In an infinitely thick formation the depth of investigation is of the order of tens of feet, much larger than a laterolog. Like any laterolog, this is reduced in thinner beds. Also like a laterolog, an invaded zone or cement that is more resistive than R_t affects strongly the measurement.

Problems

9.1 List the imaging logging instruments of Eclips-5700 system.
9.2 What are the benefits of MAC and CBIL?
9.3 What are the features of Excell 2000?
9.4 What are the features of Sondex flowmeter?
9.5 What are the advantages of multifinger imaging tool?
9.6 What are the principle of CHFR measurement?

Chapter 10
Integrated Interpretation of Well Logging Data

Well logging, has become in some ways the geologist's eye—an eye that is imperfect and sometimes distorted but nevertheless not blind—and an instrument for the reservoir engineer, occupies a special place and plays an important role in petroleum research by the economies that they bring and the amount of information they contain.

Integrated interpretation of well logging, as applied to subsurface petroleum reservoirs, has historically been defined as the practice of determining reservoir thickness, lithology, porosity, hydrocarbon saturation, and permeability, using information obtained from a borehole. This definition probably represents a consensus, which is a summary of quotations on the definition, scope, and objectives of formation evaluation from experts on the subjects.

The evaluation of a series of reservoirs based on well log data has the following essential objectives:

(a) Location of reservoirs, vertically within the drilled section, and spatially by determining the x, y, and z coordinates for the upper and lower boundaries of each reservoirs.
(b) Determination of fluid type within the reservoir: types of possible hydrocarbons, gas, oil, or bitumen; salt content of the formation water.
(c) Calculation of reserves, both moveable and in place. This involves:
determination of both the apparent and the actual thickness of each reservoir from dipmeter data;
computation of the petrophysical parameters, i.e., porosity (total, primary, secondary and effective) and mode of distribution of the porosity and geometry of the pores;

- computation of water and oil saturation;
- calculation of pay thickness;
- selection of cut-offs;
- determination of reservoir the productivity.

H. Liu, *Principles and Applications of Well Logging*, Springer Mineralogy,
DOI 10.1007/978-3-662-53383-3_10

determination of the productivity of the well, that is maximum output for optimal recovery of the hydrocarbons in place. This involves:
determination of mobility;
calculation of the total and relative permeability;
determination of the formation pressure.

(e) Determination of the lithology, facies, and depositional environment so as to get an idea of the lateral extent of the petrophysical features of the reservoir: exact nature of principal minerals and, if possible, of the accessory ones, since any error in mineral type can lead to significant errors in the calculation of porosity, of saturation and of reservoir:
percentages of the principal minerals;
clay content, clay type and distribution;
estimation of texture, grain size distribution, sorting, and grain shape.

10.1 Reservoir Classification

Clastic profile is mainly composited of sand, siltsand, and a small amount of conglomerate, and carbonated rocks in some few cases. The shoulder rocks upper and lower of the reservoir are commonly thickness impermeable shale layers. Conventional logging curves can delineate reservoir in the shale-sand profile, and the usually used curves are Spontaneous potential, Gamma ray, micro-resistivity sonde and caliper curves. For the reservoir, the main characteristics are the following:

(1) SP curve: if $R_{mf} > R_w$ (R_{mf} is the resistivity of drilling fluid, and R_w is that of formation water), the SP curve deflects, referring to the shale base line, to the negative side; inversely, if $R_{mf} < R_w$, SP curve deflects to the positive. The abnormal amplitude of SP curve depends on the volume of shale and the salinity of formation water, i.e., the value of R_{mf}/R_w. The deflection reduces with increasing of shale amount in the formation.

(2) GR curve: generally, shale has high GR value and sandstone's GR value is low, and for the pure sand, the value reaches its minimum.

(3) CAL curve: mud cake exists on the zone with certain permeability in the shaly sandstone profile. The log readings usually less than the size of Bit, and the curve relatively shows straight. Based on the features, GR is often used to calculate volume of shale.

(4) ML curve: the depth of investigation (DOI) of micro-resistivity logging is very shallow, and so will be strongly affected by the mud cake at permeable zone. On the map of overlapped micro-inverse and micro-normal resistivity logging curve, it shows positive difference for the permeable zone, and the more permeable, the more greater difference. The common law for identifying permeable zone using ML curves is: if $R_a \leq 10\ R_m$, a better permeable zone;

$10\ R_m < R_a \leq 20\ R_m$, a relative lower permeable zone; and $R_a > 20\ R_m$ while the curve shows sharp serrated shape, alternatively positive and negative difference, it is an impermeable layer.

Most of the analyses presented in earlier chapters work equally well with carbonate formations. However, the grain density used for deriving porosity from the density log needs to be set to a different value. For limestones the most common value used is 2.71 g/cc, although a direct measurement on the core is preferred, if available. Dolomite and anhydrite have higher matrix densities. In many fields with good quality carbonate reservoirs, evaluation is simpler than with sandstone because the shaly sand problem does not occur and beds tend to be thicker. In general, it will be found that Archie's model works very well.

Typical characteristics of low-permeability (<1 md) carbonate reservoirs are:

(1) Porosity may still be appreciable but be in the form of isolated pockets or vugs. This is often seen in chalk reservoirs.
(2) Entry heights and transition zones may be extremely long (up to 100 m).

Matrix permeability may be extremely low, but the well may flow due to the presence of natural (or mechanically induced) fractures in the formation.

The density log is the basic lithology tool when used in conjunction with porosity values from the neutron log. The density log alone can be used to distinguish beds of anhydrite and halite from carbonate beds because they have unique densities of 2.97 and 2.0 g/cm^3, respectively, and are typically dense (Fig. 10.1a). The combination of density and neutron logs is commonly used to identify limestone and dolomite in a carbonate sequence. Given the correct log scales, the density and neutron logs will overlie for limestone and will be separated for dolomite (Fig. 10.1b).

(1) Lithological properties of carbonate rocks
The nature of a rock and its composition are the first characteristics which the geologist attempts to determine, and a knowledge of these enables him to describe the properties of reservoir. Rock type is also his first concern in the study. Commonly included in this group are the calcite, dolomite, gypsum, and anhydrite, salt also exists. Table 10.1 shows the main physical eigenvalue of these rocks.

Frequently anhydrite, gypsum, and salt have very small voids and so are impermeable, hence, cannot be reservoirs. Through some of these parameters of them, such as photo-electronic cross section index, bulk density, acoustic wave travel time and thermal neutron capture section, we can distinguish different lithologies.

(2) Delineation of reservoir
In the carbonate rocks profile, dolomite and limestone are usually reservoir rocks, and well logs' response to these rocks have some distinguishing characteristics. The typical responding are high acoustic wave travel time, low gamma ray, low resistivity, and low neutron logging value. To identify

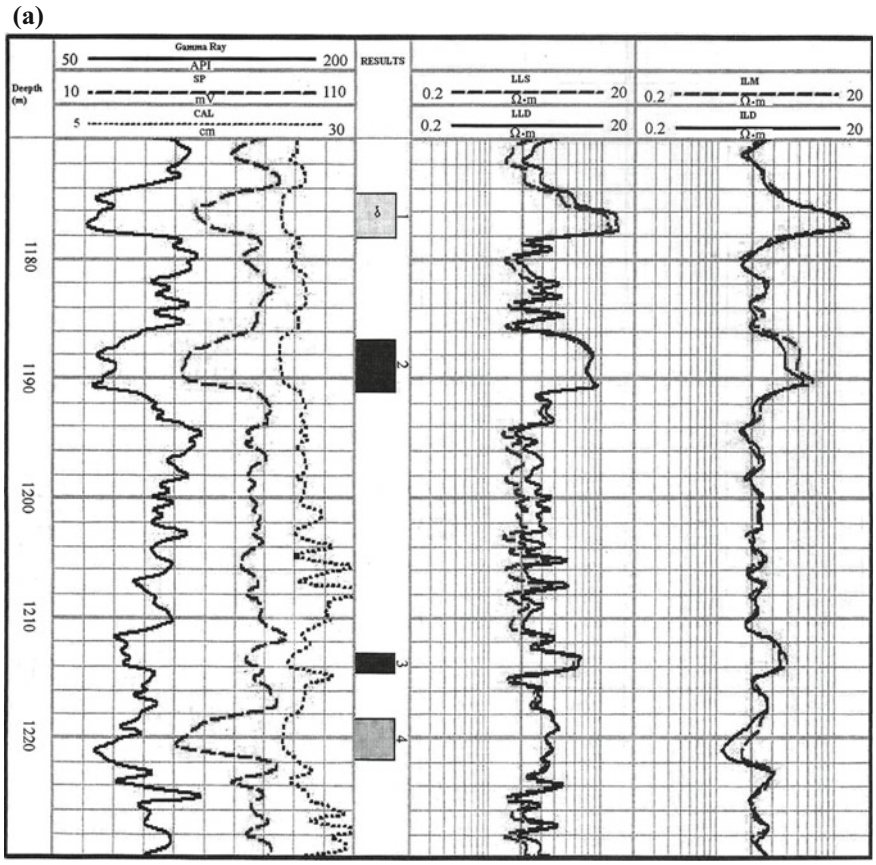

Fig. 10.1 Well *logging curves* of shaly sand and carbonate profile. **a** Well *logging curves* of shaly sand profile. **b** Well *logging curves* of porous carbonate profile. **c** Well *logging curves* of clastic and carbonate profile

(b)

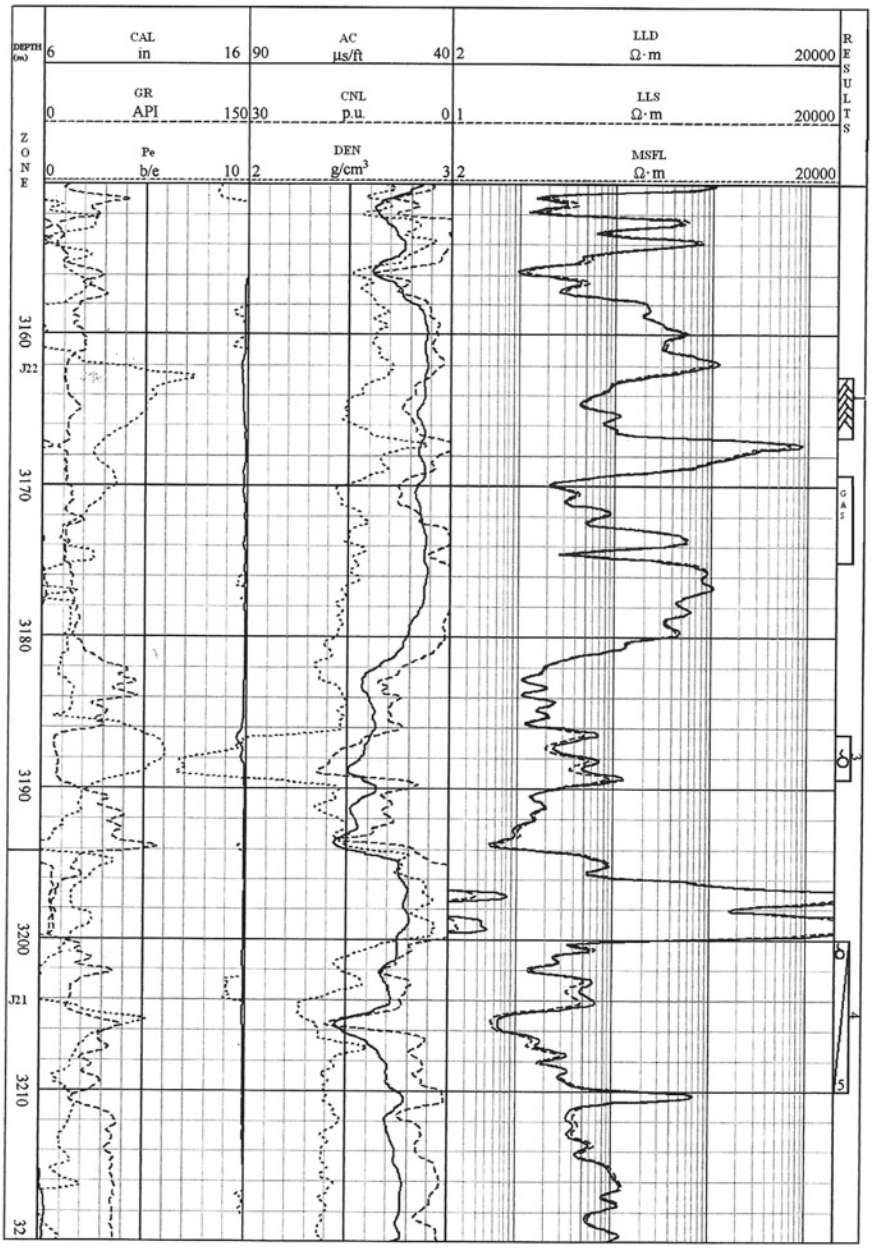

Fig. 10.1 (continued)

(c)

Fig. 10.1 (continued)

Table 10.1 Matrix and fluid coefficients of several minerals and types of porosity (liquid filled boreholes)

Mineral	Δt_{ma} (μs/ft)	ρ_{ma} (g/cm^3)	ϕ_{ma}*SNP* p.u.	ϕ_{ma}CNL p.u.
Sandstone 1 (V_{ma} = 18,000, ϕ > 10 %)	55.5	2.65	−0.035[a]	−0.05[a]
Sandstone 2 (V_{ma} = 19,500, ϕ > 10 %)	51.2	2.65	−0.035[a]	−0.05[a]
Limestone	47.5	2.71	0.00	0.00
Dolomite (ϕ = 5.5–30 %)	43.5	2.87	0.02[a]	0.065[a]
Dolomite 2 (ϕ = 1.5–5.5 %, > 30 %)	43.5	2.87	0.02[a]	0.065[a]
Dolomite 3 (ϕ = 0.0–1.5 %)	43.5	2.87	0.005[a]	0.04[a]
Anhydrite	50.0	2.98	−0.005[a]	−0.0020
Gypsum	52.0	2.35	0.49[b]	
Salt	67.0	2.03	0.04	−0.01

[a]Average values. [b]Based on hydrogen-index computation

carbonate reservoir, first, to locate the zone with low resistivity and high porosity, and then to pick out the high gamma, i.e., shale zone, and so the residual zones in the carbonate profile are permeable zones. Another method also can achieve the same effect. From the gamma log, low readings corresponding to non-shale zone, and get rid of the relative high resistive and low porosity tight zone, the remaining layers are reservoir. The interface of reservoir is usually identified using GR curve.

Sometimes, low resistive and high porosity zones with mediate or high gamma value are possible shale or shaly carbonate zones. For the pure tight carbonate zone, its behavior is low gamma value, high resistivity, and relative high porosity. Figure 10.2b shows a porous carbonate profile.

(a) Depth plot overlaying density and CNL porosity logs showing identification of halite, anhydrite, and dolomite beds.

(b) An illustration of identifying limestone, dolomite, and anhydrite beds using overlays of neutron and density porosity augmented by the PEF curve. The photoelectric log (PEF) is also a basic log for determining lithology. This log focuses on low-energy gamma rays, and the energy loss can be related directly to lithology. Photoelectric factors for common carbonate minerals can be found in Schlumberger's Log Interpretation Charts.

10.2 Formation Evaluation

10.2.1 Identification of Permeable and Non-permeable Zones from Logs

The permeable zones on a suite of logs can be identified by referring to the GR, SP, and resistivity logs. The Gamma Ray log is generally used as a depth reference tool and the Gamma Ray Sonde is therefore run with all logging tools. It is, however, primarily used from an interpretation viewpoint to differentiate between shales and other formation types. Since shales generally have a very low permeability (very common caprocks) the Gamma Ray log response can be used in a qualitative way to identify non-permeable zones. The technique for identifying permeable zones on an SP log is provided in Sect. 2.2 of Chap. 2. A comparison of the resistivity readings from the flushed zone, shallow and deep into the reservoir (Fig. 10.2) will give some indication of the depth of penetration of the borehole fluid and therefore the permeability of the formation.

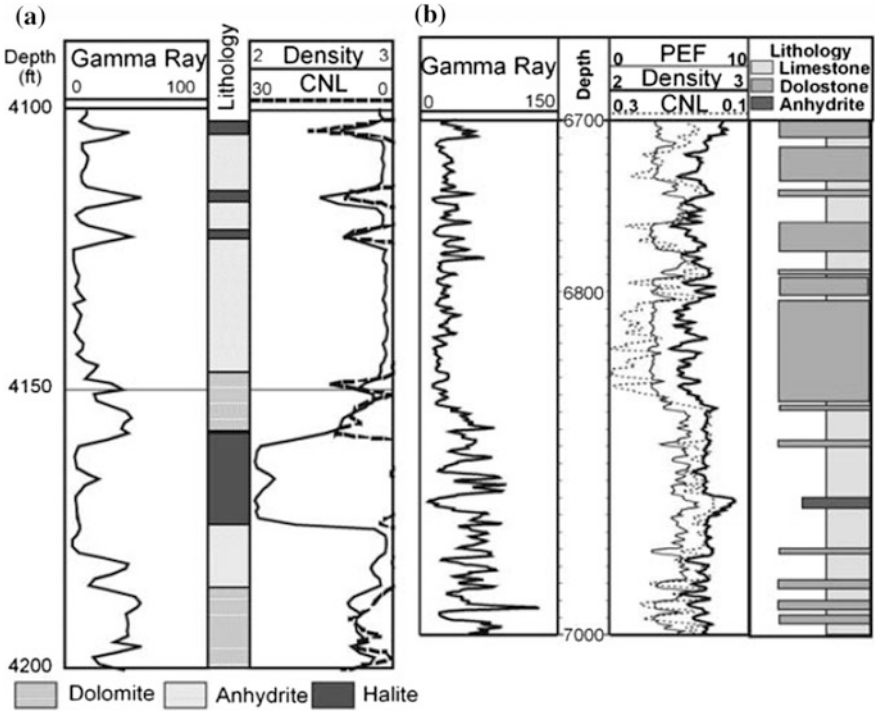

Fig. 10.2 Illustrations of lithology from wireline logs

10.2.2 Determine and Divide the Formations into Water Bearing and Hydrocarbon

The nature of the fluids in the permeable formations is determined by analysis of the porosity and resistivity logs. It is possible to differentiate between gas and liquid with the porosity logs but it is not possible to differentiate between water and oil from these logs. The characteristics of the log measurements made by porosity tools in gas-bearing and non-gas-bearing formations are shown in Fig. 10.1b. The rationale for these log responses is explained in Chap. 2. The resistivity logs can only be used to differentiate between hydrocarbons and water. This is because the conductivity of gas and oil will be similar whereas the resistivity of (salt) water and hydrocarbons will be significantly different. The interpretation of the response of the resistivity tools in water and hydrocarbon and water-bearing formations relies on an appreciation of the changes in resistivity that occurs in the region close to the wellbore of a permeable zone (Fig. 10.1a, b). When a permeable zone is penetrated by the drillbit the drilling mud will try to penetrate the permeable formation. If the sizes of the pores in the formation are smaller than the solids in the drilling fluid then the solids will be trapped on the surface of the wellbore and the fluid in the drilling mud will pass through the solids into the formation. When invasion occurs, the wellbore is coated with a thin film of solids known as the "filter cake" and the formation next to the wellbore is "flushed" by the mud filtrate moving into the formation and is therefore known as the "flushed zone." The hydrocarbon saturation in the flushed zone is a minimum and all of the formation water is removed.

The formation deeper into the zone are affected progressively less than the flushed zone until at some radial depth into the formation the fluids in the pore space are undisturbed. In a hydrocarbon-bearing formation, the hydrocarbon saturation is reduced in the flushed zone and increases in the transition zone until the original saturation is reached in the undisturbed zone. In water-bearing formation, the water saturation in the zone between the flushed zone and the undisturbed zone would not change but the salinity and therefore the resistivity may. These changes in saturation and resistivity create resistivity profiles which can be used to identify the water-bearing and hydrocarbon-bearing formations.

When using freshwater mud, the resistivity of the mud filtrate is higher than that of the formation water and therefore in water-bearing zone the resistivity of the flushed zone is high and the resistivity readings decrease with movement out into the undisturbed zone. In a hydrocarbon-bearing formation, the resistivity of the zone behind the flushed zone may be higher or lower than the flushed zone depending on the water saturation and resistivity of the formation water. The resistivity profiles and relative readings which would be expected from the shallow (*S*), medium (*M*), and deep (*D*) reading resistivity logs for each of the above conditions are shown in Fig. 10.1a, b.

When using a salt water mud the flushed zone has a lower or similar resistivity than the undisturbed zone if the undisturbed zone contains high resistivity water. The undisturbed zone will have higher resistivity if the formation contains hydrocarbons.

10.3 Method to Determine Lithology: *M–N* PLOT

In more complex mineral mixtures, lithology interpretation is facilitated by use of the *M–N* plot. These plots combine the data of all three porosity logs to provide the lithology-dependent quantities M and N. M and N are simply the slopes of the individual lithology lines on the sonic-density and density-neutron crossplot charts, respectively. Thus, M and N are essentially independent of porosity, and a crossplot provides lithology identification. M and N are defined as:

$$M = \frac{t_f - t}{\rho_b - \rho_f} \times 0.01 \tag{10.1}$$

$$N = \frac{\phi_{Nf} - \phi_N}{\rho_b - \rho_f} \tag{10.2}$$

For fresh muds, $t_f = 189\,\mu s/ft$, $\rho_f = 1 g/cc$, and $\phi_{Nf} = 1$. Neutron porosity is in limestone porosity units. The multiplier 0.01 is used to make the M values compatible for easy scaling.

If the matrix parameters $(t_f, \rho_f, \phi_{Nma})$ for a given mineral are used in (10.1) and (10.2) in place of the log values, the M and N values for that mineral are defined. For water-bearing formations, these will plot at definitive points on the *M–N* plot. Based on the matrix parameters in Table 10.1, M and N values can be calculated and are shown in Table 10.2 for several minerals in both fresh mud- and salt mud-filled holes (N is computed for the CNL log.).

Points for a mixture of three minerals will plot within the triangle formed by connecting the three respective single-mineral points. For example, suppose a rock mixture exhibits $N = 0.59$ and $M = 0.81$. In Fig. 10.3 this point falls within a

Table 10.2 M and N values for common minerals

Mineral	Fresh mud ($\rho_f = 1$)		Salt mud ($\rho_f = 1.1$)	
	M	N*	M	N*
Sandstone 1 $V_{ma} = 18{,}000$	0.810	0.636	0.835	0.667
Sandstone 2 $V_{ma} = 19{,}500$	0.835	0.636	0.862	0.667
Dolomite 1 (ϕ = 5.5–30 %)	0.827	0.585	0.854	0.621
Dolomite 2 (ϕ = 1.5–5.5 %)	0.778	0.489	0.800	0.517
Dolomite 3 (ϕ = 0–1.5 %)	0.778	0.500	0.800	0.528
Anhydrite	0.778	0.513	0.800	0.542
Gypsum	1.015	0.296	1.064	0.320
Salt			1.269	1.086

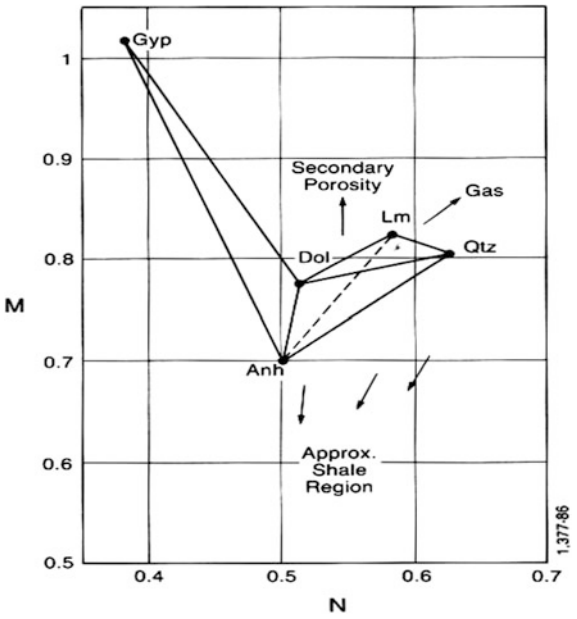

Fig. 10.3 *M–N* plot showing the points for several single-mineral formations

triangle defined by the limestone–dolomite–quartz points. It would, therefore, be interpreted in most cases as representing a mixture of limestone, dolomite, and quartz. However, it could also be a limestone–quartz–anhydrite mixture, or (less likely) a dolomite–quartz–gypsum mixture, since the point is also contained in those triangles. The combination selected would depend on the geological probability of its occurrence in the formation.

Secondary porosity, shaliness, and gas-filled porosity will shift the position of the points with respect to their true lithology, and they can even cause the *M–N* points to plot outside the triangular area defined by the primary mineral constituents.

In the case of shale, the arrow is illustrative only since the position of the shale point will vary with area and formation. In combination with the crossplots using other pairs of porosity logs and lithology sensitive measurements, the *M–N* plot aids in the choice of the probable lithology. This information is needed in the final solution for porosity and lithology fractions.

10.4 U_{maa} MID Plot

The apparent matrix volumetric cross section is computed from the photoelectric cross section index and bulk density measurements.

$$U = \sum U_i V_i$$
$$U = U_{\mathrm{ma}}(1-\phi) + U_{\mathrm{f}} \cdot \phi$$
$$U \approx U_{\mathrm{ma}}(1-\phi)$$
$$U_{\mathrm{ma}} = \frac{U}{1-\phi}$$

The apparent total porosity can be estimated from the density-neutron crossplot, if the formation is liquid filled. A simplified version is shown in Fig. 10.4.

Figure 10.4 shows the location of these minerals on the U_{maa} versus ρ_{b} crossplot. The triangle encompassing the three common matrix minerals of quartz, calcite, and dolomite has been scaled in the percentages of each mineral. For example, a point exhibiting an apparent matrix grain density of 2.76 g/cm^3 and volumetric cross section of 10.2 barns/cm^3 would be defined by 40 % calcite, 40 % dolomite, and 20 % quartz provided no other minerals exist and the pores are liquid saturated. On this crossplot, gas saturation displaces points upwards on the chart and heavy minerals displace points to the right. Clays and shales plot below the dolomite point.

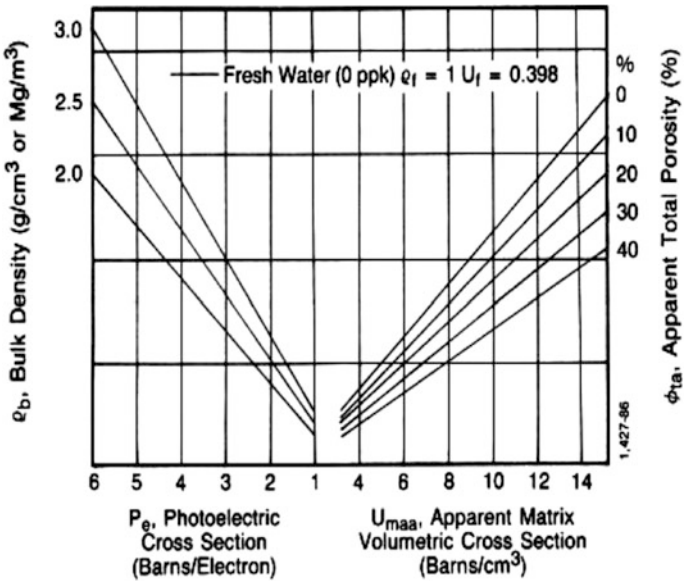

Fig. 10.4 Matrix identification plot by using P_{e}-ρ_{b} and U_{maa}-ρ_{b} cross plot

10.5 Resistivity Versus Porosity Crossplot (Pickett Map)

For this method, the knowledge of porosity is required, but the values of m, R_w, and S_w can be obtained. In this method, the power law expression for saturation is exploited by plotting on log–log scales. Starting with the general saturation expression:

$$S_w^n = \frac{a}{\phi^m}\frac{R_w}{R_t} \tag{10.3}$$

taking the log of both sides of the equation and rearranging results in:

$$\log(\phi) = -\frac{1}{m}\log(R_t) + \frac{1}{m}(\log(a) + \log(R_w) - n\log(S_w)) \tag{10.4}$$

Thus at a constant water saturation, a log–log plot of porosity versus Rt should result in a straight line (see Fig. 10.4) of negative slope whose value is the cementation exponent, and should be in the neighborhood of 2. If we consider the value of a to be unity, then we can write:

$$\log(\phi) = -\frac{1}{m}\log(R_0) + \frac{1}{m}\log(R_w) \tag{10.5}$$

which represents the line of 100 % water saturation. In this case the intercept at the 100 % porosity point gives the value of R_w directly. For values of S_w less than 100 %, the relationship between φ and R_t will be represented by lines parallel to the 100 % saturation case but is placed to the right. With a saturation exponent of 2, these lines can be placed in relation to the S_w = 1 line by recognizing that at a fixed porosity a saturation decrease by a factor of 2 (i.e., from 1 to 0.5) corresponds to a resistivity increase by a factor of four. Thus one obtains the 50 % saturation line by shifting a line parallel to the S_w = 1 line by a factor of four in resistivity, and the 25 % saturation case by shifting another factor of 2, and so forth. An example of the result of this procedure is shown in Fig. 10.5

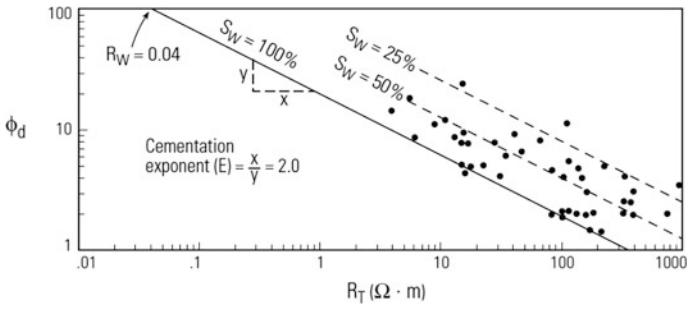

Fig. 10.5 A log–log representation of resistivity and porosity attributed to Pickett

It is useful for determining the cementation exponent that best describes a given formation.

10.6 Porosity Determination in Complex Conditions

The measurements of the neutron, density, and sonic logs depend not only on porosity (ϕ) but also on the formation lithology, on the fluid in the pores, and, in some instances, on the geometry of the pore structure. When the lithology and, therefore, the matrix parameters $(t_{ma}, \rho_{ma}, \phi_{ma})$ are known, correct porosity values can be derived from these logs, appropriately corrected for environmental effects, in clean water-filled formations. Under these conditions, a single log, either the neutron or the density or, if there is no secondary porosity, the sonic, can be used to determine porosity.

Accurate porosity determination is more difficult when the matrix lithology is unknown or consists of two or more minerals in unknown proportions. Determination is further complicated when the response of the pore fluids in the portion of the formation investigated by the tool differs appreciably from that of water. In particular, light hydrocarbons (gas) can significantly influence the response of all three porosity logs.

Even the nature of type of pore structure affects the tool response. The neutron and density logs respond to total porosity—that is, the sum of the primary (intergranular or inter-crystalline) porosity and the secondary (vugs, fissures, fractures) porosity. The sonic logs, however, tend to respond only to evenly distributed primary porosity.

To determine porosity when any of these complicating situations exists requires more data than provided by a single porosity log. Fortunately, neutron, density, and sonic logs respond differently to matrix minerals, to the presence of gas or light oils, and to the geometry of pore structure. Combinations of these logs and the photoelectric cross section index, P_e, measurement from the Litho-Density* log and the thorium, uranium, and potassium measurement from the NGS* natural gamma ray spectrometry log can be used to unravel complex matrix or fluid mixtures and thereby provide a more accurate porosity determination.

The combination of measurements depends upon the situation. For example, if a formation consists of only two known minerals in unknown proportions, the combination of density and neutron logs or the combination of bulk density (ρ_b) and photoelectric cross section will define the proportions of the two minerals and a better value of porosity. If it is known that the lithology is more complex but consists of only quartz, limestone, dolomite, and anhydrite, then a relatively accurate value of porosity can again be determined from the density-neutron combination; however, the mineral fractions of the matrix cannot be precisely determined.

Crossplots are a convenient way to demonstrate how various combinations of logs respond to lithology and porosity. They also provide visual insight into the type of mixtures that the combination is most useful in unraveling.

Figure 10.6 is an example in which neutron and density porosities are crossplotted on linear scales. Points corresponding to particular water-saturated pure lithologies define curves (sandstone, limestone, dolomite, etc.) that can be graduated in porosity units, or a single-mineral point (e.g., salt point) may be defined. This chart is entered with porosities computed as if the matrix had the same properties as water-saturated limestone; as a result, the limestone line is the straight line of equal density and neutron porosities. When the matrix lithology is a binary mixture (e.g., sandstone–lime or lime–dolomite or sandstone–dolomite) the point plotted from the log readings will fall between the corresponding lithology lines.

10.6.1 Neutron-Density Crossplots

The Fig. 10.6 was constructed for clean, liquid-saturated formations and boreholes filled with water or water-base mud. The charts should not be used for air-gas-filled boreholes; in these, the SNP matrix effect is changed. This figure is a similar plot for CNL* neutron versus density data.

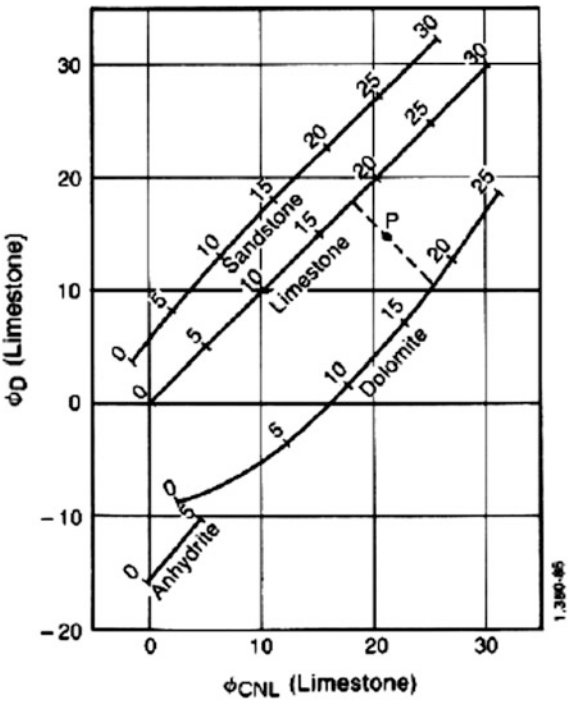

Fig. 10.6 Porosity and lithology determination from FDC density and CNL neutron logs

The separations between the quartz, limestone, and dolomite lines indicate good resolution for these lithologies. Also, the most common evaporites (rock salt, anhydrite) are easily identified.

In the example shown on Fig. 10.6, $\Phi_D = 15$ and $\Phi_N = 21$. This defines Point *P*, lying between the limestone and dolomite curves and falling near a line connecting the 18 % porosity graduations on the two curves. Assuming a matrix of limestone and dolomite and proportioning the distance between the two curves, the point corresponds to a volumetric proportion of about 40 % dolomite and 60 % limestone; porosity is 18 %.

10.6.2 Sonic-Neutron Crossplots

Figure 10.7a is a plot of sonic *t* versus porosity from an SNP log. As with the density-neutron plots, resolution between sandstone, limestone, and dolomite lithologies is good, and errors in choosing the lithology pair will have only a small effect on the porosity value found. However, resolution is lost if evaporites are present. Figure 10.7b is a similar plot of sonic *t* versus porosity from the CNL log.

The sonic crossplots are constructed for both the weighted average (Wyllie) and the observed (Raymer, Hunt, and Gardner) sonic transit time-porosity transforms. For mineral identification and porosity determination, use the transform previous experience has shown most appropriate for the area.

10.6.3 Sonic-Density Crossplot

Crossplots of sonic t versus density ρ_b or Φ_D have poor porosity and reservoir rock (sandstone, limestone, dolomite) resolution, but they are quite useful for determining some evaporite minerals. As can be seen from Fig. 10.8, an error in the choice of the lithology pair from the sandstone–limestone–dolomite group can result in an appreciable error in porosity. Likewise, a small error in the measurement of either transit time or bulk density can result in an appreciable error in porosity and lithology analysis. The good resolution given by the chart for salt, gypsum, and anhydrite is shown by the wide separation of the corresponding mineral points on the figure. Several log-data points are shown that correspond to various mixtures of anhydrite and salt and, perhaps, dolomite.

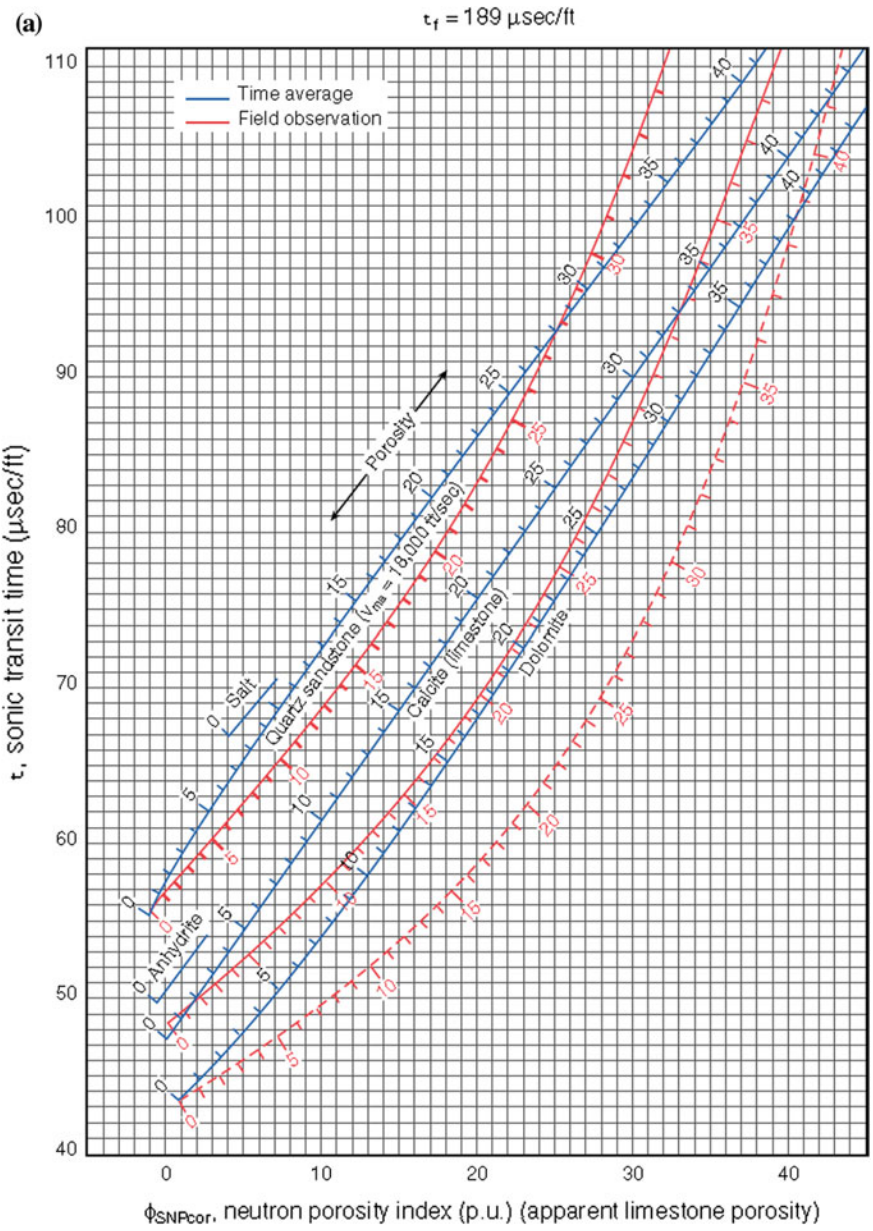

Fig. 10.7 **a** Porosity and lithology determination from sonic log and SNP sidewall neutron porosity log. **b** Porosity and lithology determination from sonic log and CNL* compensated neutron log. **c** Porosity and lithology determination from sonic log and CNL*

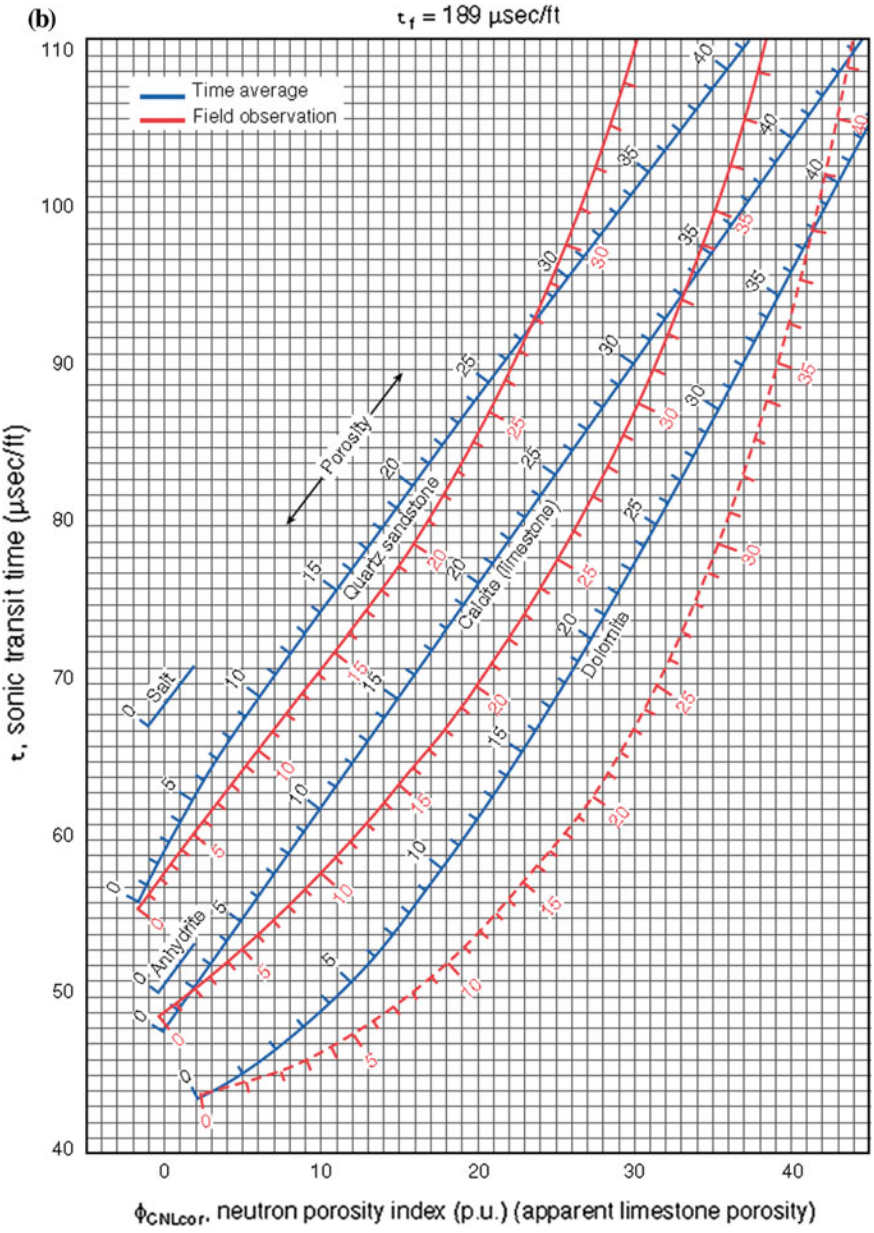

Fig. 10.7 (continued)

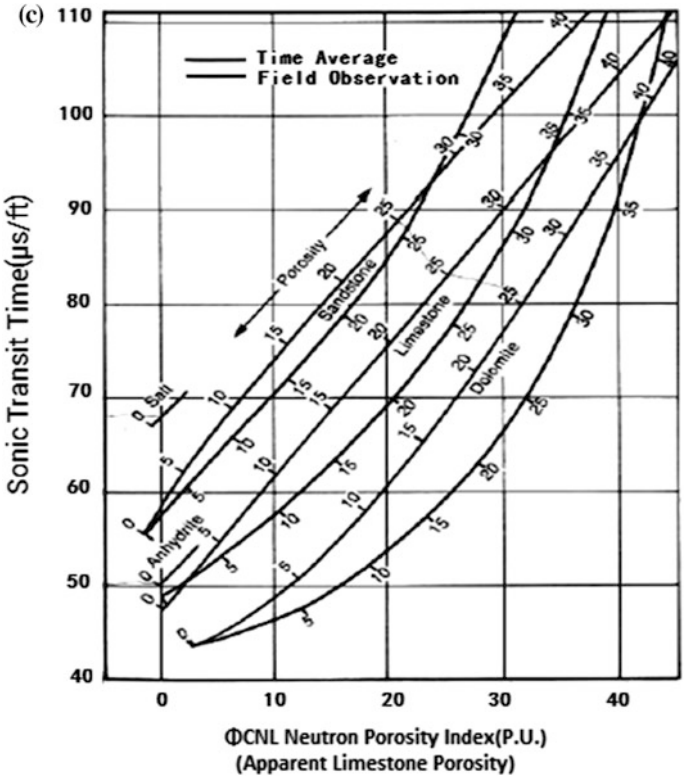

Fig. 10.7 (continued)

10.7 Resistivity Ratio Methods to Identify Fluid Type

In resistivity ratio methods, it is assumed that a formation is divided into two distinct regions, a flushed or invaded zone and a non-invaded zone. Both zones have the same f, but each contains water of a distinct resistivity R_{mf} or R_z in the invaded zone and R_w in the non-invaded zone). The resistivities of the two zones must be measurable or derivable from logs, and methods for determining the resistivity of the water in each zone must be available. Because of the necessary assumptions, the resistivity ratio methods have limitations, but when no porosity or formation factor data are available, they are sometimes the only choice. The principal limitation arises from the inability of any resistivity device be deep enough to allow a shallow-investigating resistivity device to measure R_{xo} but not so deep that a deep resistivity device cannot measure R_t.

Another difficulty appears when hydrocarbons are present. In this case, some knowledge or assumption of the value of the flushed or invaded zone saturation is necessary.

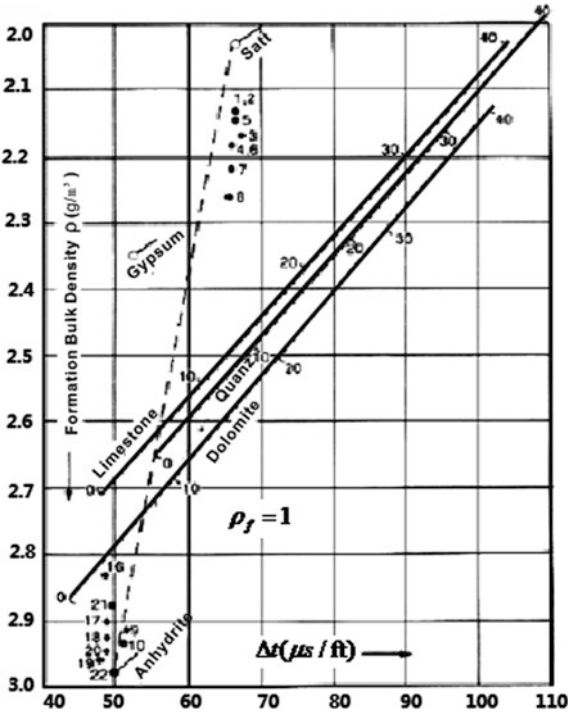

Fig. 10.8 Porosity and lithology determination from FDC density and sonic logs

If $n = 2$ is assumed and Eq. (10.1) is divided by Eq. (10.6),

$$\left(\frac{S_w}{S_{xo}}\right)^2 = \frac{R_{xo}/R_t}{R_{mf}/R_w} \tag{10.6}$$

This equation gives the ratio of S_w to S_{xo}, and no knowledge of formation factor or porosity is needed. R_{xo} may be found from a MicroSFL log, R_t from an induction or laterolog, and R_{mf}/R_w from a measured values or from the SP curve.

The ratio S_w/S_{xo}, is valuable in itself as an index of oil movability. If $S_w/S_{xo} = 1$, then no hydrocarbons have been moved by invasion, whether or not the formation contains hydrocarbons. If S_w/S_{xo} is about 0.7 or less, movable hydrocarbons are indicated. The value of S_w/S_{xo} along with ϕ and S_w, is useful in evaluating reservoirs. To determine S_w from Eq. (10.6), S_{xo} must be known. For moderate invasion and average residual oil saturation, an empirical relation between S_{xo} and S_w has been found useful: $S_{xo} = S_w/5$. Inserting this into Eq. (10.6) gives:

$$S_w = \left(\frac{R_{xo}/R_t}{R_{mf}/R_w}\right)^{5/8} \tag{10.7}$$

The relationship $S_{xo} = S_w^{1/5}$ is strictly empirical and may differ appreciably from the actual case.

Shale Resistivity

This is one of the parameters upon which the approach to shaly sands can be found. Normal practice would be to take the R_{sh} of an adjacent shale. However this presupposes the porosity, mineralogy, and R_w of the shale are the same as the shaly material in the shaly sand. While this may be appropriate in some laminated shale-sand sequences it cannot be said to be true of dispersed clays and some disseminated shale (Fig. 10.9).

Laminated Shales

The equation for laminated shales is a simple parallel flow model in which the resistivity, R_t should be,

$$1/R_t = V_{sh}/R_{sh} + (1 - V_{sh})/R_{sd} \tag{10.8}$$

Solving this for S_w using an Archie model and substituting through,

$$S_w = \sqrt[n]{\frac{abR_w}{\phi^m(1 - V_{sh})}\left(\frac{1}{R_t} - \frac{V_{sh}}{R_{sh}}\right)} \tag{10.9}$$

This model works reasonably where the sand laminae are clean. If the sands are not clean then a dispersed clay model should be used.

Dispersed Shales

More often than not, the formation shaliness consists of dispersed clay, with or without laminations. A fundamental problem is shown in the work of Hoyer and Spann, Waxman and Smits and Brown in 1988. The excess conductivity introduced by the presence of clay with a CEC does not cover the entire problem for independent of the CEC, the shale present will affect the cementation exponent, '*m*' through it micro porosity. In fact the more shale there is the higher the true m. In

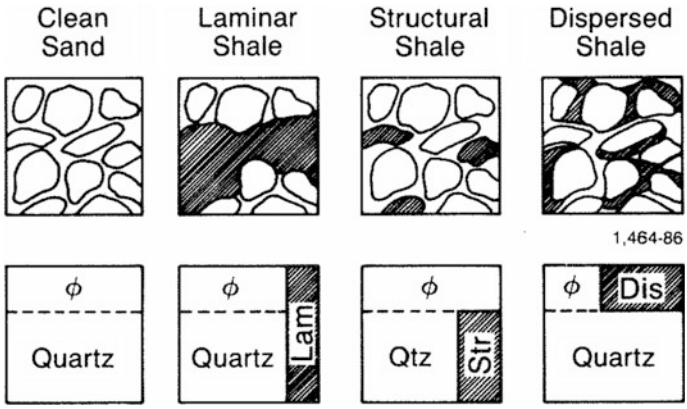

Fig. 10.9 Mixing models for shales and their volume cubes

our discussion in earlier chapters, we did not investigate this problem in any depth. Before we consider it, we must review the alternative dispersed clay models.

$$S_w = \sqrt{\frac{aR_w}{R_t\phi^2} + \left[\frac{(R_w - R_{sh}) \cdot V_{sh}}{2R_{sh} \cdot \phi}\right]^2} - \frac{V_{sh}(R_w + R_w)}{2R_{sh} \cdot \phi} \tag{10.10}$$

R_{xo}/R_t Quick-Look

The R_{xo}/R_t quick-look can be used to identify hydrocarbon-bearing formations and to indicate hydrocarbon movability (producibility). When S_w/S_{xo} is 1 in a permeable zone, the zone will produce water or be nonproductive regardless of water saturation. An S_w/S_{xo} is 1 in a permeable zone, the zone will produce water or be nonproductive regardless of water saturation. An S_w/S_{xo} significantly less than 1 indicates the zone is permeable and contains some hydrocarbons, and that the hydrocarbons have been flushed (moved) by invasion. Thus, the zone contains producible hydrocarbon.

Equation (10.6) can be re-written as

$$\frac{S_w}{S_{xo}} = \left(\frac{R_{xo}/R_t}{(R_{xo}/R_w)_{sp}}\right)^{1/2} \tag{10.11}$$

which shows that an indication of S_w/S_{xo} can be obtained by comparing R_{xo}/R_t with R_{mf}/R_w, where the subscript SP emphasizes that R_{mf}/R_w is derivable from the SP. Equivalently, the comparison can be between log R_{xo}/R_t and the SP curve for an indication of log S_w/S_{xo}.

The log R_{xo}/R_t is computed from a comparison of the deep and shallow resistivity measurements or from all three resistivity measurements or from all three resistivity measurements and is used as an overlay comparison curve with the SP. Separations between the log R_{xo}/R_t curve, properly scaled to match the SP, and the SP curve provide a quick-look location of producible hydrocarbons.

Originally, log R_{xo}/R_t was computed from R_{LLS}/R_{ID} or R_{SFL}/R_{ID}. Use was made of the observation that over a wide range of invasion diameters (from about 20 to 100 in.) R_{xo}/R_t depends primarily on the value of R_{LLS}/R_{ID} or R_{SFL}/R_{ID} (Fig. 10.10). The relationship employed for the LL8 device was

$$\frac{R_{xo}}{R_t} = 1.85(R_{LL8}/R_{ID}) - 0.85 \tag{10.12a}$$

For the SFL device, it was

$$\frac{R_{xo}}{R_t} = 1.45(R_{SFL} - R_{ID}) - 0.45 \tag{10.12b}$$

Much more sophisticated algorithms are now used to obtain R_{xo}/R_t. All three resistivity measurements of the DIL-SFL tool are employed. As a result, the

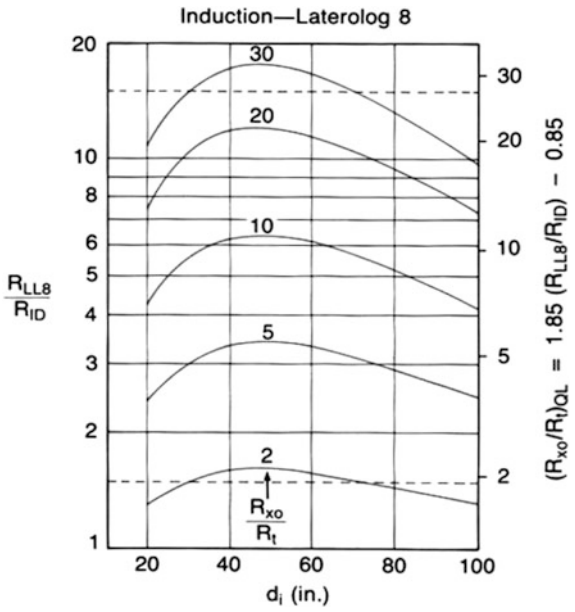

Fig. 10.10 Plot illustrating strong interdependence of RLL8/RID and R_{xo}/R_t in the range of di values from 20 to 100 in.

computed R_{xo}/R_t values more closely duplicate the values given by the relevant invasion correction chart and by Fig. 10.10 over a greater range of invasion diameters.

To interpret the R_{xo}/R_t quick-look curve, the impermeable zones must be eliminated by reference to the SP, GR, or microlog curves or by resistivity ratios. Then, if the SP and R_{xo}/R_t (actually—K log R_{xo}/R_t) curves coincide in a permeable zone, the zone will most probably produce water. If however, the R_{xo}/R_t curve reads appreciably lower (i.e., to the right) than the SP, the zone should produce hydrocarbons. An R_{xo}/R_t value less than the SP amplitude indicates movable hydrocarbons are present.

The R_{xo}/R_t quick-look technique is applicable to fresh mud conditions ($R_{xo} > R_t$) in formations where invasion falls within the limits demanded by the R_{xo}/R_t computation. For the simpler computation technique using Eq. (10.11), that is about 30–70 in.; for the more sophisticated techniques, that is between 20 and 120 in. Even in the more restrictive case, however, any errors are optimistic. In other words, water zones may appear to be hydrocarbon productive. This constitutes a safeguard against overlooking pay zones, and is considered a desirable feature in any quick-look approach. The R_{xo}/R_t technique efficiently handles variations in formation water resistivity, R_w, and in shaliness. Any change in Rw is reflected similarly into both the computed R_{xo}/R_t and the SP amplitude. Thus, comparing the two curves still permits formation fluid identification. Shaliness also affects the two curves in a similar manner. All other things remaining constant, shaliness reduces

the R_{xo}/R_t value and the SP amplitude. Finally, the R_{xo}/R_t quick-look technique does not require porosity data.

Figure 10.11a is an example of shaly gas sand at 3760 through 3788 ft and several water-productive sands with varying amounts of shale. The productive gas sand is identified by the separation between the R_{xo}/R_t and SP curves. Water-productive zones are shown by lack of separation. In shaly water zones the variation in the SP curve is essentially the same as the variation in the R_{xo}/R_t ratio—a result of the same shale; so, the comparison is not significantly disturbed by shale. Neither is it disturbed by variations in R_w. Estimates of water saturation and saturation ratio in clean formations can be made by comparing the R_{xo}/R_t and SP curves. Equation (10.11) permits S_w/S_{xo} to be estimated and Eq. (10.7) (assuming $S_{xo} = S_w$) permits S_w to be estimated.

Figure 10.11b shows another example, which plots much more curves, and present more properties of the formation and fluids. The second track from the left present Caliper, gamma ray and sonic curves, and density and neutron curves are shown in the third track, sphere focused, mediate and deep resistivity curves are plotted in the next track. From the overlapped density and neutron curves, combination with resistivity curves, the fluid type can be identified, at 13,700–13,720 ft. this section bears gas, the beneath zones contain oil, and the bottom zone has water in the pores. Lithogies can also be identified from the curves and the result is shown in the second track from the right. The last track provides the net thickness (NET), the porosity (POR), and volume of shale (Sh).

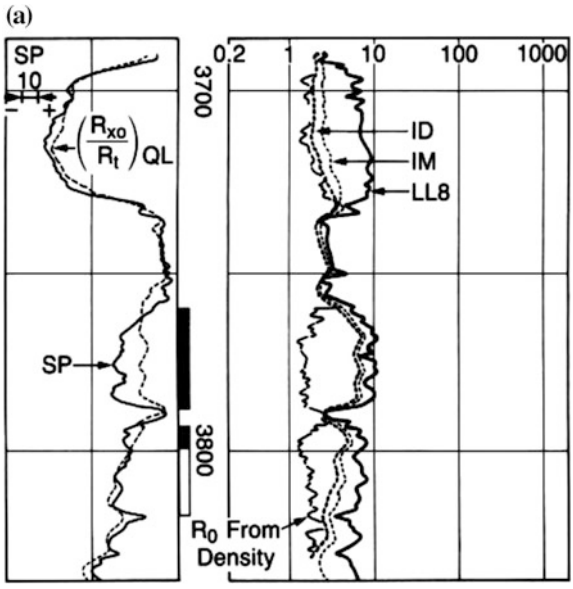

Fig. 10.11 **a** Example of (R_{xo}/R_t) curve used for comparison with SP to identify zones with movable hydrocarbons. **b** Well logging interpretation plot of some wells

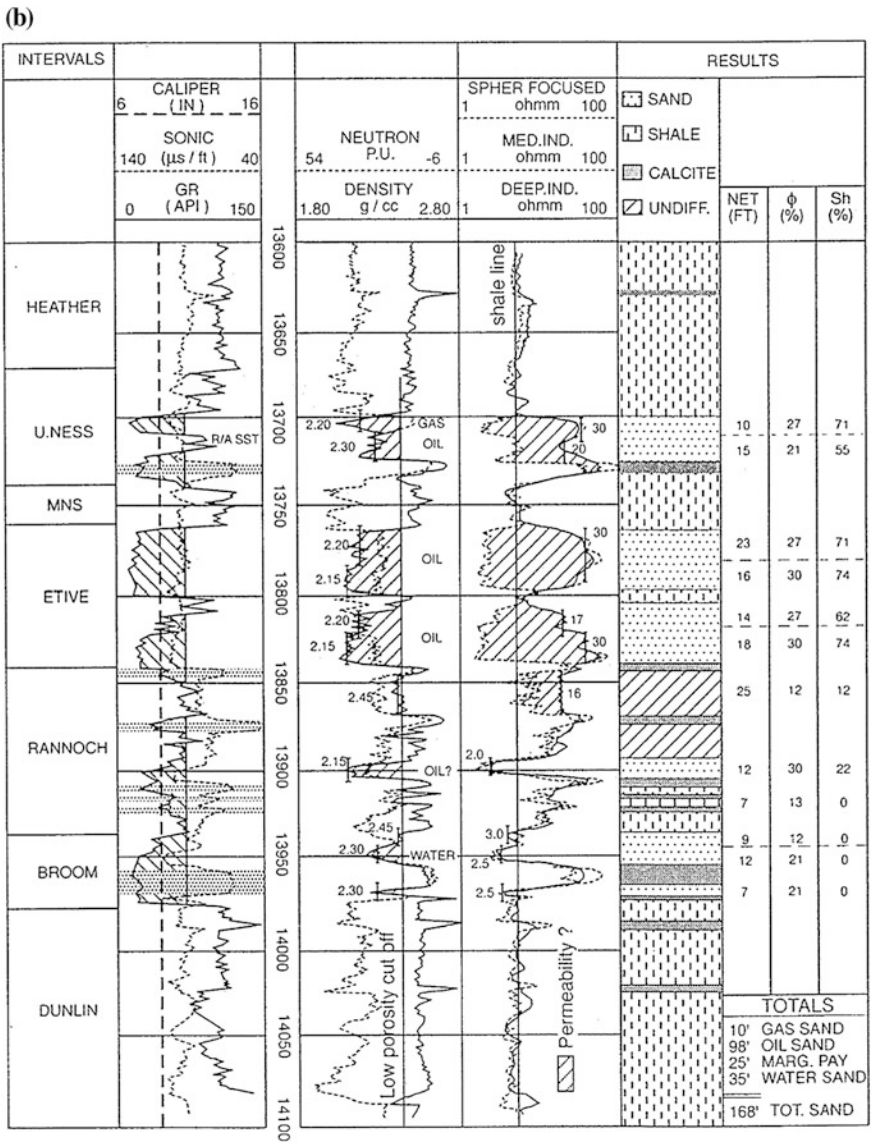

Fig. 10.11 (continued)

10.8 Permeability Calculation

Permeability is a measure of the ease with which fluids can flow through a formation. For a given sample of rock and for any homogeneous fluid, the permeability will be a constant provided the fluid does not interact with the rock itself.

The unit of permeability is darcy, which is very large; so the thousandth part is generally used: the milli-darcy (md). The symbol for permeability is K.

10.8.1 Permeability from POR

In many cases, there may exist relationships between the porosity and permeability, but such correlations usually are empirically derived for a given formation in a given area. They do not exhibit general application or validity. A more general empirical relationship, proposed by Wyllie and Rose, incorporates irreducible water saturation and has the form $K = a \cdot \phi^x / S_{\mathrm{wi}}^y$. The basis of the relationship between permeability and irreducible water saturation is usually this type. The dependency of permeability on porosity is not evident from this data, however. Based on the general expression of Wyllie and Rose, several investigators have proposed various empirical relationships with which permeability can be estimated from porosity and irreducible water saturation. Known as Timur formula, derived from well logs:

$$K = 0.136 \frac{\phi^{4.4}}{S_{\mathrm{wi}}^2} \tag{10.13}$$

10.8.2 Permeability from NMR

Several decades of methods using the nuclear magnetic logging data for permeability are given by the works of many petrophysicists, the famous ones are from Schlumberger and Coates. All of the methods are concluded into two types.

(1) K from ϕ_{NMR} and distribution of T_2

$$K = C_{\mathrm{ks}} \cdot (\phi_{\mathrm{NMR}})^{a_1} (T_{2\log})^{a_2} \tag{10.14}$$

$T_{2\log}$	mean of logarithm of T_2
ϕ_{NMR}	total porosity from NMR
C_{ks}, a_1, a_2	empirical coefficient

(2) K from ϕ_{NMR}, ϕ_{FFI}, ϕ_{BVI} calculated by NMR logging

$$K = C_{\mathrm{kc}} \cdot \phi_{\mathrm{NMR}}^{b_1} \left(\frac{\phi_{\mathrm{FFI}}}{\phi_{\mathrm{BVI}}} \right)^{b_2} \tag{10.15}$$

ϕ_{FFI}	free fluid porosity
ϕ_{BVI}	binding fluid porosity
C_{kc}, b_1, b_2	empirical coefficient

For sand $b_1 = 4$ $b_2 = 2$ lightly affected by hydrocarbonate. C_{ks} and C_{kc} in Eqs. (10.14) and (10.15) are affected by the surface relaxation ability of rock, and so, for same region, different zone, these coefficient are different, and determined by core analysis experiments.

10.8.3 Permeability from the RFT

The pressure profiles recorded using the Repeat Formation Tester (RFT*) tool give, in a qualitative way, excellent estimates of the packer. However, a more quantitative measurement may be made by analysis pressure changes. Two different techniques may be used to deduce the permeability from the measurements made during pretests.

With this technique, permeability can be estimated from the pressure drawdown data during fluid flow and from the pressure buildup data following the flow test. Assuming a spherical flow from the formation towards the packer and the sampling probe, implying a small volume of formation, equilibrium conditions are usually reached very early in the drawdown period, thus the fall in pressure may be expressed by the equation:

$$\Delta P_{ss} = C\frac{qu}{2\pi r_p k_d}\left(1 - \frac{r_p}{r_e}\right) \tag{10.16}$$

where ΔP_{ss} is pressure drop in psi during drawdown; the factor C depends on the type of flow; q is flow volume in cm^3, which may be estimated by dividing the volume of the pretest chamber by the corresponding flow time; μ is the fluid viscosity in centipoises; r_p is the probe radius in cm; r_e is the external radius of the pressure perturbation.

The ratio, r_p/r_e, is very small, r_p being very small compared to r_e. Also, the factor $C/2\pi r_p$ represents the type of flow, which is not entirely spherical depending on the packer characteristics. It is equal to 5660 for the standard probe/packer assembly and varies down to 1107 (for the large area packer) as a function of the packer and probe geometry. Thus we have:

$$k_d = 5660\frac{qu}{\Delta P_{ss}} \tag{10.17}$$

The measurement of permeability carried out by this method has two limitations:

At very high permeability the pressure drawdown is too small to be accurately measured by the strain gauge manometer whose resolution is 1 psi (0.1 psi with the

RFT-B tool). This resolution may, to an extent, be improved using a quartz manometer such as the Hewlett-Packard gauge whose resolution is 0.01 psi (0.002 psi for the RFT-B).

At very low permeability, the pressure may fall below the bubble point. When this happens the gas (or the vapor) comes out of solution and the quantity of liquid coming from the formation is less than volumetric displacement of the pretest pistons. There are several factors which must be taken into account.

10.9 Structure Analysis

A normal fault in a flexible strain of materials is submitted to compressive or tensile tectonic stresses.

10.9.1 Tensile Stress

A normal fault in a basement may be reflected in the cover by flexure of the overlying beds (Fig. 10.12). Differential compaction, or vertical movements: diapiric uplifts (diapiric shales, mud lump, or halokinesis), and magmatic intrusion, present the same situation.

10.9.2 Compressive Stress

All type of folds are possible, according to the mechanism of formation (flexure by compression or by action a torque or folding by shearing), the mechanical behavior of rocks, and their competency. The latter is a relative property that indicates the

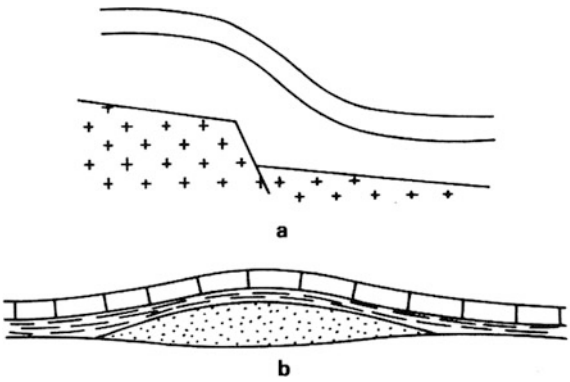

Fig. 10.12 Map of tension folds

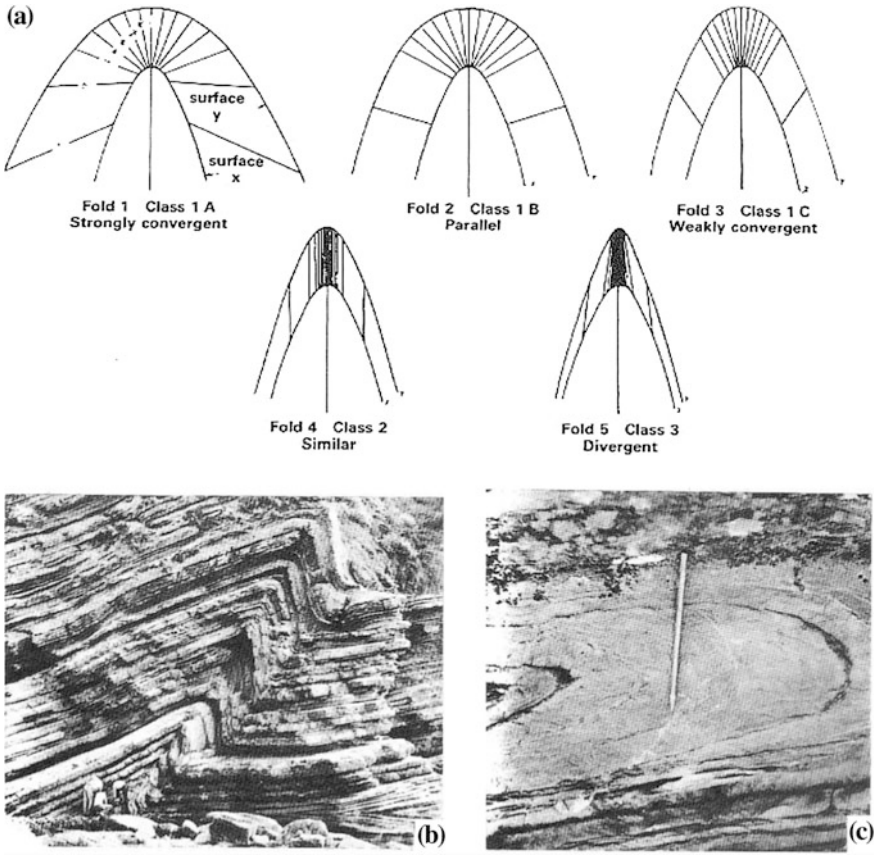

Fig. 10.13 Basic fold type: **a** theoretical fold; **b** isopach folds; **c** similar folds

capacity of a rock to withstand compression without variation in thickness. A competent bed will transmit a compressive force much farther than a weak incompetent rock. Hence, more competent beds will bend under plastic strain and slip over other beds under the effect of compression. The incompetent layers that are more passive may be subject to complex strains. In the most simple case, the fold will be an isopach type (see the definition, later). We will have similar folds (Fig. 10.13) with developing schistosity in the most complex case, or in connection with a viscous flow.

A flow usually has a general cylindrical symmetry (Fig. 10.14). However, regardless of the extent of a fold—it cannot be infinite, each extremity must develop into a conical structure (Fig. 10.15), domes (diapiric uplift) generally have conical symmetry. The apical angle is the characteristic element of a conical fold.

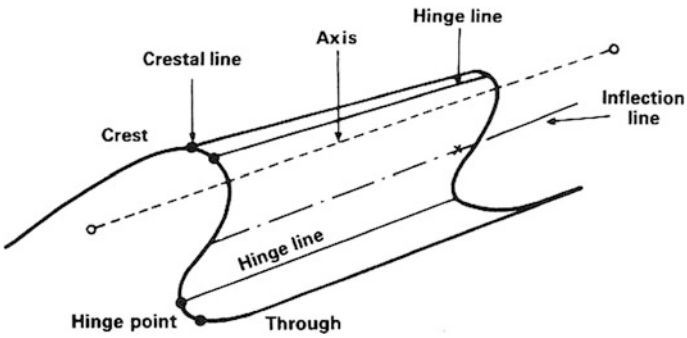

Fig. 10.14 The geometrical elements of a cylindrical fold

Fig. 10.15 The geometrical elements of a conical fold

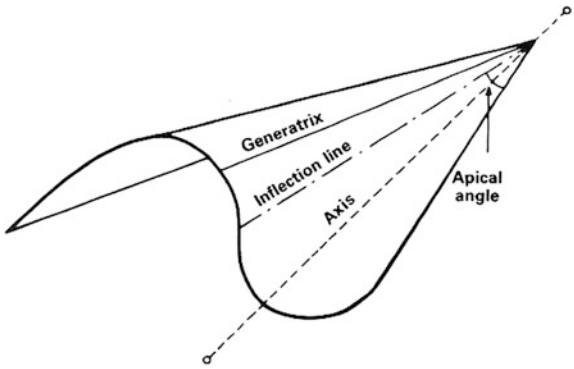

10.9.3 Structural Analysis from Dipmeters

Arrow plots or tadpole plots (Fig. 10.16), where the results of calculation are presented versus depth, often show dip arrangements or dip pattern that can be organized into four groups and coded by color.

(1) green patterns correspond to a set of dips with nearly constant magnitudes and azimuths.
(2) blue patterns correspond to dip angles of similar azimuth that decrease with increasing depth.
(3) red patterns are the inverse, the dip angle decreases with decreasing depth, the azimuth remaining essentially constant.
(4) yellow patterns correspond to adjacent dips with random magnitudes and azimuths.

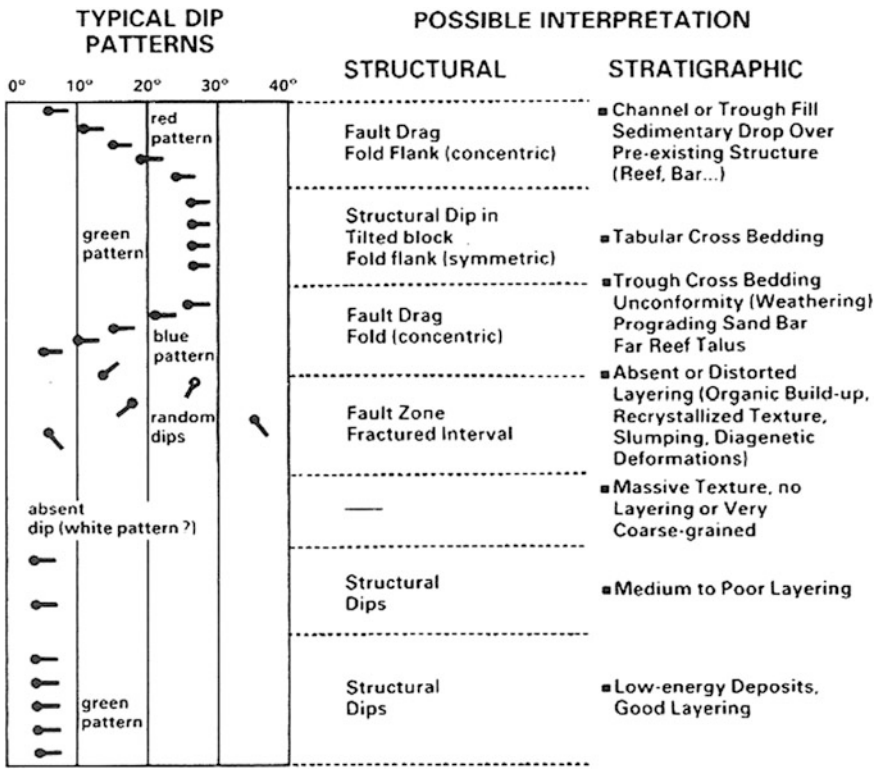

Fig. 10.16 Typical dip patterns

The diagrams in Fig. 10.17 show the theoretical responses in different cases. And green pattern, when also observed in a low-energy deposit, usually correspond to a structural dip, a monocline or a limb of a fold (Fig. 10.17a, zone 4865–4940 ft).

Figure 10.18a exhibits the cases of various folds, such as anticline and syncline asymmetric fold, overturned and recumbent anticline. For these structures, their dip shows different patterns. Figure 10.18b shows the situations of four different folds. Through these plots, the structure of the formation can be distinguished by the dips.

10.10 Multi-well Integrated Interpretation

The preceding chapters have shown the benefits to be derived from a close study of well logs in order to obtain information about geology, reservoir properties and geophysics. Clearly, the techniques used to obtain such information should be applied to the study of all the wells in a basin, an exploration area, or a field.

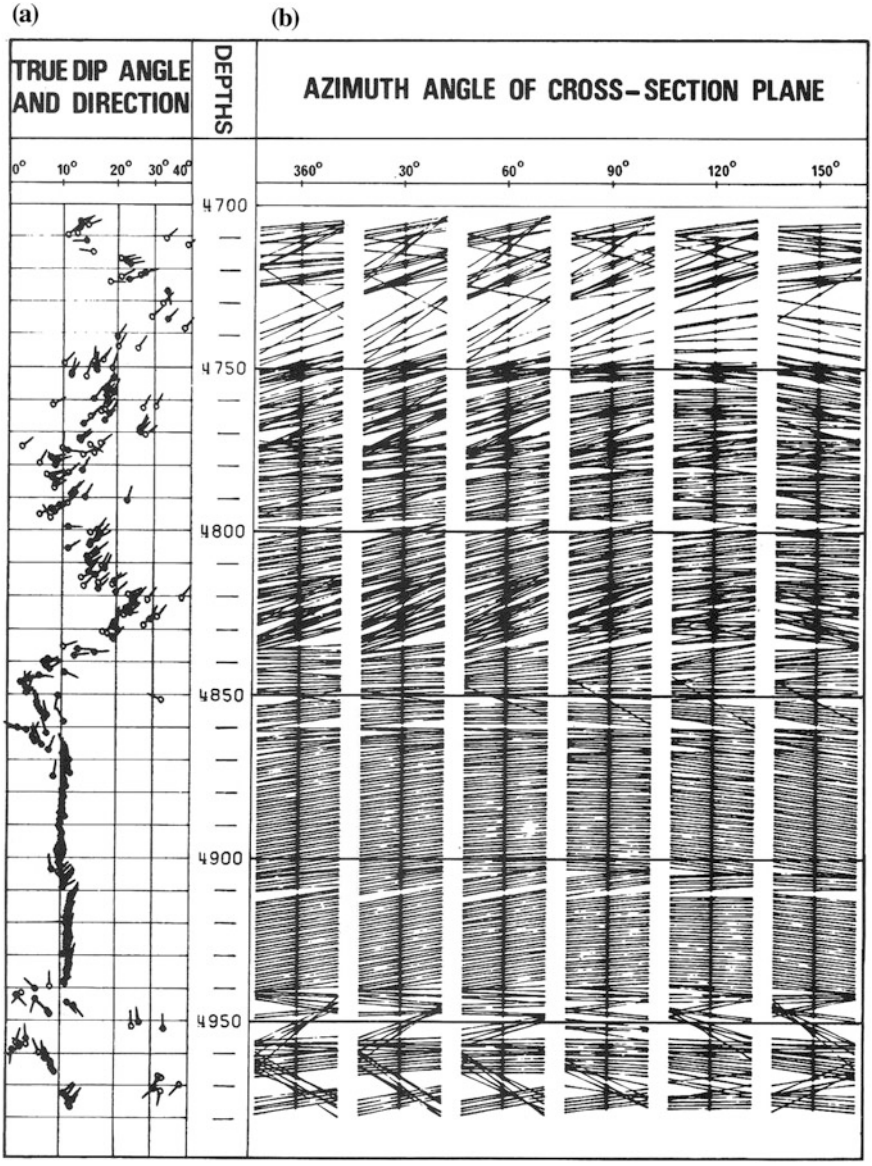

Fig. 10.17 Example of dip pattern (**a**) and "stick plots" (**b**) in planes of various strikes

By the association of several wells, we can obtain complementary information which will allow us to develop an architectural and space–time reconstruction of the formations and the evolution of their properties. However, the integration of data from several wells means that we must adapt some existing techniques and indeed

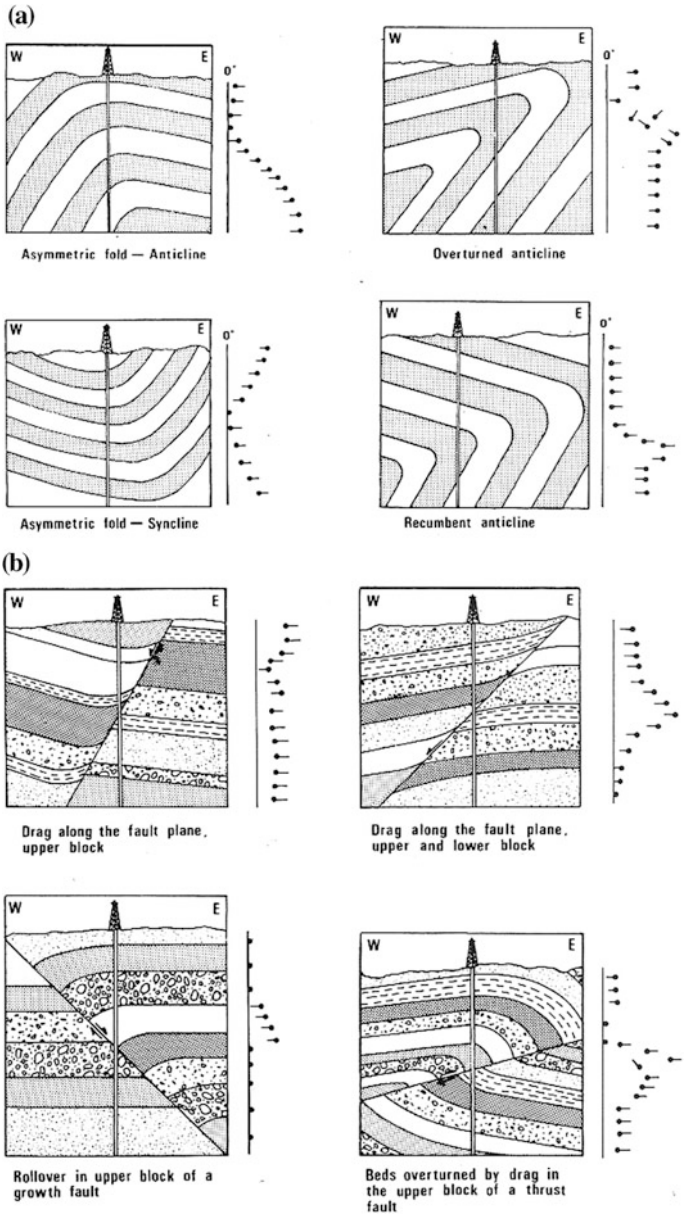

Fig. 10.18 Theoretical *arrow* plots **a** folds; **b** fault

develop some new ones. This will depend on the objectives to be met by the study of the wells.

Multi-well studies involve two general sets of problems. The first refers to geology and the second is related to the study and production of a field.

The primary objective in the first case is to establish chronostratigraphic correlations between wells using time markers, and to establish facies correlations. The aim is to produce sections and maps which will aid exploration and help to discover economically viable accumulations of hydrocarbon.

In the second case, the primary objective is to reconstitute, as closely as possible. The three-dimensional image of the field with all its characteristics (sedimentological, tectonic, and the porosity, permeability, saturation, and water table of the reservoir) are also needed.

Multi-well correlation is the basic work for an oilfield integrated study through which many cross-sections of correlation, chronostratigraphic events, and facies can be set. Figure 10.19 shows the lateral evolution or continuity of electro-facies.

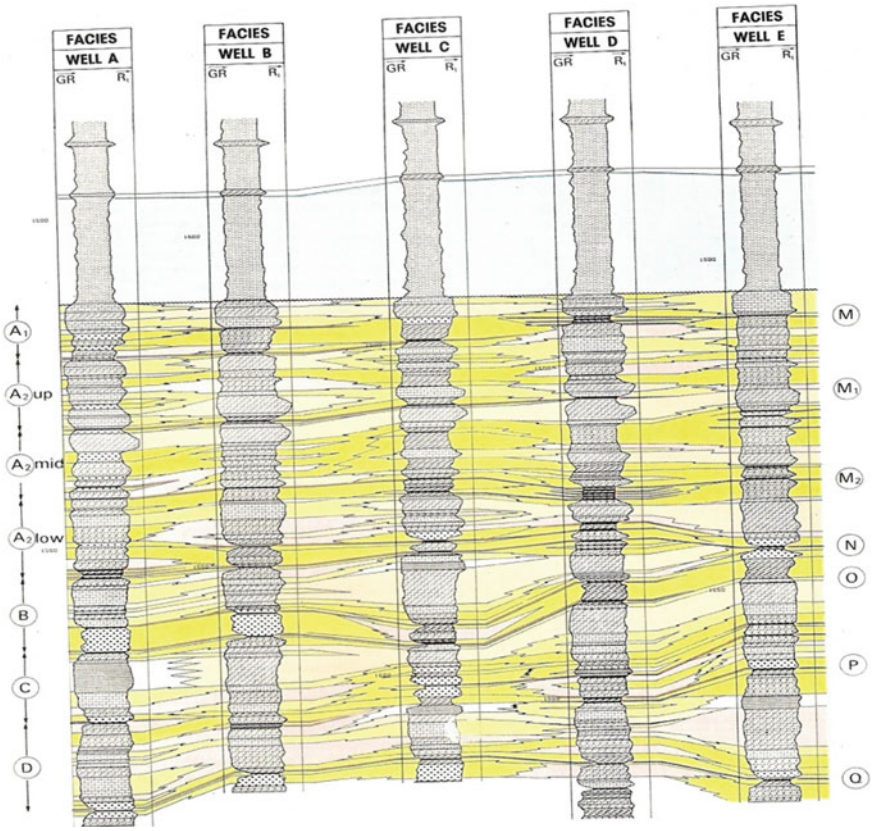

Fig. 10.19 Section showing correlations based on the results of an analysis by the FACIOLOG program using a database of electro-facies

Problems

10.1 What is the classification of reservoir?
10.2 How to identify the permeable zone?
10.3 How to identify the lithology from logging curves?
10.4 Explain the mechanism of Pickett map?
10.5 How to determine porosity based on Figs. 10.6, 10.7 and 10.8?
10.6 Explain the method of classifying the fluid type using resistivity ratio?
10.7 How to calculate permeability from POR, NMR, and RFT?
10.8 What is the objective of multi-well integrated interpretation?

Appendix A
Vocabulary

AAPG 美国石油地质家学会
abbreviation 缩写
Abscissa [数][天] 横坐标; 横线
absurdity 荒谬, 不合理
accessory 附件
accretion 增大, 堆积
acquisition 采集
adjacent 相邻
advent 来临
affinity 亲和力, 亲和性
agent 代理
algorithm 算法
aligned 对齐
alkali-lime 可溶性灰岩
alkalinity 碱度
alteration 变更
ambient 周围环境
americium 镅Am
americium-beryllium 镅-铍
amplitude 幅度, 振幅
angle 角度
angular 有角的
angular frequency 角频率
angularity 棱角度
anhydrite 硬石膏
anion 阴离子
anisotropic 各向异性的
anisotropy 各向异性
annihilation 毁灭
annulus 环
anode 阳极

H. Liu, *Principles and Applications of Well Logging*, Springer Mineralogy,
DOI 10.1007/978-3-662-53383-3

anomalies 异常
anomaly 异常, 反常事物
anormal 异常的
antennas 天线
apex 顶, 顶点
approximation 近似值
aquifer 含水层
aragonite 霰石
Archie equation 阿尔奇公式
argillaceous 泥质的, 粘土的
ascent 提升
assembly 装配, 组装
asymmetric 不对称的
atomic 原子
attenuate 衰减
attenuation 衰减
avalanche 雪崩
axially 轴向的
axis 轴
azimuth 方位
azimuthal 方位角的, 方位的
barite 重晶石
barren 贫瘠的
baseline 基线
bauxites 铝土矿
beryllium 铍Be
BHC 井底油嘴
billiard ball 台球, 撞球
bisecting 二等分
bitumen 沥青
bituminous 沥青的
blade 叶片
blurred 模糊
borehole-to-borehole 井壁稳定
breccia-dolomite 角砾云岩
brittle 易碎的, 脆弱的
burial 埋葬的
bypass 旁路
calcite 方解石
calcium 钙
calcium 钙
calibrate 校准
calibration 刻度, 校正
caliper 卡尺, 测量, 井径仪
compass 指南针

capacitance 电容
capillary-bound 毛管束缚
capture 捕捉
carbonate 碳酸盐
cased-hole 套管井
casing collar locator 套管接箍定位器
category 范畴, 种类
cathode-ray 阴极射线管
cation 阳离子
cavern 孔穴
cement bond evaluation 水泥胶结评价
centipoise 厘泊(粘度单位)
centralizer 扶正器
ceramic 陶瓷
cesium 铯
chamber 室
chip 芯片
chloride 氯化物
Chlorine 氯
chronostratigraphic 年代地层的
circuitry 线路, 电路
circumference 围
clastic 碎屑岩
CMR 可组合的核磁共振测井仪
co-axial 共轴的
coefficient 系数
cohesional 内聚力的
coil 线圈
coincide 一致
collaboration 合作
collapse 倒塌, 坍塌
collision 碰撞, 冲突
colloidal 胶体
commonest 常见, common 的变形
compatible 兼容
compensate 补偿
completion 完成
compression 压缩
computed 计算
conclusively 终局
confinement 限制
conglomerate 砾岩
conical 锥形
conjunction 连接
connate 原生的

consensus 共识
constituent 组成
constraint 约束
contaminate 污染
contaminate 污染, 污染物
content 内容
correlate 相关
correlation 相关
correlation 对比, 相关
cosine 余弦
coupling 耦合
criss-cross 纵横交错的
critical 临界的, 关键性的
crossed-dipole 交叉偶极子
crossover 交叉
crossplot 交会图
crucial 至关重要的
crystal 水晶
cumulative 累积
cutoff 截止
cylindrical 圆柱
dampening 打击
dazzle 炫目的
decay 腐烂
decentralize 权力下放
decomposition 分解
decontamination 去污
deferred 延迟的
deflect 使偏斜
deflection 挠度
deformation 变形
deformed 变形
degrade 降解
delineated 划定
densitometer 用浓度
departure 离开
depict 描绘
depletion 损耗
deployment 部署
deposit 存款, 寄存
depositional 沉积
derivable 可以
derive 汲取
desiccation 干燥
detection 检测

detector 检波器, 探测器
deviate 偏离, 使偏离, 偏转, 定向井
dewatering 脱水
DFA 分布式功能体系结构
diagenesis 成岩作用
diagnosis 诊断
diagnostic 诊断
diagonal 斜线, 斜交的, 对角线
dielectric 介电
dielectric permittivity n. [电] 介电常数, [电] 电容率
differential 微分
diffuse 扩散
diffusion 扩散
dilute 稀释
dimension 维, 尺寸
diminish 递减, 减少
dip 浸
dipmeter 地层倾角测井仪
disastrous 灾难性的
discern 辨别
discernible 可辨
discrepancies 不精确的
discrete 离散
discriminate 歧视
discuss 讨论
disintegration 解体, 蜕变, 衰减
dislodge 驱出, 移出
disperse 分散
dispersion 色散
dissociate 分解, 离解
dissolve 溶解 vi
distinct 截然不同的
distinguish 识别
distortion 失真
dolomite 白云岩
dominant 主导, 显性的
dotted 虚线
downhole 井下
drain 排水
drainage 排水
drawn 画
drift 飘移
drillability 可钻性
drillstring 钻柱
Dual Laterolog tool 双侧向测井仪

ductility 延展性, 柔顺性
duplicate 复制
dynamics 动力学
Dynamics Tester 动态测试
eccentric 偏心
eccentricity 偏心
Ecoscope 斯伦贝谢一种随钻测井系列
ejected 驱逐
elaborated 精心制作的, 详细阐述
elastic 弹性
elasticity 弹性
electrical conductivity 电导率
electrode 电极
electrokinetic电动的
electromagnetic 电磁
Electromagnetic Propagation Tool 电磁波传播测井仪
electromechanical 电机的
eliminate 消除
elliptical 椭圆的
elongate 延长, 拉长
elusive 难以捉摸的
embed 嵌入
EMF 电动势
emission 放射, 发射
emit 发出
empirically 实证
encompasses 包含, 包括
ensuing 随后
epithermal 超热的, 浅成低温热液
equilibrium 平衡
equipotential 等势的
eradicate 根除
erosion 侵蚀
erratic 飘忽不定, 古怪的
evaporite 蒸发岩
evolution 演化
excitation 励磁
excursion 偏移
expel 驱逐
exponent 指数
exponential 指数
export 出口
extensive 广泛的
extracting 提取
extrapolate 推断

extrusive 喷发的
facies 相
facilitate 促进
feldspar 长石
fiber-optic 光纤
film 电影
filtrate (泥浆)滤液
fin 翅片
finite 有限
fissures 裂缝
flexural 弯曲
flowmeter 流量计
fluorescence 荧光
Formation MicroImagertool 微电阻率成像测井
fraction 分数, 部分
fracture detection 裂缝探测
frictional 摩擦
funnel 漏斗
galvanometer 电流计, 检流计
gamma ray 伽马射线
gauge 表, 计量器
geochemical 地球化学
geology-geophysical 地球物理学的
geometry 几何
geosteering 地质导向
geothermal 地温的
glauconite 海绿石
gradient 梯度
gradient 梯度, 斜率
gradiomanometer 压差密度计
granite 花岗岩
granular 颗粒的, 颗粒状的
gravel-pack evaluation 砾石填充评价
grid 格子, 网格
grooves 槽
ground-loop 地面循环
guarantee 保证
gypsum 石膏
halite 岩盐
helical 螺旋
hoist 起重机, 吊起
homogeneous 均匀的, 同质的
horizontal 水平的
hostile 敌对
hydraulic-fracturing 水力压裂

ILD 深感应测井
Illite 伊利石
illustrative 说明性的
impart 传授, 给予, 告知
impedance 阻抗
impeller 叶轮
imperceptible 未知的, 不能感知的
impermeable 渗
impervious 非渗透的
implementation 实施
improper 不适当的, 错误的
inclination 倾向
inclinometer 倾角罗盘, 井斜计
incompatible 不相容的
incorporate 纳入
incorporate 结合, 混合
increment 间隔值, 增量
induction 感应
induction log 感应测井
inelastic 弹性
influx 涌入
inherent 固有
in-situ 原位
insofar 在…的范围
instantaneous 瞬时
insulate 绝缘
insulator 绝缘体
integral 整体
integrity 完整, 完整性
intensive 加强的, 深入仔细的
interbedded 互层的
intercept 拦截
intercrystalline 晶体粒间
interface界面
intergranular 粒间的, 晶粒间的
intergrity 完整性
intermediate 中间
intersection 路口
interstitial 间隙的, 孔隙间的
interval 区间
interwell 井间
intrinsic 本质的, 固有的
intrusive 侵入的
invade 侵入
invasion 侵入层

inversely 相反
iodine 碘
ionization 电离
ironically 具有讽刺意味的是
irreducible 不可消减的
irreducible 束缚的
isotope 同位素
isotropically 呈现等向分布之电磁波
kaolinite 高岭石
kinetic 动力学
laminate 分层, 薄层
Laterolog 侧向测井
layered clay structure 层状粘土构造
lead 铅
leakage 泄漏
leakoff 漏气
lignosulfonate 木质素磺酸盐
likelihood 可能
liquid-junction potential 液体接触电位(扩散电动势)
lithification 岩化(作用)
lithium 锂
lithology 岩性
lithology determination 岩性识别
Lithology-independent 与岩性无关的
LLD 深侧向测井
locales 地区
localize 地方化
logarithmic 对数的
logging-testing-logging 测-注-测
logging-while-drilling 随钻测井
longitudinal 纵向
longitudinal wave 纵波
LWD NMR 随钻核磁共振测井
LWD-specific 特殊的随钻测井
magmatic 岩浆的
magnesium 镁
magnet 磁铁
magnetic 磁性的
magnetic permeability 导磁率(性, 系数)
magnetometer 磁力仪
magnetostrictive 磁致伸缩的
magnitude 级
malfunctioning 故障
mandrel 芯轴
manner 方式

manometer 计
mantle地幔
marble大理石
marginal 边缘的, 界限的
matrix 骨架
mechanical 机械的, 力学的
membrane Potential 薄膜电势
Membrane 薄膜
menu 菜单
metallic ion 金属粒子
metamorphic 变质
metastable 亚稳态的, 相对稳定的
methodology 方法论
mica 云母
microlaterolog 微侧向测井
microlog 微电极测井
microscaner 微扫描仪
microSFL 微球形聚焦测井
millivolt 毫伏
mineralogy 矿物学
miscible 可溶的
mitigate 减轻
mobility 活动性, 可动性
moderation 适度
monochromatic 单色的, 单频的
monopole 单极
montmorillonite 蒙脱石
morphology 形态
MRIL-B B 型核磁共振测井
MRIL-C C 型核磁共振测井
MRIL-Prime P型核磁共振成像测井
multiple 多重的, 倍数, 并联
multisensor 多传感器
multistage fracturing 多次断裂
N.B. abbr. (拉)注意(Nota Bene)
necessitate 迫使, 使…成为必要
negatron 负电子
negligible 可忽略不计的, 不计的
neuron 神经元
neutron 中子
neutron-neutron log 中子-中子测井曲线
nil n. 无, 零
notion 观念
novice无经验者, 新手
nuclear magnetic resonance 核磁共振

nucleus 核
obtain 获得
occupy 占据
oil-based mud 油基泥浆
oil-bearing 含油的
oil-saturated 饱和油
optimization 优化
optimum 最佳的
ordinate n. 纵座标; 纵线
ore 矿
orient 东方, 向东方, 使适应
orthogonal 正交
oscillate 振荡
oscillation 振荡
oscillator 振荡器
oscilloscope 示波器
osmotic 渗透的
OT 操作时间; 输出变压器
outcrop 露头
ovalization 成椭圆形的
overlapped 重叠
overlying 叠压
pack 填塞, 充填
paleostress 古应力
parallel 平行
patches 补丁
pattern 组合
Pattern 组合
peak 峰值, 波峰
penetrate 穿透
penetrated 浸透, 穿透
penetration 渗透
perforate 射孔
perforation 射孔
permeable beds 渗透层
perpendicular 垂直
perturb 扰乱
pessimistic 悲观
phosphor 磷
phosphorite 磷灰石
photocathode 光电极
photon 光子
pH-sensitivity PH 敏感性
Picowatt 皮瓦; 微微瓦; 百亿分之一瓦
piecewise 分段的

piezoelectric 压电的
pitch 沥青, 音高, 投掷, 向前倾倒
pitfall 陷阱
placement 位置, 方位
plateau 曲线的平直段
plug 塞子, 插头接点
plunger 柱塞
plutonium 钚Pu
pointless 钝的
poise 使…平衡
polarities 极性
polarize 使极化
polycrystalline 多晶硅
polymer 聚合物
porosity 孔隙度, 孔隙性
porous 多孔的
positive 正的, 阳极的
positron 正电子
potash 钾肥, 钾化合物
potassium 钾
potential 电位, 位能
potentiometer 电位器
precise 精确的
precision 精度
predominant 主要的
pretest 预测试
prior 先前的, 以前的
probe 探针
procedure 程序
prompt 及时的, 敏捷的; 提示,初进
propagate 传播, 扩散
proportional 成比例的
propping 支撑
prospect 勘探
proton 质子
proximity 接近, 亲近
pseudostatic 伪静态的
pulse 脉冲
pulse height 脉冲高度
pulsed-neutron 脉冲中子
pulse-echo 脉波-回波
quadrant 象限, 四分之一圆
quadrupole 四极子
quantification 量化
quantify 确定…数量

quantitative 定量的
quantitatively 定量
quartz 石英
quick-look method 快速检测法
radial 径向
radial-differential-temperature log 径向微差井温测井
radiating 辐射
radii 半径(复数)
radioactive-tracer 放射性示踪剂
rarefaction 膨胀
ratio 比值, 比率
reciprocal 倒数, 可逆的
reconcile 调和
reconstitute 重新组成
refracted wave 折射波
regime 政权
regional 区域
relaxation 弛豫
remedial 补救
remnant 余剩的人
render 渲染, 给与补偿
repartition 分配, 划分
reprecipitation 再沉淀
represent 描述
representation 表示
resemble 类似, 象
residual 残余
resistivity 电阻率
resolution 决议
resonance 共振
resultant 合成
retrieval 检索, 取回
retrofit 改造
retrograde 逆行
reverberation 混响
reverse 反面, 背面, 倒退
rim 边缘
robust 鲁棒
rotary 扶轮
rotate 旋转
roundness 圆度
rugose 粗糙的, 有褶皱的
rugosity 粗糙度
salinity 盐度, 矿化度
sandwich 层状结构的

saturation 饱和度
sawtooth 锯齿形的
scatter 分散
schematic 简要的, 概要的
schistosity 片理
Schlumberger 斯伦贝谢
scintillation 闪烁, 起伏
secondary currents 次生电流
secondary 次生的
sediment 沉积物
segment 段, 层
segregate 分离的
seismic 地震
self(spontaneous) potential 自然电位
self-explanatory 不证自明的
self-potential 自然电位
semi-log 对数测井曲线
sensitivity 灵敏度
sensor 传感器
shaft 轴, 杆
shale base line 泥岩基线
shale-sand 泥质砂岩
shaliness 泥质含量
shaly 页岩
shattered 粉碎
sheath 鞘
shield 盾
short normal 短电位电极
shrinkage 收缩
silicone 硅树脂, 聚硅氧
simplicity 简单
simulate 模拟
simultaneous 同时
sinusoidal 正弦
Skin Effect 趋肤效应
slope 边坡
slug 塞
sodium 钠
solids 固体
sonde 探测器
sonic 声音的, 声波
sophisticate 复杂的, 精致的
sought寻求, 查找
spatial 空间
specific gravity 比重

spectral 光谱
spectrometry 光谱测定法
spectroscopy 能谱学
spectrum 谱
spherical 球状, 球状的
Spherically Focused Resistivity log 球形聚焦电阻率测井
spike 阻止, 钉住
spinner 转子
spinner-flowmeter 转子流量计
split 分裂
spurious 假的, 不真实的
squeeze 挤
stabilizer 稳定器
stimulate 刺激
strain 应变
stratum 地层
streak 夹层
strip 带
subaerial 接近地面的
sub-aqueous 水下的
subscript 下标
subsequent 衍生的
subsidiary 子公司
substitute 代替
subtle 微妙的
subtracte 减去器
sulphate 硫酸盐
superheterodyne 超外差的
superimpose 叠加, 重叠
suppression 抑制, 压制
surrounding 围岩
symmetrical 对称的
symmetry 对称, 对称性
syneresis 脱水收缩作用
tabulated 使成平板
tag 标签
tangential 切向
tanglesome 复杂的, 紊乱的
tectonic 构造的
telemetry 遥测
tensile 拉伸
tension 张力
terrestrially 中
terrigenous 陆生的, 陆源的
tertiary 第三记

texture 结构
thermal decay time 热中子衰减时间
thermometer 温度计
thin 薄
thorium 钍
threshold 阈值
thumb 经验方式
tight 致密的
titanium 钛
tomography 断层照相
torque 扭矩
tracer 示踪剂
track 道, 测井曲线记录道
traditional 常规的
trajectory 轨迹
transducer 传感器
transient 瞬态
transmission 传输
transmitter 发射器
transverse 横向
transverse wave 横波
traverse 穿过, 横越
tremendous 巨大的
triaxial 三轴
turbine 涡轮
turbulent 湍流
ultra-metamorphism 超变质
ultrasonic 超声
unaltered 原封不动
unambiguous 明确
undamaged 无污染的, 原状的
uniform 均匀的, 一致的
unravel 揭开
uranium 铀
utility 效用, 作用
vanish尖灭, 消失
variation 变化
velocity 速度
verification 验证
version 版本
versus 与…相对, 对抗
vertical resolution 垂向分辨率
viability 生存能力
vibration 振动
vice versa 反之亦然

vicinity 附近
viscosity 粘度
visualize 观察, 使…看得见
void 无效
voltage 电压
volumetric 容积
voyage 航海
vug 孔洞, 晶簇
vuggy 多孔的
vugular 晶簇性的, 含晶簇的
warrants 保证
washout 冲洗, 冲洗带
waveform 波形
wavefront 波前
wellsite 井场
wildcat 预探井
withdrawal 撤军, 撤退

Appendix B
Nomenclature (名词术语)

AZ	井斜方位
AZ1	1号极板方位角
API	美国石油学会、自然伽马和中子测井刻度单位
A_p、A_S	纵、横波的有效幅度
AST	阵列声波测井
BHC	井眼补偿声波测井
BHT	井底温度
BHTV	超声波电视测井
C_p	压实校正系数
C_w	地层水的矿化度
C_{mf}	泥浆滤液矿化度
CAD	环行声波测井
CAL	井径测井
CBL	水泥胶结测井
CEC	阳离子交换容量
CNL	补偿中子测井
DCA	电导率异常检测
DEN	密度测井(体积密度)
DIL-LL8	双感应一八侧向组合测井
DIL-SFL	双感应-球形聚焦组合测井
d_h	井径
d_{xo}	冲洗带直径
d_i	侵入带直径
Ec	电化学电动势
Ek	动电学电位,动电学电动势
ELJ	泥岩薄膜电位
EM	扩散电位
ES	自然电位回路总电动势
F	地层因素
Fa	视地层因素

H. Liu, *Principles and Applications of Well Logging*, Springer Mineralogy,
DOI 10.1007/978-3-662-53383-3

FS	声波测井求得的地层因素
Fsd	砂岩夹层的地层因素
FDC	补偿地层密度测井
FIL	裂缝识别测井
FMS	微电阻扫描测井
GNT	普通中子测井
GOR	油气比
GR	自然伽马测井
GRmax	最大自然伽马
GRmin	最小自然伽马
GRsd	纯砂岩自然伽马
GRsh	泥岩自然伽马
HI	含氢指数
HDT	高分辨地层倾角测井仪
I	电阻增大系数
IGR	自然伽马相对值,自然伽马泥质指数
Isp	自然电位相对值,自然电位泥质指数
Isilt(SI)	粉砂指数
DIL	双感应测井
ILD	深感应
ILM	中感应
ISF	感应一球形聚焦测井
K	绝对渗透率
Ko	原油的有效渗透率
Kw	水的有效渗透率
Kro	油的相对渗透率
Krw	水的相对渗透率
L	源距
DLL	双侧向测井
LLd	深侧向
LLs	浅侧向
MFS	多节式流体测试器
MID	骨架岩性识别图
ML	微电极测井
MLL	微侧向测井
MSFL	微球形聚焦测井
MST	微电阻扫描测井仪
Md	粒度中值
m	孔隙度指数
n	饱和度指数
ne	电子密度
NG	中子伽马测井读数
NGS	自然伽马能谱测井
NLL	中子寿命测井
Pe	光电吸收截面指数

P	地层压力
PL	邻近侧向测井
PSP	假静止自然电位,泥质砂岩静止自然电位
Qv	单位总孔隙体积的阳离子交换容量
Ra	视电阻率
Rc、Rcorr	校正后的电阻率
RFT	地层温度下的电阻率
Ri	侵入带电阻率
RIL	感应测井电阻率
RILd	深感应电阻率
RILm	中感应电阻率
RLL	侧向测井电阻率
Rm	泥浆电阻率
Rmc	泥饼电阻率
Rmf	泥浆滤液电阻率
RMLL	微侧向测井电阻率
Ro	100%含水的地层电阻率
R_{pl}	邻近侧向测井电阻率
Rs	围岩电阻率
Rsd	纯砂岩(夹层)的电阻率
Rsh	泥岩电阻率
Rt	地层(真)电阻率
Rw	地层水电阻率
Rwa	视地层水电阻率
Rwe、Rweq	地层水等效电阻率
Rxo	冲洗带电阻率
RFT	重复式地层测试器
Sg	含气饱和度
Sgxo	残余天然气饱和度
Sh	含油气饱和度
Shr、(Shy)xo	残余油气饱和度
SI	粉砂指数
Smo	可动油饱和度
So	含油饱和度
Sor	残余油饱和度
Sw	含水饱和度
Swb	束缚水饱和度
Swf	自由水饱和度
Sxo	冲洗带含水饱和度
SFL	球形聚焦测井
SFT	选择性地层测试器
SHDT	地层高分辨率倾角测井仪
SNP	井壁中子孔隙度测井
SP	自然电位
SSP	静止自然电位

TDT	热中子衰减时间测井,中子寿命测井(NLL)
U	光电吸收体积截面
U_{maa}	视骨架体积截面
v_f	流体的声波速度
v_{ma}	岩石骨架中的声波速度
V_{sh}	泥岩中的声波速度
v_p, v_s	声波的纵、横波速度
V_{clay}	粘土的相对体积
V_Φ	孔隙体积
VDL	声波变密度测井
Wclay	粘土含水量
WF	声波全波波形(显示)
WOR	油水比
Δ_t	声波间隔传播时间,声波时差
Δ_{tma}	岩石骨架的声波时差
Δ_{tsd}	砂岩的声波时差
Δ_{tsh}	泥岩的声波时差
$\Delta\Phi_N$	中子孔隙度校正值
$\Delta\rho$	密度测井泥饼补偿量
$\Delta\rho_b$	密度校正值
ρ_a	视密度,密度测井读数
ρ_b	地层体积密度
$\sum$	中子俘获截面、伽马射线的光电效应截面、光电吸收系数
$\sum_f$	流体的俘获截面
$\sum_{ma}$	骨架的俘获截面
τ	中子寿命(热中子衰减时间)
Φ	孔隙度
Φ_D	密度测井孔隙度
Φ_{DC}	油气的密度测井孔隙度
Φ_e	有效孔隙度
Φ_f	缝洞孔隙度
Φ_N	中子测井孔隙度
Φ_{ND}	中子—密度测井交会孔隙度
Φ_o	含油孔隙度
Φ_S	声波测井孔隙度
Φ_2	次生孔隙度
Φ_t	总孔隙度
Φ_{CNL}	补偿中子孔隙度
Φ_W	含水孔隙度
Φ_{XO}	冲洗带含水孔隙度

Appendix C
Conversion Factors and Tables

Length

1 m = 3.281 ft

Volume

1 barrel = 0.15899 m^3 = 5.614 cubic feet = 42 US gallons

1 US gallon = 0.1337 cuft

Pressure/Density

1 psi = 0.06895 bar = 0.068065 atm = 6895 N/m^2 (Pascal)

1 psi/ft = 2.3095 g/cc = 22.6 kPa/m

1 g/cc = 8.35 lb/gal

Temperature

Conversion from °C to °F: °C = (°F − 32)*5/9

°C = °K + 273.16

°Rankine = 1.8*°K = °F + 460

Permeability

1 darcy = 10^{-12} m^2

H. Liu, *Principles and Applications of Well Logging*, Springer Mineralogy,
DOI 10.1007/978-3-662-53383-3

Appendix D
Typical Parameters' Physical Value

Lithology	GR (API)	ρ_b (g/cc)	CNL (NPU)	AC (μs/ft)	Resistivity (Ω)	Pe	ρ_e (g/cc)	U (barn/cc)
Sandstone	Low	2.65	−5 to −3	51–56	High	1.8	2.65	4.79
Limestone	Low	2.71	0	44–48	High	5.1	2.71	13.77
Dolomite	Low	2.88	2–6	39–44	High	3.1–3.2	2.86	9.00
Anhydrite	Low	2.98	0	45–55	High	5-5.1	2.96	4.95
Salt	Low	2.03	100	180–190	High	4.65		
Chlorite	High	2.79	30–40	50–150	Low	6.3	2.79	17.58
Illite	High	2.52	30-40	50–150	Low	1–5	2.52	8.69
Kaolinite	High	2.41	30-40	50–150	Low	1–5	2.41	4.41
Montmorillonite	High	2.12	30-40	50–150	Low	1–5	2.12	4.32
Brine	0	1–1.1	100	189	0–∞	0.36	1.185	0.96
Oil	0	0.60–1.0	70–100	210–240	Very high	0.12–0.13	0.95–0.97	0.11–0.12
Gas	0	0.1–0.5	10–50	500–1500	Very high	Low	0.1–0.5	Low

H. Liu, *Principles and Applications of Well Logging*, Springer Mineralogy,
DOI 10.1007/978-3-662-53383-3

References

1. Aguilera MS, Aguilera R (2003) Improved models for petrophysical analysis of dual porosity reservoirs. Petrophysics 44(1):21–35
2. Akkurt R, Prammer MG, Moore MA (1996) Selection of optimal acquisition parameters for MRIL logs. Log Anal 37(6):43–52
3. Allen LS, Tittle CW, Mills WR, Caldwell RL (1967) Dual-spaced neutron logging for porosity. Geophysics 32(1):60–68
4. Anand V, Hirasaki G (2005) Diffusional coupling between mico and macroporosity for NMR relaxation in sandstone and grainstones. Trans SPWLA 46th Annual Logging Symposium, paper KKK
5. Anderson B, Barber TD (1997) Induction logging. Schlumberger, Houston, TX
6. Anderson B, Chang SK (1982) Synthetic induction logs by the finite element method. Log Anal 23(6):17–26
7. Arnold DM, Smith HD Jr (1981) Experimental determination of environmental corrections for a dual-spaced neutron porosity log. Trans SPWLA 22nd Annual Logging Symposium, paper W
8. Aron J, Chang SK, Dworak R, Hsu K, Lau T, Masson JP, Mayes J, McDaniel J, Randall C, Kostek S, Plona TJ (1994) Sonic compressional measurements while drilling. Trans SPWLA 35th Annual Logging Symposium, paper SS
9. Asquith G, Gibson C (1982) Basic well log analysis for geologists. AAPG, Tulsa, OK
10. Barber T, Vandermeer W, Flanagan W (1989) Method for determining induction sonde error. US Patent No 4,800,496
11. Berg CR (1996) Effective-medium resistivity models for calculating water saturation in shaly sands. Log Anal 37(3):16–28
12. Bloembergen N, Purcell EM, Pound RV (1948) Relaxation effects in nuclear magnetic resonance absorption. Phys Rev 73(7):679–703
13. Brie A, Endo T, Johnson DL, Pampuri F (2000) Quantitative formation permeability evaluation from Stoneley waves. Paper SPE 60905 in: SPE Reservoir Eval Eng 3(2):109–117
14. Brie A, Kimball CV, Pabon J, Saiki Y (1997) Shear slowness determination from dipole measurements. Trans SPWLA 38th Annual Logging Symposium, paper F
15. Brown RJS, Gamson BW (1960) Nuclear magnetism logging. Pet Trans AIME 219:201–209, paper SPE 1305
16. Bussian AE (1983) Electrical conductance in a porous medium. Geophysics 48(9):1258–1268
17. Carr HY, Purcell EM (1954) Effects of diffusion on free precession in nuclear magnetic resonance experiments. Phys Rev 94(3):630–638
18. Chang SK, Liu HL, Johnson DL (1988) Low-frequency tube waves in permeable rocks. Geophysics 44(4):519–527

H. Liu, *Principles and Applications of Well Logging*, Springer Mineralogy,
DOI 10.1007/978-3-662-53383-3

19. Chemali R, Gianzero S, Su SM (1984) The depth of investigation of compressional wave logging for the standard and the long spacing sonde. In: Ninth SAID Colloquium, Paper 13
20. Clavier C, Coates G, Dumanoir J (1984) Theoretical and experimental basis for the dual water model for interpretation of shaly sands. Paper 6859 in: SPE J April:153–168
21. Crary S, Smith D (1990) The use of electromagnetic modeling to validate environmental corrections for the dual laterolog. Trans SPWLA 31st Annual Logging Symposium, paper C
22. Davies DH, Faivre O, Gounot M-T, Seeman B, Trouiller J-C, Benimeli D, Ferreira AE, Pttman DJ, Smits J-W, Randrianavony M, Anderson BI, Lovell J (1992) Azimuthal resistivity imaging: a new generation laterolog. Presented at the 67th SPE Annual Technical Conference and Exhibition, paper SPE 24676
23. Davis RR, Hall JE, Boutemy YL (1981) A dual porosity CNL logging system. Presented at SPE 56th Annual Technical Conference and Exhibition, paper SPE 10296
24. de Kuijper A, Sandor RKJ, Hofman JP, Koelman JMVA, Hofstra P, de Waal JA (1995) Electrical conductivities in oil-bearing shaly sand accurately described with the SATORI saturation model. Trans SPWLA 36th Annual Logging Symposium, paper M
25. Dewan JT (1983) Essentials of modern open-hole log interpretation. PennWell Publishing, Tulsa, OK
26. Doll HG (1955) Electrical resistivity well logging method and apparatus. US Patent No 2712627
27. Atlas Dresser (1983) Well logging and interpretation techniques, the course for home study. Dresser Industries, Houston, TX
28. Duderstadt JJ, Hamilton LJ (1976) Nuclear reactor analysis. Wiley, New York
29. Ellis DV (1982) Correction of NGT logs for the presence of KCl and barite muds. Trans SPWLA 23rd Annual Logging Symposium, paper O
30. Ellis DV (1986) Neutron porosity devices-what do they measure? First Break 4(3):11–17
31. Ellis DV (1987) Nuclear logging techniques. In: Bradley H (ed) Petroleum production handbook. SPE, Dallas, TX
32. Ellis DV, Case CR, Chiaramonte JM (2003) Porosity from neutron logs I: measurement. Petrophysics 44(6):383–395
33. Ellis DV, Chiaramonte JM (2000) Interpreting neutron logs in horizontal wells: a forward modeling tutorial. Petrophysics 41(1):23–32
34. Evans RD (1967) The atomic nucleus. McGraw-Hill, New York
35. Evans, M, Best D, Holenka J, Kurkoski P, Sloan W (1995) Improved formation evaluation using azimuthal porosity data while drilling. Presented at the SPE 70th Annual Technical Conference and Exhibition, paper SPE 30546
36. Flanagan WD, Bramblett RL, Galford JE, Hertzog RC, Plasek RE, Olesen JR (1991) A new generation nuclear logging system. Trans SPWLA 32nd Annual Logging Symposium, paper Y
37. Gadeken LL, Madigan WP, Smith HD Jr (1995) Radial distribution of 60Co contaminants surrounding wellbores at the Hanford site. IEEE Nuclear Sci Symp Med Imaging Conf Rec 1:214–218
38. Gilchrist WA, Galford JE, Flaum C, Soran PD, Gardner JS (1986) Improved environmental corrections for compensated neutron logs. Presented at SPE 61st Annual Technical Conference and Exhibition, paper SPE 15540
39. Griffiths R, Smits JW, Faivre O, Dubourg I, Legendre E, Doduy J (1999) Better saturation from new array laterolog. Trans SPWLA 40th Annual Logging Symposium, paper DDD
40. Guyod H (1944) Fundamental data for the interpretation of electric logs. Oil Weekly 115 (38):21–27
41. Hassan M, Hossin A, Combaz A (1976) Fundamentals of the differential gamma ray log-interpretation technique. Trans SPWLA 17th Annual Logging Symposium, paper H

42. Havira RM (1982) Ultrasonic cement bond evaluation. Trans SPWLA 23rd Annual Logging Symposium, paper N
43. Hearst JR, Nelson P (1985) Well logging for physical properties. McGraw-Hill, New York
44. Herrick DC, Kennedy WD (1993) Electrical efficiency: a pore geometric model for the electrical properties of rocks. Trans SPWLA 34th Annual Logging Symposium, paper HH
45. Heslop A (1974) Gamma-ray log response of shaly sandstones. Trans SPWLA 15th Annual Logging Symposium, paper M
46. Hill HJ, Milburn JD (1956) Effect of clay and water salinity on electro-chemical behavior of reservoir rocks. Pet Trans, AIME 207:65–72
47. Holenka J, Best D, Evans M, Sloan B (1995) Azimuthal porosity while drilling. Trans SPWLA 36th Annual Logging Symposium, paper BB
48. Hottman CE, Johnson RK (1965) Estimation of formation pressures from log derived shale properties. J Pet Tech 9:717–722
49. Hsu K, Hashem M, Bean CL, Plumb R, Minerbo GN (1997) Interpretation and analysis of sonic-while-drilling data in overpressured formations. Trans SPWLA 38th Annual Logging Symposium, paper FF
50. Itskovitch GB, Mezzatesta A, Strack KM, Tabarovsky L (1998) High-definition lateral log resistivity device: basic physics and resolution. Trans SPWLA 39th Annual Logging Symposium, paper V
51. Jackson JA (2001) Los Alamos NMR well logging project. Concepts Magn Reson 13 (6):368–378
52. Jan Y-M, Harrell JW (1987) MWD directional-focused gamma ray – a new tool for formation evaluation and drilling control in horizontal wells. Trans SPWLA 28th Annual Logging Symposium, paper A
53. Keller GV, Frischknecht FC (1966) Electrical methods in geophysical prospecting. Pergamon Press, Oxford
54. Kennedy WD, Herrick DC (2004) Conductivity anisotropy in shale-free sandstone. Petrophysics 45(1):38
55. Kenyon WE (1997) Petrophysical principles of applications of NMR logging. Log Anal 38 (2):21–43
56. Kenyon WE, Howard JJ, Sezginer A, Strayley C, Matteson A, Horkowitz K, Ehrlich R (1989) Pore-size distribution and NMR in microporous cherty sandstones. Trans SPWLA 30th Annual Logging Symposium, paper LL
57. Kenyon WE, Straley C, Sen PN, Herron M, Matteson A, Takezaki H, Petricola MH (1995) A laboratory study of nuclear magnetic resonance relaxation and its relation to depositional texture and petrophysical properties – carbonate Thamama group, Mubarraz field, Abu Dhabi. SPE Middle East Oil Show, Bahrain, paper SPE 29886
58. Kitsunezaki C (1980) A new method for shear-wave logging. Geophysics 45(10):1489–1506
59. Kleinberg RL (2001) NMRwell logging at Schlumberger. Concepts Magn Reson 13 (6):396–403
60. Kleinberg RL, Straley C, Kenyon WE, Akkurt R, Farooqui S (1993) Nuclear magnetic resonance of rocks: T1 vs. T2. Presented at SPE 68th Annual Technical Conference and Exhibition, paper SPE 26470
61. Kleinberg RL, Vinegar HJ (1996) NMR properties of reservoir fluids. Log Anal 37(6):20–32
62. Korringa J, Seevers DO, Torrey HC(1962) Theory of spin pumping and relaxation in systems with a low concentration of electron spin resonance centers. Phys Rev 127 (4):1143–1150
63. Liu HL, Johnson DL (1996) Effects of an elastic membrane on tube waves in permeable formations. J Acoustic Soc Am 101(6):3322–3329

64. Lo S-W, Hirasaki GJ, House WV, and Kobayashi R (2000) Correlations of NMR relaxation time with viscosity, diffusivity and gas/oil ratio of methane/hydrocarbon mixtures. Presented at the SPE 75th Annual Technical Conference and Exhibition, paper SPE 63217
65. Loren JD, Robinson JD (1969) Relations between pore size fluid and matrix properties, and NML measurements. Presented at the SPE 44th Annual Technical Conference, paper SPE 2529
66. Lynch EJ (1962) Formation evaluation. Harper & Row, New York, p 213
67. Marett G, Chevalier P, Souhaite P, Suau J (1976) Shaly sand evaluation using gamma ray spectrometry applied to the North Sea Jurassic. Trans SPWLA 17th Annual Logging Symposium, paper DD
68. Maute RE, Lyle WD, Sprunt ES (1992) Improved data-analysis method determines Archie parameters from core data. Paper 19399 in: J Pet Tech January: 103–107
69. McKeon DC, Scott HD (1988) SNUPAR – a nuclear parameter code for nuclear geophysics applications. Nucl Geophys 2(4):215–230
70. Meiboom S, Gill D (1958) Modified spin-echo method for measuring nuclear relaxation times. Rev Sci Instrum 29:688–691
71. Melcher CL, Schweitzer JS, Utsu T, Akiyama S (1990) Scintillation properties of GSO. IEEE Trans Nucl Sci 37(2):161–164
72. Mirotchnik KD, Allsopp K, Kantzas A, Curwen D, Badry R (1999) Low field NMR-tool for bitumen sands characterization: a new approach. Presented at the SPE 74th Annual Technical Conference and Exhibition, paper SPE56764
73. Moran JH (1982) Induction logging – geometrical factors with skin effect. The Log Analyst 23(6):4–10
74. Morley J, Heidler R, Horkowitz J, Luong B, Woodburn C, Poitsch M, Borbas T, Wendt B (2002) Field testing of a new nuclear magnetic resonance logging while drilling tool. Presented at the SPE 77th Annual Technical Conference and Exhibition, paper SPE 77477
75. Morris CF, Little TM, Letton W(1984) A new sonic array tool for full waveform logging. Presented at the 59th SPE Annual Technical Exhibition and Conference, Paper SPE 13285
76. Paillet FL (1980) Acoustic propagation in the vicinity of fractures which intersect a fluid-filled borehole. Trans SPWLA, 21st Annual Logging Symposium, paper DD
77. Pickett GR (1974) Formation evaluation. Unpublished lecture notes, Colorado School of Mines, Golden CO
78. Plona T, Kane M, Alford J, Endo T, Walsh J, Murray D (2005) Slowness frequency projection logs: a new QC method for accurate sonic slowness evaluation. Trans SPWLA 46th Annual Logging Symposium, paper T
79. Plona T, Sinha B, Kane M, Shenoy R, Bose S, Walsh J, Endo T, Ikegami T, Skelton O (2002) Mechanical damage detection and anisotropy evaluation using dipole sonic dispersion analysis. Trans SPWLA 43rd Annual Logging Symposium, paper F
80. Plumb R, Edwards S, Pidcock G, Lee D, Stacey B (2000) The mechanical earth model concept and its application to high-risk well construction projects. Presented at the 2000 IADC/SPE Drilling Conference, paper SPE 59128
81. Prammer MG, Drack E, Goodman G, Masak P, Menger S, Morys M, Zannoni S, Suddarth B, Dudley J (2000) The magnetic resonance while-drilling tool: theory and operation. Presented at the SPE 75th Annual Technical Conference and Exhibition, paper SPE 62981
82. Quirein JA, Gardner JS, Watson JT (1982) Combined natural gamma spectral/ litho-density measurement applied to complex lithologies. Presented at the 57th SPE Annual Technical Conference and Exhibition, paper SPE 11143
83. Roberts JN, Schwartz LM (1985) Grain consolidation and electrical conductivity in porous media. Phys Rev B 31(9):5990–5997

84. Schlumberger (1985) Interpretation charts. Schlumberger, New York
85. Schwartz LM, Kimminau S (1987) Analysis of electrical conduction in the grain consolidation model. Geophysics 52(10):1402–1411
86. Scott HD, Flaum C, Sherman H (1982) Dual porosity CNL count rate processing. Presented at SPE 57th Annual Technical Conference and Exhibition, paper SPE 11146
87. Scott HD, Wraight PD, Thornton JL, Olesen J-R, Hertzog RC, McKeon DC, DasGupta T, Albertin IJ (1994) Response of a multidetector pulsed neutron porosity tool. Trans SPWLA 35th Annual Logging Symposium, paper J
88. Seevers DO (1967) A nuclear magnetic method for determining the permeability of sandstone. Trans SPWLA Annual Logging Symposium, paper L
89. Segesman FF (1995) Measurement while drilling. Reprint No 40, SPE Reprint Series, SPE, Dallas, TX
90. Sen PN (2004) Time-dependent diffusion coefficient as a probe of geometry. Concepts Magn Reson Part A 23A(1):1–21
91. Sinha BK, Asvadurov S (2004) Dispersion and radial depth of investigation of borehole modes. Geophys Prospect 52(44):271–286
92. Smith HD Jr, Robbins A, Arnold DM, Gadeken LL, Deaton JG (1983) A multifunction compensated spectral natural gamma ray logging system. Presented at the 58th Annual Technical Conference and Exhibition, paper SPE 12050
93. Straley C, Morriss CE, Kenyon WE, Howard JJ (1991) NMRin partially saturated rocks: laboratory insights on free fluid index and comparison with borehole logs. Trans SPWLA 32nd Annual Logging Symposium, paper CC
94. Straley C, Rossini D, Vinegar HJ, Tutunjian PN, Morriss CE (1997) Core analysis by low-field NMR. The Log Analyst 38(2):84–94
95. Taherian MR, Habashy TM, Schroeder RJ, Mariani DR, Chen M-Y (1995) Laboratory study of the spontaneous potential – experimental and modeling results. The Log Analyst 36(5):34–48
96. Timur A (1968) An investigation of permeability, porosity and residual water saturation relationships for sandstone reservoirs. Log Anal 9(4):8–17
97. Timur AT (1972) Nuclear magnetism studies of carbonate rocks. Trans SPWLA 13th Annual Logging Symposium, paper N
98. Tittman J, Sherman H, Nagel WA, Alger RP (1966) The sidewall epithermal neutron porosity log. J Pet Tech 18:1351–1362
99. Trouiller JC, Dubourg I (1994) A better deep laterolog compensated for Groningen and reference effects. Trans SPWLA 35th Annual Logging Symposium, paper VV
100. Truax JA, Jacobson LA, Simpson GA, Durbin DP, Vasquez Q (2001) Field experience and results obtained with an improved carbon/oxygen logging system for reservoir optimization. Trans SPWLA 42nd Annual Logging Symposium, paper V
101. Winkler KW (1997) Acoustic evidence of mechanical damage surrounding stressed boreholes. Geophysics 62(1):16–22
102. Winkler KW, Liu HL, Johnson DL (1989) Permeability and borehole Stoneley waves: comparison between experiment and theory. Geophysics 54(1):66–75
103. Wong P-Z, Koplik J, Tomanic JP Conductivity and permeability of rocks. Phys Rev B 30 (11):6606–6614
104. Zienkiewicz OC (1971) The finite element method in engineering sciences. McGraw-Hill, New York
105. Orlowska S (2003) Conception et prediction des characteristiques dielectric des materiaux composites a deux et trois phases par la modelisation et la validation experimentale. PhD thesis, Ecole Centrale de Lyon
106. Hizem M (2006) Personal communication.

107. Bona N, Rossi E, Capaccioli S (2001) Electrical measurements in the 100 Hz to 10 GHz frequency range for efficient wettability determination. Paper SPE 69741 in: SPE J March:80–88
108. Kenyon WE, Baker PL (1984) EPT interpretation in carbonates drilled with salt muds. Presented at the 59th SPE Annual Technical Conference and Exhibition, paper 13192
109. Sen P (1980) The dielectric and conductivity response of sedimentary rocks. Presented at the 55th SPE Annual Technical Conference and Exhibition, paper 9379
110. http://www.slb.com
111. http://www.halliburton.com.cn
112. http://www.bakerhughes.com/
113. http://www.weatherford.com/
114. http://www.shell.com.cn